Imperial College London
Department of Materials

Nitrogen and Fatigue on Ti-6Al-4V

Christopher R Collins

Submitted in part fulfilment of the requirements
for the degree of Doctor of Philosophy at
Imperial College London, July 2022

I hereby declare that this thesis and the work reported herein was composed by and originated entirely from me. Information derived from the published and unpublished work of others has been acknowledged in the text and references are given in the list of sources.

Christopher R Collins (2022)

The copyright of this thesis rests with the author. Unless otherwise indicated,its contents are licensed under a Creative Commons Attribution-Non Commercial 4.0 International Licence (CC BY-NC).

Under this licence, you may copy and redistribute the material in any medium or format. You may also create and distribute modified versions of the work. This is on the condition that: you credit the author and do not use it, or any derivative works, for a commercial purpose.

When reusing or sharing this work, ensure you make the licence terms clear to others by naming the licence and linking to the licence text. Where a work has been adapted, you should indicate that the work has been changed and describe those changes.

Please seek permission from the copyright holder for uses of this work that are not included in this licence or permitted under UK Copyright Law.

Abstract

The work in this thesis was designed to aid the understanding of the effect of the ingress of nitrogen on diffusion bonded super plastically formed structures manufactured from the ubiquitous titanium alloy - Ti-6Al-4V. This wasn't an abstract question but one originating from a desire to improve the communities knowledge of the integrity of in-service components that may have been affected by an ingress of air/nitrogen during manufacture. To achieve this, that aim was split down into smaller questions with experiments designed to answer each of those smaller questions allowing for a picture of the answer to the overall aim to be established. Those smaller questions were:

- What effect does nitrogen have on the mechanical properties of Ti-6Al-4V?
- What effect does a vacuum environment have on the fatigue properties of Ti-6Al-4V?
- What effect does a vacuum environment coupled with a diffused gradient of nitrogen have on the fatigue properties of Ti-6Al-4V?

The main takeaway conclusions for the reader should be the following:

- A gradient of nitrogen diffused into an internal surface in a super-plastically formed component will lead to a reduction in the mechanical capability of that surface.
- The nature of the gradient has a significant effect, a shallow deep diffusion profile will have less of a deleterious effect than a steep shallow diffusion profile as the higher concentrated content in the second case will lower the required localised strain to failure at the surface causing a crack to be initiated. However the depth of the diffusion profile will have a large bearing on the capability of the component to survive that initial starter crack.
- Nitrogen content, the presence of a vacuum and the dominant underlying crystallographic texture of the material have significant effects on mode of fracture and the subsequent observable fractographic features. Care needs to be taken when examining fracture faces from super-plasctically formed titanium components or test samples to ensure the underlying crystallographic texture is understood and the presence of any diffused interstitial species is determined and characterised appropriately to enable more accurate conclusion to be drawn from any fractographic work.

Acknowledgements

- David Dye - Professor of Metallurgy Imperial College for his supervision guidance and technical input
- Ben Wood - Imperial College Laboratory Technician for all his support in running tests, machining of jigs and fixtures and morning coffees!
- Felicity Dear - Fellow PhD candidate for her support in EBSD and TEM work
- Gary Gao - Fellow PhD candidate for his support in fatigue loading of my ex-situ CT scanned samples
- Yitong Shi - Post-Doc for her support in the proof of vacuum experiment
- Richard Chater - Imperial College Instrumentation Research Fellow for his support in the proof of vacuum experiment
- Dave Rugg - Retired Rolls-Royce Senior Fellow for Materials for all his guidance, reassurance and support during my early career at Rolls-Royce and for his championing of this work
- Mike Wallis - Retired Rolls-Royce Commodity Lead WCFB for his input on defining the questions this project aims to answer
- Jonathan Green - Rolls-Royce Image Resource Senior Photographer for his support in optical imaging of fracture faces
- Mohammed Azeem - Lecturer at Leicester University for his support in undertaking Micro-CT scans of my hollow samples
- Graham Clark - Technician at Leicester University for his support in undertaking Micro-CT scans of my hollow samples
- Chris Harvey - Senior Lecturer in Structural Mechanics at Loughborough University for his support with LaTeX issues
- Loughborough Surface Analysis - DSIMS provider for their all round helpfulness and discussions around determining surface chemistry in titanium surfaces
- EBP Welding - Electron Beam Welders for vacuum samples

To my wife Rachel, sons Sam and Matt (both born during the course of this work) and my colleagues past and present at Rolls-Royce and Imperial College.

I have made you a tester of metals among my people, that you may know and test their ways.

- ESV Jeremiah 6:27

Contents

Abstract **3**

Acknowledgements **4**

1 Introduction **10**
1.1 The Problem . . . 10
1.2 Layout and Contents of the Following Chapters . . . 11

2 Literature Review **14**
2.1 Titanium processing . . . 14
2.1.1 Microstructure . . . 15
2.1.2 Crystallographic Texture . . . 17
2.1.3 Diffusion Bonding and Superplastic Forming (DB/SPF) . . . 20
2.2 Fatigue of Titanium Alloys . . . 21
2.2.1 Initiation . . . 22
2.2.2 Fatigue Crack Growth . . . 23
2.2.3 Fractography of Fatigue - Facets and Striations . . . 24
2.2.4 Lifing of Fatigue Cracks . . . 26
2.3 The Effect of Testing Atmosphere on Fatigue Crack Growth . . . 27
2.3.1 Requirements for vacuum . . . 27
2.3.2 Changes in Crack Growth Threshold . . . 28
2.3.3 Fatigue Crack Growth Rates . . . 29
2.3.4 Plastic Zone Size . . . 29
2.3.5 Fractography . . . 30
2.4 The Effects of Interstitials on Titanium . . . 31
2.4.1 Oxygen, Nitrogen and the β solvus . . . 31
2.4.2 Mechanical Property Effect of Interstitial Additions . . . 31
2.4.3 Interstitial Additions and α-phase Lattice Parameters . . . 32
2.5 Tomography of Fatigue Cracks . . . 33
2.5.1 Monitoring crack growth . . . 33
2.5.2 Sample properties . . . 34
2.5.3 Fatigue and CT . . . 34
2.6 Summary of Literature Review . . . 35
2.6.1 Titanium processing . . . 35
2.6.2 Fatigue in Titanium Alloys . . . 35
2.6.3 The Effect of Testing Atmosphere on Fatigue Crack Growth . . . 36
2.6.4 The Effects of Interstitials on Titanium . . . 36
2.6.5 Tomography of Fatigue Cracks . . . 37

2.7 Figures and Tables . . . 38

3 Investigative techniques and methods 60
3.1 Introduction . . . 60
3.2 Core Techniques . . . 61
3.2.1 Automated 3D optical microscopy . . . 61
3.2.2 Automated SEM image collation and capture . . . 61
3.2.3 EBSD fractography . . . 62
3.3 Specialist Techniques . . . 62
3.3.1 Focussed ion beam secondary ion mass spectrometry (FIB-SIMS) . . . 62
3.3.2 Dynamic secondary ion mass spectrometry (DSIMS) . . . 63
3.3.3 Widefield confocal microscopy . . . 63
3.3.4 Spatially resolved acoustic spectroscopy (SRAS) . . . 63
3.3.5 FIB lift-outs . . . 64
3.3.6 Atom Probe Tomography (APT) . . . 64
3.4 Novel Techniques . . . 64
3.4.1 Micromechanical testing . . . 64
3.4.2 High speed atomic force microscopy (HS-AFM) . . . 65
3.4.3 Micro-computed tomography (µCT) . . . 65
3.5 Conclusions . . . 65
3.6 Figures . . . 67

4 Nitrogen and Ti-6Al-4V 72
4.1 Introduction . . . 73
4.2 Experimental Procedure . . . 74
4.3 Results . . . 76
4.4 Discussion . . . 79
4.4.1 Composition . . . 79
4.4.2 Tensile and basic mechanical properties . . . 80
4.4.3 Fatigue lifetimes . . . 81
4.4.4 Fatigue fractography . . . 81
4.5 Conclusions . . . 83
4.6 Figures and Tables . . . 85

5 Air vs Vacuum 97
5.1 Introduction . . . 97
5.2 Experimental Procedure . . . 98
5.3 Results . . . 100
5.4 Discussion . . . 102
5.4.1 Testing Level of Vacuum in the Samples . . . 102
5.4.2 Fractographic Results . . . 102
5.4.3 Air vs Vacuum . . . 103
5.4.4 Effect of Nitrogen . . . 104
5.4.5 Novel test method . . . 105
5.5 Conclusions . . . 105
5.6 Figures and Tables . . . 107

6 Surface Gradient Effect **136**
6.1 Introduction . . . 136
6.2 Experimental Procedure . . . 137
6.3 Results . . . 139
6.4 Discussion . . . 140
6.4.1 Sample production . . . 140
6.4.2 Numerical Results . . . 140
6.4.3 CT and Fractographic Results . . . 141
6.5 Conclusions . . . 143
6.6 Figures and Tables . . . 144

7 Conclusions and Further Work **164**
7.1 Overview of Chapter Conclusions . . . 164
7.1.1 Chapter 4 - What effect does nitrogen have on the mechanical properties of Ti-6Al-4V? . . . 164
7.1.2 Chapter 5 - What effect does a vacuum environment have on the fatigue properties of Ti-6Al-4V? . . . 165
7.1.3 Chapter 6 - What effect does a vacuum environment coupled with a diffused gradient of nitrogen have on the fatigue properties of Ti-6Al-4V? 166
7.2 Summary of Conclusions and Review of the Problem . . . 167
7.3 Lessons learnt . . . 168
7.4 Further work . . . 169

References **171**

List of Tables

2.1 Titanium alloying additions 59
2.2 Comparison of material properties between Ti-6Al-4V (MSRR8672 TFH) and Commercially available CPTi Grade 4 59

4.1 Measured oxygen/nitrogen compositions obtained (ppmw, average and standard deviation). Typical nominal Ti-6Al-4V plate product is around 2000 ppmwO and $\leq$ 300 ppmwN. 95
4.2 Showing measured α_p widths from the images in Figure 4.5 95
4.3 Effect of nitrogen content on LCF life, at low nitrogen contents where reasonable ductility remained. 96
4.4 Effect of nitrogen content of high cycle fatigue test lifetime and HCF strength. . 96

5.1 Test Sample Matrix 133
5.2 Hiden cracking pattern guide excerpt [29] 133
5.3 Life test results 133
5.4 Ex-situ CT scan intervals 134
5.5 Testing results for ex-situ monitored samples. *HF022 and HF036 were left to fail at the same stress despite going past the previously used step cycle limit. HCF strengths have been calculated on the basis of the samples being a run out. 134
5.6 Overall HCF strength for each composition and environmental condition measured during this work. *HF022 and HF036 were left to fail at the same stress despite going past the step length, HCF strengths have been calculated on the basis of the samples being a run out. **These values have been calculated disregarding HF036. 135
5.7 This table shows the data from the quantitative fractography 135

6.1 This table shows the results of the life tests carried out to determine test conditions for the ex-situ CT work 162
6.2 This table shows the initiation life in cycles, as a percentage of total life, total samples lives and the calculated HCF strengths from the ex-situ testing 162
6.3 This table shows the average calculated HCF strength from the results of all the tested samples 162
6.4 This table shows the scan intervals for the ex-situ CT scans - All cycles testing at a peak stress of 250MPa 163
6.5 This table shows the data from the quantitative fractography 163

List of Figures

2.1 a: HCP unit cell - b: BCC unit cell - adapted from Lutjering and Williams - Titanium . . . 38
2.2 Range of Ti alloys as a function of volume fraction of β . . . 38
2.3 3D phase diagram showing the range of Ti alloys adapted from Leyens [39] . . . 38
2.4 a) Showing process route for fully lamellar titanium microstructures [41, 40] b) Schematic microstructure . . . 39
2.5 a) Showing process route for fully equiaxed and bi-modal titanium microstructures [41, 40] b) Schematic fully equiaxed microstructure c) Schematic bi-modal microstructure . . . 39
2.6 Schematic showing the response of a variety of primary-α colonies to rolling [20] 40
2.7 A microstructural deformation mechanism map for Ti-6Al-4V taken from [69] . . 41
2.8 Figure showing how modulus changes with orientation of the c-axis within a HCP unit cell. [12] . . . 41
2.9 Schematic showing textures of samples taken from XR and UD plate. Adapted from [8] . . . 42
2.10 a) Trent 700 Cutaway Schematic b) Trent 1000 WCFB - Credit Rolls-Royce Image Resource . . . 42
2.11 Schematic of microstructural changes during diffusion bonding [68] . . . 43
2.12 Schematic cross section of a DB/SPF fan blade within the steel dies. The blue represents the argon gas used to inflate the blade, adapted from [55] . . . 43
2.13 Schematic adapted from [24] showing extrusions and intrusions on a material surface . . . 43
2.14 Figure from Ritchie et al. [64] for Ti-6Al-4V showing crack growth rate against ΔK for a range of R-ratios. Note the increase in $\Delta K_{threshold}$ as the R-ratio decreases 44
2.15 Figure from Ritchie et al. [64] for Ti-6Al-4V showing the variation for $\Delta K_{max,threshold}$ and $\Delta K_{threshold}$ as a function of R-ratio . . . 44
2.16 Figure from [11] showing the transition from stage 1 to stage 2 in a cross-sectional micrograph and in a growth rate as a function of depth chart . . . 45
2.17 Taken from [36] Commercial titanium, 675°C/1h/AC, tensile tested at room temperature. High-magnification SEM fractograph of the conical dimples shows serpentine glide (stretch-like regions) surrounded by fine dimples. . . . 45
2.18 Taken from [10] Serpentine glide surface in annealed Armco iron. This glide was produced by slip when the root of a notch in this wire specimen was opened up by bending at room temperature. The dark surfaces (A) apparently were a single surface before slip on a second series of parallel planes produced the light parallel surfaces (B). Examples of ripples may be seen between the arrows (C). Palladium-shadowed direct-carbon replica (x9000). . . . 46

2.19 a) Showing optical image of LCF fracture face. Yellow area fatigue, Orange area ductile overload fracture, Red area shear lips. b) Compound SEM images of same fracture as is shown in a). c) Region of striated fatigue crack growth within Yellow area. d) Region of ductile overload within the Orange area. 47
2.20 a) SEM fractograph showing a fracture surface where the fractographic features have changed as a function of primary-α grain orientation. b) Close-up of region A. c) Close-up of region B. From [9] 48
2.21 Laird model of striation formation. The idle crack (a) opens under tensile load which activates two slip planes at the crack tip (b) and the crack opens out (c). Upon unloading the crack tip blunting does not fully reverse (d) this causes the crack to propagate one increment (e). This process repeats with further load cycling (f). From [49, 38, 82] 48
2.22 S-N curve showing a comparison of the fatigue behaviour of steel and aluminium, adapted from [3] 49
2.23 Schematic of a δa/δN vs log-ΔK plot adapted from [80] 49
2.24 Figure recreated from [85] showing the effect of vacuum on threshold of fatigue cracks for metallic materials 50
2.25 Figure from Ritchie et al. [64] for Ti-6Al-4V showing crack growth rate against ΔK for air vs vacuum. 50
2.26 Figure recreated from [92] showing fatigue crack growth against ΔK as a function of environment 51
2.27 Figure recreated from [92] showing crack length against number of cycles as a function of environment 51
2.28 Figure from [31] showing SN curves for CPTi samples tested in air and vacuum. Black triangles are from tests that experienced a violent damping phenomena - there is no further explanation of what this phenomena was in the source paper 52
2.29 Figure from [79] showing an SN curves for a range of CPTi samples tested in air and vacuum. The hollow triangles are tests that experienced a violent damping phenomena at the test frequency 52
2.30 Figure from [79] showing a sample life vs test pressure curve for CPTi samples tested in varying levels of air pressure 53
2.31 Figure from [31] showing the relative sizes of plastics zones formed in air and vacuum during fatigue testing of CPTi samples at a peak stress of 160MPa . . . 53
2.32 Titanium nitrogen phase diagram taken from McDonald and Wallwork [46] . . . 54
2.33 Titanium nitrogen phase diagram taken from Kessler [37] 55
2.34 Effect of nitrogen on room-temperature tensile properties and hardness of iodide titanium adapted from ([26, 57]) 56
2.35 Effect of nitrogen on lattice parameters c, a and the c/a ratio [1] 57
2.36 Schematic chart showing capture rates against spatial resolution of laboratory based CT and synchrotron adapted from [44] 57
2.37 Schematic chart showing the relationship between CT method, object size and spatial resolution, adapted from [23] 58
2.38 Schematic showing overview of the CT process adapted from [5] 58

3.1 Several factors determine the usage of techniques in failure investigation, schematically shown here in radar plots. (a) Optical microscopy provides a rapid overview of samples and is used in every investigation, while microcantilever testing of local mechanical properties is still under development as an investigative tool. (b) FIB-SIMS is commonly applied in academic research, but DSIMS results are more accessible for industry. 67
3.2 A 3D optical micrograph of a high cycle fatigue fracture in a compressor blade aerofoil, captured with a Zeiss SmartZoom 5 system. Optical images are recorded in a stitched focus stack, calibrated so that accurate topographical information can be extracted, as demonstrated in the three height profiles shown. 68
3.3 (a) An example of image collation in Zeiss's SmartBrowse software, showing SEM images located relative to one another using metadata. Here, the boundary between regions of different fracture behaviour was clearly identified in the context of the fracture surface as a whole. (b) A stitched image of a fracture surface captured using Zeiss's SmartStitch software, providing a large field of view while retaining good resolution. 68
3.4 EBSD fractography of a facetted fracture surface, demonstrating the capabilities and limitations of current systems. Although several facets have been successfully indexed, the surface roughness of the fracture prevents complete mapping and remains challenging. 69
3.5 Two SIMS techniques are applicable to failure investigation. (a) An SEM image shows FIB-SIMS trenches made to create a coarse depth profile across a fracture surface, requiring prior flattening with glancing-angle FIB milling for comparable measurements. (b) DSIMS provides finer-scale depth profiling of nitrogen concentration in ten different Ti-6Al-4V (wt.%) surfaces, and is made fully quantitative by calibration to a standard. Inset is an SEM micrograph showing a sputtered crater after measurement. 69
3.6 Widefield confocal microscopy analysis of a fracture surface on a compressor blade, acquired using a Zeiss SmartProof 5 system to produce a height map (a) and an optical image (b). The arc-like feature indicated in the images is a beach-mark resulting from high cycle fatigue. 70
3.7 A SRAS velocity map of two Ti-6Al-4V (wt.%) plates that have been diffusion bonded together (bond line indicated by red arrows). The differences in both grain size (finer in the LHS plate) and texture (macrozones evident in the RHS plate) are evident. 70
3.8 An SEM image of a FIB-milled microcantilever in a titanium alloy, ready for loading with an indenter to investigate the orientation dependence of slip behaviour. In industrial applications, this could be used to probe slip behaviours in specific grains or features of interest on ex-service parts. 71
3.9 (a) A 3D µCT isosurface reconstruction of a hollow fatigue test specimen, showing a fatigue crack during propagation. (b) The specimen geometry shown in a CAD model. 71

4.1 Effect dissolved interstitial solid solution elements on yield strength, adapted from Conrad [22]. 85
4.2 Optical micrograph showing the microstructure of a reference standard industrial plate product. 85

4.3 Sample drawings for specimens tested in this study, a) tensile and b) high cycle fatigue . . . 86
4.4 β-transus curves from literature, PANDAT and this experimental work (Black points with green error bars) [91] [57] [84]. . . . 86
4.5 Optical images showing the microstructures of the four alloys produced. . . . 87
4.6 EBSD maps showing HCP textures of the four compositions . . . 88
4.7 Effect of nitrogen additions, processed to achieve similar microstructures, on yield strength (green), ultimate tensile strength, UTS (Blue), and % elongation (Red). 88
4.8 Effects of N additions on the β transus temperatures, measured metallographically by reheating and quenching globularised material, and on the hardness of materials processed to achieve similar, near-equiaxed microstructures. . . . 89
4.9 Effect of nitrogen additions (ppmwN) on calculated HCF strength, inferred from the HCF step test data. The value at 50 ppmwN is for commercial reference material. . . . 89
4.10 Optical overviews of a fracture face from HCF samples of 240 and 1800 ppmwN 90
4.11 SEM fractographs of an HCF step test sample of 240 ppmwN composition. the fracture appearance at the initiation (green and blue) is shown, in contrast to the subsequent conventional striated fatigue crack growth regime at longer crack lengths (red). . . . 91
4.12 SEM fractographs showing a variety of views of the fracture face from a HCF sample of 3600 ppmwN composition . . . 92
4.13 Fractographic vs texture EBSD mapping for HCF step tested sample of 240 ppmwN 93
4.14 Fractographic vs texture EBSD mapping for HCF step tested sample of 3600 ppmwN . . . 94
4.15 Striation count data from HCF step tested samples containing 240 (in blue) and 560 ppmwN (in red). The cumulative cycles on the x axis start at 0 with the first striation measurement, not the crack initiation cycle. . . . 95

5.1 This schematic shows the steps taken to produce the samples for this study . . . 107
5.2 This schematic shows a cross-section representation of the samples tested in this work . . . 108
5.3 Chart showing the HCF strengths calculated of each of the test conditions. Note: the value for 560ppmwN at vacuum, hollow dot, has been changed. The reason for the change is that the sample tested had a poorly aligned notched causing premature failure. The value was adjusted based on the average debit seen air to vacuum from the other two compositions - 84MPa . . . 108
5.4 These photo's show how a 4-way vacuum crucifix was used to carryout the vacuum proof tests. A) shows the complete setup B) shows a close-up of the crucifix C) shows the view down the vertical axis of the crucifix looking at the ram profile contacting the sample. . . . 109
5.5 This chart shows the results of the vacuum proof tests. This chart shows the pressure change for a number of mass weights against analysis cycles. The red traces represent a known trace pattern for a methane signal . . . 110
5.6 This figure shows the optical overview from HF035 with the notch surface highlighted in red shading and the testing induced fracture shaded yellow. It can be seen from this figure that the notch isn't quite uniform in size or quite centred to the central axis of the test sample . . . 111

5.7 This figure shows a) an optical overview of a fracture from HF022 240ppmwN air sample and b) an SEM overview of the same fracture face (SE, 5.00kV, WD 4.8mm) . . . 112
5.8 This figure shows an SEM fractograph showing a) a region of facetted growth originating from the notch (SE, 5.00kV, WD 4.9mm) and b) a region of striated growth (SE, 5.00kV, WD 5.0mm) from HF022 240ppmwN air sample . . . 113
5.9 This figure shows the crack growth rates in µm per cycle at isolated locations as determined by SEM fractography for HF022 240ppmwN air sample, the red star indicates the approximate area of initiation. Inset is a schematic showing the macro crack propagation pattern . . . 114
5.10 This figure shows a) an optical overview of a fracture from HF028 240ppmwN vacuum sample and b) an SEM overview of the same fracture face (SE, 5.00kV, WD 4.7mm) . . . 115
5.11 This figure shows an SEM fractograph showing a) a region of facetted growth originating from the notch (SE, 5.00kV, WD 4.8mm) and b) a region of striated growth (SE, 5.00kV, WD 4.7mm) from HF028 240ppmwN vacuum sample . . . 116
5.12 This figure shows the crack growth rates in µm per cycle at isolated locations as determined by SEM fractography for HF028 240ppmwN vacuum sample, the red star indicates the approximate area of intiation . . . 117
5.13 This figure shows a) an optical overview of a fracture from HF002 500ppmwN air sample and b) an SEM overview of the same fracture face (SE, 5.00kV, WD 4.7mm) . . . 118
5.14 This figure shows an SEM fractograph showing a) a region of facetted growth originating from the notch (SE, 5.00kV, WD 4.7mm) and b) a region of striated growth (SE, 5.00kV, WD 4.7mm) from HF002 500ppmwN air sample . . . 119
5.15 This figure shows the crack growth rates in µm per cycle at isolated locations as determined by SEM fractography for HF002 500ppmwN air sample, the red star indicates the approximate area of intiation . . . 120
5.16 This figure shows a) an optical overview of a fracture from HF010 500ppmwN vacuum sample and b) an SEM overview of the same fracture face (SE, 5.00kV, WD 5.6mm) The flat regions of fracture face are from where the two sides of the fracture collided during run down on the test frame. . . . 121
5.17 This figure shows an SEM fractograph showing a) a region of facetted growth originating from the notch (SE, 5.00kV, WD 5.6mm) and b) a region of striated growth (SE, 5.00kV, WD 5.8mm) from HF010 500ppmwN vacuum sample . . . 122
5.18 This figure shows the crack growth rates in µm per cycle at isolated locations as determined by SEM fractography for HF010 500ppmwN vacuum sample, the red star indicates the approximate area of initiation. The flat regions of fracture face are from where the two sides of the fracture collided during run down on the test frame. . . . 123
5.19 This figure shows a) an optical overview of a fracture from HF036 Cross-rolled plate air sample and b) an SEM overview of the same fracture face (SE, 5.00kV, WD 4.9mm) . . . 124
5.20 This figure shows an SEM fractograph showing a) a region of facetted growth originating from the notch (SE, 5.00kV, WD 4.8mm) and b) a region of striated growth (SE, 5.00kV, WD 4.7mm) from HF036 Cross-rolled plate air sample . . . 125

5.21 This figure shows the crack growth rates in µm per cycle at isolated locations as determined by SEM fractography for HF036 Cross-rolled plate air sample, the red star indicates the approximate area of intiation 126
5.22 This figure shows an SEM fractograph showing a) a region of facetted growth originating from the notch (SE, 5.00kV, WD 4.8mm) and b) a region of striated growth (SE, 5.00kV, WD 5.1mm) from HF035 Cross-rolled plate vacuum sample 127
5.23 This figure shows an SEM fractograph showing a) a region of facetted growth originating from the notch (SE, 5.00kV, WD 4.9mm) and b) a region of striated growth (SE, 5.00kV, WD 4.9mm) from HF035 Cross-rolled plate vacuum sample 128
5.24 This figure shows the crack growth rates in µm per cycle at isolated locations as determined by SEM fractography for HF035 Cross-rolled plate vacuum sample, the red star indicates the approximate area of intiation 129
5.25 This figure shows a schematic indicating the general macroscopic crack propagation observed from the samples in this chapter 130
5.26 This figure shows a comparison of the range of crack propagation rates captured from the quantitative SEM fractography. Blue traces are Cross-rolled plate, Red traces are 240ppmwN and Green traces are 500ppmwN. This shows that the range of crack propagation rates was similar between all the samples measured . 131
5.27 This figure shows a comparison of the probability distribution curves for each of the ex-situ samples using data from Figure 5.26. The information drawn from this plot is that all the samples have a similar spread of observed crack growth rates 132

6.1 This schematic shows the steps taken to produce the samples for this study . . . 144
6.2 This schematic shows a cross-section representation of the samples tested in this work 145
6.3 This chart shows the measured interstitial gradient via DSIMS of the lower and higher gradient samples. For reference, these gradients up to around 3 to 5µm, contain in the order of 3000-4000ppmw O + N 146
6.4 This chart shows the measured interstitial gradient via DSIMS of the lower and higher gradient samples compared to some component results 147
6.5 This figure shows the optical overview from HF035 with the notch surface highlighted in blue shading, the testing induced fracture shaded yellow and the red shading representing the material affected by the gradient of interstitials. . . 148
6.6 This figure shows a CAD representation of the custom tensile rig used during the ex-situ CT work. The base plate was movable by X and Y micrometers to allow for centring to the centreline of the detector. The sleeve around the sample (set to transparency here) had mating faces that allowed for rapid sample exchange keeping it straight in the vertical axis. 149
6.7 This figure shows a) an optical overview of a fracture from S022 Low gradient sample and b) an SEM overview of the same fracture face (SE, 5.00kV, WD 9.3mm) 150
6.8 This figure shows an SEM fractograph showing a) a region of facetted growth originating from the notch (SE, 5.00kV, WD 9.4mm) and b) a region of striated growth (SE, 5.00kV, WD 9.4mm) from S022 Low gradient sample 151
6.9 This figure shows a number of 3D CT reconstructions (unregistered) of S022 Low gradient sample illustrating the coarse crack growth through the sample. The number next to each image signifies the CT scan number and the red arrows are there to aid the reader to spot the extent of cracking 152

6.10 This figure shows the crack growth rates in µm per cycle at isolated locations as determined by SEM fractography for S022 Low gradient sample 152
6.11 This figure shows a) an optical overview of a fracture from S013 High gradient sample and b) an SEM overview of the same fracture face (SE, 5.00kV, WD 5.3mm) 153
6.12 This figure shows an SEM fractograph showing a) a region of facetted growth originating from the notch (SE, 5.00kV, WD 5.0mm) and b) a region of striated growth (SE, 5.00kV, WD 5.1mm) from S013 High gradient sample 154
6.13 This figure shows a number of 3D CT reconstructions (unregistered) of S013 High gradient sample illustrating the coarse crack growth through the sample. The number next to each image signifies the CT scan number and the red arrows are there to aid the reader to spot the extent of cracking 155
6.14 This figure shows the crack growth rates in µm per cycle at isolated locations as determined by SEM fractography for S013 High gradient sample 156
6.15 This figure shows a) an optical overview of a fracture from S026 No gradient sample and b) an SEM overview of the same fracture face (SE, 5.00kV, WD 4.7mm) 157
6.16 This figure shows an SEM fractograph showing a) a region of facetted growth originating from the notch (SE, 5.00kV, WD 4.7mm) and b) a region of striated growth (SE, 5.00kV, WD 4.7mm) from S013 No gradient sample 158
6.17 This figure shows a number of 3D CT reconstructions (unregistered) of S026 No gradient sample illustrating the coarse crack growth through the sample. The number next to each image signifies the CT scan number and the red arrows are there to aid the reader to spot the extent of cracking 159
6.18 This figure shows the crack growth rates in µm per cycle at isolated locations as determined by SEM fractography for S026 No gradient sample 159
6.19 This figure shows two schematics indicating the general macroscopic crack propagation behaviours observed from the samples in this chapter. The top schematic shows what was observed on samples with a gradient and the lower schematic what was observed on the samples with no gradient (as was also observed in chapter 5) 160
6.20 This figure shows a comparison of the range of crack propagation rates captured from the quantitative SEM fractography, all the data points have been captured from baseline material 161

Chapter 1

Introduction

1.1 The Problem

This PhD was started following a package of work undertaken by the author in their day job as a Materials Engineer with Rolls-Royce. That work involved characterising the internal cavity surfaces of super-plastically formed titanium components. It was found that some components, on occasion, exhibited stabilised alpha surface microstructures along with diffused gradients of oxygen and nitrogen. It was postulated that the diffused gradient of oxygen and nitrogen had occurred due to an unintentional ingress of air during the super-plastic process. These findings caused the author to pose a number of questions around the effect an ingress of nitrogen could have in the integrity of super-plastically formed titanium components. Following discussions with Professors David Dye and David Rugg it was concluded that there was a lack of knowledge in published literature to answer those questions. Further discussion led to the formation of three clear interdependent subquestions that could be examined scientifically and when combined would enable the author and you the reader to have a greater understanding of the primary question - "What effect does an ingress of nitrogen have on the integrity of super-plastically formed titanium components?". The three subquestions are:

- What effect does nitrogen have on the mechanical properties of Ti-6Al-4V?
- What effect does a vacuum environment have on the fatigue properties of Ti-6Al-4V?

- What effect does a vacuum environment coupled with a diffused gradient of nitrogen have on the fatigue properties of Ti-6Al-4V?

The author has undertaken a review of the literature and subsequently was able to design a series of interdependent experiments each tailored to provide answers to the above questions and once combined provide answers to the primary question.

1.2 Layout and Contents of the Following Chapters

This thesis consists of a literature review followed by a discussion of available analysis techniques and then three chapters cataloguing the work undertaken to answer each of the above subquestions. At the end there is a chapter summarising the conclusions from each experimental chapter and a revisit of the primary question to see how far this work has progressed knowledge to enable an answer to be reached. There is also space given to a discussion of the lessons learnt during this work and suggestions for further work.

A more detailed outline of each chapter is given below:

- Chapter 2 contains the results of a thorough review of the pertinent literature around the technical fields identified at the start of this work. These fields include:

  1. Titanium processing, including the fundamental basics of microstructural and crystallographic texture developments during thermomechanical processing and the implications of those variations

  2. Fatigue of titanium alloys from initiation behaviour to steady crack growth and subsequent post failure analysis

  3. The effect of testing atmosphere on the fatigue behaviour of titanium alloys, with a specific focus on the effect of vacuum on crack growth rates and fractography

  4. How interstitial elements interact with titanium alloys and their resultant effect on mechanical properties

  5. The use of computed tomography in fatigue crack growth monitoring

- Chapter 3 is taken from a paper published by the author [18] exhibiting a number of techniques used during characterisation of the samples in this work and the authors day job. Techniques have been separated into the following types:

  1. Core techniques such as automated SEM and EBSD fractography

  2. Specialist techniques such as SIMS (dynamic and focussed ion beam) and spatially resolved acoustic spectroscopy

  3. Novel techniques including micro-computed tomography of growing cracks

- Chapter 4 is also taken from a paper published by the author [19] presenting the experimental work and analysis carried out on samples of Ti-6Al-4V that had been custom manufactured with a systematic wide range of nitrogen levels to explore the effect of increasing nitrogen content on Ti-6Al-4V. Observations were made around the following aspects:

  1. The effect of nitrogen on the tensile and basic mechanical properties

  2. The effect of nitrogen on the fatigue properties of Ti-6Al-4V

  3. The effect of nitrogen on the fractography of fatigue tested samples

- Chapter 5 is a continuation of the work in Chapter 4 taking material produced during that work and developing a novel test method. The test method was designed to try and provide further information around the effect of vacuum on the fatigue crack growth properties of Ti-6Al-4V. Key portions of this work are:

  1. Development of a new test methodology including complex sample fabrication and test method to determine the success of the novel samples

  2. The use of ex-situ computed tomography for crack growth monitoring and characterisation

  3. The effect of vacuum on fatigue crack growth in Ti-6Al-4V and subsequent fractographic analysis

- Chapter 6 builds on the work of Chapters 4 and 5, by taking the knowledge of the effect of

nitrogen on Ti-6Al-4V and using the novel test method to closer replicate the conditions needed to fulfil the aims of this work. Points of particular interest in this chapter include:

1. Introduction of a gradient of nitrogen to the cavity surfaces of hollow samples from Chapter 5

2. Analysis of the effect on fatigue crack growth of the presence of the gradient of nitrogen

- Chapter 7 contains an overview of the conclusions reached during the experimental work along with an evaluative summary of the issues that arose during work. It also contains reflections on lessons learnt followed by ideas for how to take this work forward. It needs to be said that this work was subject to a number of interruptions and trials arising from global events and the ambitious nature of the test work undertaken.

Chapter 2

Literature Review

2.1 Titanium processing

Commercially pure titanium is typically supplied in four grades (1-4), with the main variations between them being in the oxygen content. The intention of the addition of oxygen is to increase the ultimate tensile strength (240-550 MPa) and yield stress (170-483 MPa) at the expense of a reduction in elongation to failure (15-24%). However, strength retention with temperature is a short fall of CP grades. To address this and improve overall property balance alloys are used where increased strength and temperature capability are increased. However, to fully realise the advantages of titanium over other pure metals, it needs to be alloyed with other elements, common alloying additions include, O, Al, V, Sn, Zr, Mo and Si. Titanium possesses a high temperature BCC phase, β, and a low temperature HCP phase, α, Figure 2.1. For pure titanium, the transition or β-transus is circa 882°C [91]. Alloying additions are typically classified according to their effect on the β-transus and can be classified into four groups, Table 2.1: α stabilisers that raise the transus, β stabilisers that lower the transus, neutral elements that do not affect the transus and β eutectoids that form inter metallic compounds during cooling from the β phase.

Depending on the differing amounts of those alloying additions, the resulting alloys are then classified by their room temperature microstructural condition. Figure 2.2 shows the range possible as a function of volume fraction of β; Figure 2.3 shows the conditions under which each

of those exist. Note the M_s line which denotes the point at which during cooling the propensity to transform into a martensitic structure on cooling increases.

The most commonly used titanium alloy in the aerospace industry is Ti-6Al-4V which is an $\alpha + \beta$ alloy (aluminium being an α stabiliser and vanadium a β stabiliser), and is used in this study. The typical properties of Ti-6Al-4V are shown in Table 2.2 and compared to commercially pure grade 4, to illustrate the advantages of alloying titanium.

2.1.1 Microstructure

As well as the addition of alloying elements, the thermomechanical processing has a distinct effect on the mechanical properties of titanium alloys. Thermomechanical processing is undertaken to refine the microstructure of a given alloys to achieve the desired balance of mechanical properties.

Three distinct types of microstructure are obtainable in $\alpha+\beta$ Ti alloys; fully lamellar, fully equiaxed and bi-modal. The main differences lie in the quantity and characteristics of the constituent phases i.e. primary-α, secondary-α and retained-β.

Fully lamellar microstructures consist of prior β grains containing α in the form of colonies of lamellae within the β grains. The thickness of these lamellae is controlled by the cooling rate from the β phase field, with slower cooling rates giving larger lamellae and grain boundary α and faster cooling rates giving finer lamellae. A generic processing route and resultant microstructure is shown in Figure 2.4.

Bi-modal microstructures consist of primary α grains in a secondary α matrix. Primary α may contain Ti_3Al. The deformation stage controls the type of crystallographic texture and the intensity and symmetry of that texture. The annealing stage controls the size of the primary α and its volume fraction; it also controls the width of the secondary α lamellae. It should be noted that bi-modal microstructures can lead to a reduction in High Cycle Fatigue (HCF) strength with increasing primary α volume fraction. [40] Figure 2.5.

Fully equiaxed microstructures are very similar to bi-modal microstructures; however a change in the temperature used during the recrystallisation stage or a decrease in the cooling

rate during processing means that only primary α is found with retained β at triple points. This change leads to a larger primary α grain size compared to a bimodal structure and correspondingly a larger volume fraction of primary α. It is possible to change a fully equiaxed microstructure to a bi-modal microstructure by reheating the material into the α+β phase field and cooling at a higher rate to form α lamellae in the β grains.

Rolled Ti-6Al-4V, for use in wide chord fan blades for gas turbine engines, is produced, in part, by following these basic steps:

1. α+β roll to slab - The ingot is taken and rolled in the α+β phase region to produce pre-strain in the structure so that there is enough stored energy to nucleate and grow new β grains during the next step.

2. β_{RX} (Recrystallisation) - The slab is then heated into the β phase region to recrystallise and give a uniform β grain size. On cooling from the β phase region, primary-α platelet colonies grow inwards from the β grain boundaries. This resultant microstructure has poor HCF properties so further mechanical work is required in the α+β region to globulise the primary-α platelets. If the recrystallisation is carried out too soon during processing, then the β grain size will be too large, the grain boundary α will be thicker and the primary-α platelets will be thicker with the resultant colonies larger. If the recrystallisation is carried out too late during processing, then there will not be enough α+β processing strain to spheroidise and refine primary-α platelets.

3. Deformation of α+β colonies through rolling - The next stage involves thermomechanical work in the α+β region with the aim to reduce the cross-sectional area by around 75 percent to enable subsequent good microstructural development. The volume of the primary-α colonies is conserved during this stage of mechanical work, with elongated primary-α colonies being broken down into distinct spheroid primary-α grains separated by β driven along some of the activated slip bands. Due to common slip planes and physical hard body constraints, the primary-α grains will tend to behave in a similar manner to their nearest neighbour. It should be noted that there is a marked difference in the stress required to deform the α and β phases, in the region of 4:1 / α:β [42]. The

orientation of the primary-α grains has a distinct effect on the deformation properties as previously mentioned; this means that the way in which the α colonies break-up is also different based on the orientation. When the force from rolling is applied parallel to the prismatic plane $< a >$ type slip occurs, whereas if the force is applied perpendicular to the prismatic plane then $< c + a >$ slip occurs. Figure 2.6 shows a schematic of the response of primary-α colonies to rolling. [20] Note, there is a slight error in that figure as given the preferred growth orientations of alpha platelets, it would normally be expected for the c-axis to be aligned with the primary axis of the colony unlike what is shown in the first part of line c.

Figure 2.7 taken from [69] shows how Ti-6Al-4V responds to varying levels of strain rate and temperature during deformation to achieve the aims as laid out above.

Both small α grain and colony sizes give an increase in proof stress, strain to failure, HCF strength and resistance to micro crack propagation. However, this also decreases resistance to macro crack propagation. The size of the primary-α colonies can be controlled by keeping the β grain size small [40]. Small secondary-α grains of random variants provide good resistance to macro crack propagation.

2.1.2 Crystallographic Texture

Texture refers to the distribution of crystallographic orientations within a polycrystalline material. The main features of texture that will have an effect on the loading response of a piece of metal are the intensity and symmetry. Texture intensity is influenced by the level of strain, for example the rolling reduction during a pass; where as texture symmetry is driven by the type of deformation, ie. rolling or forging.

In the case of Ti-6Al-4V it is vital to understand the texture of the primary-α as this will constitute the bulk volume of the metal and hence dominate the response to macroscopic loading. It should also be noted that with nucleation and growth of the secondary-α from the primary-α, under sufficiently slow cooling, the effective unit size can be larger than would be anticipated by optical microscopy. The α phase forms, on cooling, from β grains in one of twelve orientations.

These orientations are determined by the orientation of the (110) planes of the prior β grains which during nucleation of the primary-α form the (0001) planes in the HCP crystal. There are six possible (110) planes in the BCC crystal and two possible HCP $< 11\bar{2}0 >$ directions from each of those (110) planes giving twelve HCP orientations. This is known as the Burgers orientation relationship defined as $(0002)\alpha \mid\mid \{110\}\beta$ and $< 11\bar{2}0 > \alpha < 111 > \beta$. [76] Texture 'memory' of the α phase is possible from common β (110) boundaries.

The HCP structure is inherently anisotropic as it is a hexagonal prism with six prismatic and two basal faces, when load is applied parallel to the prismatic faces the modulus is in the region of 145GPa whereas when applied parallel to the basal plane, it is 100GPa - see Figure 2.8. It is the inherent anisotropy of the HCP structure that makes controlling the texture so important to optimise mechanical properties. The stiffness and strength of the material is strongly influenced by the macroscopic texture; the largest extremes of this are exhibited by single crystals.

Macrotexture regions (MTRs) or macrozones are examples of homogeneous textured regions in titanium alloys. There is debate around the limits required to define an MTR; for example, what limits are applied to the misorientation of the relative c-axises of adjacent grains, these limits will define the bounds of the MTR.

Other factors to be considered when thinking about the effect of macrozones on fatigue crack growth include:

- Size of the macrozone - The size of an area that could be susceptible to faster than expected initial crack growth. i.e. how large is the area that could grow in a rapid manner between inspections during stage I fatigue crack growth

- Aspect Ratio of the macrozone - Similar to size, understanding the shape of any region of material susceptible to faster than expected initial crack growth as that will have an effect on grow rates between inspections during stage I fatigue crack growth.

- Intensity of orientation within the macrozone - The intensity of a macrozone will impact the speed of crack growth through the macrozone. A more intensely orientated macrozone (One where a larger number of primary-α grains are of a very similar crystallographic orientation) will lead to lower resistance to crack growth during stage I fatigue crack

growth.

- Dominant orientation within the macrozone - Depending of the dominant orientation of the macrozone in reference to the principle stress axis direction will affect how that macrozone shapes crack propagation speed and directionality. In cross-rolled (XR) plate there are predominately two dominant orientations due to the cross-rolling process one where the primary-α grains are soft in the principle stress axis and the other primary-α grains are hard in the principle stress axis.

- Nearest Neighbour properties - The above listed properties of a macrozone will be heavily affected the same properties of any nearest neighbour macrozones.

Factors that determine MTR size are as follows:

- β grain size following β_{RX} - Larger β grain size leads to a larger α colony size, which in turn leads to larger macrozones

- Intensity of β texture following β_{RX} - The more intense the β texture the more chance there is of similarly oriented adjacent β grains and the more chance there is of larger macrozones

- Strain before and after β_{RX} - As eluded to previously, β_{RX} too early leads to larger colonies and hence larger primary-α macrozones.

- Cooling rate from β_{RX} - Slower cooling rates will lead to larger α laths resulting in larger macrozones

- Amount of deformation during α+β processing - The greater the amount of deformation during α+β rolling the larger the aspect ratio of macrozones will be and the crystallographic intensity will increase

The Ti-6Al-4V used in fan blades is a rolled product. There are two commonly available types of rolled Ti-6Al-4V plate; unidirectional (UD) and cross-rolled (XR). UD rolled plate has a texture where the basal planes of the primary α grains are found to lie parallel to the rolling direction. XR plate, due to the second rolling direction, shows a less organised texture with

the basal planes of the primary α grains lying either parallel to the primary rolling direction or parallel to the transverse or secondary rolling direction. Coupling the anisotropy of the HCP structure with the texture of UD plate gives highly anisotropic mechanical properties. XR plate with its secondary rolling direction helps towards balancing out the mechanical properties between the primary rolling direction and the transverse direction. Figure 2.9 illustrates the texture of these product forms.

Both of these plate types are effectively made up of stacked macrozones similar to bricks in a wall. This has effects on the way in which through cracks are formed and their growth rates. For instance, if a microstructurally short crack encounters a macrozone that is favourably orientated for crack growth, then it is thought highly likely that the crack will advance much faster than would be predicted from component modelling. This makes in-service management of components produced from product forms that contain a high volume fraction of macrozones crucial to prevent premature failure. The stacked effect of macrozones also has an effect on the fractography as the crack grow through the thickness; as the stress field, ΔK and texture all combine and interact to determine the nature of the fracture mode, most commonly in a fatigue application, between striated and facetted growth. Small and medium scale microstructural effects aren't properly captured in test samples due to the complex geometry and the stress state in components coupled with complex and mixed LCF and HCF loading in-service.

2.1.3 Diffusion Bonding and Superplastic Forming (DB/SPF)

The process of diffusion bonding followed by superplastic forming, commonly referred to as DB/SPF, is used in the manufacturing of wide chord fan blades (WCFB's) utilised by Rolls-Royce in its Trent series of turbo fan gas turbine engines. Figure 2.10 shows a schematic of a Trent 700 along with a Trent 1000 WCFB.

This manufacturing process was first used on WCFB's for the Trent 700 (entry into service March 1995) replacing the previous technology which used a low temperature cupronickel braze honeycomb structure between two Ti-6Al-4V plates.

The process of diffusion bonding involves bringing two surfaces into contact under an applied load in the $\alpha + \beta$ phase field [67]. As pressure is applied, the two metal surfaces deform and

diffuse to form one continuous piece. This process leaves a witness or bond line which can be removed by continuing to apply pressure at temperature, promoting grain growth across the interface. See Figure 2.11 for a schematic showing the process. The vast majority of contaminants present on the bondline will fully or partially diffuse into the substrate but may effect the interface behaviour. Interstitials and beta eutectoids are known to be very fast diffusers in titanium. A partially diffused contaminant may act as a defect and cause premature crack initiation. For a structurally sound bond it is essential to prepare the bonding surface carefully. This commonly involves chemical treatment to minimise oxide films or other contaminants, typically using a nitric-hydrofluoric acid combination.

SPF involves plastic deformation of the work piece under heat and at a low strain rate; these parameters increase formability. In the context of WCFBs, the main concern during superplastic forming, is control of the resultant geometry rather than fully exploiting the limits of the process window. In the manufacture of WCFB's, plastic deformation is achieved by applying internal pressure to the blade using an inert gas [86, 2]. It is essential that an inert gas is used due to the reactivity of titanium to atmospheric gases such as oxygen and nitrogen, which if absorbed would stabilise the α phase at the exposed surface. The Ti-6Al-4V is inflated into a steel die at high temperature; controlling the cooling rate (i.e. keeping it slow) can lead to the resultant component having lower residual stresses than an equivalent part produced by more conventional means [27]. When processed under ideal conditions the bondline will have parent metal microstructure and properties. See Figure 2.12 for a schematic cross section of a WCFB in the context of the SPF process.

2.2 Fatigue of Titanium Alloys

Fatigue as a phenomena has been under observation for close to 200 years [75]. Fundamentally, it is the repeated application of a load to a component and in the context of turbo-machinery, fatigue is one of the main considerations during design and operation of components whilst also being the primary cause of in-service failure. The phenomena of fatigue is best understood by separating initiation, stage I and stage II fatigue crack growth, final failure and fractography

into sections to be discussed separately.

2.2.1 Initiation

Initiation of fatigue cracks often occurs at surfaces due to a lack of physical constraint of the material and environmental coupling with the deformation process. Areas of local stress concentration, including but not limited too, features such as machining marks and notches will reduce fatigue strength in comparison with a smooth polished sample. The geometry of a component can also effect initiation due to either the creation of a notch like feature or through creating a non-uniform stress field across a component. The mechanisms of surface crack initiation under fatigue loading has been investigated in single crystal materials to gain an understanding of the mechanism independently of microstructural influences [63]. During cyclic loading the material hardens; once a certain amount of plastic strain has been induced, crystallographic slip localises in the form of persistent slip bands. The regions of localised slip are separated by comparatively undeformed material. As the material is cyclically loaded these persistent slip bands start to penetrate the crystal surface in the form of small extrusions. These small extrusions, due to resistance to slip reversibility, do not fully retract under the compressive stage of the loading cycle. As such the remnant of these extrusions remain on the material surface forming intrusions and extrusions. [80, 74] Figure 2.13 shows a schematic of extrusions.

These features act as a localised stress raiser and it is from the interface between these features and the surrounding matrix that crack initiation can occur and are augmented by de-cohesion of the slip band.

Fatigue crack initiation in polycrystalline alloys is more complex as it is a function of a number of different parameters with different mechanisms being proposed for both surface and sub-surface initiation. Microstructural inhomogeneity (inherent or otherwise) is seen as a key function in sub-surface initiation in titanium alloys. This variety could include features such as; a large mismatch in crystallographic or morphological orientation of neighbouring grains, the distribution of secondary phases and grains that lie outside the normal distribution of grain size [8]. Inclusions and precipitates such as carbides can also act as stress raisers e.g. in Ni superalloys or in steels, which can also result in locating a site for crack initiation.

Initiation of a fatigue crack also requires the applied load to have exceeded the required ΔK threshold (ΔK_{th}) for the material and environmental conditions. Schmidt also gives an equation to determine the ΔK_{th}:

$\Delta K_{th} = (\Delta K_{cl} + \Delta K_0)(1\text{-}R)$

where: ΔK_{cl} is the stress intensity necessary to open the crack ΔK_0 is the portion of the stress intensity range necessary to produce crack growth at threshold whilst R, is the ratio of applied load (min/max)

Figure 2.14 shows a number of da/dN vs ΔK plots from samples tested at a variety of R-ratios. It shows that as the R-ratio moves closer to 0 (from 1) that the threshold for initiation increases. Figure 2.15 shows just the threshold data for a range of R-ratios, showing the same trend as can be in seen in the previous figure. For WCFBs the dominant load regimes are Low Cycle Fatigue (LCF) axially at low R-ratios (e.g. 0.1) and HCF driven bending at higher R-ratios (e.g. 0.8). It is recognised that crack initiation is effectively very short crack growth or slip band de-cohesion and that the modelling and understanding of the physical mechanisms is in its infancy.

2.2.2 Fatigue Crack Growth

Fatigue crack growth is typically characterised by three microscopic stages. These are Stage I short crack growth, Stage II long crack growth and final failure.

1. Stage I fatigue, also known as near-threshold fatigue crack growth, is the initial stage of crack propagation where the plastic zone ahead of the crack tip is of the order of few grain diameters. During this stage, crack growth is sensitive to the microstructure and as such, crack growth will predominantly occur along favourable crystallographic planes. Fractographically stage I fatigue leads to 'zig zag' crack paths with cracks exhibiting faceted or serrated features [80]. Note the aforementioned effect of MTRs on this stage of fatigue crack growth.

2. Stage II fatigue occurs once the crack has enough energy at the crack tip to overcome the constraints of microstructure and will typically propagate macroscopically on a plane

normal to the loading direction, assuming simple unidirectional loading. Fractographically, the observer is looking for a series of typical fractographic features associated with plastic deformation due to fatigue loading. In the examination of bi-modal Ti-6Al-4V an observer will be looking for facets and striations with the aim of being able to either correlate the fractographic features with the loading regime applied to the test piece or, in the case of in-service components to give clues as to the mechanical loading that has driven the fatigue crack. Figure 2.16 shows an example of a fatigue crack that has been cross-sectioned to show the change in crack path as a function of the stage of crack growth.

3. Final failure is reached when the tensile limit of the remaining ligament of material is reached, or when the fast fracture toughness K_{1c} is reached. Typically, this region consists of ductile overload features at angles of 45 degrees to the principal applied stress also known as shear lips. In some applications features similar in appearance to striations can be observed; this is known as serpentine glide and is a well reported ductile feature on fracture surfaces. [36, 43, 89, 71, 10, 81] Figure 2.17 and Figure 2.18 show examples of serpentine glide. Care must be taken during fractographic analysis to ensure serpentine glide isn't mistaken for another common ductile feature, striations, which are of particular use in understanding the life of a fatigue crack.

Figure 2.19 shows images of a fractured test piece to illustrate the macro stages of crack growth: fatigue, overload, final failure. From initial examination of a fracture face, the macro crack surface roughness can indicate the amount of energy involved in forming the fracture in different regions. For example, a very rough fracture face will have been formed during a high energy event and conversely a flat fracture surface will have been formed during a comparatively low energy event.

2.2.3 Fractography of Fatigue - Facets and Striations

Both facets and striations are fractographic features relating to the fatigue crack growth response as a function of microstructure and loading. Facets can be observed during both stage I and stage II crack growth with striations forming once the crack has transitioned into stage II

growth [87]. It is possible to see both facets and striations at the same crack depth and even facets at depths greater than striations are first observed. It is thought this occurs due to primary-α orientation effects with that and stress intensity at the crack tip being the main factors in the formation of both types of fractographic feature. Work by Bantounas [9] has shown how primary-α orientation can affect the fractographic features observed (see Figure 2.20). The shape of the crack front is also a factor as at a grain level this is unlikely to be a smooth curve due to local stress varying due to crystallographic type i.e. BCC/HCP and orientation.

Facets

The term facet is potentially misleading and has been the subject of debate. Pilchak et al. [61] have written a paper outlining their opinion that the usage of the term quasi-cleavage facets is incorrect or misleading as they have shown fatigue facets are produced over multiple loading cycles, so they have recommended that the term low ΔK faceted growth is used instead. The level of faceting observed before the crack transitions into striated growth is a function of the applied stress and R-ratio; where an increase in R-ratio leads to a greater level of faceting but an increase in stress leads to a lower level. This is also affected by the grain size, with larger grains more susceptible to faceting. Faceted growth is linked with low ΔK conditions when the crack plastic zone size is small in comparison to the grain size. There are also constraints based on crystallographic orientation, some α grains won't be favourably orientated and so will fail via rupture due to an increase in localised stress as the crack progresses beyond the grain.

Striations

Striations appear as curved linear features typically close to parallel with each other and are witness marks of the progression of the crack front as it has propagated through the material. In bi-modal Ti-6Al-4V striated growth tends to be observed in pockets, these relate to a primary-α grain or chain of primary-α grains. Striations are observed when a fatigue crack under specific load conditions propagates through a primary-α grain which is orientated favourably for striated growth. There are a number of proposed theories for how striations form. One of the earliest and best known is the Laird model [38] as shown below (Figure 2.21). This model theorises that on the tensile portion of a load cycle, as the crack is opening, two slip planes are activated at the crack tip. As the load is removed the crack blunts but not fully, this allows the crack to

advance. On the compressive stage of loading the crack tip is re-sharpened allowing the process to be repeated during the next loading cycle.

Striations can be used to determine the crack propagation rate. A number of striation counting methods are used with differing levels of complexity used depending on necessity for absolute accuracy or time required to produce a life estimate. Care needs to be taken to account for mixed mode (where main loading is LCF with a HCF contribution on top) loading regimes, i.e. mixed magnitudes or spacings of striated growth and for regions of striations that are not perpendicular to the SEM beam when being assessed, as foreshortening can affect the spacing measurements, artificially increasing life predictions [24, 28, 21, 17]. A review of the literature shows how capability of striation counting has increased in recent years with the development of high resolution SEMs and a greater understanding of the nature of fine striated growth. Although caution should still be applied when looking for striations to analyse to ensure that the features being looked at are actually striations and not another non-cyclically formed plastic deformation linear feature. Quantitative tilt fractography is a technique that has been developed to counter the effects of foreshortening; it utilises multiple images of a region taken at different known beam incident angles to allow for corrections to be applied [62].

2.2.4 Lifing of Fatigue Cracks

S-N Curves

S-N curves plot stress amplitude (S) against cycles to failure (N), as shown below in Figure 2.22. These plots are then used to define an allowable stress for a given component life. Some materials such as some steels show a fatigue limit [3] which at loads below that limit have been shown experimentally to have extensive lives. A comparison between a steel with an endurance limit and an aluminium alloy that doesn't have an endurance limit is shown in Figure 2.22.

Fatigue Crack Growth Curves

Paris, in his paper "A Rational Analytic Theory of Fatigue" [59]; discusses how the stress intensity factor, K, is equal to the applied stress multiplied by a, where $2a$ is the crack length. Therefore, the stress intensity factor, K, is a measure of the effects of both the geometry of the component being loaded and the applied stress on the stress intensity at or near the crack

tip. As it is a function of the crack geometry, K is constantly evolving as the crack grows. ΔK therefore is a measure of the change in stress intensity during loading and unloading at a certain crack length, and will increase with an increase in crack length for constant loading conditions.

The δa/δN vs log-ΔK plot (see Figure 2.23) is a useful graphical representation of the three regimes of fatigue crack growth. In regime A, or near-threshold, the growth rate is very slow and fractographically faceting will be the dominant feature. Crack closure effects will be at their highest during this stage of crack growth as the crack tip plastic zone is relatively large in comparison to the size of the crack. Regime B, or the 'Paris regime', consists of a region of mid-growth rate. Fractographically striated growth, condition dependent, will be the most common feature observed with the inter-striation spacing increasing with increasing crack length. The final regime has a rapid crack growth rate and dependent on the material properties fractography will be dominated by either ductile overload or cleavage faceting. [80]

2.3 The Effect of Testing Atmosphere on Fatigue Crack Growth

Environment is an important factor in fatigue growth in titanium alloys. For the purposes of this study it is of interest to understand the effects of vacuum and inert gas atmospheres on crack threshold, crack growth rate, the plastic zone size and the effect on the fractography of the subsequent fracture faces.

2.3.1 Requirements for vacuum

In their review paper focussed on the required vacuum levels to simulate internally initiating and propagating fatigue cracks, Sinha and Larsen [72] look at the conditions in a vacuum environment from the perspective of the thermodynamics involved in the oxidation process. The reason for this, stems from the theory of initiation (previously discussed) and the relationship between surface oxidation and slip reversibility. For example, if the surface extrusions remain unoxidised as in a subsurface crack they are able to reverse freely and not locate initiation. The

determined value of vacuum level required is expressed as an oxygen partial pressure at a given temperature; (for the purposes of this study - room temperature.) this value is equal to a ρO_2 of less than 10^{-155}Pa. That means that for a test carried out "in vacuum" that the required pressure would be very low, in fact significantly below the level achievable utilising modern vacuum pumps where a ρO_2 of around 8.4×10^{-8}Pa is possible.

2.3.2 Changes in Crack Growth Threshold

Numerous studies have shown a vacuum environment increases the $\Delta K_{threshold}$, with variations seen in the values obtained as a function of level of vacuum. Back in 1974, Irving and Beevers [30] carried out a study where they tested Ti-6Al-4V in both air and vacuum (1.3×10^{-9}MPa) where they found the $\Delta K_{threshold}$ to increase from around 3.5-4MPa$\sqrt{m}$ to 8MPa$\sqrt{m}$. A study by Oguma and Nakamura in 2013 [58] showed that the $\Delta K_{threshold}$ for Ti-6Al-4V increased from 4MPa$\sqrt{m}$ to 7.2MPa$\sqrt{m}$ when the vacuum condition used was 2.7×10^{-11}MPa. In contrast Ritchie et al. [64] showed at higher frequencies that the $\Delta K_{threshold}$ did not change as a function of air pressure.

If the theory of surface fatigue crack initiation, as outlined above, is correct, then one suggestion of the change in rate at the near threshold loading conditions would be that without the presence of oxygen the slip extrusions that locate initiation sites are able to retract under cyclic loading; whereas with oxygen present they oxidise preventing reversal. Wei and Ritter [65] suggest that residual moisture is a key driver in fatigue crack growth in these tests, and that it is this moisture that causes the rate change rather than oxygen. A study by Shimojo [70] investigated the differences between: air, vacuum and a range of inert gases on fatigue crack growth. He found that even in the presence of inert gases there was a deleterious effect on the $\Delta K_{threshold}$ and crack growth rates. He postulates that the effect being observed is due to physisorbing of the gas molecules into the fresh slip band surfaces which restrict slip reversal in a similar but less effective manner to oxidation.

Work by Vasudevan et al. [85] showed an increase in $\Delta K_{threshold}$ as the R-ratio decreases when testing in a vacuum (1.15×10^{-13}MPa). These findings agree with those of Ritchie et al. [64] for samples testing air as shown in Figure 2.14. Figure 2.25 shows a comparison between vacuum

and air for crack growth rates, these plots show that there is approximately a $1x10^2$ difference in the crack growth rate with vacuum being much slower at the same value of ΔK.

2.3.3 Fatigue Crack Growth Rates

A recent study by Yoshinaka et al. [92] compared the fatigue crack growth rates and crack lengths as a function of cycles for Ti-6Al-4V samples in a range of different environments, including a variety of levels of vacuum, air and argon. Their findings showed that even an inert (i.e. argon) gas environment has a deleterious effect on the fatigue properties of Ti-6Al-4V. Figures 2.26 and 2.27 show data from that study.

SN curve data produced by Ismarrubie et al. [31], as shown in Figure 2.28, here you can see a clear difference between samples tested in air and vacuum. The vacuum samples were able to sustain significantly higher loads at equivalent lives of over 10^6 cycles. Work by Sugano et al. [79] broadly agrees with Ismarrubie et al. data shown in figure 2.29 shows a similar debit but over a wider range of sample lives. Figure 2.30 again from Sugano et al. [79] shows clearly the effect of different environmental pressures on the fatigue life of titanium samples. There are two clear steps where a small change downward in pressure leads to a marked increase in sample life.

2.3.4 Plastic Zone Size

Ismarrubie et al. [31] studied the effects of vacuum on fatigue crack growth of CPTi. They measured plastic zone size and the changes in temperature on the sample during load cycling. The temperature of samples tested in air and vacuum were measured and recorded as a function of stress cycle. Their findings showed that on average from $1x10^5$-$1x10^6$ applied stress cycles, the air tested sample showed a temperature gain of 2K whilst the vacuum sample showed an increase of 20K, a 10 times increase. It was postulated that the temperature increase would enable greater slip activity around the crack tip in a vacuum environment. Also within this study by Ismarrubie et al., the plastic zone sizes were monitored and compared between cracks grown in vacuum and air. It was found that at crack lengths of 0.2-3mm from the root of the crack that the plastic zone size was much larger as illustrated in figure 2.31. These two sets of

observations were discussed and combined into a theory that the internal heating generated at the crack has enabled the plastic deformation to spread reducing its intensity.

2.3.5 Fractography

A variety of views have been outlined in the literature for the effect of testing atmosphere on the fatigue life of titanium alloys. In 2012, Sinha and Larsen [72] wrote a review paper comparing the findings of McClung et al. [45], Irving and Beevers [30] and Bache et al. [6] amongst others. Their findings suggest that samples tested at atmospheric conditions and those tested under vacuum, have crack growth rates between normal and 3-4 times lower, in the upper section of the Paris regime. However, at near threshold conditions there is a significant reduction in crack growth rates under vacuum, in the region of 3 orders of magnitude. They all note that there is a significantly higher ΔK threshold under vacuum than under atmospheric conditions. Literature is unclear on the effect of vacuum on striation formation as there are papers supporting normal formation and others supporting a suppression. [88]

Much of this research was hindered by the examination method and the relatively low resolution electron optics available at the time. Typically the techniques being utilised were carbon replicas in an early TEM with varying levels of tilt (up to 30 degrees) to reveal contrast to enable analysis of striated features. Using today's current generation of SEMs to examine fractures directly allows for much better feature detection as your sample size is less limited. With modern SEMs you not only have much greater resolution optics, but they also have a variety of software options that allow for both collation of images as they are captured and for the automated capture of large stitched images. Both of these methods allow for a much better sense of overall fracture context when examining a fracture in detail. In particular the large stitches allow for a much greater area to be examined in detail as there is no lag when wanting move around the sample even at high captured resolution.

Bache et al. [6] found that as oxygen contents increased in samples, that facet formation was enhanced and reciprocally striated growth was suppressed. Their test range of oxygen contents was from 2000 to 5100ppm O.

2.4 The Effects of Interstitials on Titanium

In 1981, Hans Conrad wrote a seminal paper on the influence of interstitial solutes on the strength and ductility of titanium [22]. This work provided a large amount of data and collated the findings of a wide array of investigators providing a comprehensive summary of the work carried out in that area of research. This thesis by no means aims to replicate that work, the following section will focus on previous work related to the research being undertaken, for example looking into the effect on Ti alloys (ideally Ti-6Al-4V or binary systems where not possible) rather than CP Ti.

2.4.1 Oxygen, Nitrogen and the β solvus

The alloys under investigation here are categorised as $\alpha + \beta$ alloys or using Ogden and Jaffee's [56] classification they are lean β alloys as they contain 2-5% β solutes. Both oxygen and nitrogen are readily soluble in α phase titanium and will raise the temperature at which the α phase is stable [84]. Various attempts have been made to compile a phase diagram for nitrogen and titanium (or alloys of). Examples from McDonald et al. and Kessler et al.([46, 37]) are shown in figures Figure 2.32 and Figure 2.33.

Ogden and Jaffee [56] suggest a general figure for the increase in the β transus is 50°C for each 0.1wt. percent nitrogen. From analysis of Figure 2.33 the data suggests an increase of 10°C per 0.1wt. percent nitrogen on the α to $\alpha+\beta$ phase field boundary. With interstitials being found to partition towards the α phase this leads to a greater strengthening of the α phase over the β phase. This in turn means that for $\alpha + \beta$ alloys the overall strengthening effect of interstitials is heavily dependent on the volume fraction of primary α in the alloy.

2.4.2 Mechanical Property Effect of Interstitial Additions

Interstitial additions to titanium alloys have been shown to affect the general mechanical properties in the following ways:

- Increase strength [48, 26, 57]
- Increase hardness [47, 26, 57]

- Decrease impact resistance/fracture toughness [48, 26, 57]

Figure 2.34 shows combined data from Jaffee et al., McQuillan and Finlay and Snyder for basic mechanical properties of iodide titanium as a function of nitrogen content.

As well as testing the fatigue crack growth response to gas pressure Bache et al. [6] also investigated the effect of oxygen on fatigue life. They found that as the oxygen content is increased from 900ppm to 5100ppm oxygen fatigue life is degraded .

2.4.3 Interstitial Additions and α-phase Lattice Parameters

Work by Ando et al. [1] suggested that changes in the measured tensile strength of titanium alloys when nitrogen was added was accompanied by an increase in c/a ratio. Figure 2.35 illustrates the changes measured.

Other experimental work has been carried out to determine the effect of common interstitial elements on the lattice parameters a and c. The changes observed for N are, per wt. percent a 0.002Å and for c 0.023Å, whereas for O they are, a 0.000Å and c 0.015Å from work by McQuillan and McQuillan [48]. Work by [50] Montanari et al. somewhat corroborate these measurements having observed that interstitials introduce a greater level of strain to the lattice in the c-axis than in the a-axis in the basal plane. Values are given for the changes in a and c as a function of the amount of interstitial atoms present in the lattice (n); $\delta a/\delta$n and $\delta c/\delta$n. For N the values are $\delta a/\delta$n - 2.0x10^{-4} nm per at. percent and $\delta c/\delta$n - 6.7x10^{-4} nm per at. percent. Work by Conrad [22] has shown that the addition of 0.01 wt. percent of interstitials leads to deformation on the prism plane $(10\bar{1}0)$ with some basal slip. However, from 0.01wt. percent up to 0.1wt. percent interstitial content, that changes to slip occurring mainly on the $(10\bar{1}\bar{1})$ pyramidal planes.

2.5 Tomography of Fatigue Cracks

2.5.1 Monitoring crack growth

Fatigue crack growth rates have been measured, during testing, in a number of ways over the years. From visual monitoring of surface breaking cracks to potential drop techniques to computed tomography (CT). The first two in that list are able to be undertaken in-situ, CT however, is dependent on the light source used as to whether it is available in or ex-situ. Imaging using CT is much like imaging utilising a conventional light camera; it requires a balancing act of parameters to allow enough light to be received at the detector to be able to resolve an image. When capturing an image of a stationary subject, these parameters are more forgiving as the exposure time can be easily increased to allow enough light to enter the detector. However, when trying to capture an image of a moving object (or in this case a growing crack) the rate of movement of the subject makes the exposure time a restricted parameter meaning light intensity becomes a major factor in the ability to capture an image. Given a bright enough light source, it is possible to capture a fast moving object but in the case of CT, this increase in required light means that lab based systems do not produce sufficient light for the task and a more advanced light source is required such as a synchrotron. Laboratory based CT systems have the advantage of being more readily available than the synchrotron based technique, but trade availability for lower resolution and slower scanning. Laboratory based CT systems though readily available do not have the required brightness to allow for the fast capture times required for in-situ FCG monitoring and so have to be used ex-situ. A synchrotron light source however, provides a much higher level of brightness allowing for much shorter exposure times and hence allowing for faster scans which make in-situ FCG monitoring possible. Maire et. al. [44] summarised data showing the differences in spatial resolution and capture times, the figure from that paper has been adapted in Figure 2.36 Another review paper by DeChiffre et. al. [23] illustrated the relationship between CT method, object size and spatial resolution, the figure has been adapted can be seen in Figure 2.37

2.5.2 Sample properties

Other restrictions incurred in using a CT system to capture an image of a subject are the size, shape and density of the subject to be imaged. Unlike a conventional light camera, the light in a CT system has to pass through the subject rather than be reflected off it. This means that a thicker more dense subject will restrict the resolution of capture as well as the speed of capture. Typically the best results are achieved when low density and/or small cross section samples are the subject being imaged. The thicker the sample the more light is required to be exposed to the subject to achieve the same amount of transmitted light to be detected. As well as the overall size of the cross-section, the shape of the cross-section is important due to the fact that CT is a 3D imaging technique. The 3D nature of a CT scan is the product of multiple radiographs being captured at known stepped rotations around a sample; this can be achieved via rotating the subject (in one axis of rotation) or moving the light source and detector around the subject. Finally, density of the subject is important, as similar to thickness a more dense sample will require more light to achieve the same result.

2.5.3 Fatigue and CT

Even once a sample has been prepared in a manner that is suitable for the available CT system, there is still more work to do to allow for FCGR monitoring. The main complication in monitoring FCGR's is the ability to know where in the sample the crack will initiate. Both visual monitoring and potential drop methods require surface initiating cracks, typically initiated at fabricated surface defects such as notches. CT allows for monitoring of fatigue cracks that initiate internally; however, it is still preferable for those cracks to initiate at a predetermined location via notching or a seeded defect. [16] The reason for this, is that by keeping the distance between both the detector and light source as low as possible to aid resolution and light transmission, you minimise the field of view of the detector and hence have less chance of locating your capture frame in the region where the crack initiates. Detection limits vary depending on the technique being used, the machine being used and the features trying to be resolved. Round features such as pores, for instance, are more readily resolved than cracks as cracks need to be open, typically

under tensile load, to give enough separation to provide sufficient contrast for detection. [90, 77] Figure 2.38 shows a schematic of the process that is used from image acquisition through to a reconstructed 3D volume taken from [5] and adapted with images from this work.

2.6 Summary of Literature Review

2.6.1 Titanium processing

It is clear from a review of literature that the thermomechanical processing of titanium and its alloys is key to obtaining optimised properties. The direct correlation between the resultant microstructure and micro/macro textures to the method and temperature at which the metal is deformed shows that production of material for this study needs to be undertaken with great care. The effect of nitrogen on the β-transus will need to be carefully characterised to ensure that the different compositions are processed appropriately as a function of vicinity to the β-transus. This is important as the desired imparted strain during deformation steps is related to the temperature delta to the β-transus. This means that each material composition will require a different temperature for a deformation stage to keep that strain per step as close as possible. The control variable of choice in this study is the microstructure with the aim to try and maintain microstructures comparable to a relevant commercial product; so where compromises need to be made they will be made with that aim in mind.

2.6.2 Fatigue in Titanium Alloys

Fatigue testing of titanium alloys is a rich area of research with a multitude of published papers and PhD projects focussed on this topic. For the experimental work in this study, the main lessons to take from the literature are the background of how titanium responds to fatigue loading when tested in air and with standard chemistries. For instance, it is clear that a good surface finish is key to ensure that features such surface roughness or handling damage do not affect the determination of $\Delta K_{threshold}$. Another interesting part of this work will be the examination of fracture faces from samples tested with a chemistry variation across the test

sample and seeing how that interacts with the traditional progression from initiation to stage I and stage II fatigue crack growth.

2.6.3 The Effect of Testing Atmosphere on Fatigue Crack Growth

There appears to be a real mix of opinions in the literature around the effect of the test environment (air vs vacuum). There is however a clear guide for the criteria of what counts as a vacuum and so that will be taken into account when designing any experimental work for this study and verifying the results. Another point that will be considered when designing the experimental work will be to see if any further information on crack growth characteristics as a function of testing environment is possible, for instance through the use of ex-situ CT monitoring. One uncertainty of particular interest to the author, is the variety of opinions around the effect on fractography of a change in test atmosphere. Fractography of tested samples in this study will have a particular focus on looking for any striated growth in cracks grown in vacuum and characterising any that may be present. If clarity on this issue is found through this study, that would be of great value to the industrial failure analysis community when examining fracture faces from components that experience loading under vacuum conditions.

2.6.4 The Effects of Interstitials on Titanium

Reviewing the pertinent literature around the effects of nitrogen on titanium alloys showed that the theme isn't one that has had much work since the pioneering days of the 1950s and 1960s. The work carried out then was thorough and well executed, however it was very broadly spread making specific application of the data towards solving today's engineering challenges problematic. With nitrogen not being an element that is intentionally added to titanium alloys, less characterisation of its effects have been made than for oxygen which is commonly used for strengthening titanium alloys. Any data produced during this work around the effect of nitrogen on the ubiquitous alloy Ti-6Al-4V will be the first of it's kind in published literature.

2.6.5 Tomography of Fatigue Cracks

There has been remarkably little work done using CT to monitor cracks growing in metallic samples. One of the research groups that has been active in this area, is led by Professor Peter Lee. It is planned for any work in this study using CT to monitoring cracks will be done in conjunction with Professor Lee's group to make use of the expertise and equipment developed to make monitoring cracks in metallic samples possible.

2.7 Figures and Tables

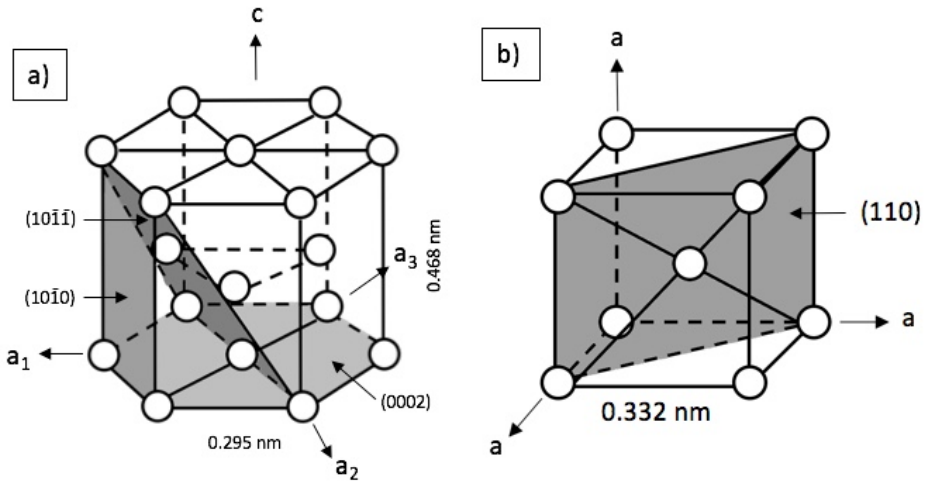

Figure 2.1: a: HCP unit cell - b: BCC unit cell - adapted from Lutjering and Williams - Titanium

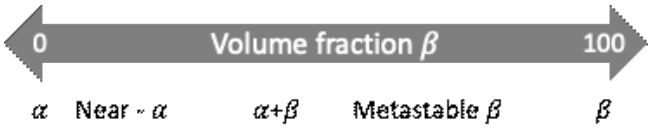

Figure 2.2: Range of Ti alloys as a function of volume fraction of β

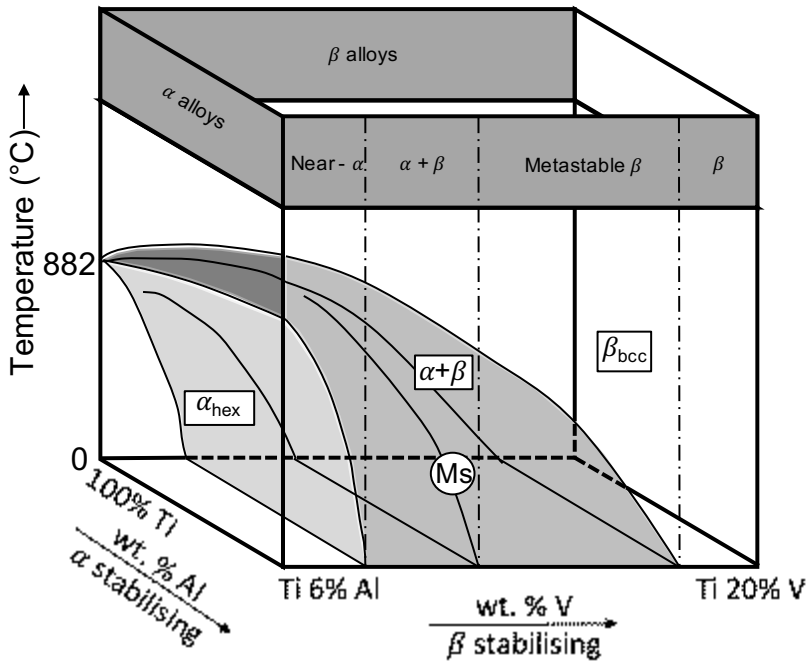

Figure 2.3: 3D phase diagram showing the range of Ti alloys adapted from Leyens [39]

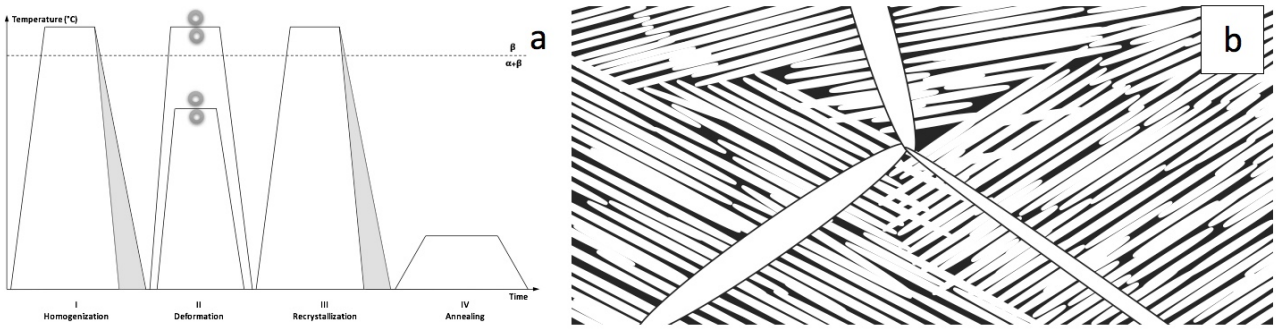

Figure 2.4: a) Showing process route for fully lamellar titanium microstructures [41, 40] b) Schematic microstructure

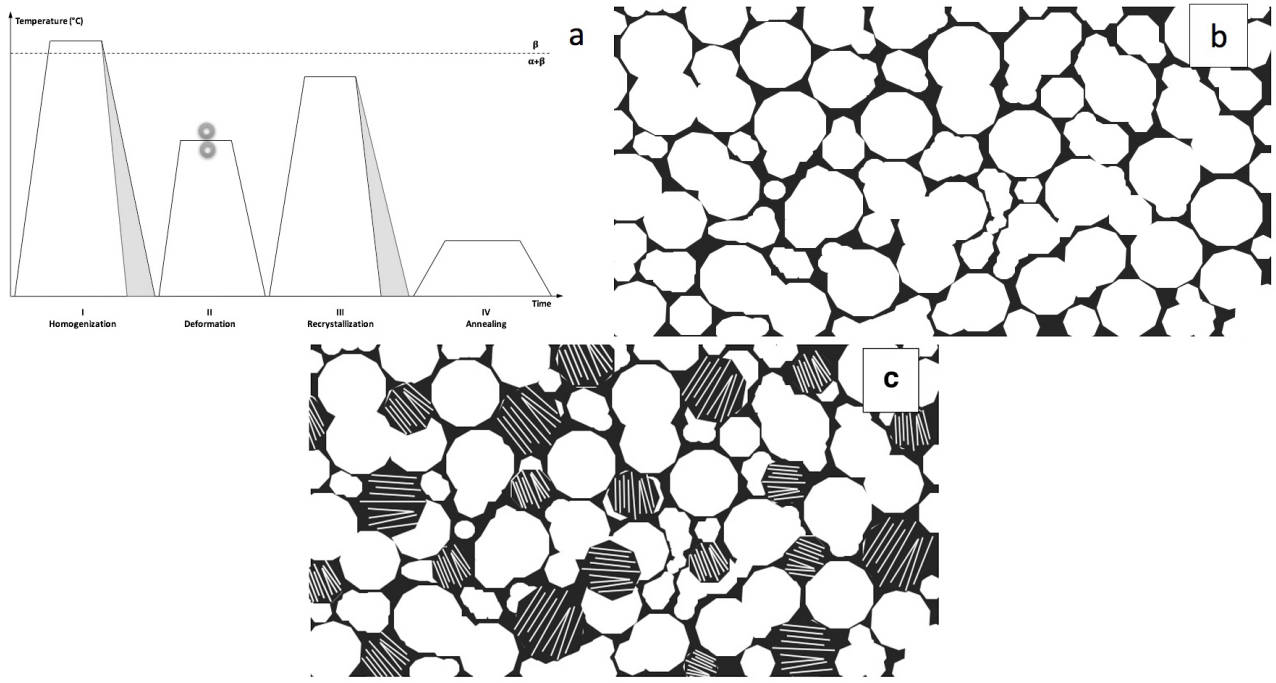

Figure 2.5: a) Showing process route for fully equiaxed and bi-modal titanium microstructures [41, 40] b) Schematic fully equiaxed microstructure c) Schematic bi-modal microstructure

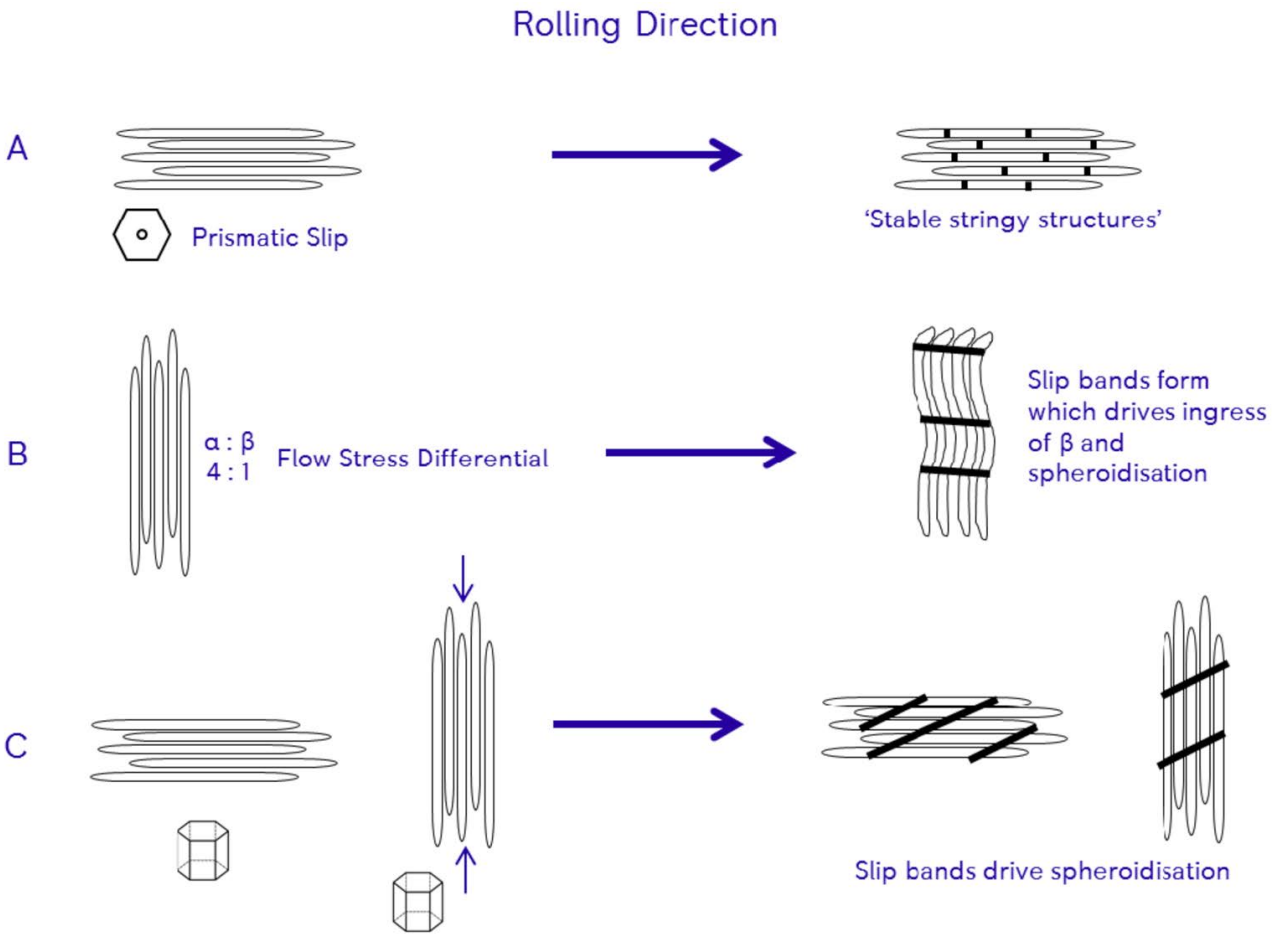

Figure 2.6: Schematic showing the response of a variety of primary-α colonies to rolling [20]

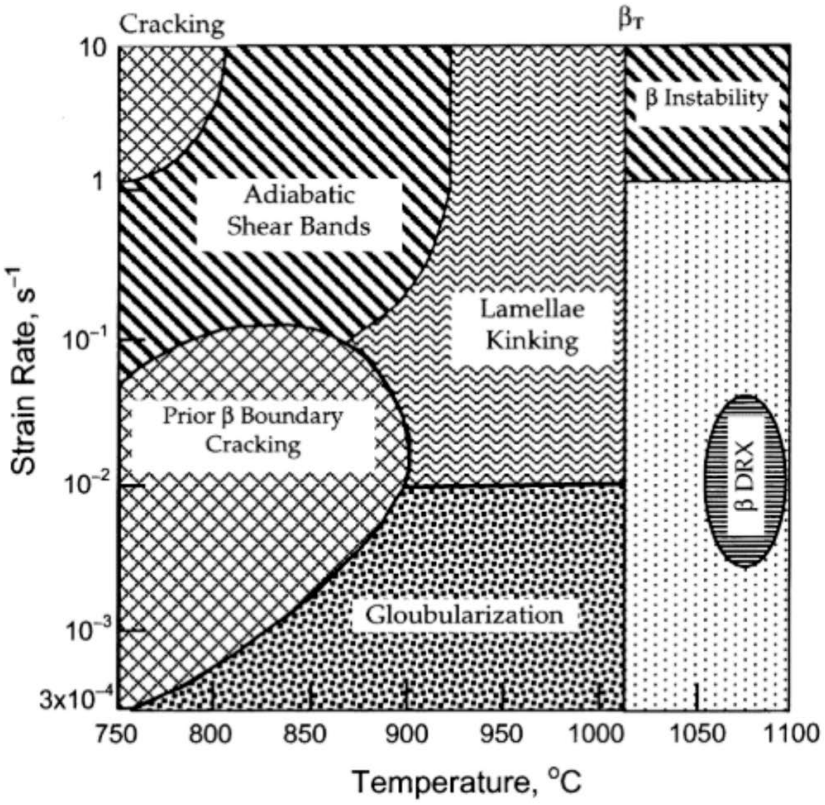

Figure 2.7: A microstructural deformation mechanism map for Ti-6Al-4V taken from [69]

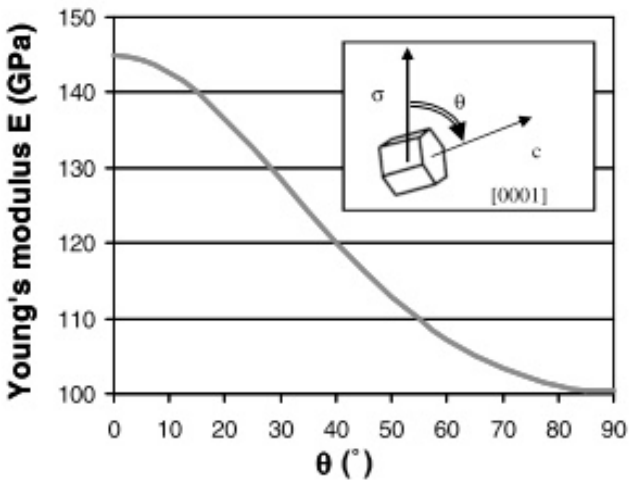

Figure 2.8: Figure showing how modulus changes with orientation of the c-axis within a HCP unit cell. [12]

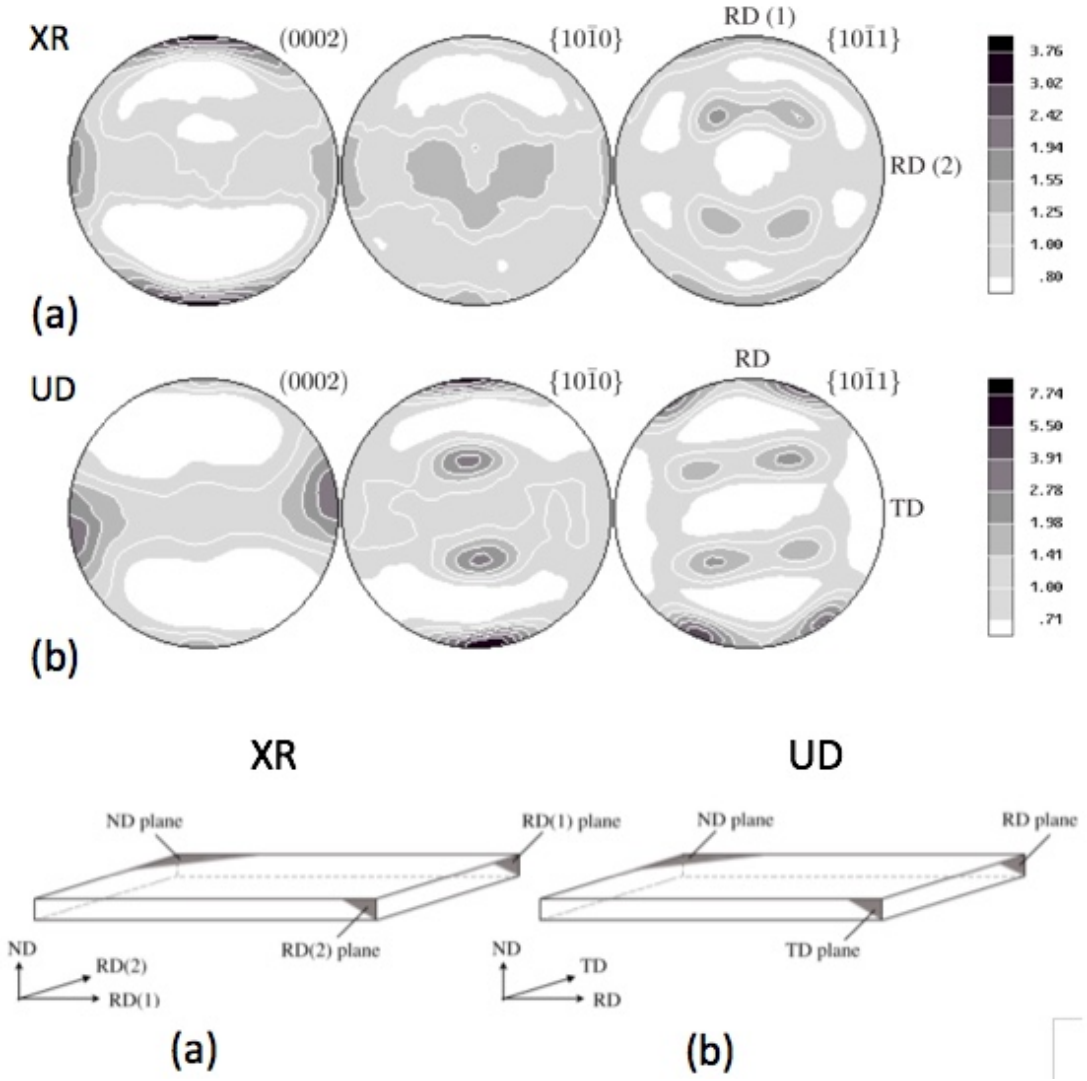

Figure 2.9: Schematic showing textures of samples taken from XR and UD plate. Adapted from [8]

Figure 2.10: a) Trent 700 Cutaway Schematic b) Trent 1000 WCFB - Credit Rolls-Royce Image Resource

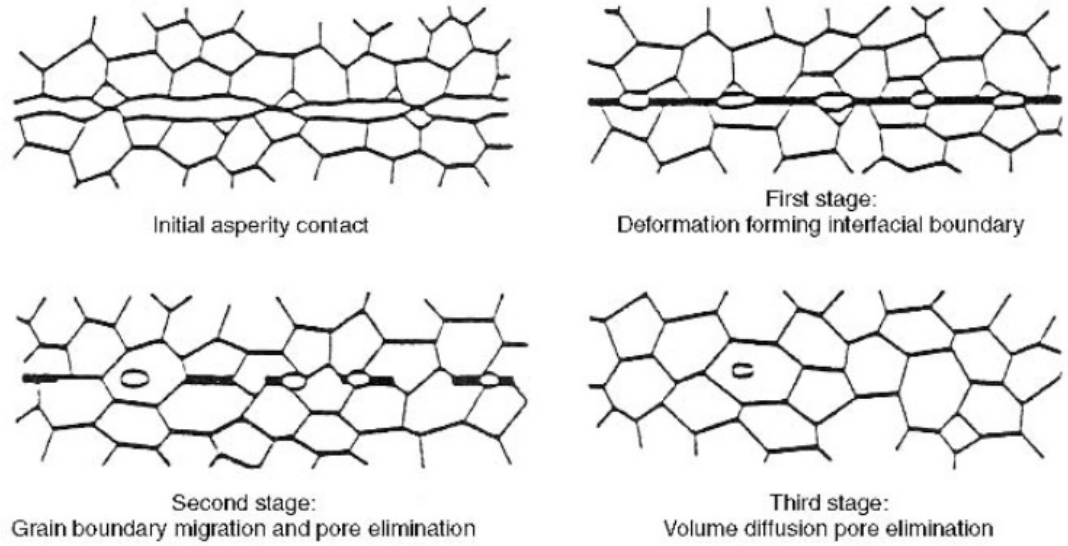

Figure 2.11: Schematic of microstructural changes during diffusion bonding [68]

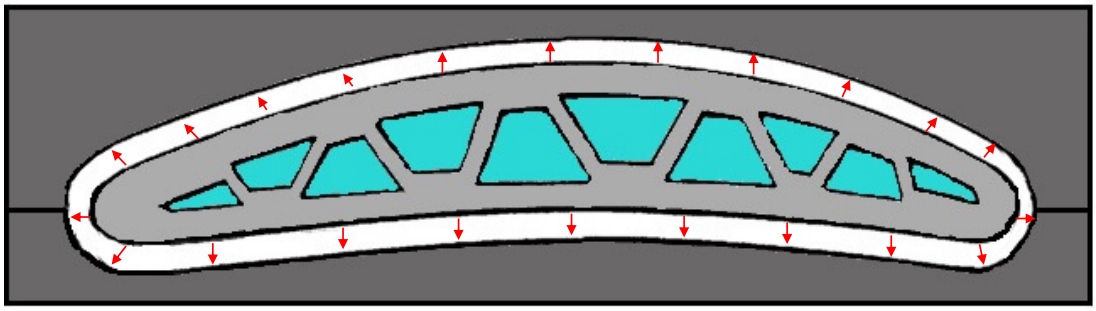

Figure 2.12: Schematic cross section of a DB/SPF fan blade within the steel dies. The blue represents the argon gas used to inflate the blade, adapted from [55]

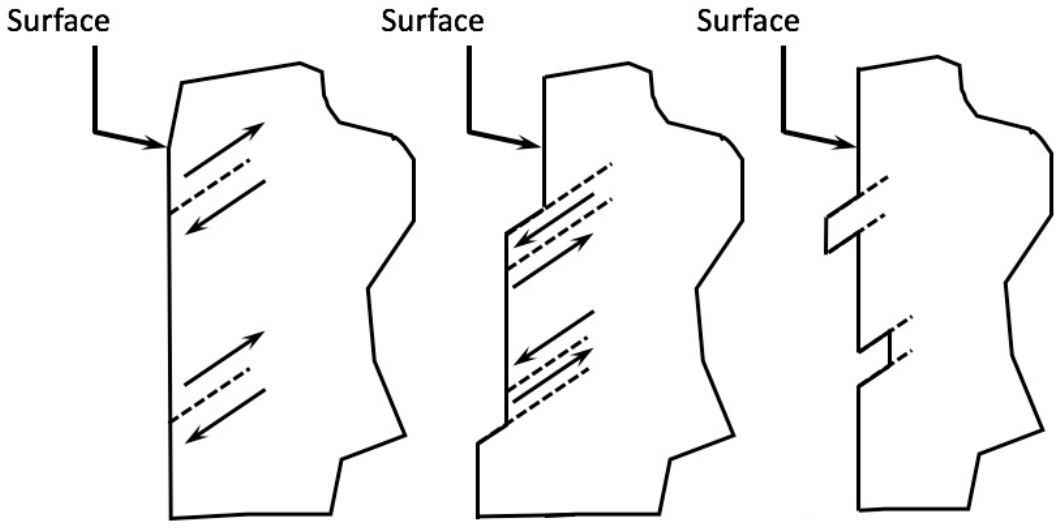

Figure 2.13: Schematic adapted from [24] showing extrusions and intrusions on a material surface

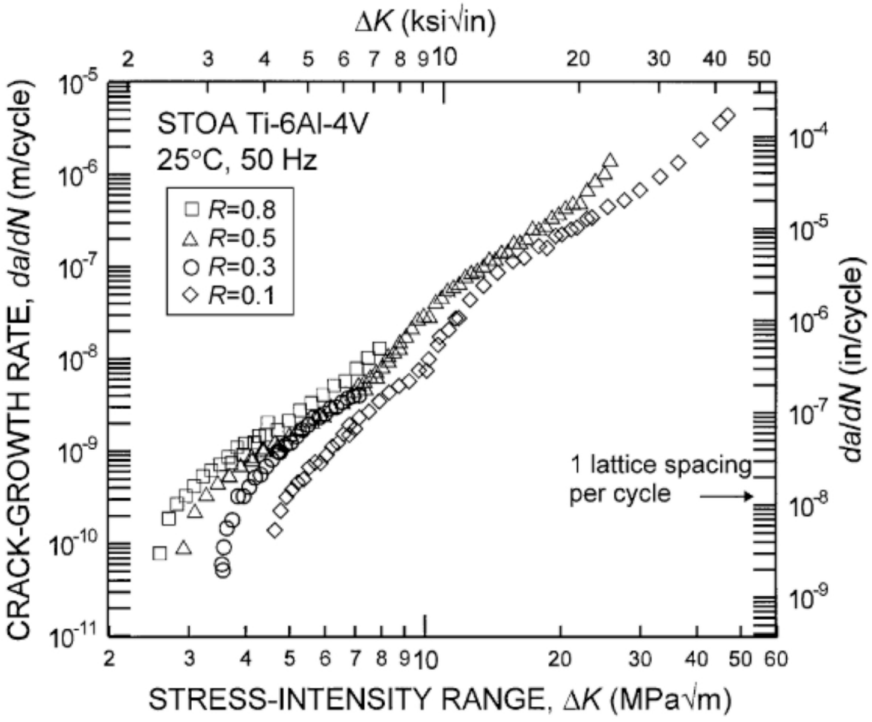

Figure 2.14: Figure from Ritchie et al. [64] for Ti-6Al-4V showing crack growth rate against ΔK for a range of R-ratios. Note the increase in $\Delta K_{threshold}$ as the R-ratio decreases

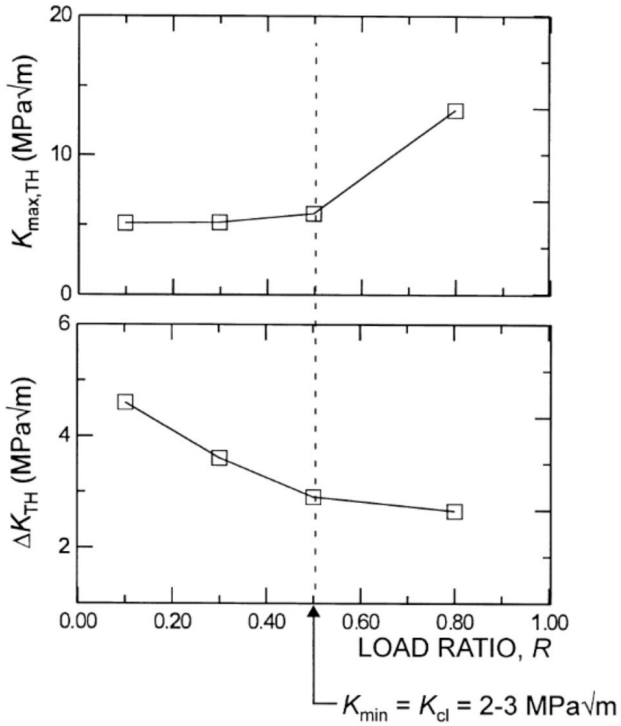

Figure 2.15: Figure from Ritchie et al. [64] for Ti-6Al-4V showing the variation for $\Delta K_{max,threshold}$ and $\Delta K_{threshold}$ as a function of R-ratio

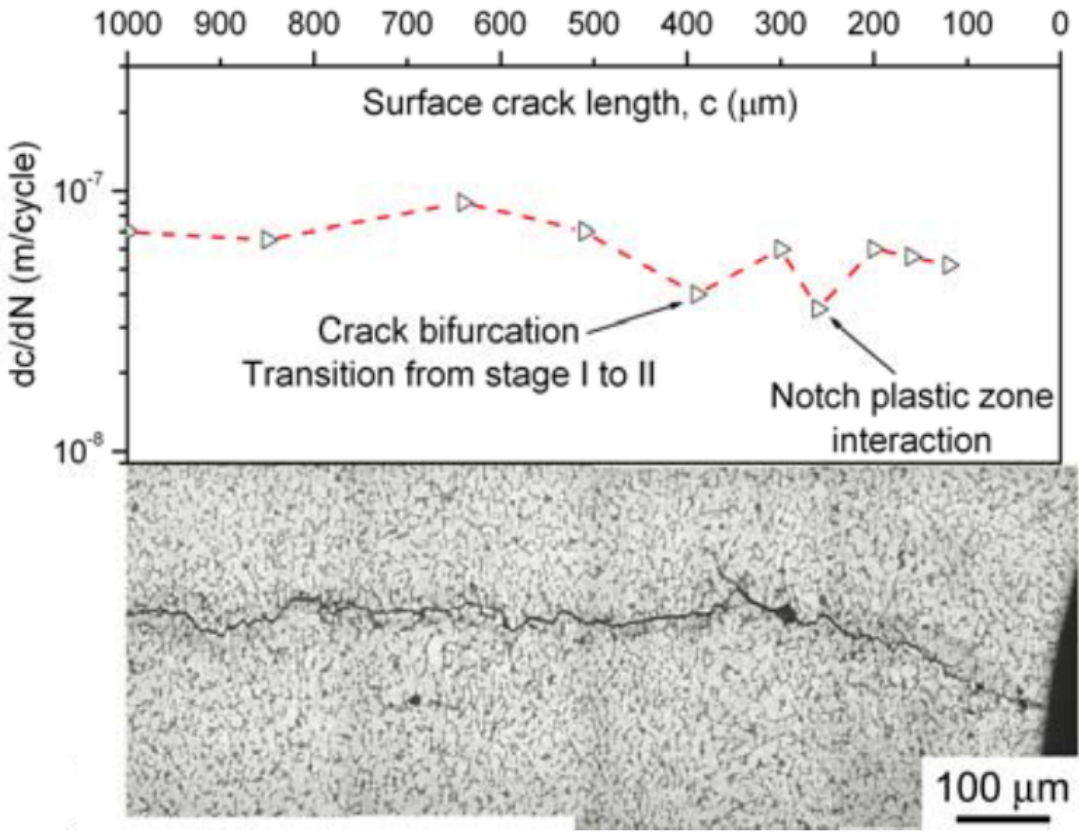

Figure 2.16: Figure from [11] showing the transition from stage 1 to stage 2 in a cross-sectional micrograph and in a growth rate as a function of depth chart

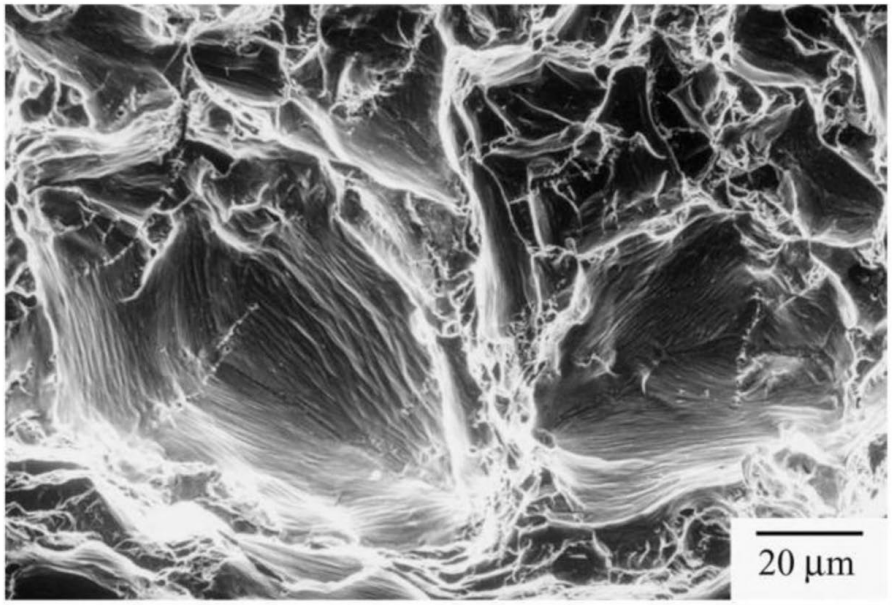

Figure 2.17: Taken from [36] Commercial titanium, 675°C/1h/AC, tensile tested at room temperature. High-magnification SEM fractograph of the conical dimples shows serpentine glide (stretch-like regions) surrounded by fine dimples.

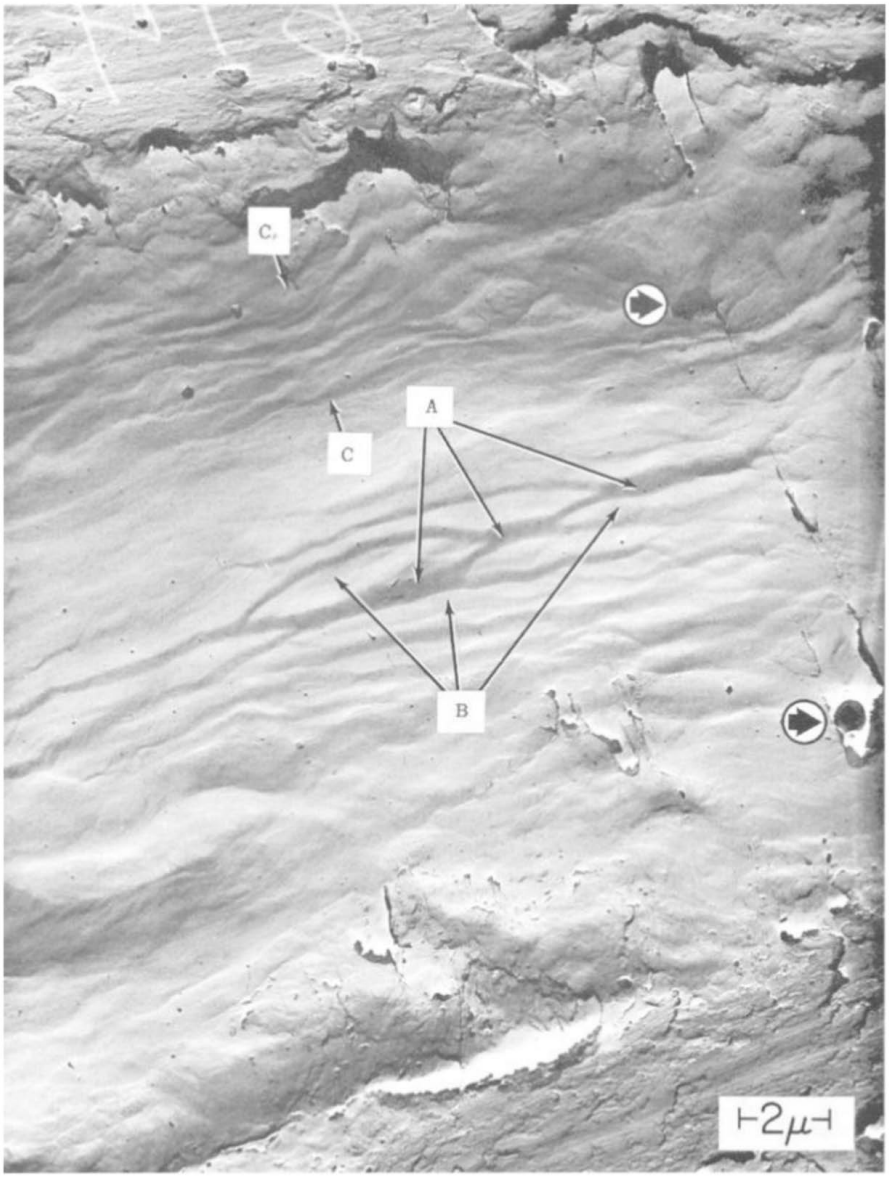

Figure 2.18: Taken from [10] Serpentine glide surface in annealed Armco iron. This glide was produced by slip when the root of a notch in this wire specimen was opened up by bending at room temperature. The dark surfaces (A) apparently were a single surface before slip on a second series of parallel planes produced the light parallel surfaces (B). Examples of ripples may be seen between the arrows (C). Palladium-shadowed direct-carbon replica (x9000).

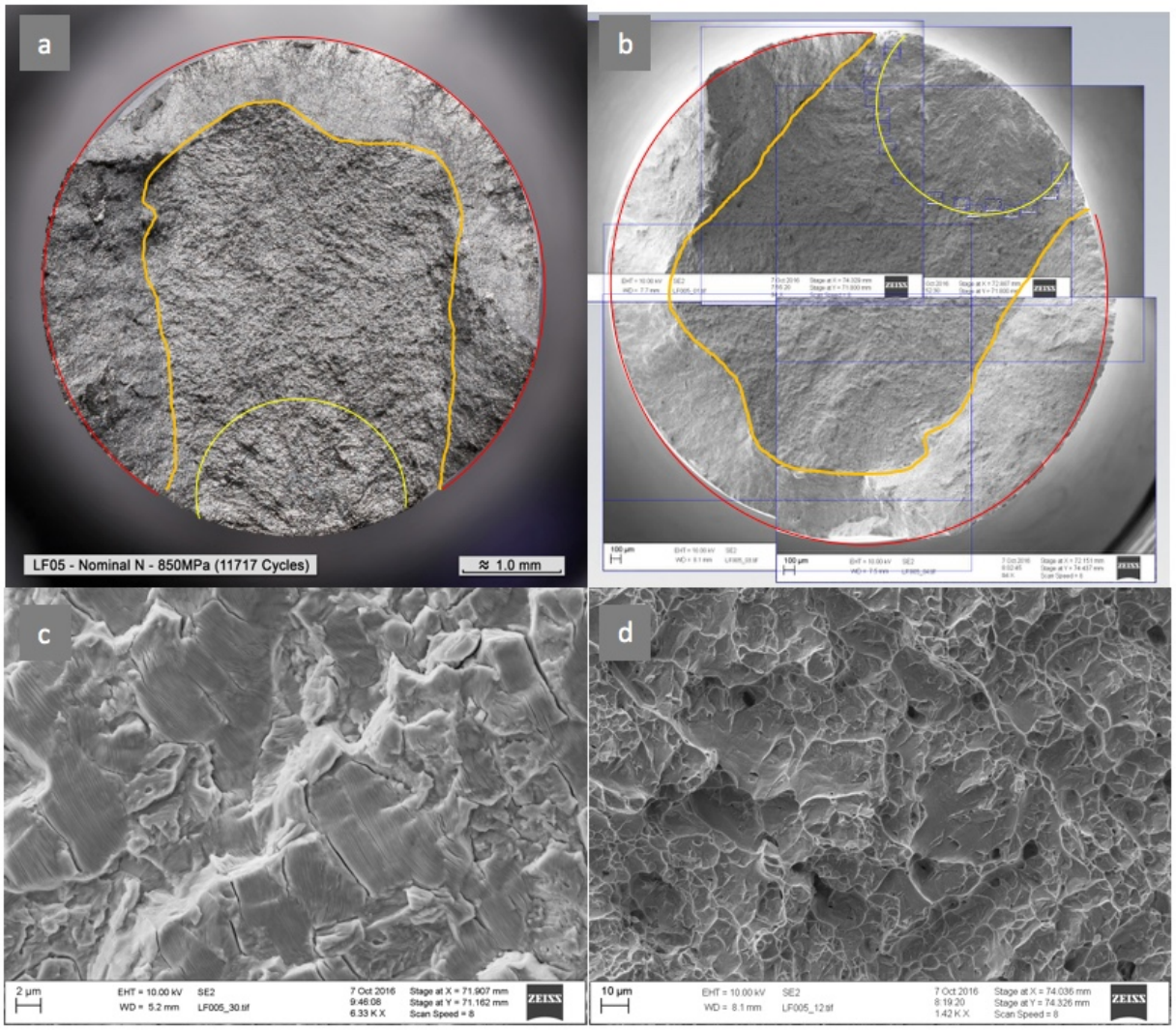

Figure 2.19: a) Showing optical image of LCF fracture face. Yellow area fatigue, Orange area ductile overload fracture, Red area shear lips. b) Compound SEM images of same fracture as is shown in a). c) Region of striated fatigue crack growth within Yellow area. d) Region of ductile overload within the Orange area.

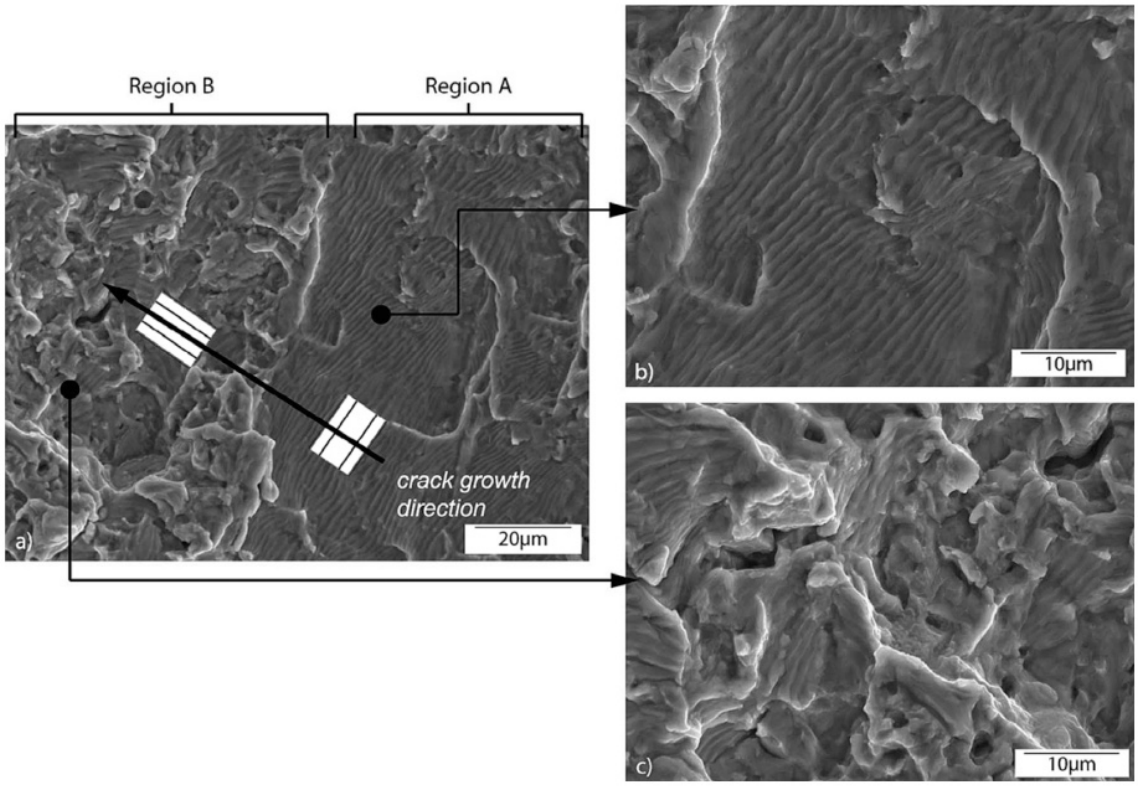

Figure 2.20: a) SEM fractograph showing a fracture surface where the fractographic features have changed as a function of primary-α grain orientation. b) Close-up of region A. c) Close-up of region B. From [9]

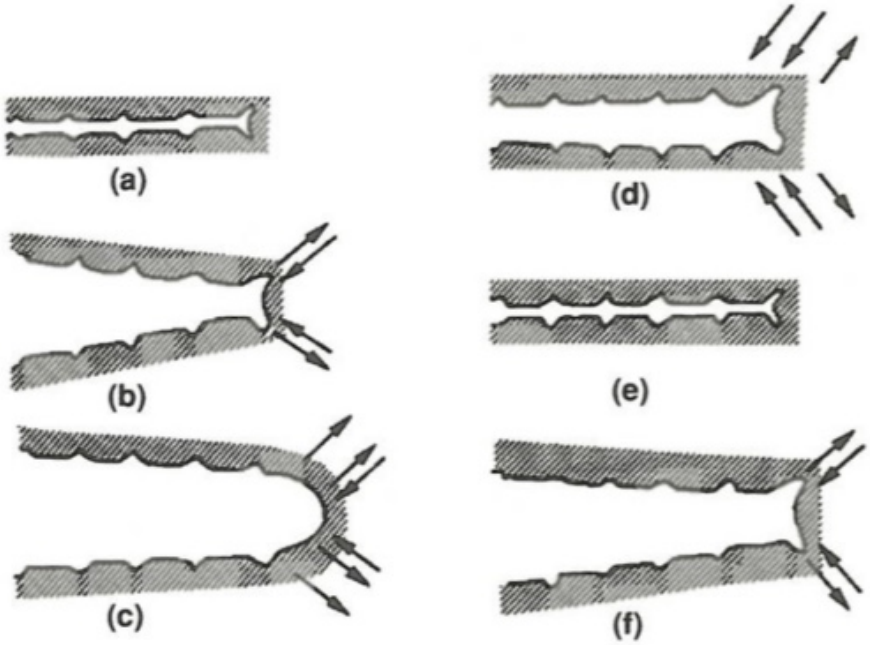

Figure 2.21: Laird model of striation formation. The idle crack (a) opens under tensile load which activates two slip planes at the crack tip (b) and the crack opens out (c). Upon unloading the crack tip blunting does not fully reverse (d) this causes the crack to propagate one increment (e). This process repeats with further load cycling (f). From [49, 38, 82]

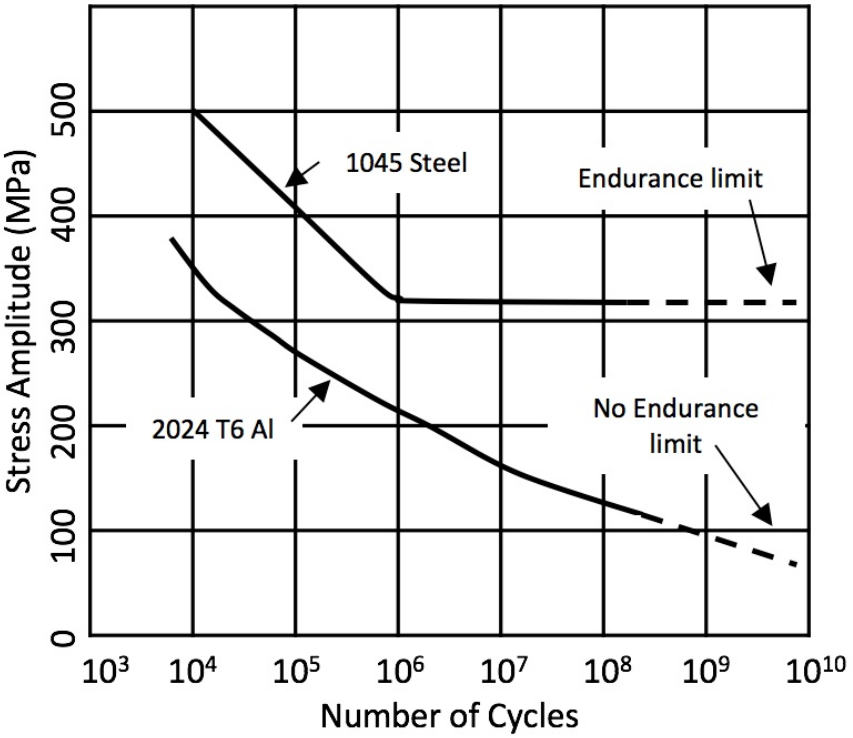

Figure 2.22: S-N curve showing a comparison of the fatigue behaviour of steel and aluminium, adapted from [3]

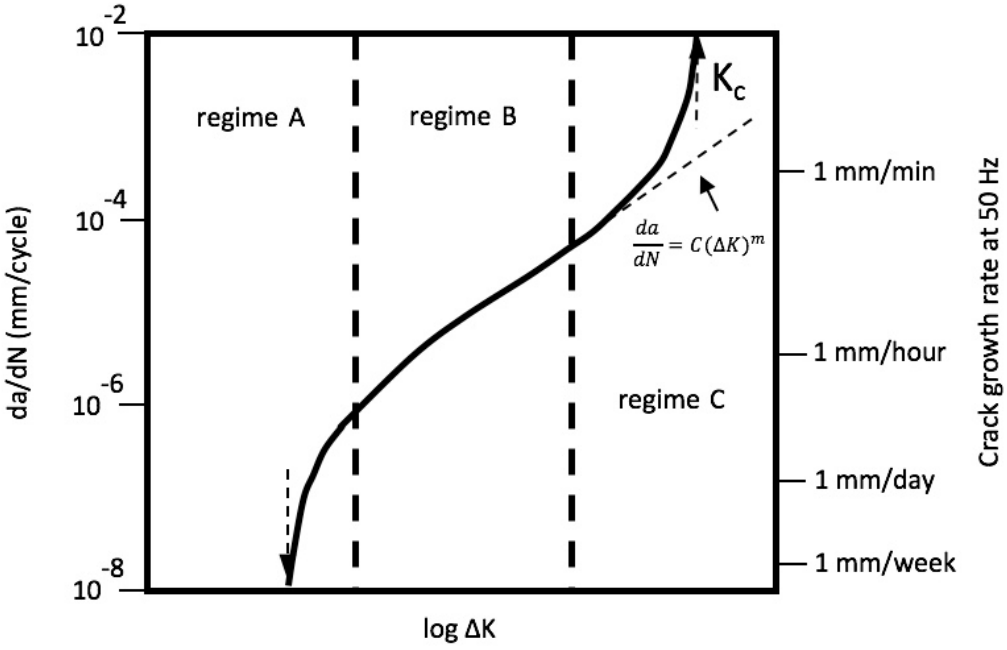

Figure 2.23: Schematic of a δa/δN vs log-ΔK plot adapted from [80]

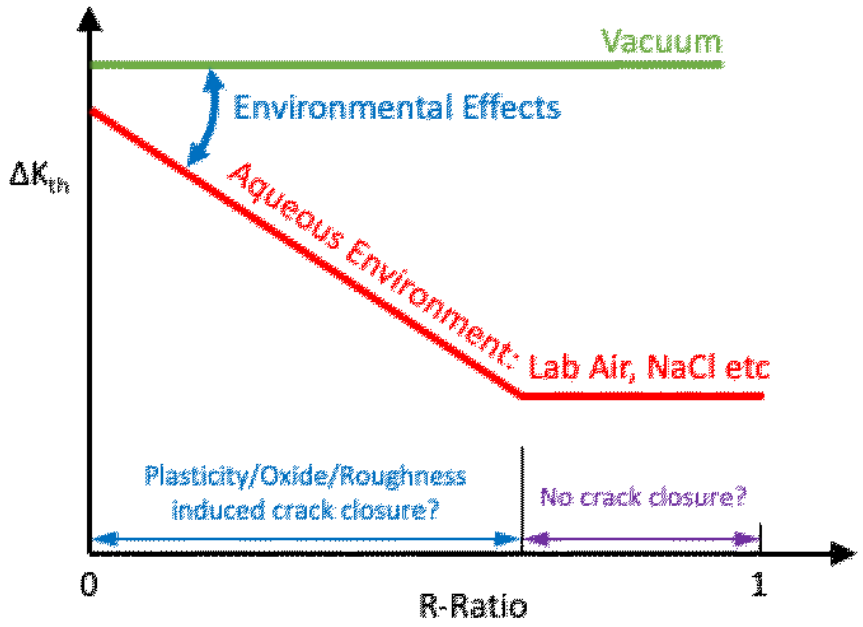

Figure 2.24: Figure recreated from [85] showing the effect of vacuum on threshold of fatigue cracks for metallic materials

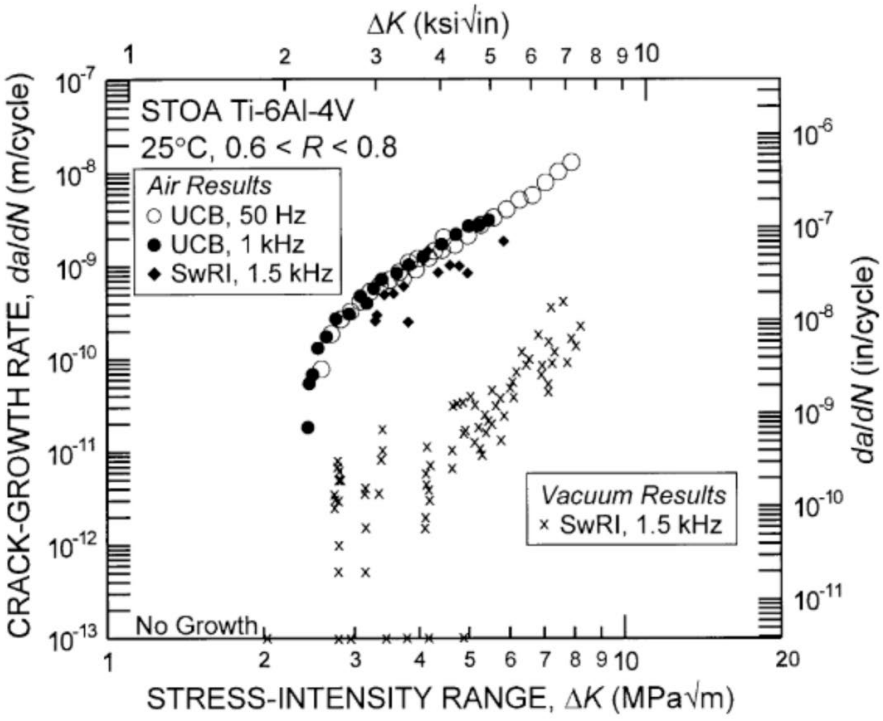

Figure 2.25: Figure from Ritchie et al. [64] for Ti-6Al-4V showing crack growth rate against ΔK for air vs vacuum.

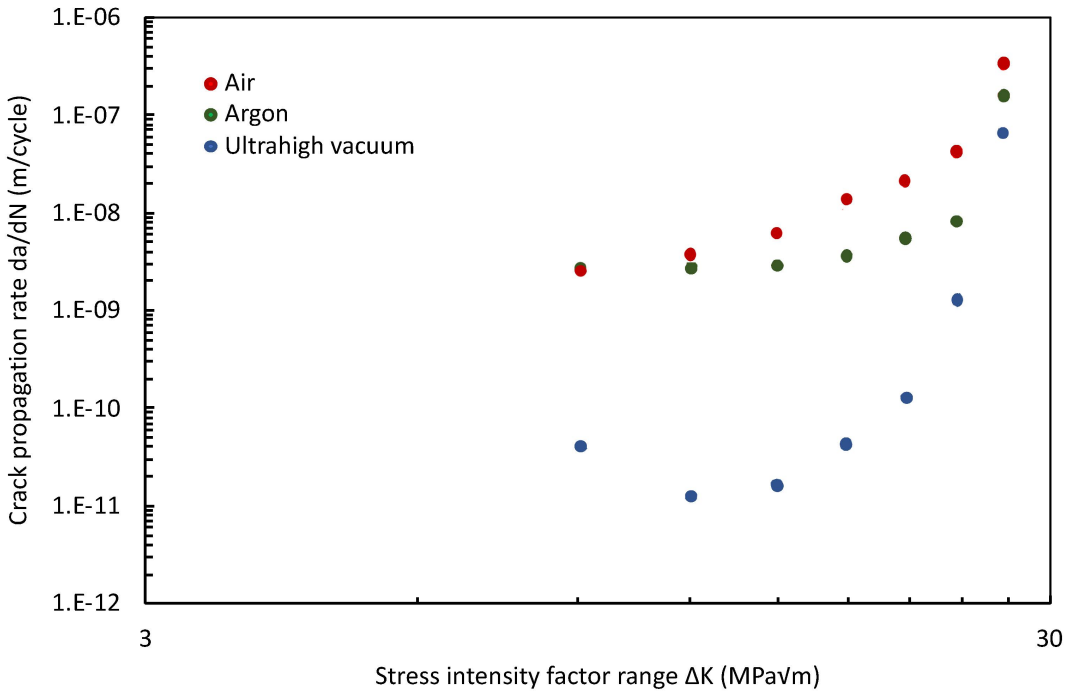

Figure 2.26: Figure recreated from [92] showing fatigue crack growth against ΔK as a function of environment

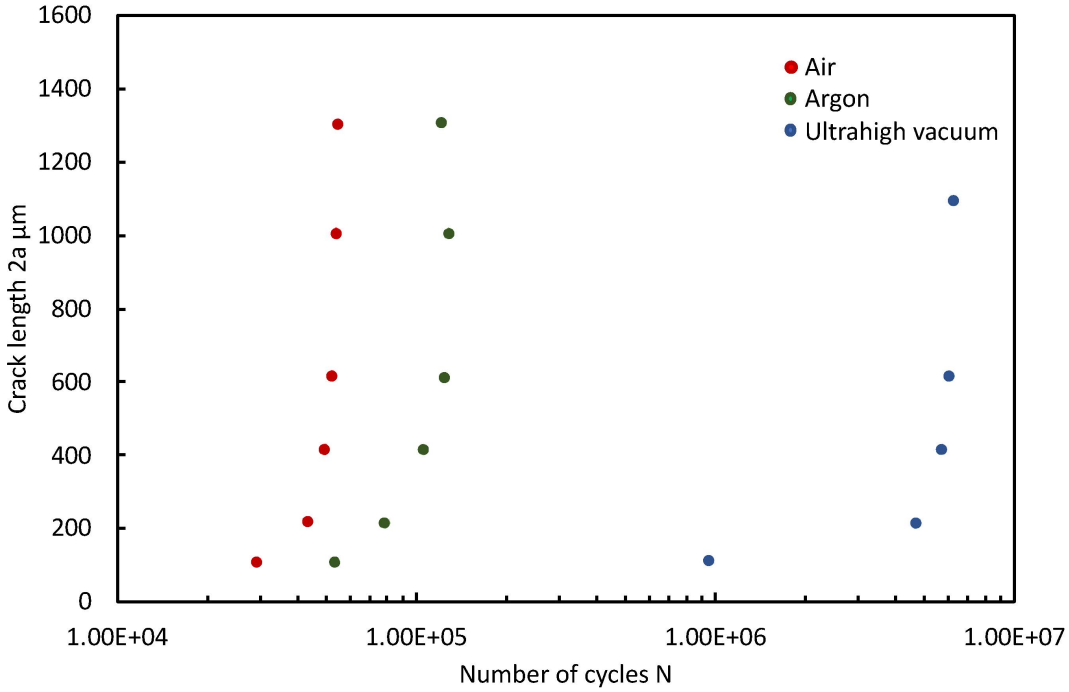

Figure 2.27: Figure recreated from [92] showing crack length against number of cycles as a function of environment

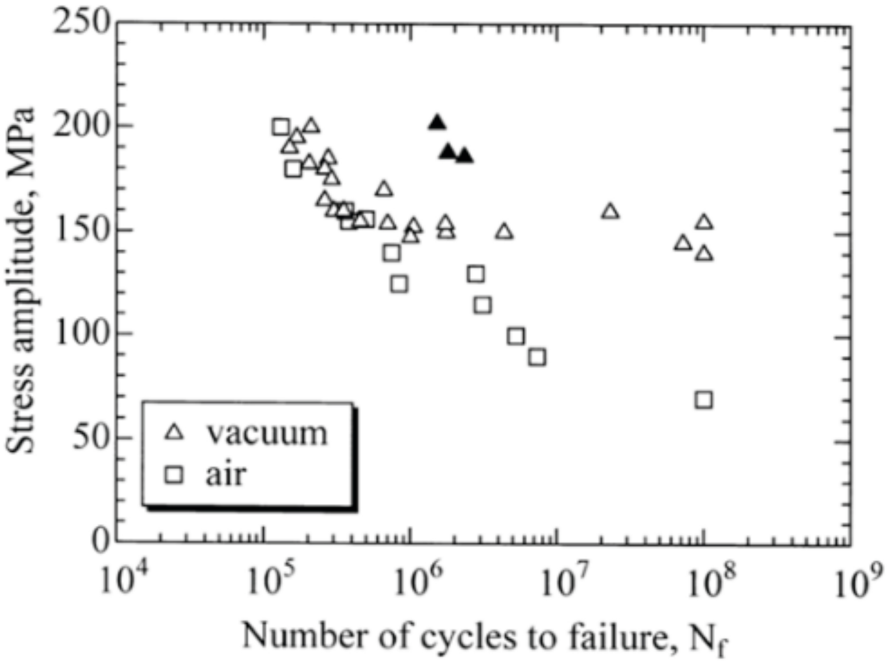

Figure 2.28: Figure from [31] showing SN curves for CPTi samples tested in air and vacuum. Black triangles are from tests that experienced a violent damping phenomena - there is no further explanation of what this phenomena was in the source paper

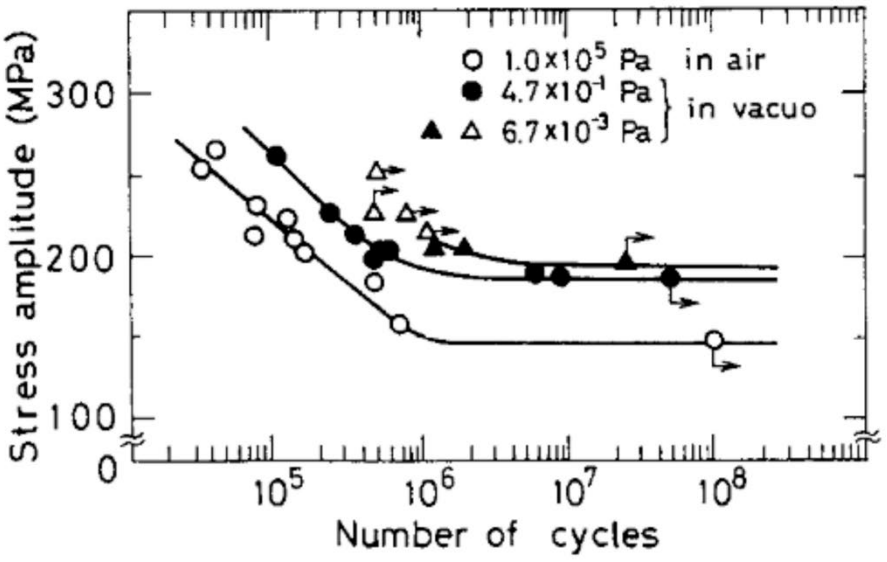

Figure 2.29: Figure from [79] showing an SN curves for a range of CPTi samples tested in air and vacuum. The hollow triangles are tests that experienced a violent damping phenomena at the test frequency

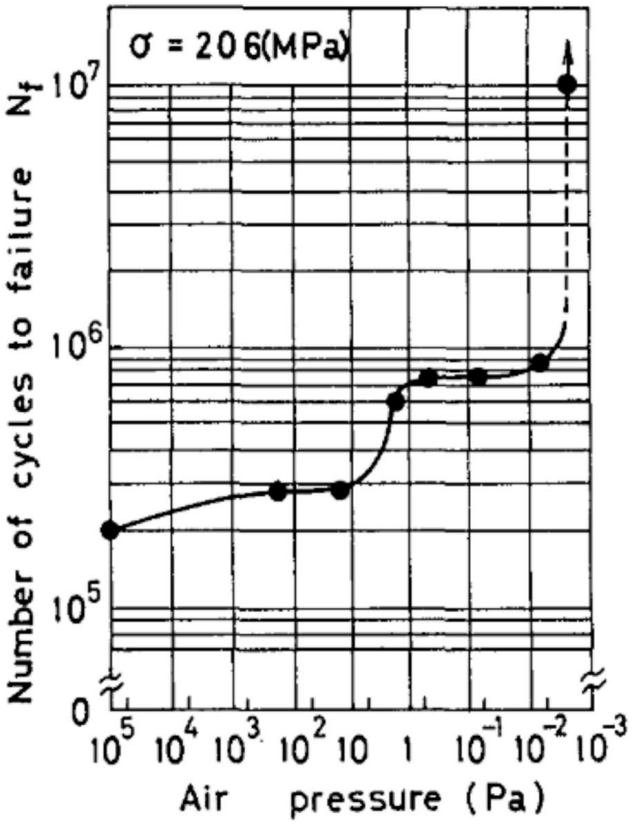

Figure 2.30: Figure from [79] showing a sample life vs test pressure curve for CPTi samples tested in varying levels of air pressure

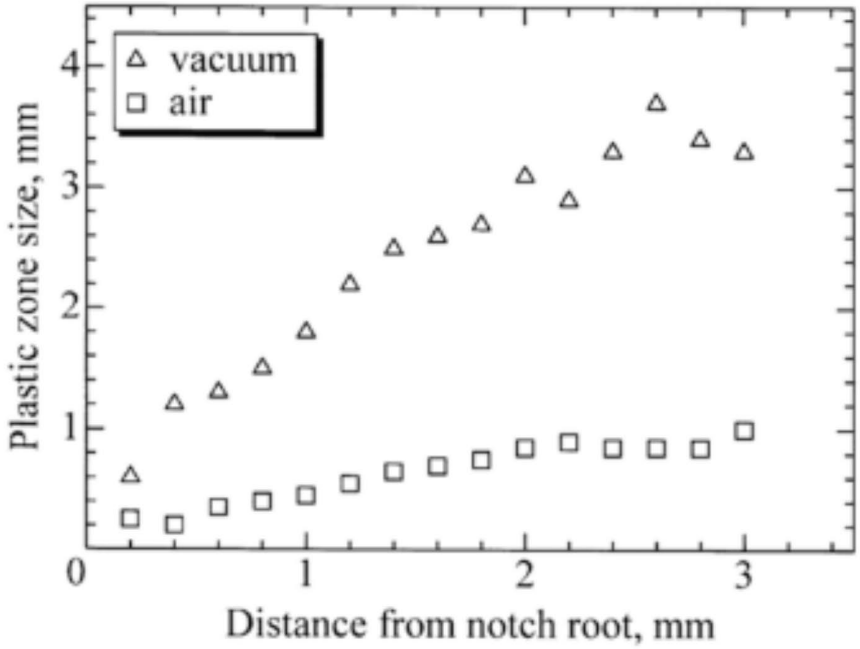

Figure 2.31: Figure from [31] showing the relative sizes of plastics zones formed in air and vacuum during fatigue testing of CPTi samples at a peak stress of 160MPa

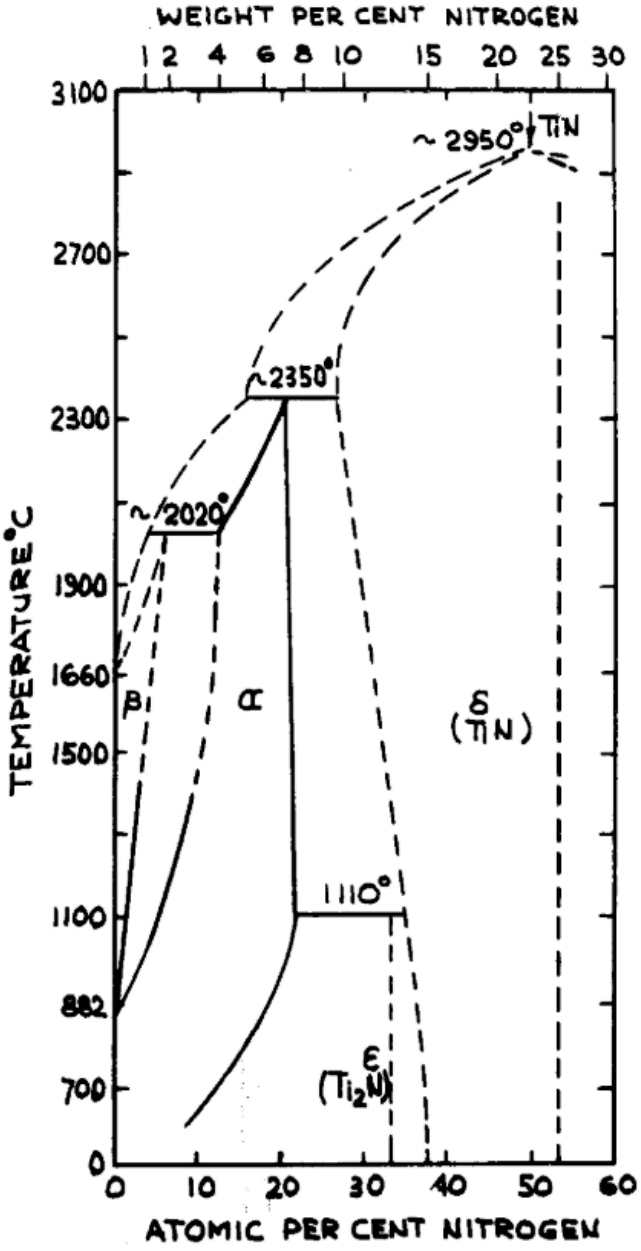

Figure 2.32: Titanium nitrogen phase diagram taken from McDonald and Wallwork [46]

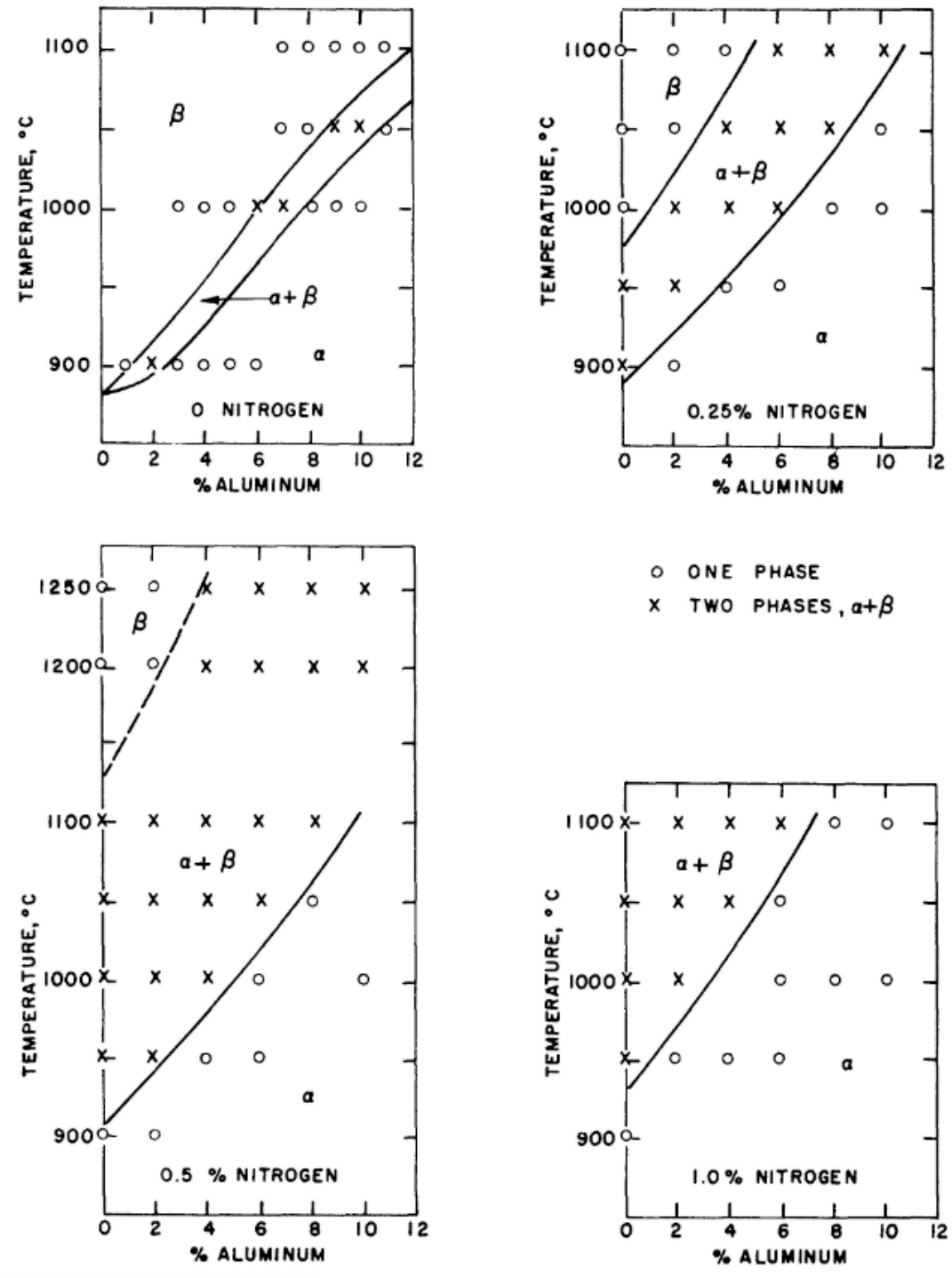

Figure 2.33: Titanium nitrogen phase diagram taken from Kessler [37]

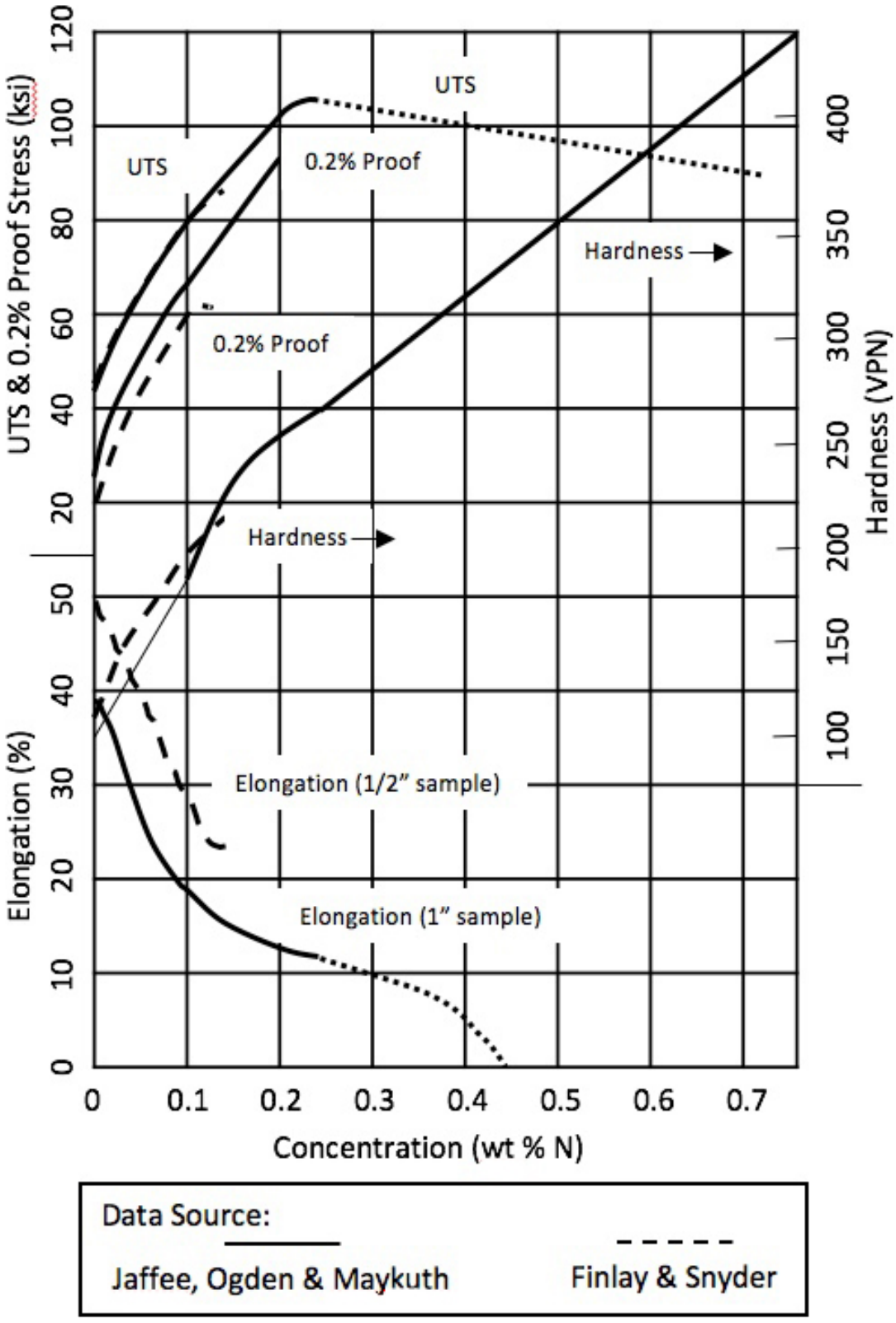

Figure 2.34: Effect of nitrogen on room-temperature tensile properties and hardness of iodide titanium adapted from ([26, 57])

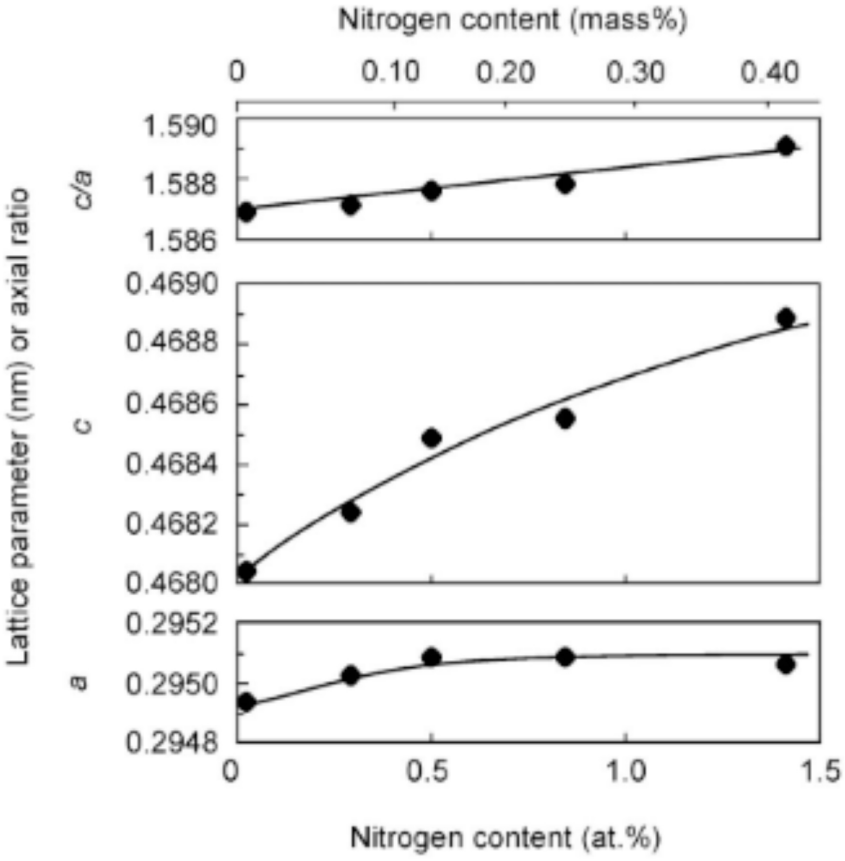

Figure 2.35: Effect of nitrogen on lattice parameters c, a and the c/a ratio [1]

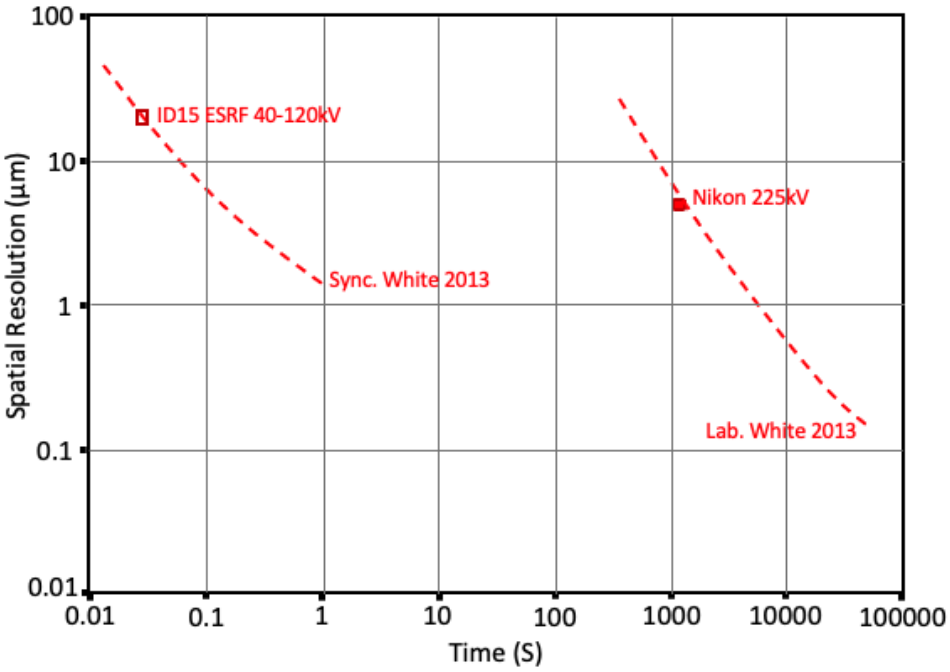

Figure 2.36: Schematic chart showing capture rates against spatial resolution of laboratory based CT and synchrotron adapted from [44]

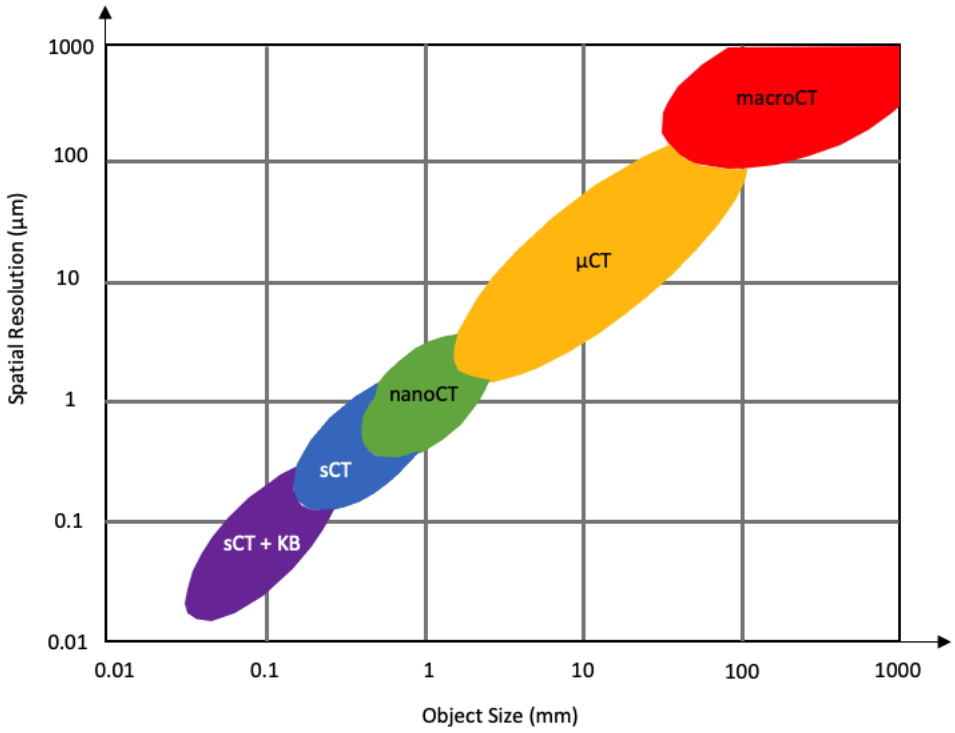

Figure 2.37: Schematic chart showing the relationship between CT method, object size and spatial resolution, adapted from [23]

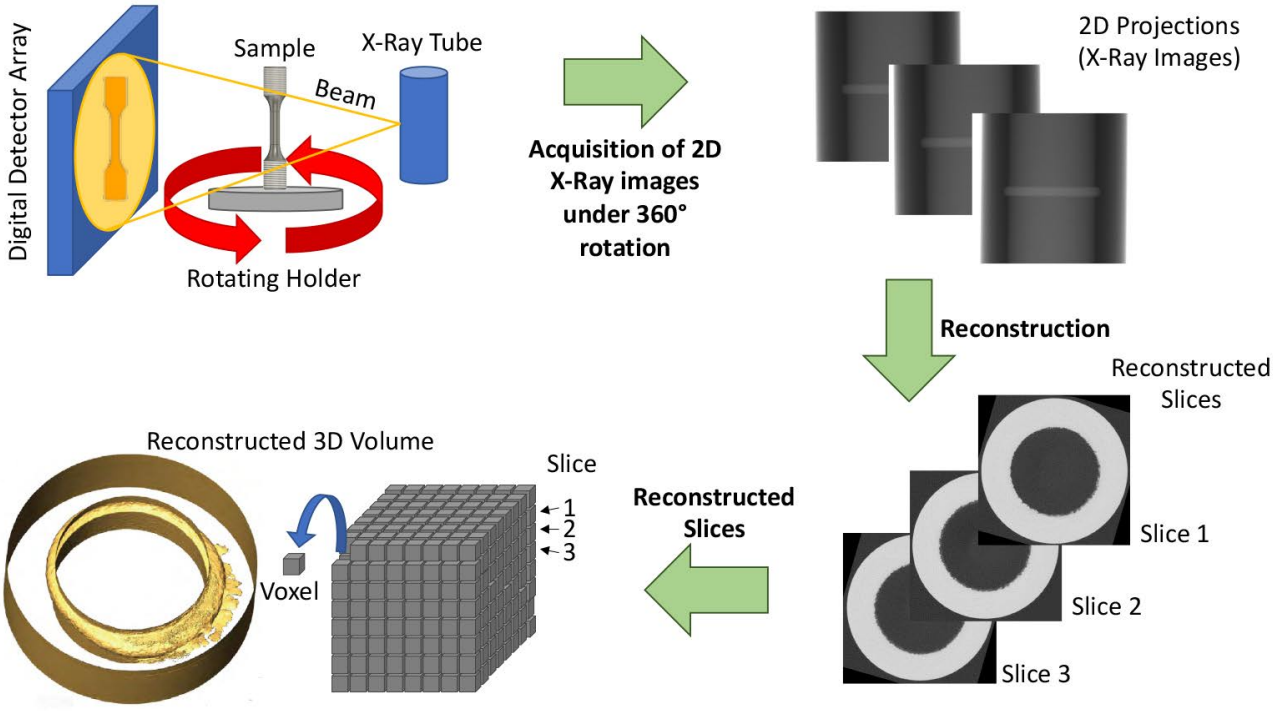

Figure 2.38: Schematic showing overview of the CT process adapted from [5]

Table 2.1: Titanium alloying additions

α Stabilisers	Neutral	β Stabilisers	β Eutectoids
O, N, Al, C	Sn, Zr	V, Mo	Fe, Cr, Mn, Cu, Si

Table 2.2: Comparison of material properties between Ti-6Al-4V (MSRR8672 TFH) and Commercially available CPTi Grade 4

	O wt%	Fe wt%	N wt%	UTS (MPa) min	YS 0.2% (MPa)	Elongation %
Ti-6Al-4V	0.17-0.23	<0.30	<0.03	>930	>830	>8
CPTi Grade 4	0.40	0.50	0.05	550	483	15

Chapter 3

Investigative techniques and methods

Abstract

Increasing demands on titanium alloys in aerospace applications have driven a push towards deeper understanding of their behaviour in service. This extends from component performance during planned operation, damage mechanisms, and how they may ultimately fail. Investigation of damage and failure requires a comprehensive framework of techniques in order to identify a root cause, further failure mechanism understanding, and is crucial to defining and improving component lifetimes. This chapter presents an overview of the techniques used in state of the art industrial titanium alloy failure investigation, highlighting the inherent reciprocal links to frontline research and the need for constant innovation.

3.1 Introduction

This review surveys the usage of several techniques, divided into core, specialist and future categories according to their levels of industrial access and readiness. Good understanding of when and how best to apply these techniques is key to unlocking the complexities of in-service component failures. Core techniques available in-house are used in both routine and highly detailed investigations, and form a broad basis from which externally supplied specialist or novel techniques can be employed as required. A number of factors determine the applicability of each technique to different types of investigation, Figure 3.1, and these have been used to divide up the categories in this paper.

3.2 Core Techniques

Many of the techniques used routinely in industrial failure investigation have been available for decades but remain essential. Among these are high-quality macro photography, stereo-microscopy and secondary electron imaging in scanning electron microscopy (SEM). Recent refinements and advances in hardware and software increase the depth of insight provided while also allowing for faster response times, which can be crucial in supporting root cause understanding in the hours and days immediately following an in-service event. This section explores some of these.

3.2.1 Automated 3D optical microscopy

Optical microscopy is the first port of call for many investigations and has benefited greatly from the development of automated focus stack imaging. Quantitative topographical information can be extracted from the stitched image dataset, allowing 3D representations of the region of interest to be made, as well as allowing features such as surface relief depths or fracture surface inclinations to be measured, Figure 3.2 [95]. These systems allow such data to be recorded at coarser length scales and for larger areas than are feasibly observed in analogous SEM systems.

3.2.2 Automated SEM image collation and capture

Recent SEM software advances [93] have enabled a step change in SEM usage for the analysis of fracture surfaces. Using the metadata for each image to locate it in space, a 3D collation of all images in a dataset can be produced automatically to give much better and faster contextualisation of feature locations, Figure 3.3(a). This contextualisation also enables data input for cross-checking of stress modelling by providing quantitative data regarding the transition from fatigue to fast fracture. Comparison to earlier optical examinations is also possible with software capable of calibrating stage coordinates to an optical micrograph or macro photograph. Another software development of great advantage to industrial SEM users is automatic capture of images across a large (x, y) area with automatic focussing on each tile of a stitched image, Figure 3.3(b). This allows SEMs to be used around the clock without

the need for an investigator to be present, freeing up time for analysis and improving the cost effectiveness of the equipment. This type of software also allows imaging of very large areas, along with easy contextualisation of features.

3.2.3 EBSD fractography

While a standard technique on flat, polished specimens, the use of EBSD on fracture surfaces is less well established and presents a range of challenges [54]. Surface roughness is the first barrier to using this technique on fracture surfaces, but it is possible to successfully index patterns on low-ΔK fatigue facets and other relatively flat features, Figure 3.4 Inclination of the fracture surface relative to part geometry is often a complicating factor. Low indexing rates mean that care must be taken in interpreting results. It is anticipated that the development of CMOS detectors will allow for improvements in this technique. As well as surface roughness, surface plastic strain must also be considered as this will have a bearing on the success of an EBSD scan.

3.3 Specialist Techniques

A range of more specialist techniques has become part of the arsenal of Rolls-Royce failure investigators, used to complement our core techniques where greater complexity is encountered during an investigation. These techniques are typically provided by academic institutions or specialist contract companies with which Rolls-Royce maintains close working relationships. This expands the toolkit of investigators beyond what is feasibly performed in-house, allowing access to highly specific expertise in cases where it is required only rarely.

3.3.1 Focussed ion beam secondary ion mass spectrometry (FIB-SIMS)

In cases where SEM-EDX is unable to chemically or spatially resolve features under investigation, for instance where light elements are of interest, FIB-SIMS may be used. A FIB is used to sputter ions from a specified area, which are then measured in a mass spectrometer to identify

their chemical species. This chemical analysis can be performed at very shallow depths [15], to analyse surface layers, or to construct coarse depth profiling of a cross-section, Figure 3.5(a).

3.3.2 Dynamic secondary ion mass spectrometry (DSIMS)

DSIMS involves similar methods to FIB-SIMS, but measures bulk composition by targeting a larger area with FIB sputtering. This can sample at depths up to 30 µm for typical industrial alloys, and can be used in either a relative sense, comparing numbers of counts, or an absolute sense, when calibrated against a standard specimen. Measurement of oxygen, carbon and nitrogen in titanium alloys is possible, Figure 3.5(b), and Rolls-Royce has been active in driving this technique forward to achieve repeatability in measurement of these species at the 10 ppm level in calibrated materials.

3.3.3 Widefield confocal microscopy

Confocal microscopy is another recent addition to the failure investigation toolkit, allowing quantitative topographical examination of as-machined surfaces or fracture surfaces [94]. In the observation of fractures, it provides a useful route to understanding crack path behaviour, Figure 3.6.

3.3.4 Spatially resolved acoustic spectroscopy (SRAS)

For instances where texture information is required across large areas, EBSD may be too slow for industrial response times, so that the development of SRAS provides a useful alternative [14]. Laser-induced acoustic pulses are sent through the sample, and the acoustic velocity response is measured, which depends on crystallographically-determined acoustic impedance. Although it does not quantify specific grain orientations, the resulting velocity map gives an indication of grain size and texture intensity, Figure 3.7 As with EBSD, the surface needs to be prepared to a high polish finish, but larger samples may be inspected.

3.3.5 FIB lift-outs

Local structure and chemistry at the sub-micron scale may be of interest for more in-depth investigations, making FIB lift-out of a feature for subsequent transmission electron microscopy (TEM) useful. A dual-beam FIB-SEM is used to locate the region of interest with the electron column, before milling around the feature with the ion beam to enable its removal from the bulk with a micromanipulator. By thinning the sample to electron transparency, TEM can be used to determine crystallography and morphology of nanoscale features, dislocation density and type, and local chemistry.

3.3.6 Atom Probe Tomography (APT)

When it is deemed necessary to understand the chemical composition of a nanometre-scale feature, or to determine the compositional change across a microstructural interface, the high compositional and spatial resolution of APT has been shown to be industrially applicable [7].

3.4 Novel Techniques

Rolls-Royce's work with a number of leading research establishments in the UK aims to develop new techniques and exploit cutting-edge science for industrial applications.

3.4.1 Micromechanical testing

Failure investigation currently focusses on characterisation of surfaces and microstructural features to determine the likely root cause of failure. This may seek to infer whether the material's mechanical behaviour at the region of damage initiation was as expected or had been degraded prior to cracking, leading to early failure. Conventional mechanical testing of surrounding material is often insufficiently representative of the region of interest, due to practical difficulties with specimen size and achievable proximity to the feature.

The advent of micro- and mesomechanical testing has made possible the direct measurement of monotonic and fatigue properties across sub-micron to 100 µm length scales, Figure 3.8 [66].

Complex environmentally degraded surfaces [78] and bulk material can be analysed, as well as fatigue testing of individual or combined microstructural components. This offers a potential step-change in significant investigations that extend to include research activity, as well as more standard usage in future. Another advantage could be testing the effect of non-standard surface conditions such as roughness, residual stress or damage, generally not captured by conventional testing.

3.4.2 High speed atomic force microscopy (HS-AFM)

AFM offers high-resolution 3D measurement of topography, by tracking the deflection of a sharp tip rastered over the surface. Development of AFM towards use in failure investigation could offer insight into sample stress histories. Imaging of fatigue striations has been achieved in research [83], but conventional apparatus is unable to cope with micron-scale height changes commonly seen on fracture surfaces, and is subject to several artefacts and slow scan times. HS-AFM has recently been developed and offers real-time, live imaging across large areas [13]. If challenges with large height ranges can be overcome, HS-AFM may be a useful investigative tool in future.

3.4.3 Micro-computed tomography (µCT)

Using µCT to examine cracks in test samples has been shown to be feasible [16], Figure 3.9 The transition to using it for ex-service components to identify crack locations and growth paths remains challenging. The complex geometries and sizes of jet engine components cause issues around achieving clear transmission of X-rays while maintaining high resolution.

3.5 Conclusions

Selecting the right combination of contemporary techniques for failure investigation of an ex-service component allows for much more clarity around the root cause of the failure, alongside deeper understanding of the underlying mechanisms. The field has progressed significantly from a previously limited suite of techniques and continues to develop rapidly. It should also be

recognised that, in a commercial environment, there remains a tension between the required level of characterisation of a failed component and the time and cost incurred in performing such analysis. The importance of strategic development of advanced characterisation techniques for failure investigation cannot be overstated. It is of extreme value to manufacturers to have a wide range of techniques available, ready to be used as and when required. For this reason, Rolls-Royce continues to build and sustain relationships with academia and specialist technique providers to further the development and adaptation of existing and emerging characterisation techniques.

3.6 Figures

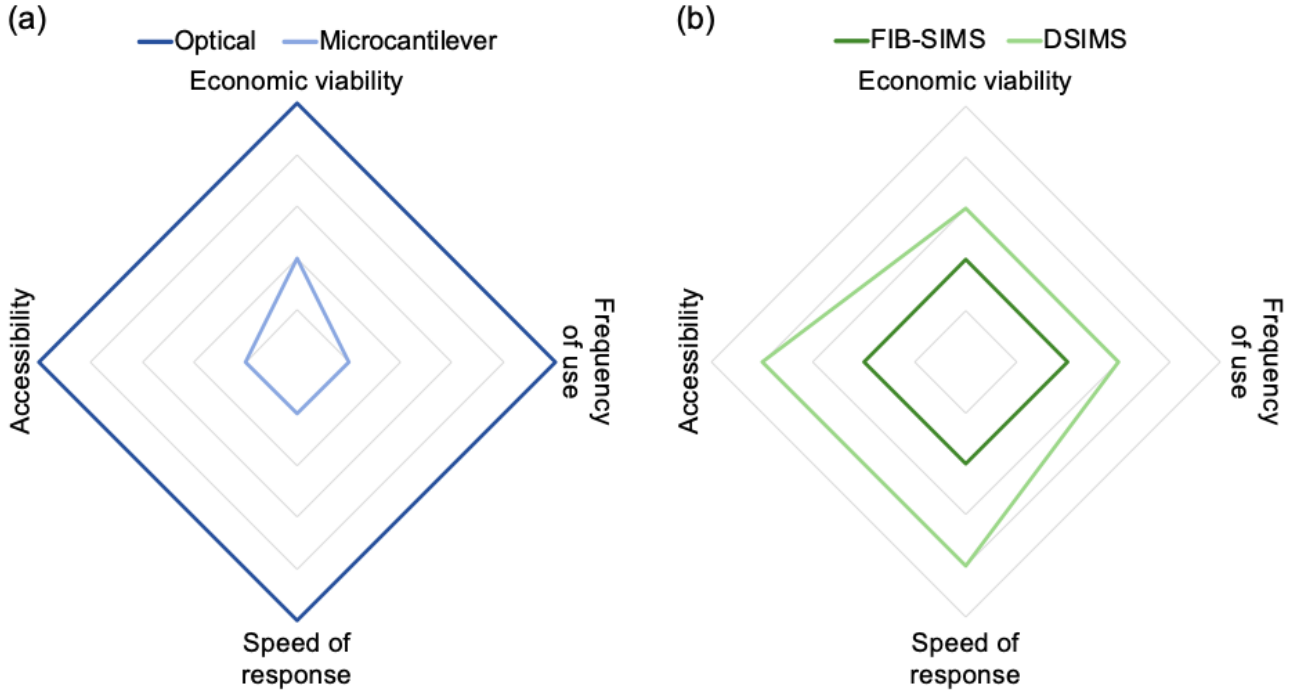

Figure 3.1: Several factors determine the usage of techniques in failure investigation, schematically shown here in radar plots. (a) Optical microscopy provides a rapid overview of samples and is used in every investigation, while microcantilever testing of local mechanical properties is still under development as an investigative tool. (b) FIB-SIMS is commonly applied in academic research, but DSIMS results are more accessible for industry.

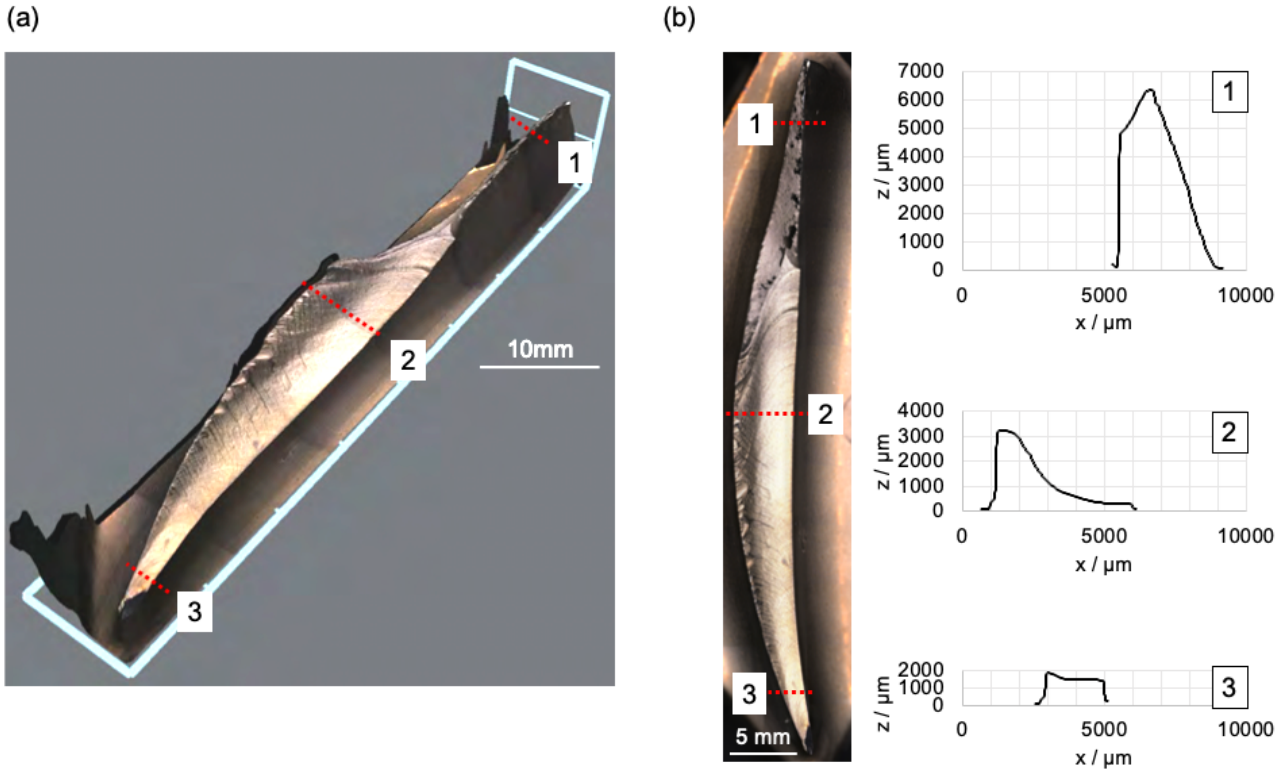

Figure 3.2: A 3D optical micrograph of a high cycle fatigue fracture in a compressor blade aerofoil, captured with a Zeiss SmartZoom 5 system. Optical images are recorded in a stitched focus stack, calibrated so that accurate topographical information can be extracted, as demonstrated in the three height profiles shown.

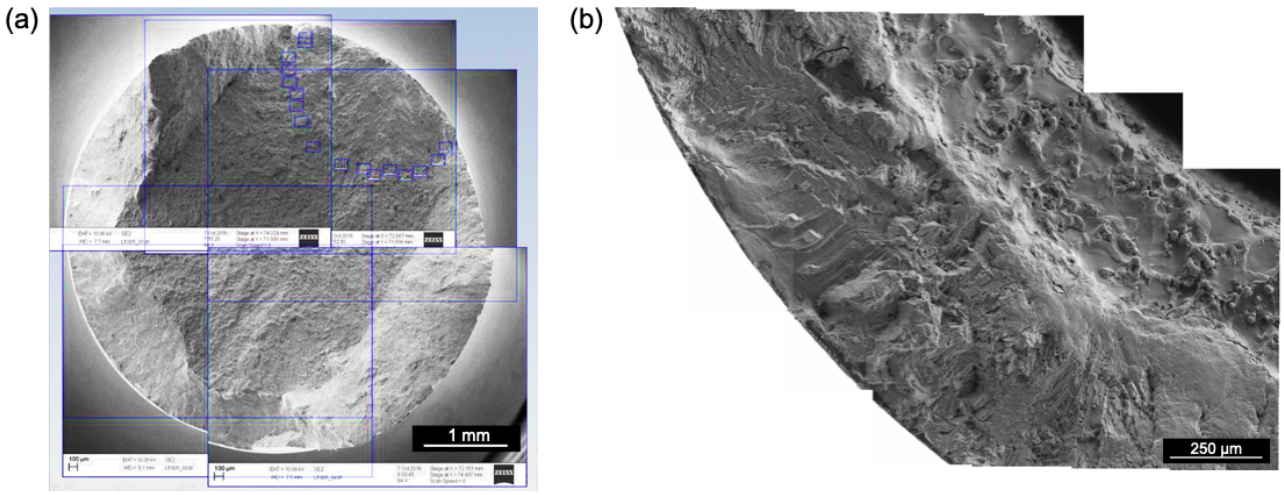

Figure 3.3: (a) An example of image collation in Zeiss's SmartBrowse software, showing SEM images located relative to one another using metadata. Here, the boundary between regions of different fracture behaviour was clearly identified in the context of the fracture surface as a whole. (b) A stitched image of a fracture surface captured using Zeiss's SmartStitch software, providing a large field of view while retaining good resolution.

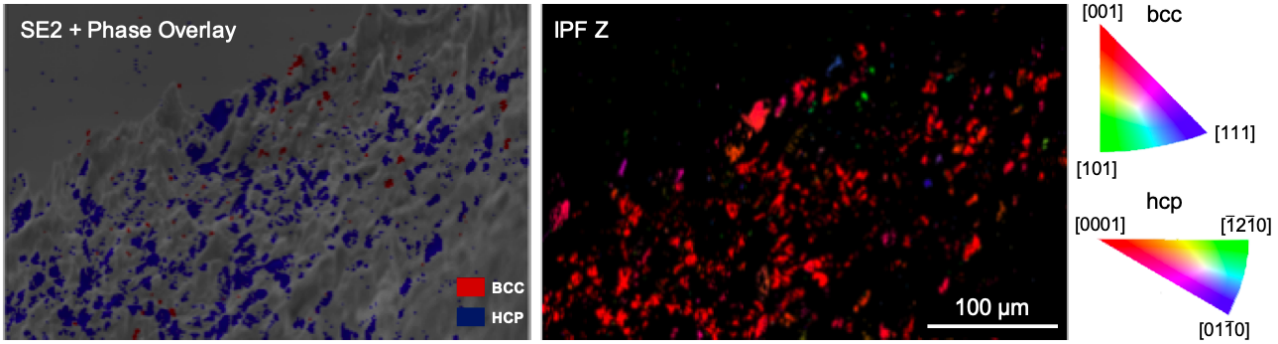

Figure 3.4: EBSD fractography of a facetted fracture surface, demonstrating the capabilities and limitations of current systems. Although several facets have been successfully indexed, the surface roughness of the fracture prevents complete mapping and remains challenging.

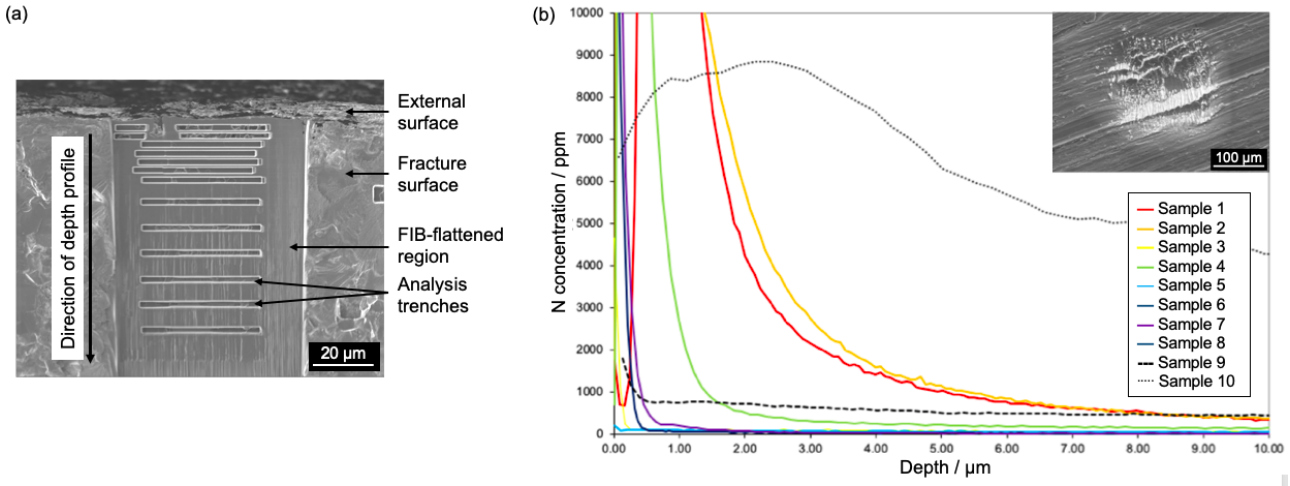

Figure 3.5: Two SIMS techniques are applicable to failure investigation. (a) An SEM image shows FIB-SIMS trenches made to create a coarse depth profile across a fracture surface, requiring prior flattening with glancing-angle FIB milling for comparable measurements. (b) DSIMS provides finer-scale depth profiling of nitrogen concentration in ten different Ti-6Al-4V (wt.%) surfaces, and is made fully quantitative by calibration to a standard. Inset is an SEM micrograph showing a sputtered crater after measurement.

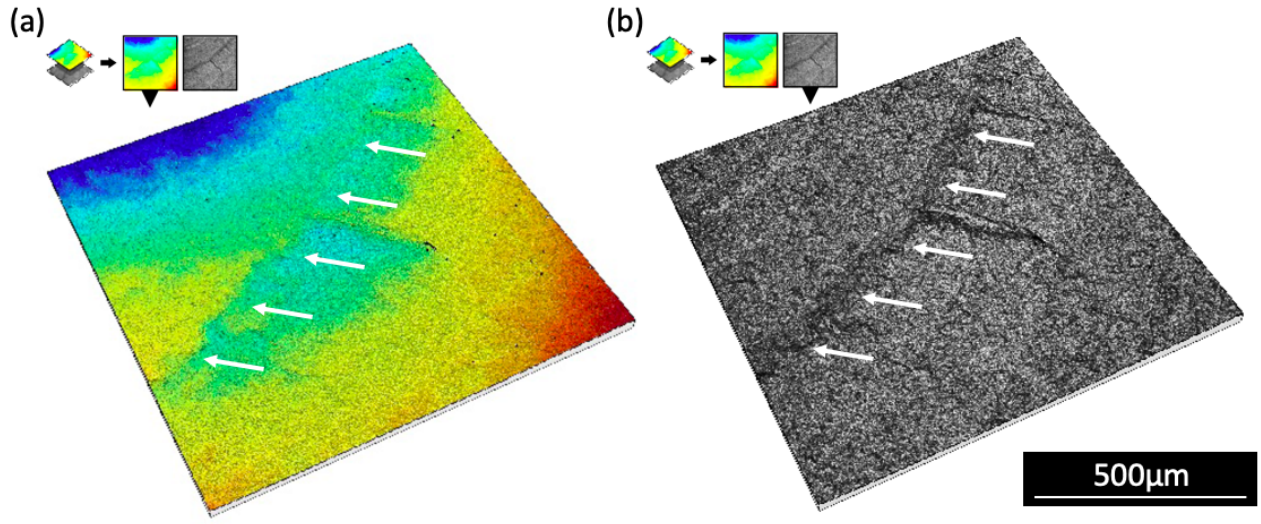

Figure 3.6: Widefield confocal microscopy analysis of a fracture surface on a compressor blade, acquired using a Zeiss SmartProof 5 system to produce a height map (a) and an optical image (b). The arc-like feature indicated in the images is a beach-mark resulting from high cycle fatigue.

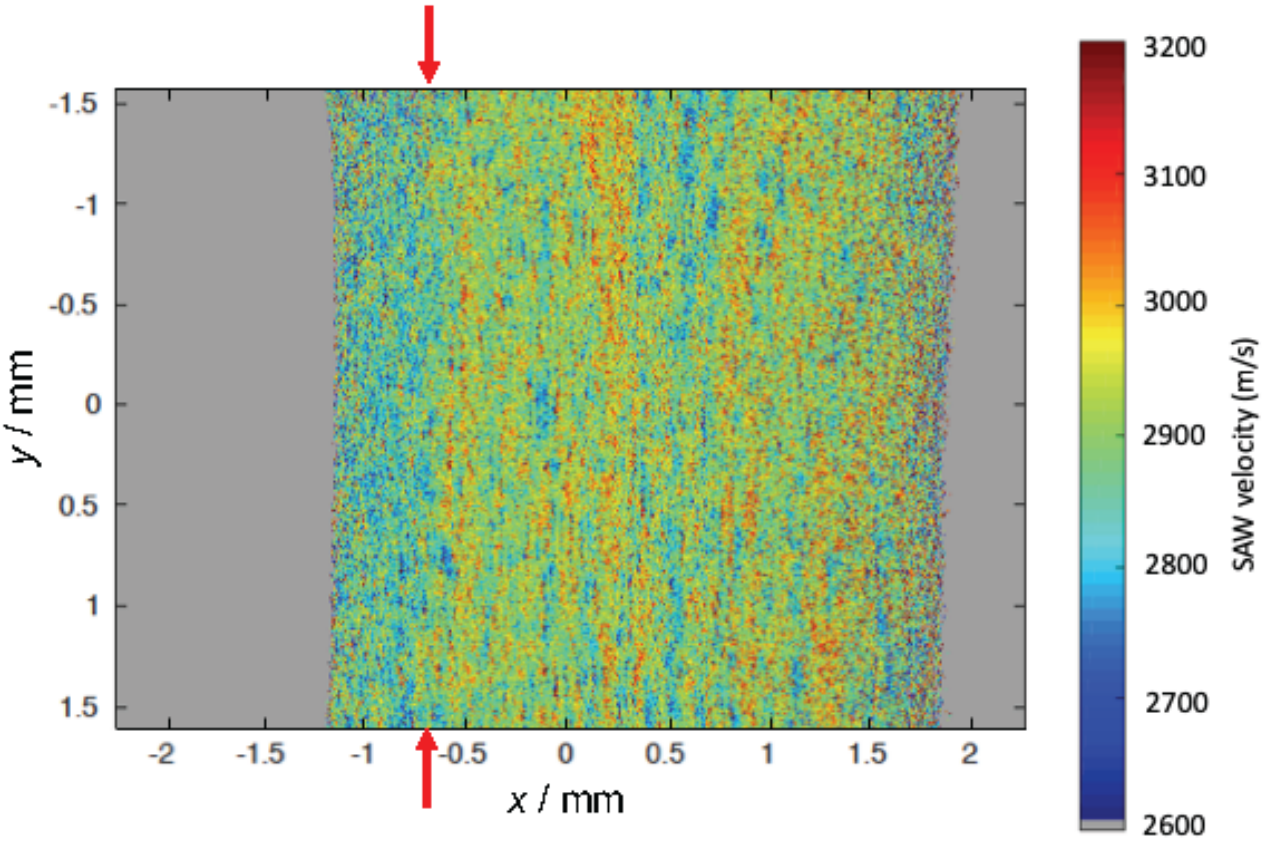

Figure 3.7: A SRAS velocity map of two Ti-6Al-4V (wt.%) plates that have been diffusion bonded together (bond line indicated by red arrows). The differences in both grain size (finer in the LHS plate) and texture (macrozones evident in the RHS plate) are evident.

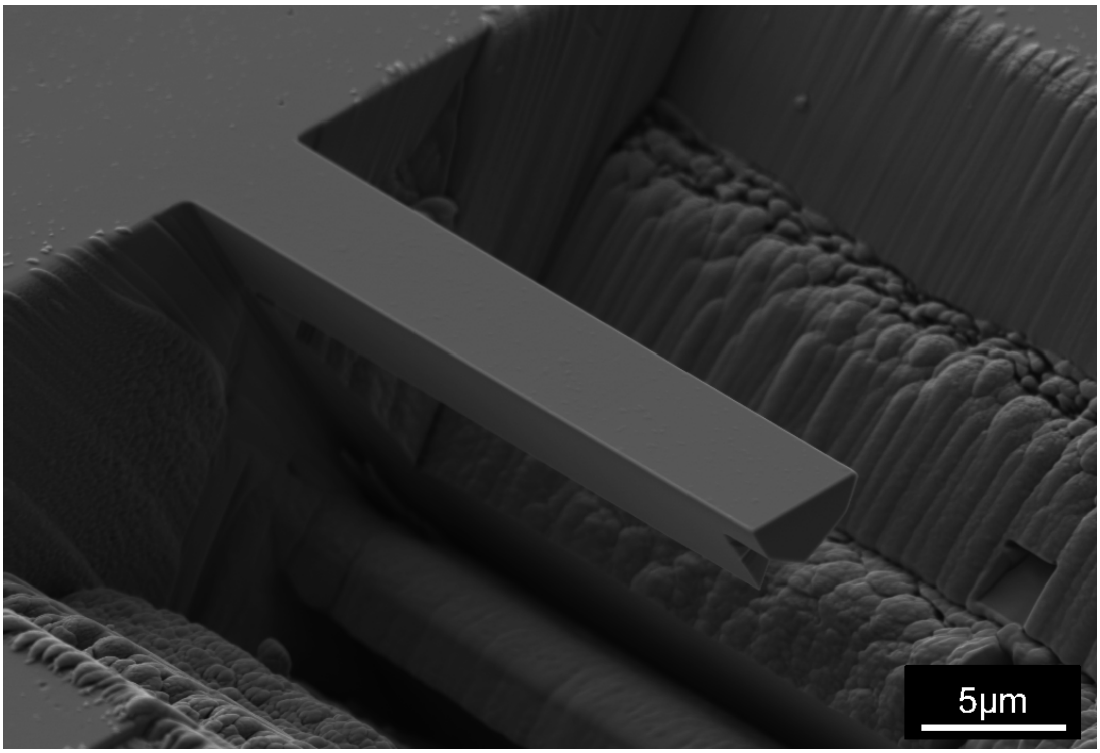

Figure 3.8: An SEM image of a FIB-milled microcantilever in a titanium alloy, ready for loading with an indenter to investigate the orientation dependence of slip behaviour. In industrial applications, this could be used to probe slip behaviours in specific grains or features of interest on ex-service parts.

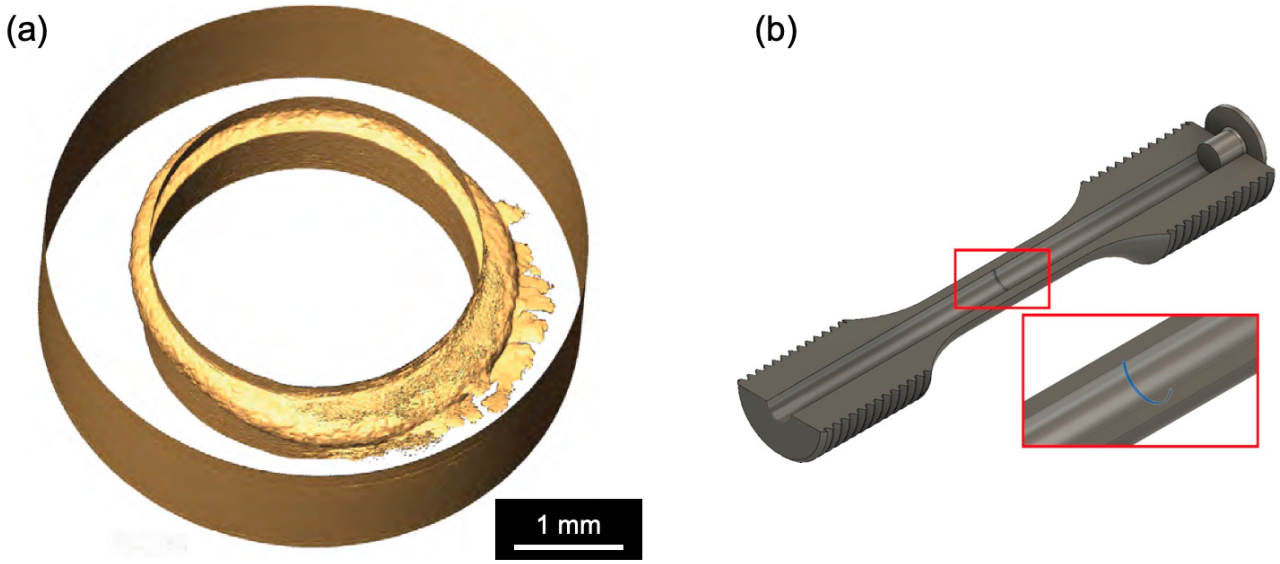

Figure 3.9: (a) A 3D µCT isosurface reconstruction of a hollow fatigue test specimen, showing a fatigue crack during propagation. (b) The specimen geometry shown in a CAD model.

Chapter 4

The Effects of Nitrogen on the Mechanical Properties of Ti-6Al-4V

Abstract

In this chapter the effect of nitrogen additions on fatigue behaviour have been examined in near-equiaxed, rolled Ti-6Al-4V bar. This is the first-time nitrogen content has been systematically explored with respect to monotonic and cyclic properties in a Ti-6Al-4V alloy base composition. Nitrogen additions were found to increase the β-transus temperature and strength but to decrease ductility, even in microstructures where some β phase remained. This carried across into both the low and high cycle fatigue behaviour; even small contents of 240 and 560ppmwN caused reductions in both low cycle fatigue life and high cycle fatigue strength. In samples containing 240 and 560 ppmwN, a conventional striated fractographic appearance was observed, but a dramatic change to a macroscopically brittle fracture surface was observed at 1800 and 3600ppmwN, but still with substantial evidence of plasticity at the microscale. Therefore neither microstructure or fractographic examination, nor EDX-based compositional analysis in the electron microscope are necessarily a reliable indicator of an absence of deleterious nitrogen contamination. This is significant for the investigation of potentially nitrogen-contaminated surface-initiated cracks, either due to service or processing exposures.

4.1 Introduction

There is a wealth of knowledge and published data exploring the effects of oxygen on titanium alloys, however, nitrogen has received significantly less attention. Work was undertaken in the 1950's [48, 26, 57, 84, 35] on the effects of nitrogen on titanium alloys but this data is limited in scope and availability of advanced experimental techniques, e.g. to yield strength and hardness data, with little or no public data being available on the fatigue implications.

This is important because the high temperature solid state processing of titanium can lead to the introduction of interstitial-enriched surfaces. Usually these are mitigated through finishing operations and/or processing in a vacuum or inert atmosphere, however, guaranteeing complete removal of interstitial-enriched surfaces is not trivial. The local properties that occur at the surface of a titanium component, particularly around a geometric feature that may act as a stress raiser, will then often form the basis of the assessment of fitness-for-service. In such conditions, elevated levels of oxygen and/or nitrogen may be found, as both these elements have significant solubility in *hcp* α-titanium. The effects of interstitials in titanium have been extensively reviewed by Conrad [22]; in general terms both oxygen and nitrogen are α stabilisers that provide solid solution strengthening to the α phase, and oxygen is added for this reason to many titanium alloys. However, there is an upper bound of useful oxygen content, for Ti-6Al-4V this is $\leq$ 2400 ppmwO.

The addition of oxygen and nitrogen to titanium alloys has been shown to increase the strength by a very large amount per at%, Figure 4.1; this also has the undesired effect of embrittling the alloys. It is observed that nitrogen is a more potent solution strengthener than oxygen, which is in turn more effective than carbon. It is thought that the reason behind this, is the change in slip tendency from $\{10\bar{1}0\} < 11\bar{2}0 >< \bar{1}100 >$ prism slip to $\{10\bar{1}1\} < 11\bar{2}0 >< 11\bar{2}3 >$ pyramidal slip. Nayak et al. [52] have suggested that the interstitials interact with dislocations due to the production of asymmetric strain fields.

However, less is known about the effect of nitrogen on fatigue performance and this work was performed in order to investigate this question. A series of Ti-6Al-4V based alloys were prepared and processed to achieve similar microstructures, in order to isolate the effect of α

stabilisation on microstructure from the underlying alloying effect. The levels of nitrogen added where chosen based on comparisons with benchmarks seen from components. Their un-notched fatigue performance was quantified, in addition, fractography and crystallographic orientation analysis was undertaken to assist in the interpretation of the fracture surfaces which might be observed in service components [9, 8].

4.2 Experimental Procedure

Stock Ti-6Al-4V aerofoil plate supplied by Rolls-Royce plc was re-melted using an Arcast200 vacuum arc melter with nitrogen introduced using powdered titanium nitride in pure titanium foil packets. This re-melted material was then β and $\alpha + \beta$ profile rolled to produce $13 \times 13\,\text{mm}$ bars that were then recrystallised, with the temperatures optimised to provide the desired volume fraction of α_p. The production route was tailored for each composition to replicate the structure shown in Figure 4.2.

To achieve this, material from each of the four compositions was globlurised by heating in the $\alpha + \beta$ phase field and water quenched at a variety of temperatures to determine the β-transus approach curve. It was also necessary to alter the rolling temperatures for each composition due to alloys with higher levels of nitrogen stalling the laboratory rollers at the processing temperatures used for nominal Ti-6Al-4V. It was important to achieve the same rolling reductions to ensure the same level of strain was experienced by each composition to try and ensure as similar as possible final microstructural conditions.

The composition of the material was determined using Dynamic Secondary Ion Mass Spectroscopy (DSIMS) depth profiling. Composition analysis in round-robin testing using IGF (Inert Gas Fusion) proved problematic at the nitrogen levels studied, which were above the ASTM standard (ASTM E1409-23 [4]) limits for using IGF for nitrogen determination in titanium. The author has used DSIMS depth profiling extensively in previous commercial work to determine nitrogen levels in Ti-6Al-4V so had prior knowledge that this method produces reliable and repeatable compositional results when used in conjunction with appropriate reference standards. For this work a standard from Alpha Resources (AR641 batch 315A) was used, with

an interstitial content of 1960 ± 60 ppmwO, 304 ± 38 ppmwN and 39 ± 6 ppmwH.

The β approach curve was determined metallographically for each composition. Previous studies had given estimates of the effect of nitrogen on the β transus in a range of titanium alloys, however, no previous study was found for Ti-6Al-4V. This means that when drawing comparisons to the reference data, the effect of the β stabilising alloying addition vanadium must be taken into account. Figure 4.4 shows the β transus approach curves determined from this work with example microstructures shown for each of the four compositions shown in Figure 4.5. For comparison, predictions made using the titanium database in the PANDAT™package are also shown.

Texture measurements were made on samples prepared from the gauge length of tested High Cycle Fatigue (HCF) samples. Samples were prepared from the surface with the sample normal parallel to the rolling direction of the bar. A Zeiss Sigma VP FEGSEM equipped with an Oxford NordlysMax EBSD detector was used to collect the data, at an accelerating voltage of 20 KV. The field of view was chosen to allow for a number of prior β grains to be analysed.

Tensile tests were performed at a nominal strain rate of $1 \times 10^{-3} s^{-1}$ on 1.0×1.5 mm gauge section specimens using a 10 mm extensometer at room temperature on a 100 KN Zwick/Roell BZC-MM14740.ZW02 electromechanical testing machine. (See Figure 4.3 for the drawing) The extensometer was removed after 5% strain and the test run to failure. Hardness testing was undertaken on polished cross sections from the as-tested gauge length.

Low Cycle Fatigue (LCF) testing was undertaken on round un-notched threaded samples of 240 ppmwN and 560 ppmwN compositions using a Mayes servo-hydraulic machine with an Instron 8800MT controller. The load regime consisted of an even trapezoidal waveform with a frequency of 0.25 Hz, an R-ratio of 0.1 and a range of peak stress values of 820, 790 and 760 MPa. These peak stress values were chosen with the aim of achieving a life of around 20 000 cycles to failure, with changes to the stress made based on results.

HCF testing was undertaken on round un-notched threaded samples of all four compositions using an Amsler vibrophore. (See Figure 4.3 for the sample drawing) The load regime consisted of a sinusoidal wave form with a frequency of approximately 85 Hz and an R-ratio of 0.1. Step testing was utilised with a starting peak stress of 400 MPa, a step length of 10^6cycles and step

height of 50 MPa.

Fracture faces from tested HCF samples were prepared such that EBSD could be undertaken on a polished section perpendicular to the fracture face to allow for a comparison of fractographic features to the underlying grain orientation. This work was undertaken on 240 ppmwN and 560 ppmwN for both striated regions and facetted regions with a comparison undertaken on a 3600 ppmwN sample for a facetted region.

4.3 Results

No evidence could be found of titanium nitride particulate in the product in DSIMS or SEM examination, nor was there any evidence of titanium nitride inclusions at the fatigue crack initiation sites examined. The lack of observed particles suggests that complete dissolution was achieved during the melt stage. Previous work by Van Thyne et al. [84] has shown solubility of nitrogen in titanium-aluminium alloys with investigated levels up to 1 %wt nitrogen. Analysis of the material produced in this study was undertaken by Loughborough Surface Analysis using DSIMS with the results shown in Table 4.1, as discussed earlier the measurements were calibrated against a standard of known composition from Alpha Resources AR641.

The rolled material was globularised at temperatures between 930 and 1055 °C (chosen to develop high α_p fractions in each of the samples), furnace cooled to 650 °C and then air cooled. The fraction of α_p present at equilibrium at a series of temperatures was then established by holding at a temperature T for 30 min and water quenching, in order to measure the transus curves shown in Figure 4.4. The transus temperature increased from 1000 °C at 240 ppmwN (0.08 at.%) to 1200 °C at 3600 ppmwN (1.17 at.%), an increase of 180 K/at.%. As shown in Figure 4.4, this correlates reasonably well with the literature for Ti-6Al [37], and is a slightly greater sensitivity than in pure titanium [91]. The temperature for 50% volume fraction of α phase was found to be less sensitive to nitrogen content, 946 °C at 240 ppmwN (0.08 at.%) to 1005 °C at 3600 ppmwN (1.17 at.%), an increase of 50 K/at.%. The transus curve results provide additional credibility to the DSIMS analysis, as the transus curves follow the same trend.

β rolling temperatures were then picked to be at least 50 K above the solvus temperature in

each alloy, and the $\alpha+\beta$ rolling and globularisation temperatures were chosen to be in the region of 40-60% α_p volume fraction. The α_p content present in the final product, Figure 4.5, was much higher due to α_p growth during furnace cooling from globularisation heat treatment [25]. The product microstructures obtained show partially globularized α_p in a matrix of retained β. The α_p fraction obtained from BSE imaging was 90% in the 240 ppmwN alloy and was only very marginally lower at 89% in the 3600 ppmwN alloy; however, it was observed that the α_p grain size was larger for alloys with higher nitrogen contents. This is important as it illustrates that even 3600 ppmwN may be insufficient to be easily detectable by metallographic examination. Of course, if all the compositions had been processed in the same way, the fraction of retained β would decrease with increasing nitrogen content. Compared to a standard plate product, Figure 4.2, these α_p contents were slightly higher and the α_p grain morphology different, however, the microstructures are felt to be comparable to each other for the purposes of this study. The data in Table 4.2 shows the measured average alpha grain width for each of the four compositions.

The texture of each of the four compositions was investigated to see if material that had been mechanically processed in the same manner showed any differences in texture as a function of nitrogen content. Figure 4.6 shows that there were no obvious differences between the textures of each of the four compositions at the lengths scales of interest.

The addition of 560 ppmwN to the source material increased the ultimate tensile strength (UTS) from 980 MPa to 1100 MPa, Figure 4.7, with a consequent decrease in ductility from 10.8% to 3.5%. Higher nitrogen additions decreased the ductility further until in the 3600 ppmwN sample, only a failure stress with essentially nil (0.4%) ductility was observed, which was lower (890 MPa) than in the baseline material. Industrially, localised increases in oxygen content in solution can sometimes be diagnosed using hardness, for example see Rugg et al [66]. This can arise in product due to localised heating or atmospheric exposure during service or production, for example. Therefore the correlation between bulk nitrogen content, hardness and solvus was also examined, Figure 4.8. It was observed that the effect of nitrogen on hardness saturated beyond around 2000 ppmwN, in the same fashion as the effect on the transus, and therefore hardness in this microstructural condition can be used as an indicator of transus

temperature and interstitial content, at least in industrially useful nitrogen ranges.

Nitrogen addition resulted in a marked drop in LCF life, with the addition of 320 ppmwN resulting in a life drop of 40% at 820 MPa, or out another way, a drop in strength of 30 MPa at a life of 10^4 cycles, Table 4.3.

The HCF test results are shown in Table 4.4 and Figure 4.9. HCF step testing consists of repeatedly testing at monotonically higher stresses until failure is observed. At each stress level a cutoff 'survival' life (N_{life}) is used, in this case 10^6 cycles. A clear trend is visible whereby the HCF strength is reduced by the addition of nitrogen. Nicholas [53] defined an HCF strength σ_e from the fraction of the 'survival' cutoff life $N_{\text{fail}}/N_{\text{life}}$ and the stress increment $\Delta\sigma$ over the preceding stress level σ_0;

$$\sigma_e = \sigma_0 + \Delta\sigma \frac{N_{\text{fail}}}{N_{\text{life}}} \tag{4.1}$$

So, for example, if a sample is tested at a peak stress of 300MPa (σ_0) and survives to N_{life}, the sample is then restarted at 325MPa ($\sigma_0 + \Delta\sigma$ where $\Delta\sigma$ here equals 25MPa). If the sample fails before N_{life} is reached, the cycle count is then counted as N_{fail}. In this example if the sample failed at 500 000 cycles then the HCF strength calculation would be as follows:

$$\sigma_e = 300MPa + 25MPa \frac{500000}{1000000} = 312.5MPa \tag{4.2}$$

The standard deviation of the inferred HCF strengths were found to be less than 5% for each composition. The biggest drop in fatigue strength appears to be between 560 and 1800 ppmwN; possible reasons for this will be discussed subsequently. It is evident that, even where similar microstructures are produced even small amounts of contamination by nitrogen can have quite dramatic effects, even within the range of normal Ti-6Al-4V specification (300 ppmwN). This implies that nitrogen contamination due to, e.g. vacuum leaks in production heat treatments, can be both undetectable even by batch testing and sectioning of samples for optical microscopy, and have significant effects on lifetime hence, there being a typical requirement to remove material from the surface of a component during production.

An example fracture face of each composition was examined in detail and striation counting undertaken where applicable. Examination via optical microscopy showed clear differences

between the four compositions, with the 1800 and 3600 ppmwN fractures having a greater level of surface topography in comparison to the other samples. Striated growth was observed in areas on both the 240 and 560 ppmwN fractures interspersed with fatigue facets. The fracture faces from 1800 and 3600 ppmwN samples did not contain any areas of striated growth. These fracture faces were dominated by colonies of macroscopic fatigue facets that had propagated along the elongated α_p grains present in their microstructures.

When the sample of composition 240 ppmwN was investigated it was found that striated regions of the fracture were orientated such that the crack had grown through α_p angled close to the $[12\bar{1}0]$ plane (Figure 4.13), as would be expected. Comparison with a fracture from a 560 ppmwN sample showed that striated growth occurred on the $[\bar{1}100]$ plane of the α_p grains with facetted growth on [0001] planes. Further comparison was made with a sample of 3600 ppmwN as that sample did not exhibit any striated growth; the results of that analysis showed that similarly to the 560 ppmwN sample, the faceting occurred close to the [0001] plane (Figure 4.14).

4.4 Discussion

4.4.1 Composition

The accurate measurement of dissolved nitrogen is crucial to this work, but can be challenging. The established technique for measuring interstitial elements in titanium is IGF, using e.g. a LECO analyser, however measurements carried out using this technique did not give results in line with expectations from the melt compositions. It is thought that this was due to the values of nitrogen introduced during alloy production being outside of the calibration range of the technique, therefore the results obtained on alloys with nitrogen contents outside the calibration range are not warranted for accuracy. ASTM E1409-13 [4] is the relevant standard and gives detection limits of 100-500 ppmw for oxygen and 30-1100 ppmw for nitrogen. These compare to an intended range of 1800-2300 ppmw oxygen and 50-4000 ppmw nitrogen for this work. In contrast, the use of DSIMS reported here requires a calibrated standard as close as possible in composition to the samples being measured. A calibration sample was obtained from Alpha Resources with a composition very close to one of the intended compositions. This standard

was certified using IGF calibrated to ASTM E1409-13, from a supplier certified to be compliant with ISO guide 31 [32], ISO 17034:2016 [33] and ISO/IEC 17025 [34]. One of the primary standards used for calibration by the supplier is BCR-059; this certified reference material was been measured 106 times for the nitrogen quantification as part of the BCR-059 [60] round-robin. The methods used by the measuring laboratories included: 14 MeV neutron activation analysis, reducing fusion, Triton activation analysis, Surface analysis by prompt (d,p) reaction, the Kjeldahl method, Heat extraction, charged particle activation analysis, fast neutron activation analysis, photon activation analysis and surface analysis by measurement of charged particles from nuclear reactions.

A further question is around the solubility of nitrogen in Ti-6Al-4V. Jaffee's discussion [35] of the solubility of nitrogen in the α-titanium phase suggests the solubility limit is 18.7 at% or 6.3 wt%; Conrad [22] suggests 19 at% or 7.2 wt%. In this study a maximum of 1.17 at% and 0.36 wt% were added, well below the suggested solubility limit; this is further supported by the absence of observation titanium nitrate precipitate on the fracture faces of the tested samples.

4.4.2 Tensile and basic mechanical properties

Nitrogen shows similar trends to oxygen in its strengthening effects on titanium alloys, as would be expected from previous studies that have shown them both to be α stabilising interstitials. It has been reported by Ogden et al. [57] that the effects of nitrogen can be taken to be twice as potent as oxygen. It was observed that a limit was reached after which increases in nitrogen content resulted in a plateau and then a drop in strength, similar to oxygen. However, it is unclear whether this is a result of the level of just nitrogen or the combined interstitial content.

Hardness was observed to increase at a rate of 305 H_v/wt% (95 H_v/at%). McKinley [47] found in pure titanium (with 0.065 wt% O) that the hardness increased at 567 H_v/wt% (160 H_v/at%). Ogden et al. [57] suggested that at room temperature these interstitial element additions have little effect on tensile ductility in pure titanium but they did also suggest that they have a negative effect on toughness. When they examined titanium-aluminium binary alloys they observed that additions of nitrogen had a much greater effect on ductility. In the present study, alloys with >1000 ppmwN possessed only very limited ductility.

In terms of fabricability, Ogden at al. [57] suggest that although the effect of interstitials on the strength of titanium alloys decreases as temperatures reach 650 °C (which is around the temperature at which α_2 would dissolve, if present), their effect on strain rate sensitivity remains which will affect the primary mechanical processing parameters as these are high strain rate deformation processes. This was noticed when rolling the four compositions during this work, as the temperatures used to achieve the same rolling reduction route across the compositions were quite different, in-line with the change in β-transus. This reflects the flow stress being a strong function of the α_p volume fraction rather than chemistry per se.

4.4.3 Fatigue lifetimes

Clear conclusions can be drawn as to the effect of nitrogen on the fatigue properties of Ti-6Al-4V; both the LCF and HCF testing carried out in this work show that nitrogen has a negative effect on the fatigue strength of Ti-6Al-4V. As with the change in tensile properties, in particular the trend in the HCF strength results show a rapid initial drop-off which stabilises with further nitrogen additions. Striation counting [24] is a technique where the striation density is evaluated repeatedly at different crack lengths and the number of cycles then inferred by integration, assuming a one-to-one correspondence of striations to cycles. Particular care is required where the striation spacing is small (<50 nm) or where $K_{\max}$ approaches K_{IC}. Only the 240 and 560 ppmwN samples were appropriate to examine by this approach due to a lack of striations on the other compositions. Up to around 1500 cycles (from first striated growth) the growth rates were similar between these materials, Figure 4.15, but after this the crack growth rates diverged, with the higher-nitrogen, stronger material showing slower fatigue crack growth.

4.4.4 Fatigue fractography

The samples with a higher nitrogen level exhibited a suppression of striated growth (promotion of faceted growth). On the samples with lower levels of nitrogen, large areas of the fracture face were striated; these regions covered many α_p grains which were visible through the striations. These large areas (greater than 2×2 mm) are thought to be of greater size than the prior β grains, which suggests that either adjacent prior β grains were of similar orientation, or that

the colonies that formed from them selected similar variants. Alternatively, the ΔK at the crack depths where these striated regions were observed was sufficiently high to overcome the restriction that orientation places on striation formation in less favourable orientations.

The results of the striation counting exercise are interesting as the two curves show the reverse of what had been expected prior to undertaking the counts. With the reduction in plasticity observed in the tensile tests of the 560 ppmwN composition it was expected that the fatigue sample of that composition would have a faster crack growth rate as the resistance to crack growth would have been reduced by the materials reduced capability for plastic deformation. However, that is not what has been observed through the striations counts which show that the sample of 560 ppmwN composition started to striate earlier and kept a slower propagation rate whilst also growing for longer before reaching K_{1c}. It is postulated that the reason for this is that the HCF tests were all carried out following the same step loading regime, which in this case would mean that the test was undertaken at a lower proportion of the material's strength. The 560 ppmwN composition sample failed on a step where the maximum load was 450 MPa which is approximately 40% of that composition's UTS; where as the 240 ppmwN composition sample failed at a max load of 500 MPa which is approximately 50% of that composition's UTS. The observation that compositions with higher nitrogen contents exhibited a lower crack growth rate but also had lower lives, implies that the main effect of nitrogen contamination is to lower the number of cycles to crack initiation.

There was a dramatic difference between the fracture appearance of the 240 and 560 ppmwN samples, and the 1800 and 3600 ppmwN samples; for the sake of brevity only the 240 and 3600 ppmwN fracture surfaces are shown, in Figure 4.10, Figure 4.11 and Figure 4.12. The 240 ppmwN sample shows a fracture appearance typical of near-equiaxed Ti-6Al-4V fatigue. In the initiation (blue and green) region, the crack has a relatively flat appearance but with evidence of plasticity and linear features along the direction of crack growth within each apparently facetted primary alpha grain. Once the crack grows into the conventional Paris regime, striated fatigue crack growth dominated in most grains orientation [9, 8]; the underlying α/β microstructure is still visible but within a colony, well formed striations were observed.

The higher nitrogen containing samples showed ductile feathered fatigue faceting following

the colonies of α_p grains (from the prior β grains) with large secondary cracks between these colonies. It was observed that across all orientations at all crack depths, only facets were observed, i.e., even prismatic and pyramidal grains faceted regardless of the local ΔK at the time of failure. The feathering on the facets is uniform in its directionality within each colony, suggesting that the orientation of those colonies dominated the growth direction. The amount of feathering was much lower in the initiation region, which was only barely subsurface, than it was further along the crack length. The fracture surface as a whole showed a much rougher surface, but actually a fairly substantial region of fatigue crack growth rather than simply tensile fracture. The abundant plasticity on the fracture surface suggests that a view of nitrogen-containing titanium as simply being brittle is rather deceptive. Rather, once plasticity and cracking occur, crack growth is quite rapid, suggesting either limited ductility before exhaustion occurs or a reduction in work hardening rate leading to more rapid cracking, or both; in either case it is clear that this reduction in ductility is associated with much plastic deformation.

4.5 Conclusions

The effect of nitrogen additions on the fatigue behaviour of Ti-6Al-4V have been examined in a series of test bars that were processed to achieve nominally identical, near-equiaxed microstructures. The following conclusions can be drawn.

1. Nitrogen additions increased the beta transus temperature, whilst also making the alloys more difficult to hot processing. Increasing the nitrogen content up to around 560 ppmwN shows a benefit to UTS with a small trade-off in ductility; however, beyond this point unacceptably low levels of ductility remained.

2. In R=0.1 testing at 820 MPa, low cycle fatigue endurance approximately halved from 22,000 to 13,000 cycles with doubling of nitrogen content from 240 to 560ppmwN. Similarly, a continuous decrease in HCF strength at the 10^6 cycle level was observed, from around 560 MPa in commercial product to around 360 MPa in heavily nitrogen-contaminated (3600ppmwN) material. No lower bound of additional nitrogen content was observed that did not have a detrimental effect - even levels of 240ppmwN and 560ppmwN showed a deficit compared to

commercial product, and the effect of nitrogen on HCF strength per at.% was greater at smaller levels of addition, inversely following the effects on strength.

3. The HCF fracture surfaces in the samples with only small nitrogen additions were similar to those observed in conventional product, as previously reported by Bantounas et al [9], with striated fatigue crack growth in grains well oriented for <a>slip, but relatively flat fractography near the initiation site, which was just subsurface, although still with some evidence of plasticity. In contrast at high nitrogen contents, 1800ppmwN and above, the fracture surfaces showed a macroscopically rougher and more brittle appearance was observed, but with extensive evidence of ductility running along the length of each α_p plate and no observation of conventional striations that would aid in post-hoc fatigue crack growth lifetime assessment. Therefore metallographic microstructure examination is not necessarily a reliable indicator of an absence of deleterious nitrogen contamination in surfaces; given the difficulty of measuring low levels of nitrogen in the electron microscope, this should be carefully recalled when assessing fracture initiation in potentially nitrogen-affected components.

4.6 Figures and Tables

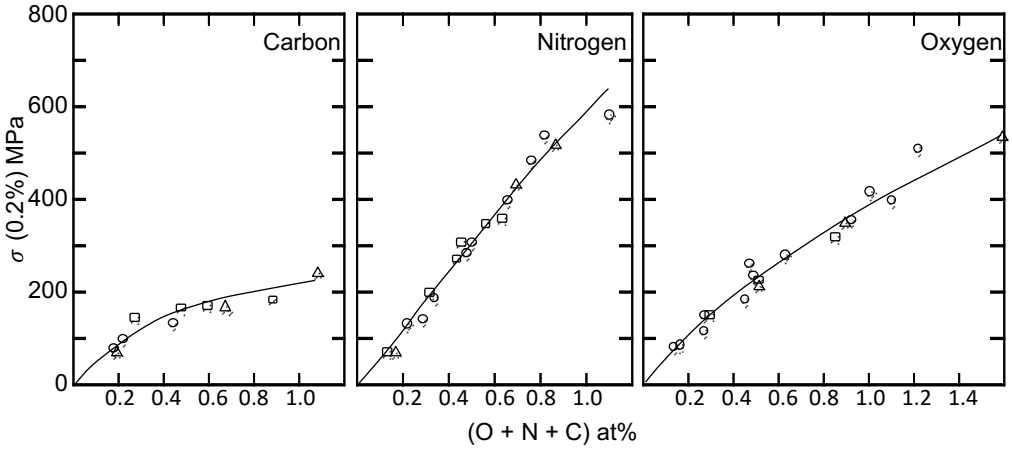

Figure 4.1: Effect dissolved interstitial solid solution elements on yield strength, adapted from Conrad [22].

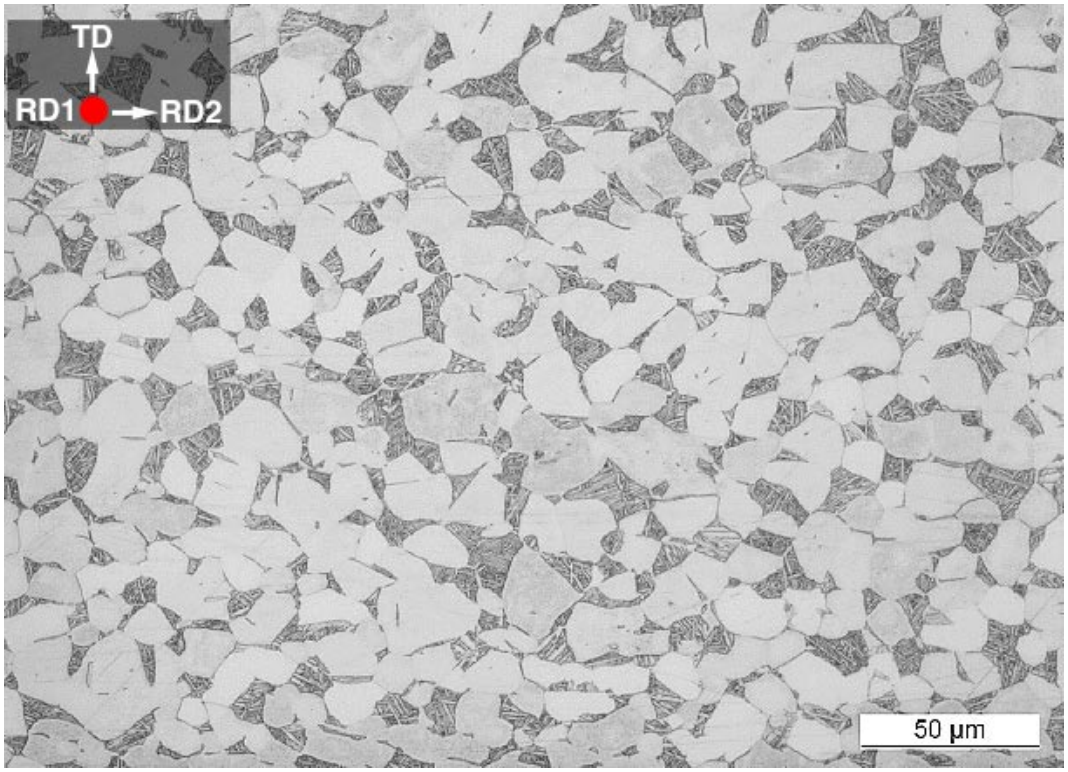

Figure 4.2: Optical micrograph showing the microstructure of a reference standard industrial plate product.

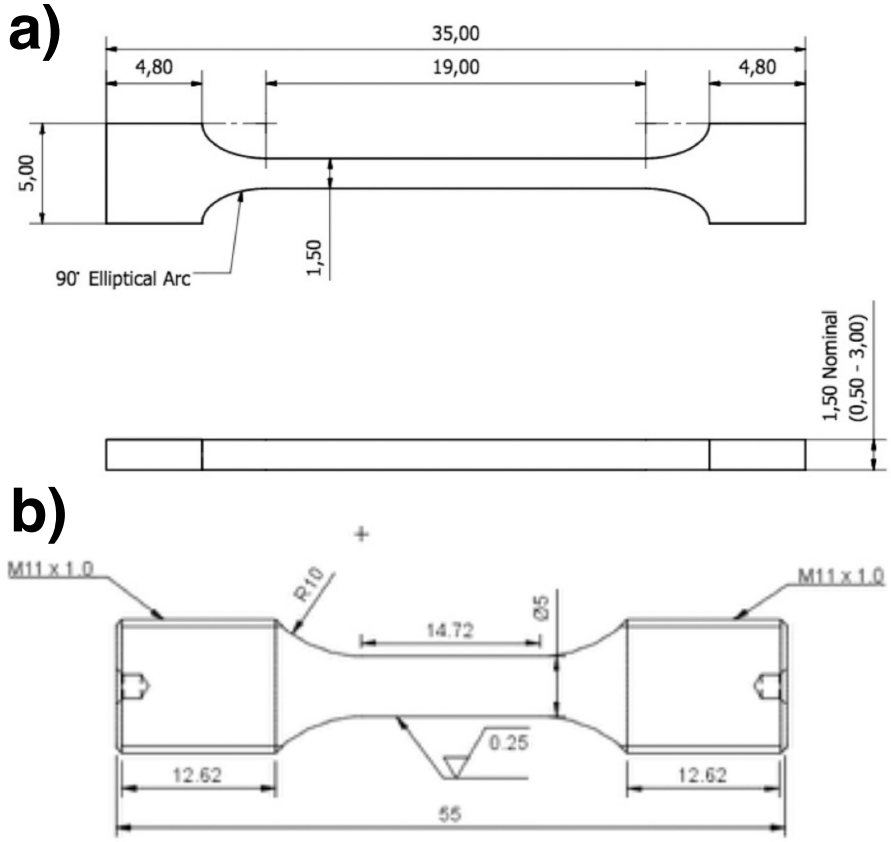

Figure 4.3: Sample drawings for specimens tested in this study, a) tensile and b) high cycle fatigue

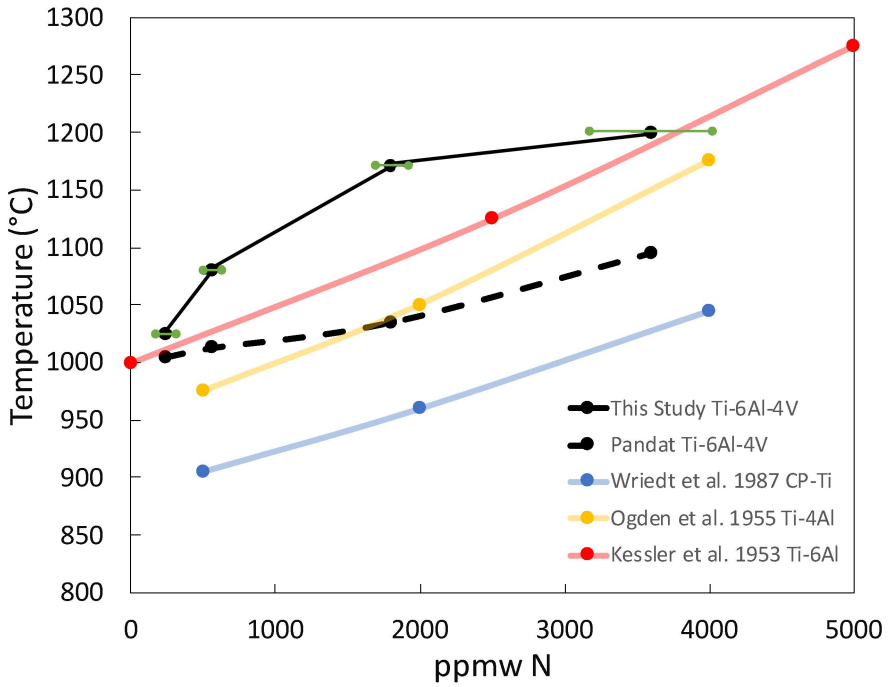

Figure 4.4: β-transus curves from literature, PANDAT and this experimental work (Black points with green error bars) [91] [57] [84].

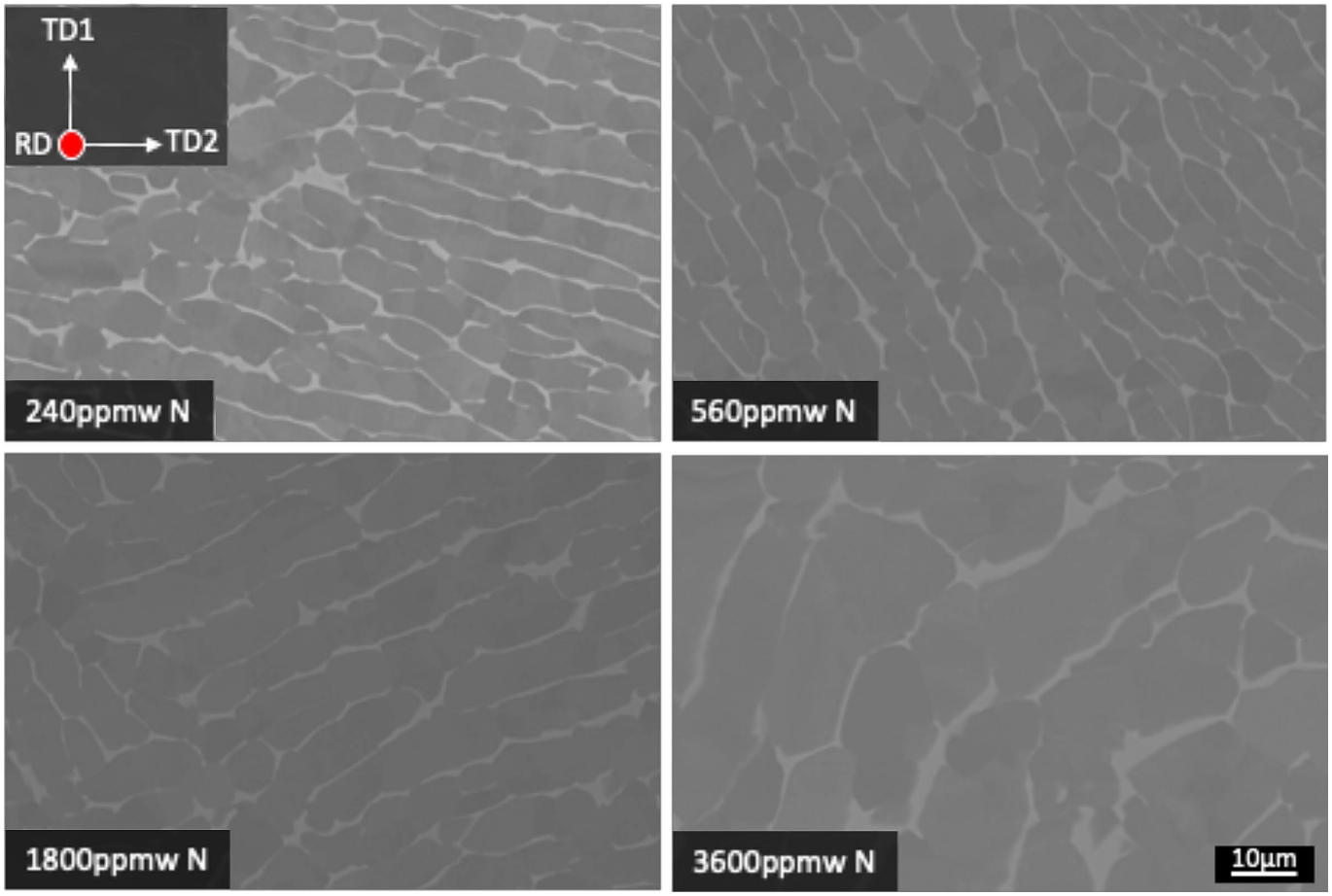

Figure 4.5: Optical images showing the microstructures of the four alloys produced.

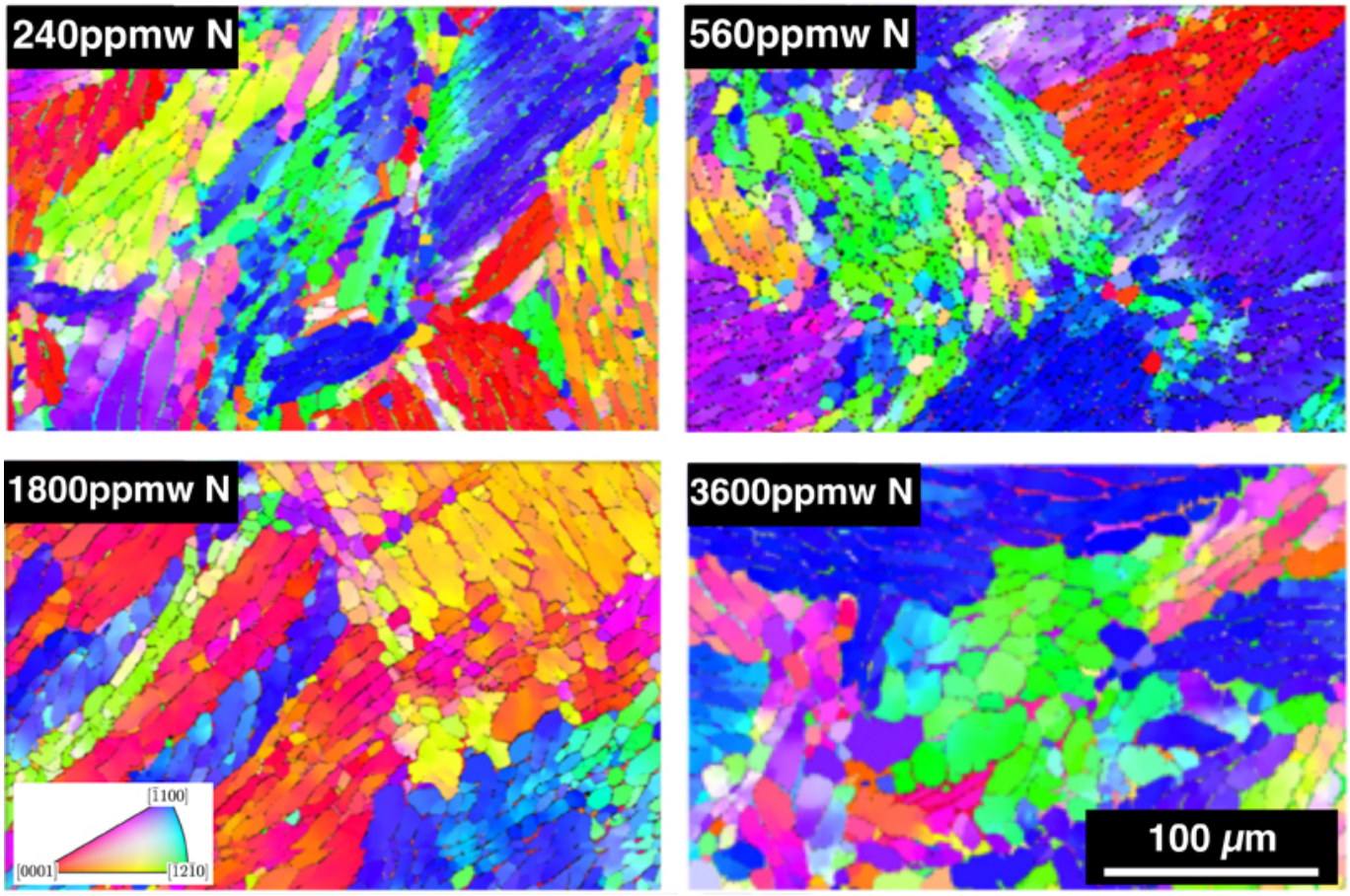

Figure 4.6: EBSD maps showing HCP textures of the four compositions

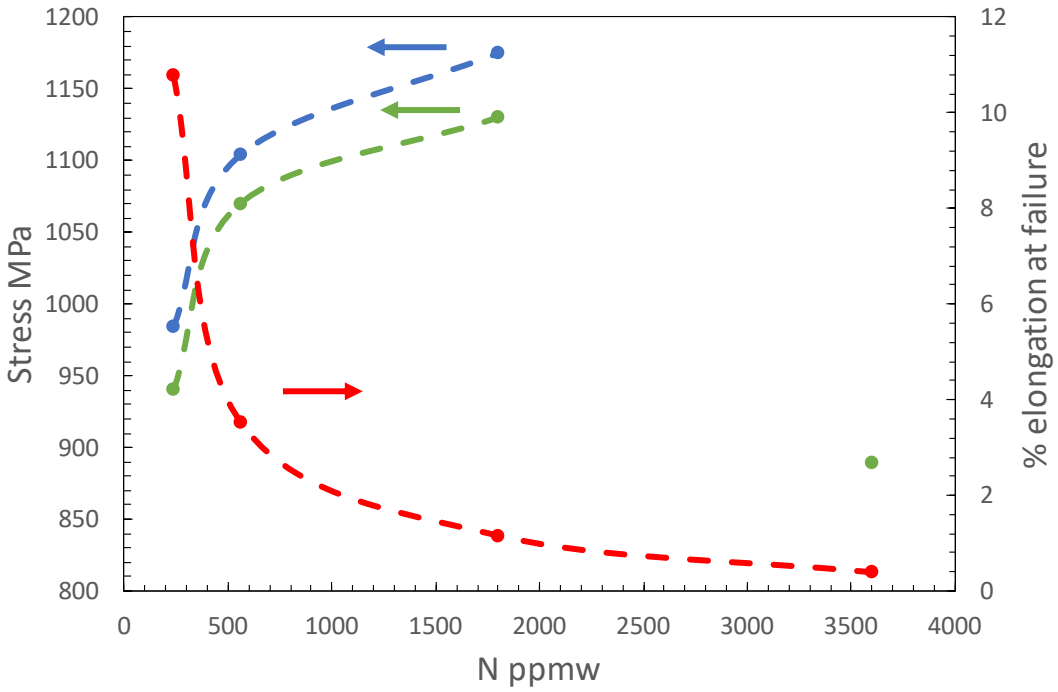

Figure 4.7: Effect of nitrogen additions, processed to achieve similar microstructures, on yield strength (green), ultimate tensile strength, UTS (Blue), and % elongation (Red).

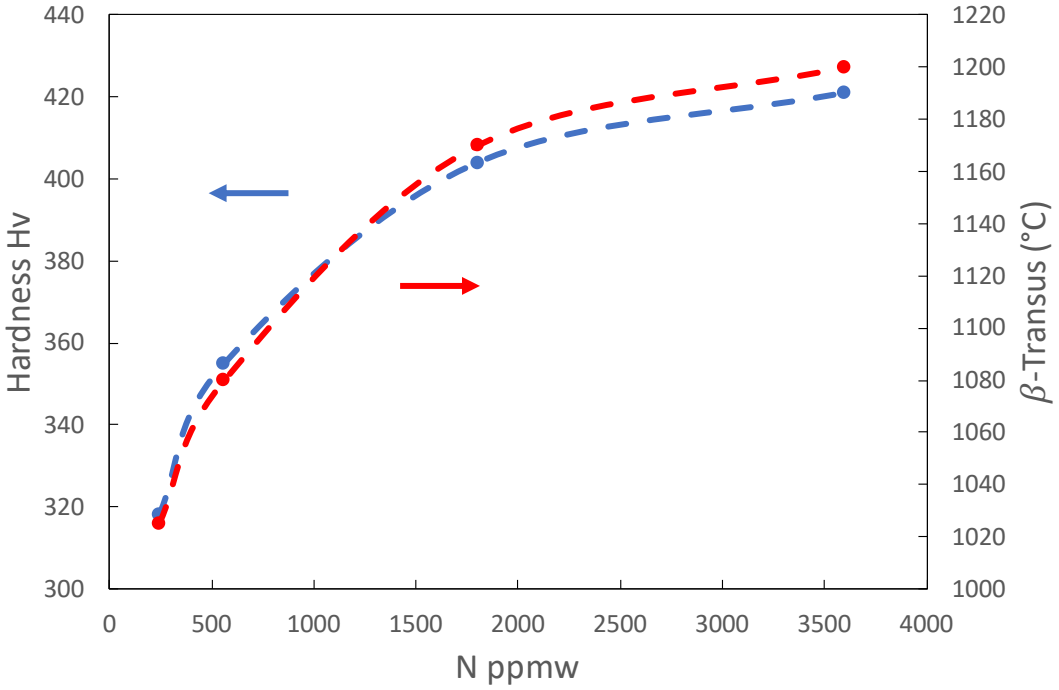

Figure 4.8: Effects of N additions on the β transus temperatures, measured metallographically by reheating and quenching globularised material, and on the hardness of materials processed to achieve similar, near-equiaxed microstructures.

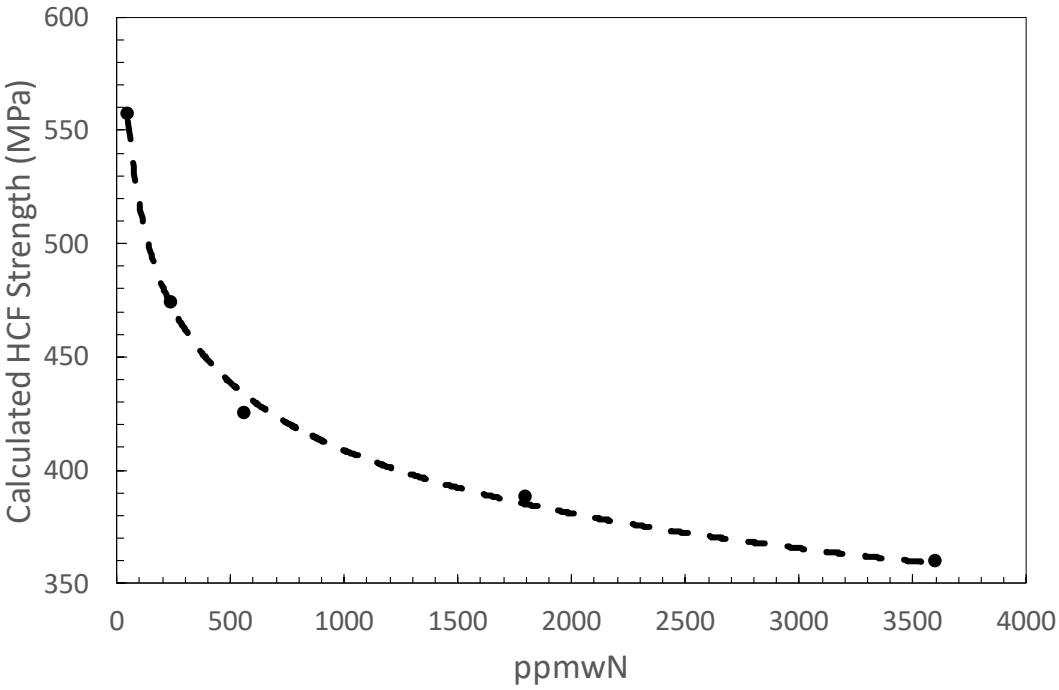

Figure 4.9: Effect of nitrogen additions (ppmwN) on calculated HCF strength, inferred from the HCF step test data. The value at 50 ppmwN is for commercial reference material.

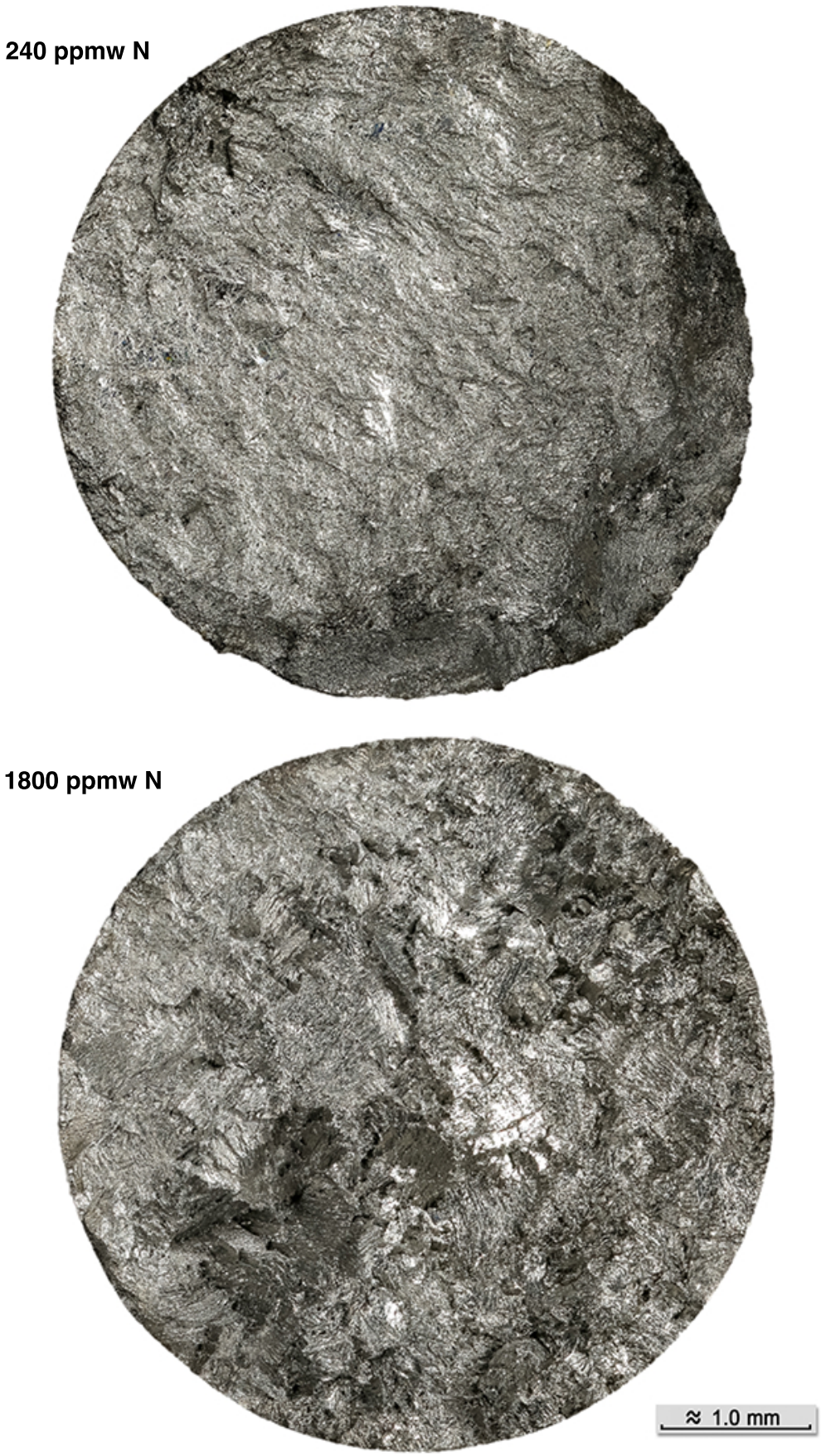

Figure 4.10: Optical overviews of a fracture face from HCF samples of 240 and 1800 ppmwN

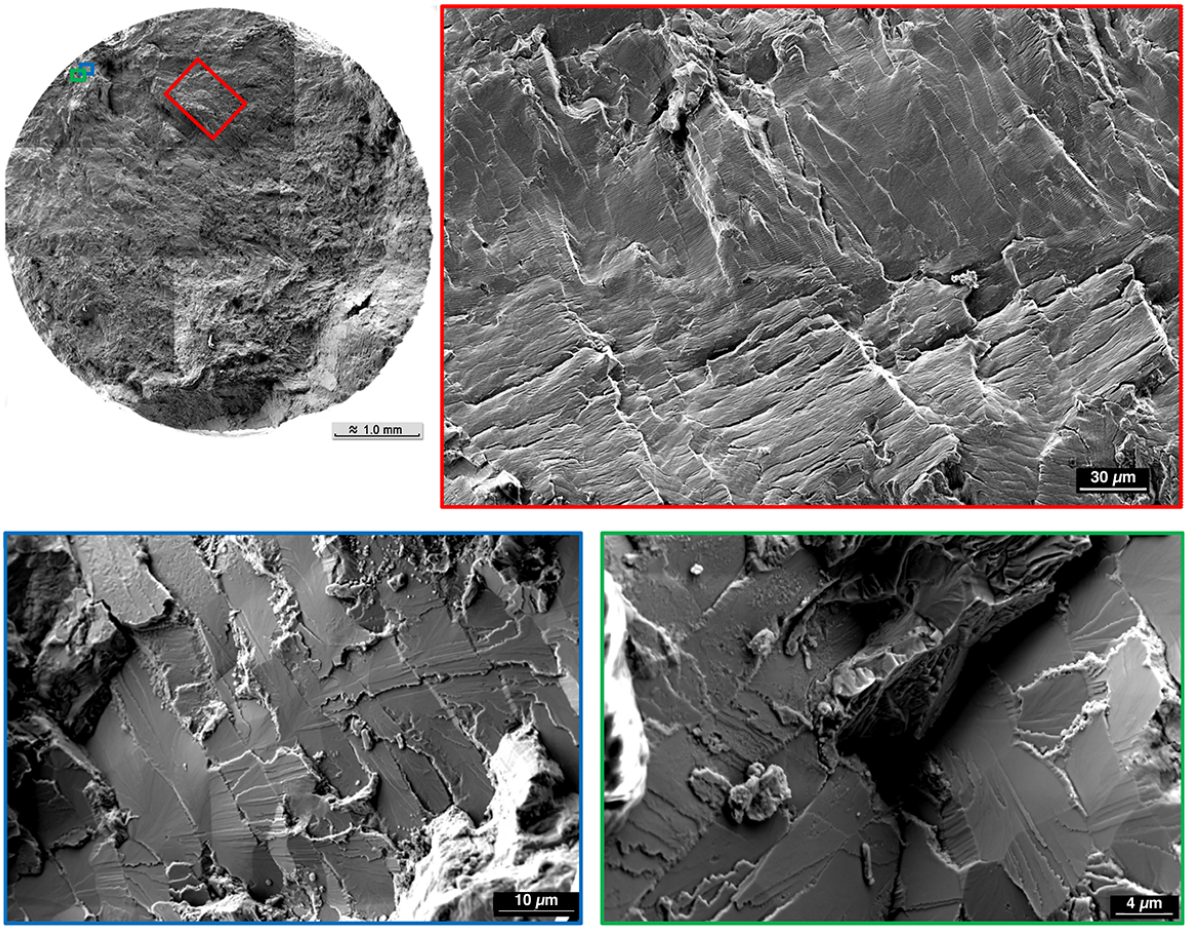

Figure 4.11: SEM fractographs of an HCF step test sample of 240 ppmwN composition. the fracture appearance at the initiation (green and blue) is shown, in contrast to the subsequent conventional striated fatigue crack growth regime at longer crack lengths (red).

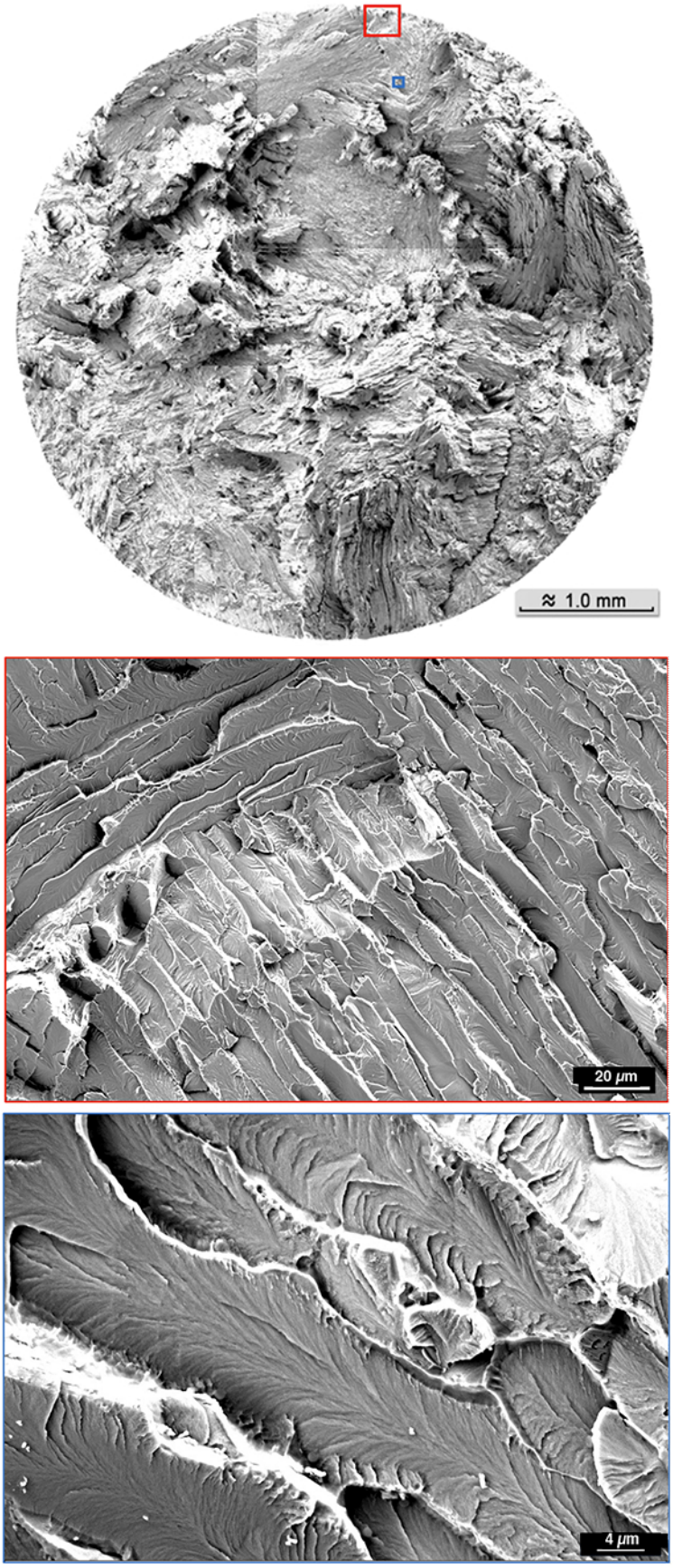

Figure 4.12: SEM fractographs showing a variety of views of the fracture face from a HCF sample of 3600 ppmwN composition

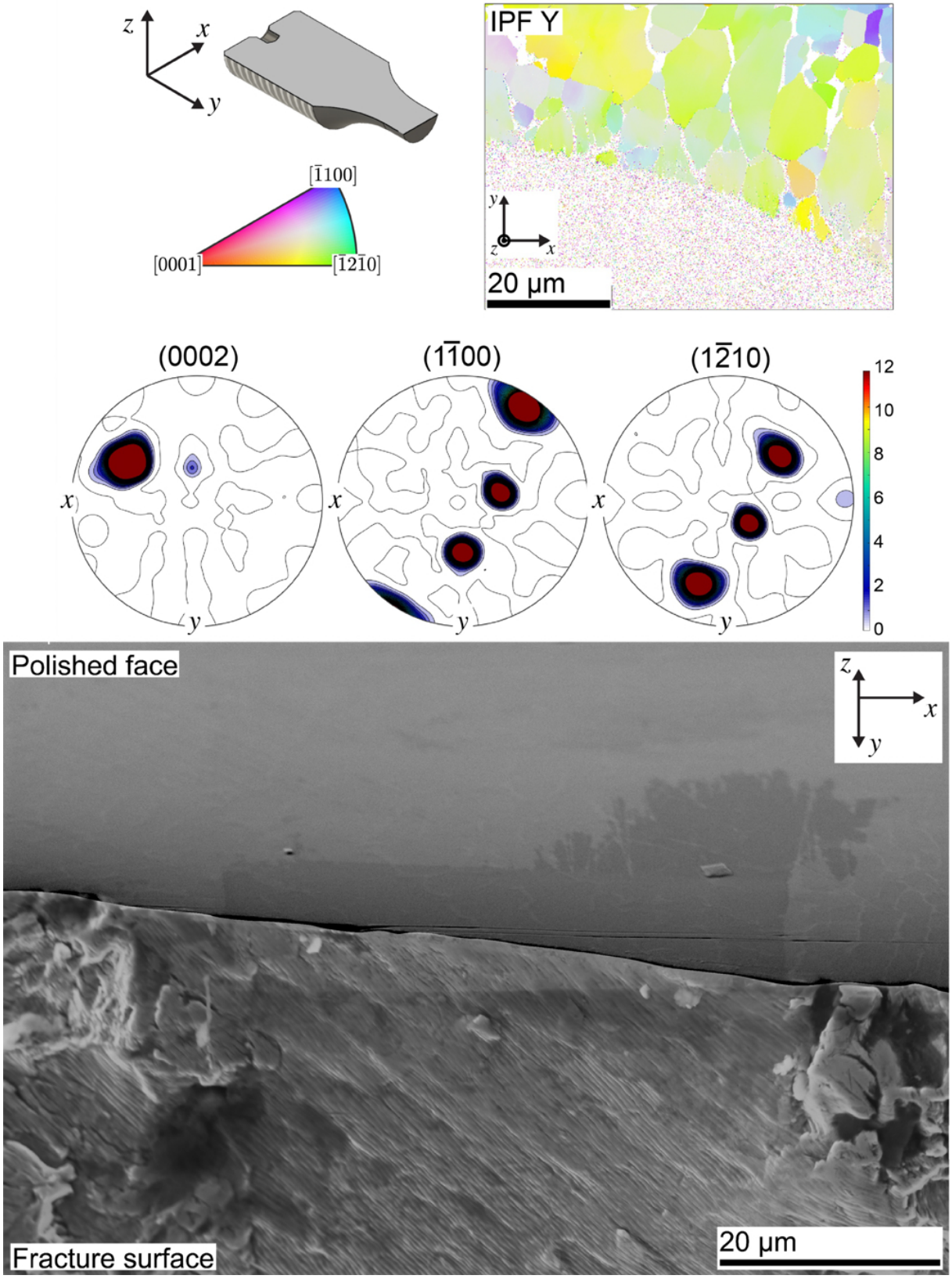

Figure 4.13: Fractographic vs texture EBSD mapping for HCF step tested sample of 240 ppmwN

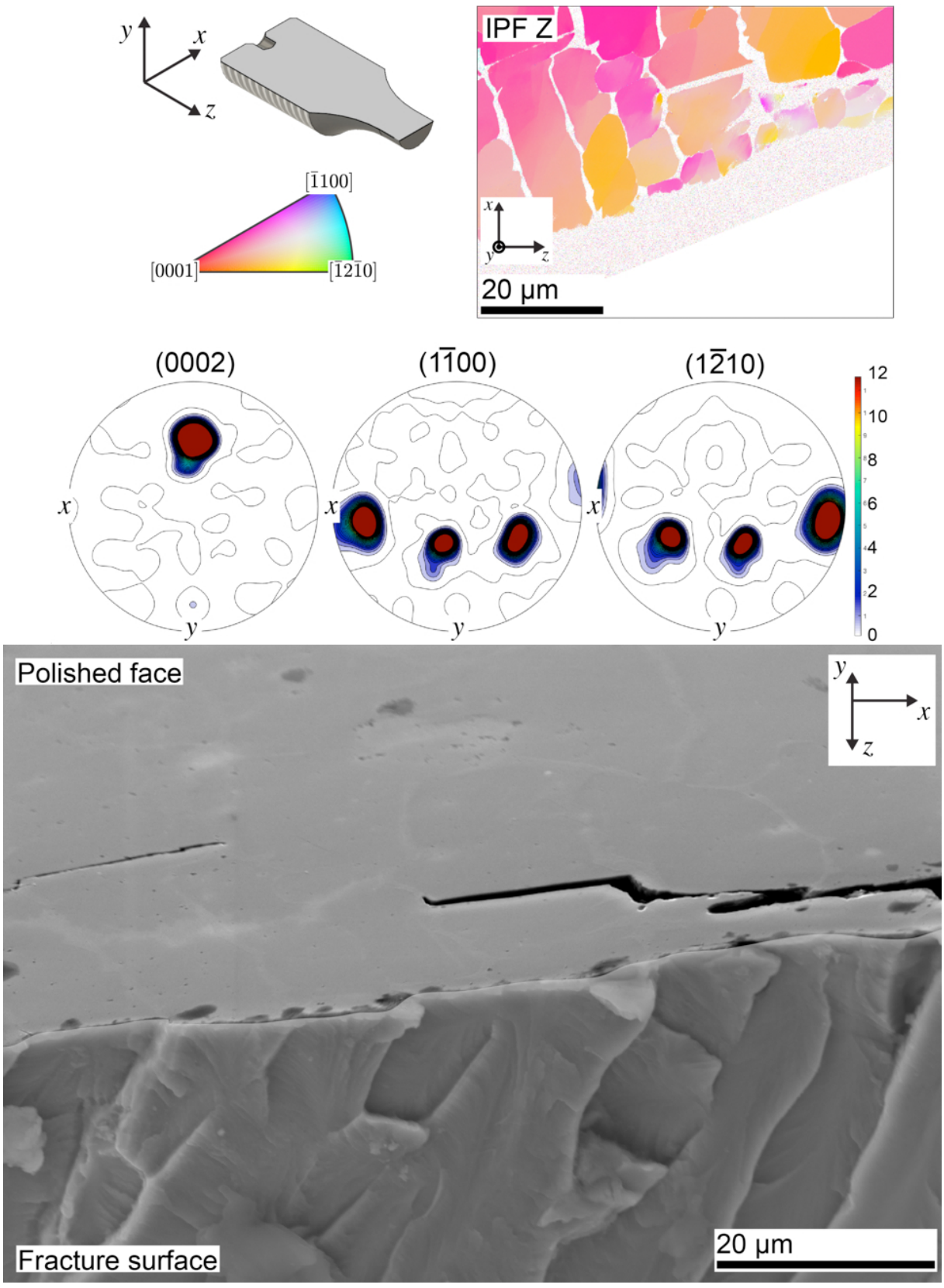

Figure 4.14: Fractographic vs texture EBSD mapping for HCF step tested sample of 3600 ppmwN

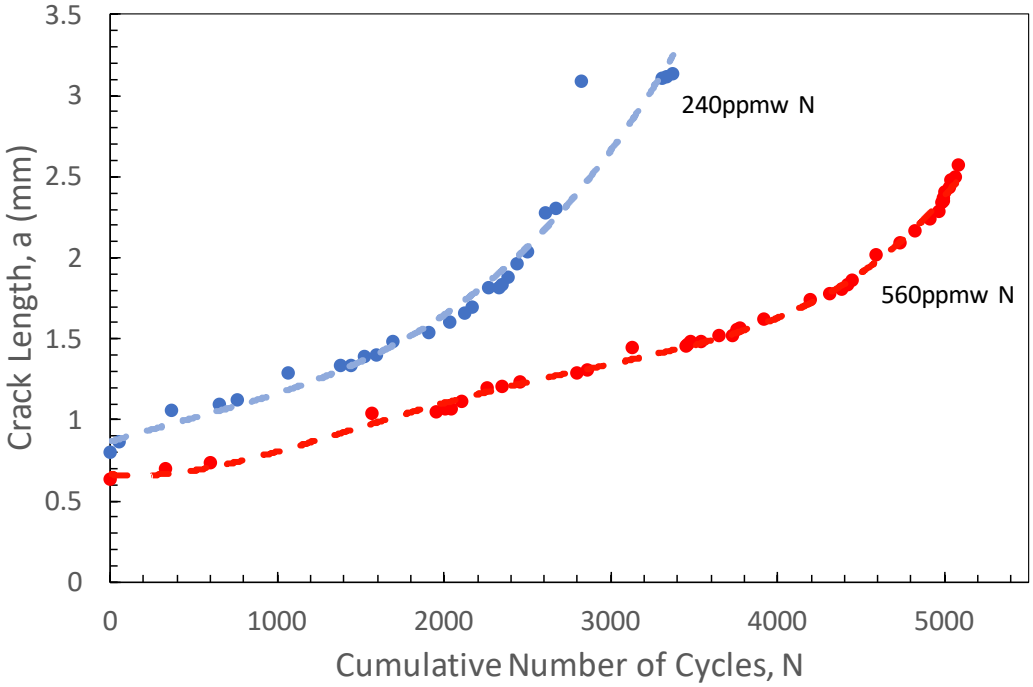

Figure 4.15: Striation count data from HCF step tested samples containing 240 (in blue) and 560 ppmwN (in red). The cumulative cycles on the x axis start at 0 with the first striation measurement, not the crack initiation cycle.

Table 4.1: Measured oxygen/nitrogen compositions obtained (ppmw, average and standard deviation). Typical nominal Ti-6Al-4V plate product is around 2000 ppmwO and $\leq$ 300 ppmwN.

Aim N content	O	N	O+N
Nominal	2300 ± 250	240 ± 140	2500
500	2400 ± 140	560 ± 90	3000
2000	2800 ± 550	1800 ± 230	4600
4000	2600 ± 550	3600 ± 850	6200

Table 4.2: Showing measured α_p widths from the images in Figure 4.5

Composition ppmwN	α_p width (µm)
240	5.4
560	7.4
1800	6.4
3600	9.3

Table 4.3: Effect of nitrogen content on LCF life, at low nitrogen contents where reasonable ductility remained.

N (ppmw)	Test Stress (MPa)	Cycles	Average
240	850	11,717	
	820	18,874	22,300
		20,996	
		26,908	
560	820	16,302	12,900
		10,332	
		12,004	
	790	28,900	19,000
		14,888	
		13,086	

Table 4.4: Effect of nitrogen content of high cycle fatigue test lifetime and HCF strength.

N (ppmw)	Failure step (MPa) (σ_0+$\Delta\sigma$)	Cycles	HCF Strength (MPa)
Commercial Product	600	208,300	560
	600	79,300	554
		Average	557±3
240	500	688,800	484
	500	951,300	498
	500	448,600	472
	450	847,900	442
		Average	474±24
560	450	280,200	414
	450	329,100	416
	450	639,900	432
	450	722,100	436
		Average	425±10
1800	400	803,300	390
	400	662,000	383
	400	741,500	387
	400	869,800	393
		Average	388±5
3600	400	196,900	360
	400	224,800	361
	400	245,100	362
	400	100,500	355
		Average	360±4

Chapter 5

The effect of air vs vacuum as a function of nitrogen on the HCF properties of Ti-6Al-4V

Abstract

Investigations into the effect of atmosphere on fatigue cracks in titanium have been carried out many times before. [65, 30, 79, 6, 45, 64, 70, 85, 51, 31, 58, 92] However, these investigations have relied upon the tests being carried out on conventional test samples on a test frame within a vacuum chamber. This work allowed truly representative vacuum levels of finished components avoiding potential contamination problems with vacuum chamber testing by producing a sealed chamber within the sample. A hollow sample design with an internal vacuum was suggested and this chapter shows the process that has been carried out to prove the concept.

5.1 Introduction

The investigative work in this chapter aimed to trial a new way of testing the effect of vacuum on fatigue crack initiation, growth and fractography. By producing a vacuum within the sample itself it has been postulated that the restrictions provided by testing within a vacuum chamber can be avoided. However, the additional challenges of characterising fatigue crack growth on a crack initiating internally required some alternative methods over the commonly used PD

(Potential Drop) method. The methods and outcomes of the testing both in terms of the applicability of the methods used and the actual results are discussed.

5.2 Experimental Procedure

Sinha and Larsen [73] have written a comprehensive summary of vacuum testing of titanium and nickel base-superalloys; their summation is that for a test to be truly representative of vacuum conditions, the air pressure is required to be below 1.33x10^{-4}Pa to ensure no oxidation of the titanium with a partial pressure for O_2 of $\approx$ <1x10^{-145}Pa. Conventional vacuum testing methods typically produce a vacuum level between 1.33x10^{-4} and 1.33x10^{-7}Pa, this testing methodology was designed to produce a better (i.e. lower) vacuum level than those traditional methods. The basis for the sample design used in this work, is an M11 round dogbone sample as used in Chapter 4. In this chapter the sample design has been modified so that the centre of the sample has been bored out and honed (honing being the process of grinding a machined surface to give a precise surface finish) to give a good surface finish; that has then been followed by the creation of a circumferential notch at the centre point of bore. Following the boring, honing and notch creation, the samples were sent to have plugs electron beam welded into the ends of the sample. Once the end plugs were welded in, the samples were vacuum heat treated to drive any residual gases from the cavity into the sample internal surface. Figure 5.1 details the manufacturing steps for the test samples for this work and figure 5.2 shows a schematic of the sample design.

To determine the level of vacuum within the sample and to identify the composition of any residual chemical species within the cavity, a separate experiment was designed. This involved taking a small number of samples, thinning down the wall by grinding, heat treating the samples in air at 700 °C for 4 hours followed by a furnace cool to embrittle the outer material and then scribing (marking the surface with a hard sharp point, in this case marking a ring around the outer circumference axially co-located with the internal notch) the outer surface. The samples were then loaded into a 4-way crucifix as part of a pre-existing vacuum setup. The samples were broken by a linear actuator with a sharp profile ram on the end. The change in pressure against

time as a function of mass weight was measured by a Hiden HAL 201 RC residual gas analyser (RGA) see Figure 5.4. Although the vacuum setup's volume was larger than the sample volume, the methodology used to measure the residual gas would not have been affected by that volume difference. The vacuum setup was sealed using a gate valve before a sampling leak valve situated at the entry to the Hiden RGA was opened to allow a small leak into the Hiden RGA. This methodology would have caused any gases being released during fracture of the sample to be drawn into the detector.

Twelve samples were tested during this work, table 5.1 details the samples. Four samples directly from cross-rolled Ti-6Al-4V plate and eight samples remaining from the work in Chapter 4. The samples were tested in batches of three; one of each composition at vacuum followed by the second batch of three with the vacuum broken. The samples tested in air were manufactured identically to the vacuum samples with the vacuum broken by drilling into one of the end plugs to allow air to enter the cavity. Five of the samples were life tested to provide estimations for when to remove the samples for ex-situ CT scanning.

All of the samples were subjected to High Cycle Fatigue (HCF) loading using an Amsler Vibraphore with an R-Ratio of 0.1. For the life tests, the samples were step tested with a step height ($\Delta\sigma$) of 25MPa and a step length (N_{life}) of 10^6 cycles (see Section 4.3 for explanation of test methodology). From the life test results peak stress values for the crack growth tests were chosen to attempt to ensure sensible lifetimes for all the samples to enable a sufficient number of CT scans to be carried out (Figure 5.3 shows how one value was estimated. The hollow purple dot is the adjusted datapoint. It has been adjusted as the sample tested was found to have a notch that wasn't centrally aligned to the axial centreline causing a significant change to the stress field around the notch leading to premature failure. The differential between vacuum and air samples for the other compositions was averaged and applied to the air result for the 560ppmwN composition). As the CT testing went on, it became apparent that the stress levels chosen for the air samples were not high enough to initiate cracking soon enough so the stress levels for the three samples were raised by 25MPa. This change is indicated in table 5.4 by an asterisk. The pre and post stress change cycle counts have been included for transparency.

Ex-situ CT scans were undertaken on a Nikon (XTech) XT H 225 utilising a custom tensile

rig (Further description in chapter 6) with an applied load of approximately 1.06kN. The data was examined using ImageJ.

Examination of the fracture faces started with capturing optical overviews using a computer controlled stepper motor mounted SLR. These images were then used for registration purposes for the SEM fractography. SEM work, undertaken on a Zeiss Sigma 300 Field Emission Gun - Scanning Electron Microscope (FEG-SEM), started with capturing low magnification overviews comparative to the optical overviews with subsequent higher magnification work then carried out on regions of interest such as areas of potential initiation locations. Where striations were present they were counted using a Rolls-Royce proprietary method to provide density measurements at a range of locations around the sample. The density measurements were compared to the CT crack growth information.

5.3 Results

The testing for determining the level and quality of the vacuum within the samples yielded results that showed only a small number of mass weights increased on rupture of the sample. Figure 5.5 shows the output from a test. The data has been filtered to show the mass weights that showed a change when the sample ruptured (at around cycle number 180). Utilising the data published on Hiden's website [29] (see table 5.2) it was possible to work out likely sources for those changes. The three red lines (mass weights 14, 15 and 16) match up with expected responses from the cracking pattern of methane. The two blue lines represent H and H_2. The other mass weights that changed, albeit at very low levels were 12, 13, 26, 27 and 29.

The results from the life tests (see table 5.3) showed a large increase in HCF strength for the samples tested in vacuum over the samples tested in air. It should be noted that the data point for 560ppmwN at vacuum is an estimated value as the notch machined into HF014 was off-centre leading to an incorrect stress field around the notch causing premature failure. The value was estimated by taking the difference between the air and vacuum results for the other compositions and averaging those to determine the difference for the 560ppmwN samples.

Table 5.4 details the cumulative cycles between CT scans on the ex-situ monitored samples,

illustrating the variable intervals between scans. The intervals were changed based on reviews of the CT data after each scan. Analysing the CT data between scans was tricky due to some shadowing artefacts caused by the notch geometry and its interaction with the CT beam casting a dark crack like feature in the sample wall.

Table 5.5 details the numerical results of the ex-situ CT test results including initiation life, cycles to failure and calculated HCF strength. Generally the HCF strengths obtained from the ex-situ CT samples are marginally lower than the life tests with a debit of approximately 21MPa or around 7%, however, the overall trends are the same in that the vacuum samples achieved higher HCF strengths than the air samples (see table 5.6). The exception to this was the result obtained from HF036, this result sits outside of the rest of the test results but is most likely down to the inherent variability of fatigue testing.

Each of the six samples monitored by ex-situ CT was photographed and examined in the SEM after failure. Figures 5.7, 5.10, 5.13, 5.16, 5.19 and 5.22 show optical and SEM overviews of each sample. Figure 5.6 shows which portion of the fracture face represents the notch surface with red shading for the notch and yellow shading for the testing fracture. Figure 5.6 also shows how the notch isn't quite uniform in its depth or centrally aligned to the central axis of the sample; this was a variable during testing with some samples more or less away from the sample drawing geometry. Examples of common fractographic features from each sample are shown in figures 5.8, 5.11, 5.14, 5.17, 5.20 and 5.23 and include both facets and striations.

Quantitative SEM fractography was carried out with µm per cycle values located where the analysis was undertaken as shown in figures 5.9, 5.12, 5.15, 5.18, 5.21 and 5.24. For complex fractures such as these, the striation densities can also give an indication of where the crack has initiated, a cluster of low crack growth values indicates that the origin is close by; and likewise, higher growth rates indicate being further from the origin. Figure 5.26 shows a plot of the crack growth rate in µm per cycle against an arbitrary frame number ordered slowest to fastest. Table 5.7 shows the lowest, highest, range of rates and average fatigue crack growth rates for each of the ex-situ CT samples. Figure 5.27 shows a comparison of the probability distribution curves for the measurement fatigue crack growth rates of the ex-situ samples.

5.4 Discussion

5.4.1 Testing Level of Vacuum in the Samples

Direct measurement of the vacuum level within the samples was deemed to be near impossible due to the requirement of somehow puncturing the sample within a small enough vacuum chamber to make any pressure differential measurable. It was decided to investigate the vacuum using a non-direct measurement based on analysing any gaseous species that were emitted during a sample being ruptured. This method was found to work but required some custom component design (threaded spacers and ram profile) and different thinking to get the samples to fail just using the linear actuator.

As stated in the results section, the molecular cracking pattern data (see table 5.2) on the Hiden website [29] was used to analyse the data. The main mass weights of interest were 1, 14, 15 and 16. 1 represents hydrogen and is indicative of some water vapour being present in the samples. Mass weights 14, 15 and 16 represent methane, the likely source of the methane is the vacuum system used at EB welding which as an industrial system its not unreasonable to expect some hydrocarbon contamination. There were no mass weight pressure changes that would have been expected from O_2 at mass weight 32 or N_2 at mass weight 28.

The findings of this work mean that the samples tested here are confirmed to be at ultra high vacuum, and are in accordance with the requirements laid out by Sinha and Larsen [73] for true vacuum testing.

5.4.2 Fractographic Results

Figure 5.26 shows the range of crack propagation data captured during the quantitative SEM fractography. Ordinarily this type of data would be correlated to crack depth; however, this sample geometry makes determining that in an accurate manner all but impossible. So, for the purposes of this figure, the data has been presented as isolated measurements showing the range of crack growth rates observed. Those striation density measurements are heavily influenced by the underlying texture of the primary alpha grain that has striated and the relative ease with which the grain was able to accommodate the required plastic deformation to form striations.

Figure 5.27 shows that the distribution of striation widths between the samples as a function of either air vs vacuum or nitrogen content is very similar with the exception of HF022. This exception is down to the off-centre nature of the notch in HF022 which will have caused a different stress field in this sample. It should be noted that all the samples in this chapter show the same macro crack growth directionality behaviour as shown in figure 5.25.

One other observation was that the fracture from HF002 560ppmwN air sample exhibited a significant amount of secondary cracking associated with primary-α grain boundaries in the regions of striated growth (see figure 5.14). This same feature was seen on the equivalent vacuum sample but not on the other samples of different chemistries. One explanation could be that the nitrogen has segregated towards the primary-α grain boundaries causing a noticeable reduction in ductility between primary-α grains. In chapter 4 it was shown that nitrogen has a significant effect on the fractography of fatigue samples and this appears to be a continuation of that observation, clarifying that the test environment appears to have had no difference.

The comparison of crack growth rates shown in figure 5.26 and table 5.7 indicate that there is no real trend as a function of composition which was surprising at first review. On further consideration, it is possibly inline with what was observed in Chapter 4 where any difference in crack growth rates was attributed to the difference in proportion of yield that the samples were being cycled at. The 240ppmwN sample was being tested comparatively much closer to its yield (325MPa - 940MPa) than the 560ppmwN (300MPa - 1075MPa). In Chapter 4 the peak stress difference was 50MPa whereas in this chapter that was reduced to 25MPa. There is a slight trend on the average values that suggests that the air samples had marginally faster crack growth rates than the vacuum samples but on a limited sample set this is only suggestion.

5.4.3 Air vs Vacuum

Prior to commencing this work it was postulated that a vacuum environment would delay initiation, slow crack growth and prevent the formation of striated growth as has been published in prior literature such as [73]. The test data showed that the initiation characteristics for air vs vacuum had changed, with the vacuum samples requiring higher loads to be applied to the samples to initiate cracks; this is in agreement with the published literature. Published

literature such as Yoshinaka et. al. [92] details their findings that cracks in vacuum samples were shown to take longer to initiate and then subsequently take longer to break out of stage I fatigue crack growth, due to using different test stresses in this work, direct comparisons of initiation lives are of limited usefulness. In contrast it is possible to compare HCF strengths as a function of test environment. A clear trend was observed where a significant debit air to vacuum was found in the region of 20%. The crack growth rates determined by quantitative SEM fractography were found to similar between the vacuum and air samples which is not as expected from reading Yoshinaka et. al. [92]. Not only did Yoshinaka et. al. suggest that stage I fatigue crack growth would be slower in vacuum but they also found that stage II fatigue crack growth rates were highly dependent on testing atmosphere. It is postulated that the difference in observation has been caused by some of the deficiencies in the crack growth measurements, the non-uniform nature of the sample notches and the limited number of samples tested.

The SEM fractography revealed a significant proportion of the fracture faces consisting of striated growth even on the samples tested in vacuum. This observation goes against what is catalogued in published literature although there has been a lack of clarity around that [88, 92]. On top of that, it was also noted that the striations observed were well defined which is also in disagreement with published data, see also [88, 92].

5.4.4 Effect of Nitrogen

As a secondary aspect to the investigation, the effect of bulk interstitials was also investigated. The results were surprising as they showed a different pattern to the HCF response to that observed in the chapter 4. In chapter 4 the commercial product was found to be stronger than the 240ppmwN material which in turn was stronger than 560ppmwN material; however, in this chapter the commercial product and 240ppmwN material were found to be the other way around. In Chapter 4, the HCF strength ratio for 560ppmwN to 240ppmwN to commercial product was 1 : 1.12 : 1.31, in this chapter its 1 : 1.0 : 1.01 which is quite a drop-off for the commercial product. An additional observation is that all the values were much lower in this chapter, that observation is explained by the fact that the samples in this chapter are all notched rather than plain section, hence a reduction in life to crack initiation due to the increased stress

concentration.

5.4.5 Novel test method

The novel sample designed for this work was extremely difficult and expensive to produce. To have been able to produce the volume of samples that have been used in this work, with the general consistency of the notch geometry achieved, is a great achievement that many people thought wouldn't be possible. If this work was to be repeated, it would be beneficial to increase the size of the samples to aid even further consistency of the notch from sample to sample. Increasing the number of samples used for lifing would be enable streamlining of the ex-situ test work, in this study the limited data meant there were large inefficiencies in the ex-situ scheduling with far too many scans of un-cracked samples.

5.5 Conclusions

1. The test method devised and undertaken in this chapter has proved to be successful at allowing a crack to be initiated and grown in a vacuum environment without relying on a vacuum test chamber. The quality of the vacuum in the samples was found to be very high when analysed. Although the cost and complexity in creating the samples could be seen as prohibitive, it has enabled the differences between laboratory test samples and in-service components to be reduced which adds real value in reading across the test results.

2. A clear debit in the region of 20% has been found for sample lives when tested in air as opposed to vacuum. This makes a significant difference when component lifetimes are taken into consideration. Typical fatigue testing is undertaken in air and so could be found to give pessimistic life data when compared to a component being operated in a vacuum. Fatigue crack growth rates were found to be similar between air and vacuum samples with only a slight upward trend on the average growth rates in air vs vacuum. This finding is in disagreement with literature with the cause being put down to issues with inconsistent notch geometry, the coarse nature of the crack growth measurements and the limited number of samples tested.

3. From a fractography perspective, the presence of striations on the fracture faces from the samples tested with a vacuum environment was a finding that is in disagreement with published literature. The amount of striated growth was seen to be fairly consistent across all the samples examined with underlying crystallographic texture and composition differences found to be the primary factors in inhibiting striation formation. The quality of the striations formed in a vacuum was also found to be perfectly clear enough for analysis with no noticeable difference to air samples.

5.6 Figures and Tables

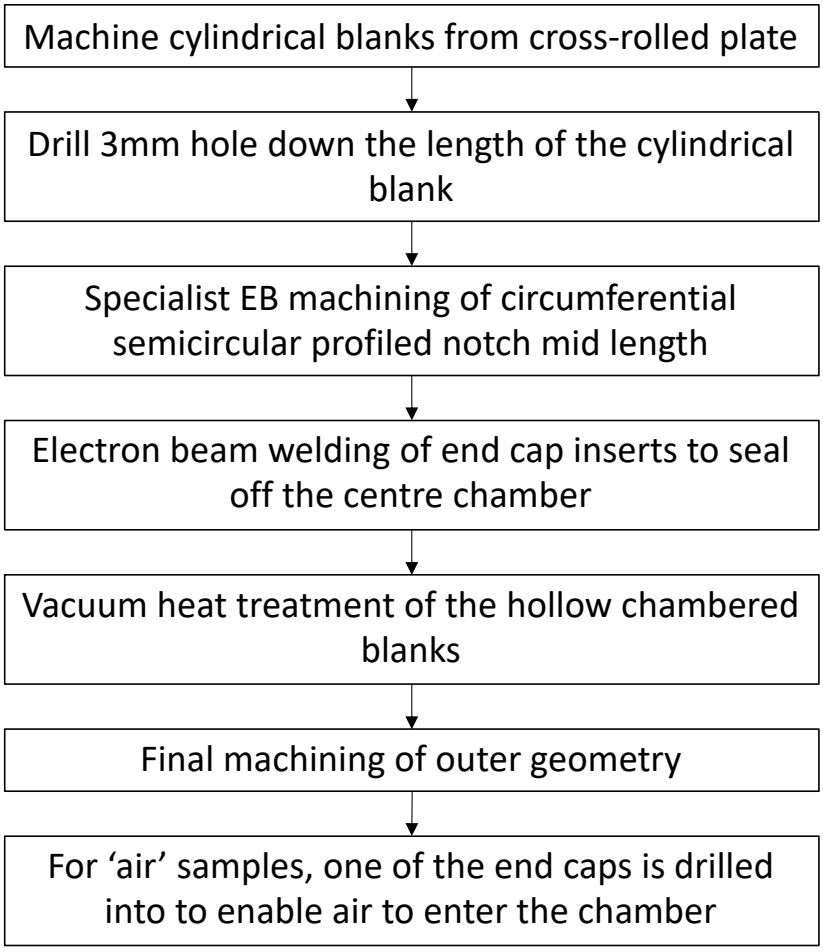

Figure 5.1: This schematic shows the steps taken to produce the samples for this study

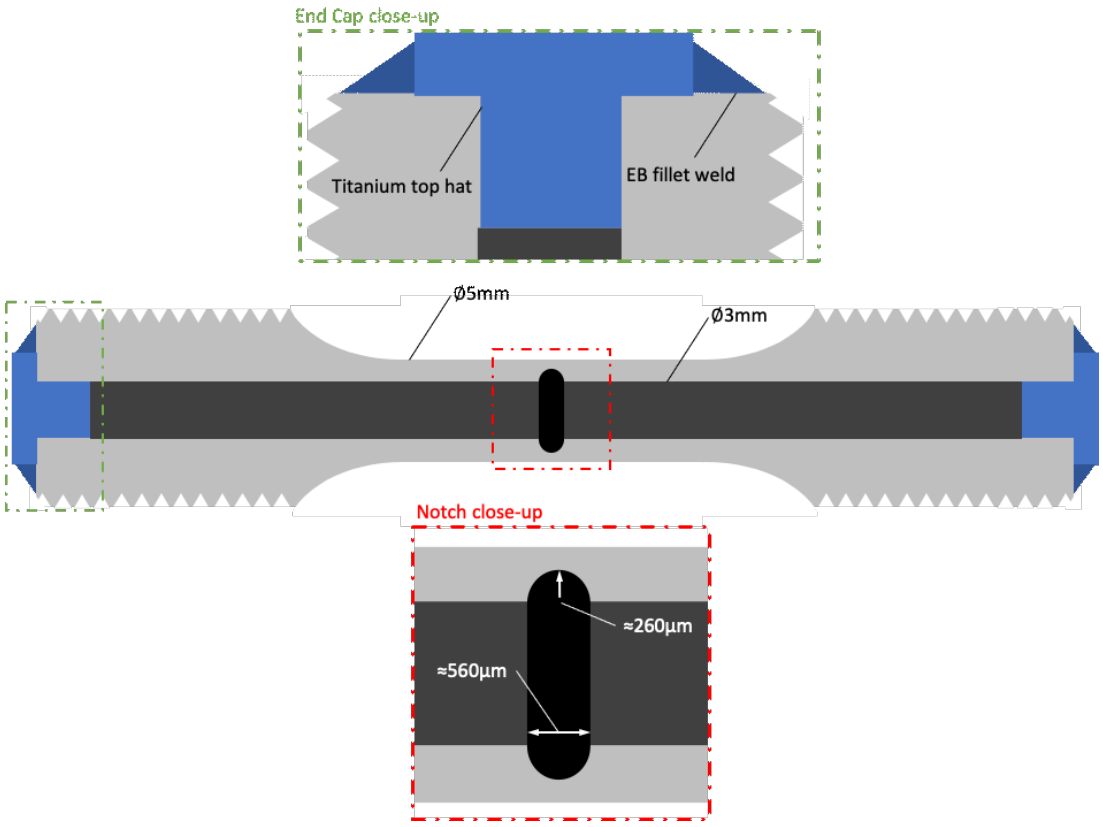

Figure 5.2: This schematic shows a cross-section representation of the samples tested in this work

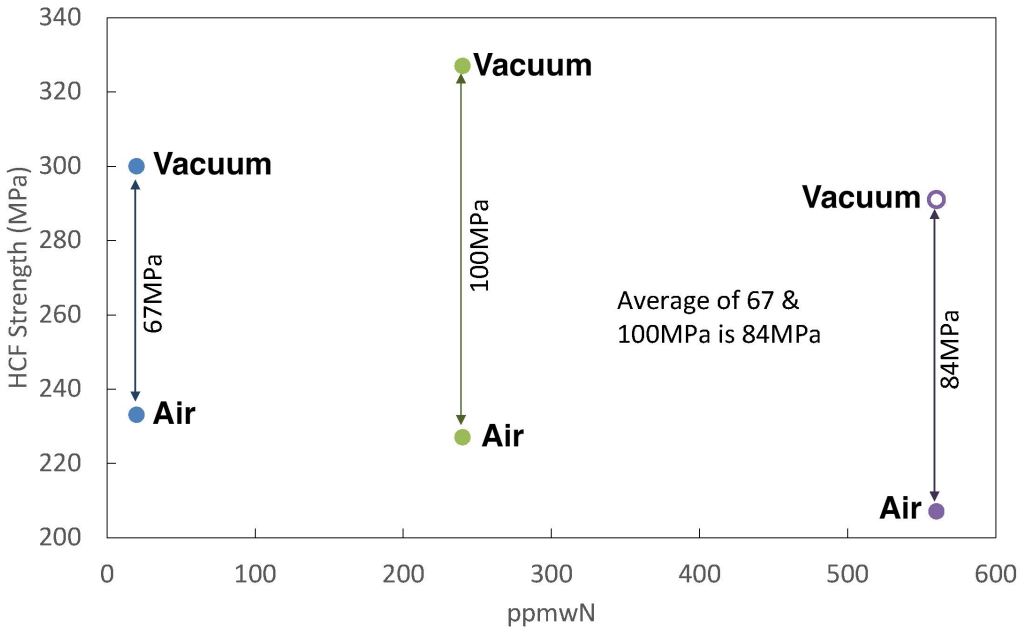

Figure 5.3: Chart showing the HCF strengths calculated of each of the test conditions. Note: the value for 560ppmwN at vacuum, hollow dot, has been changed. The reason for the change is that the sample tested had a poorly aligned notched causing premature failure. The value was adjusted based on the average debit seen air to vacuum from the other two compositions - 84MPa

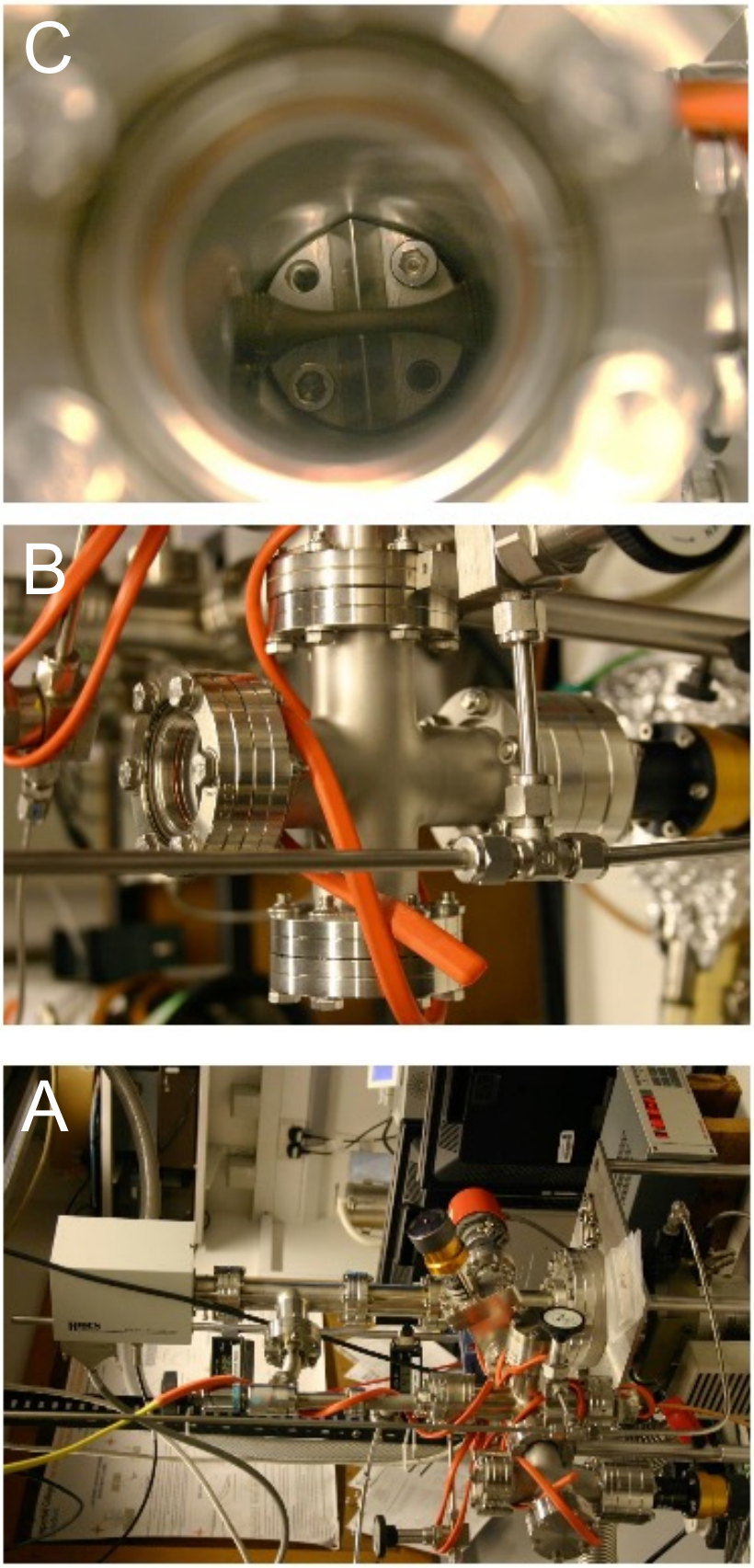

Figure 5.4: These photo's show how a 4-way vacuum crucifix was used to carryout the vacuum proof tests. A) shows the complete setup B) shows a close-up of the crucifix C) shows the view down the vertical axis of the crucifix looking at the ram profile contacting the sample.

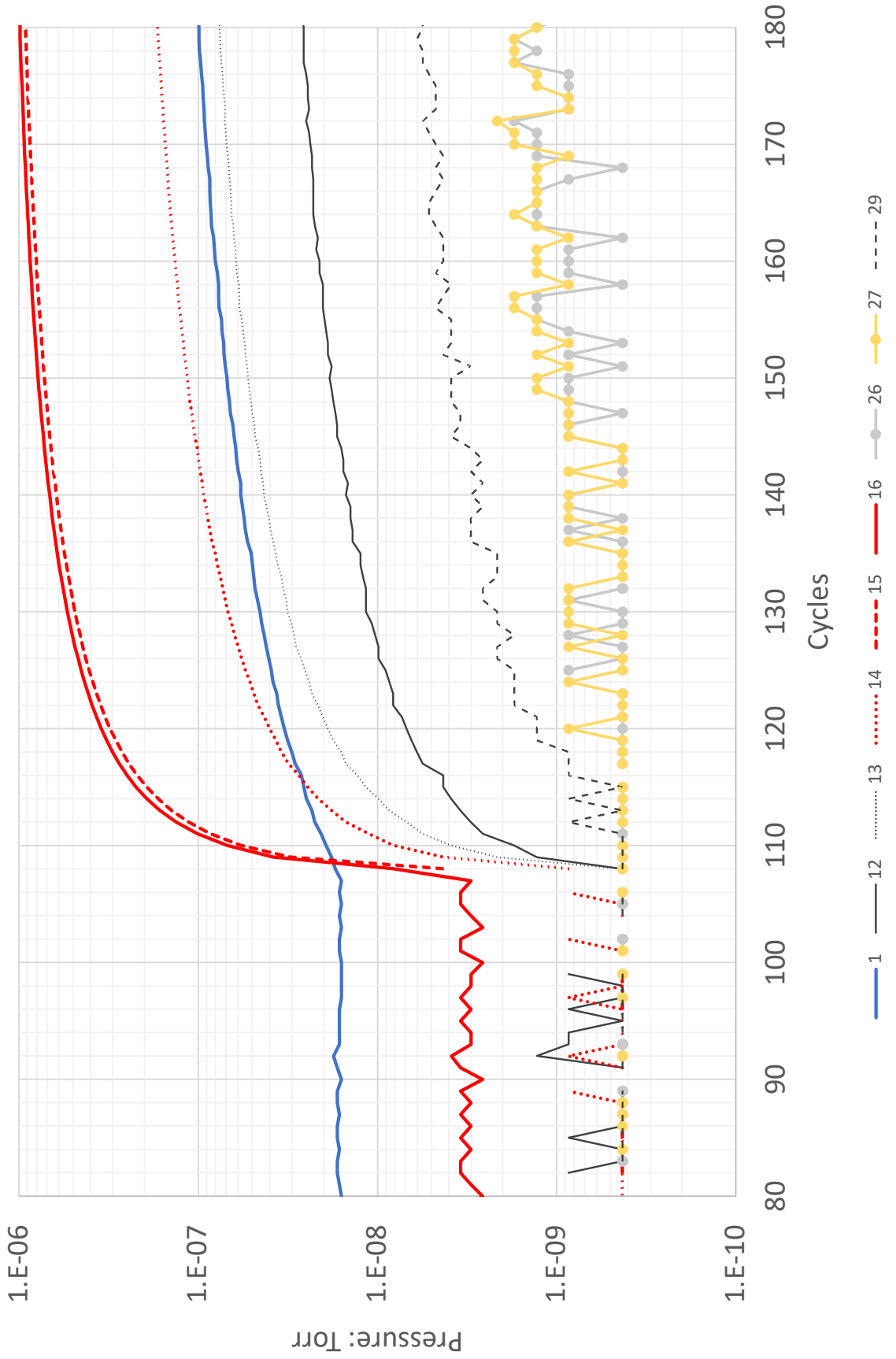

Figure 5.5: This chart shows the results of the vacuum proof tests. This chart shows the pressure change for a number of mass weights against analysis cycles. The red traces represent a known trace pattern for a methane signal

Figure 5.6: This figure shows the optical overview from HF035 with the notch surface highlighted in red shading and the testing induced fracture shaded yellow. It can be seen from this figure that the notch isn't quite uniform in size or quite centred to the central axis of the test sample

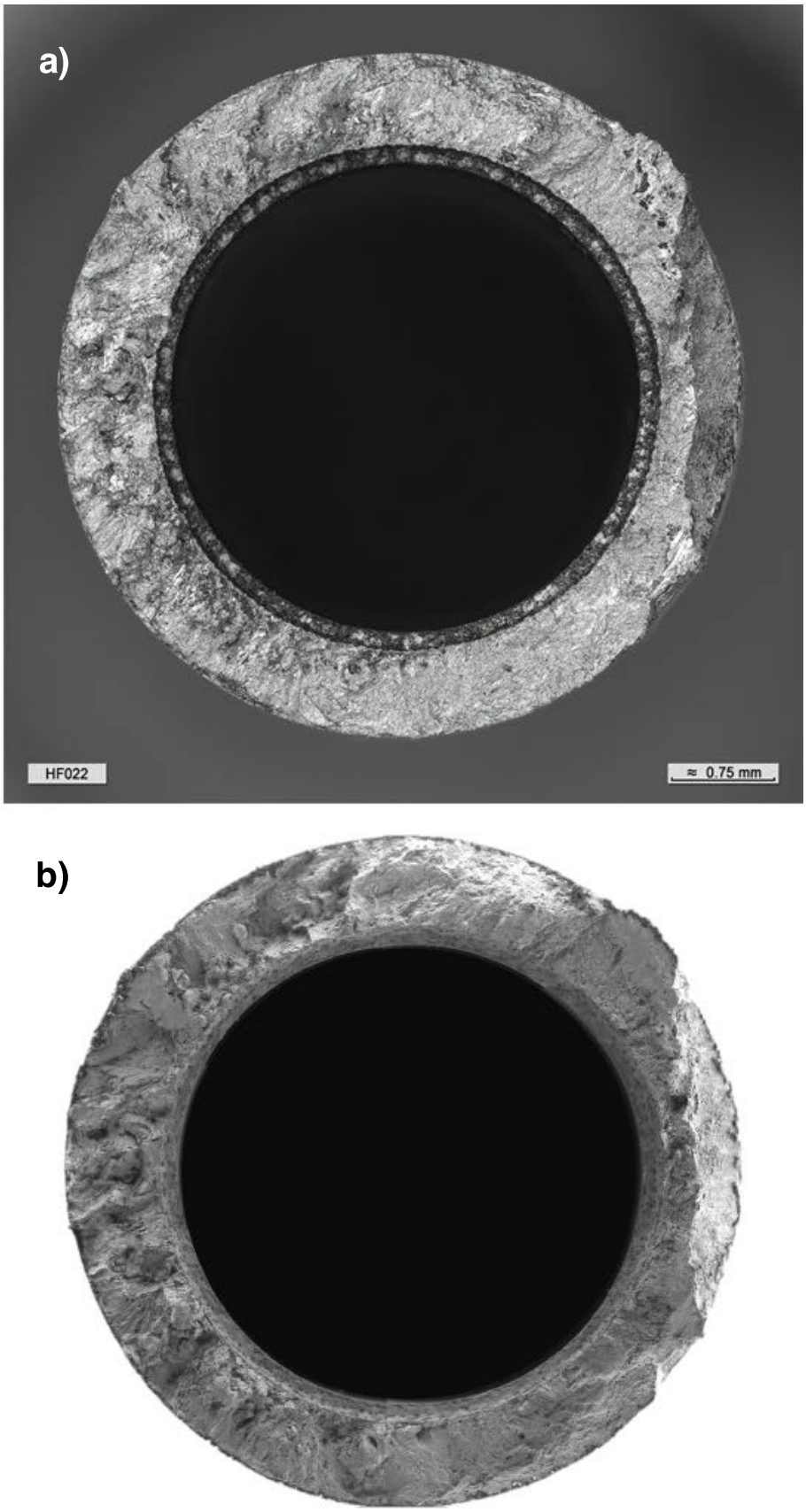

Figure 5.7: This figure shows a) an optical overview of a fracture from HF022 240ppmwN air sample and b) an SEM overview of the same fracture face (SE, 5.00kV, WD 4.8mm)

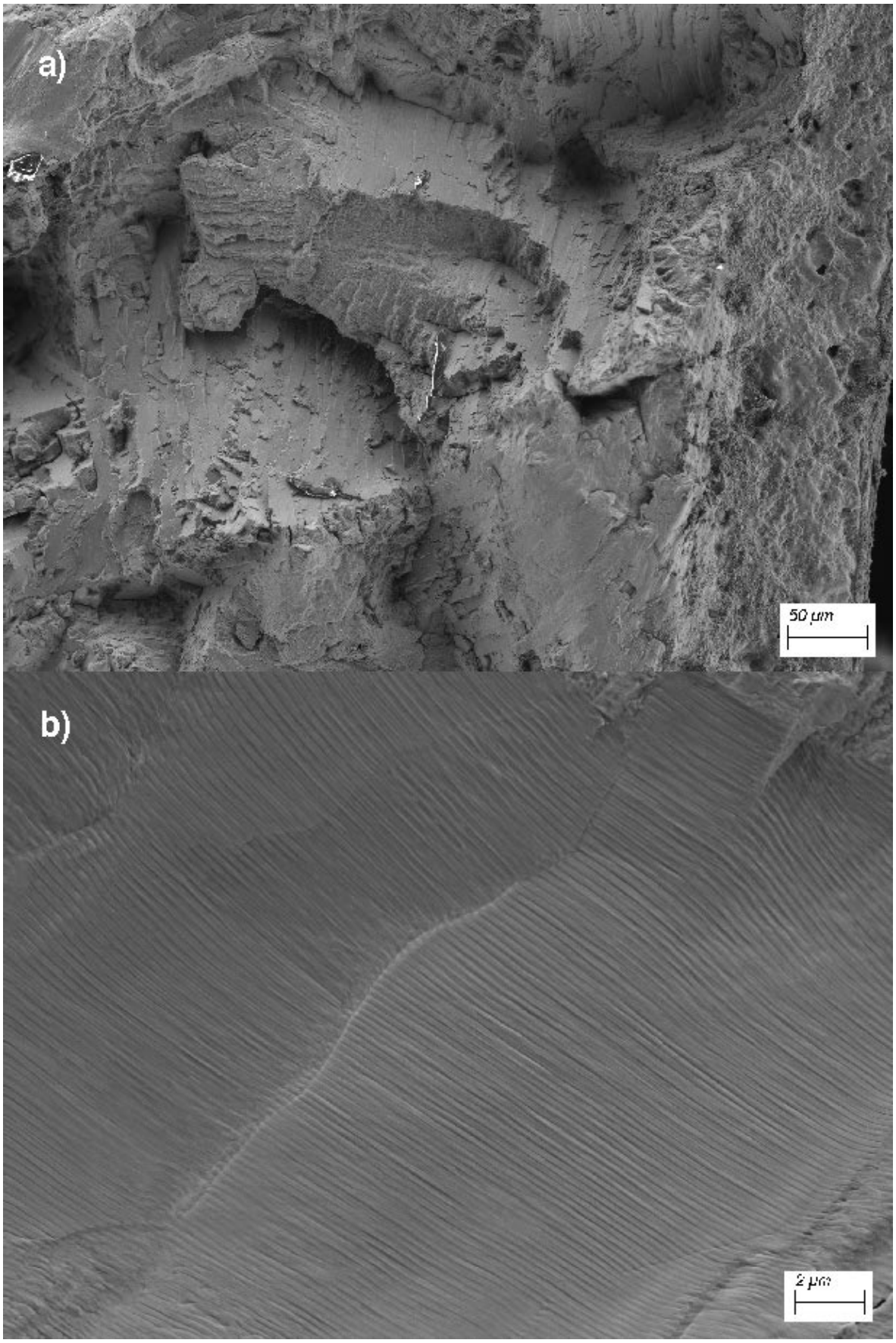

Figure 5.8: This figure shows an SEM fractograph showing a) a region of facetted growth originating from the notch (SE, 5.00kV, WD 4.9mm) and b) a region of striated growth (SE, 5.00kV, WD 5.0mm) from HF022 240ppmwN air sample

Figure 5.9: This figure shows the crack growth rates in µm per cycle at isolated locations as determined by SEM fractography for HF022 240ppmwN air sample, the red star indicates the approximate area of initiation. Inset is a schematic showing the macro crack propagation pattern

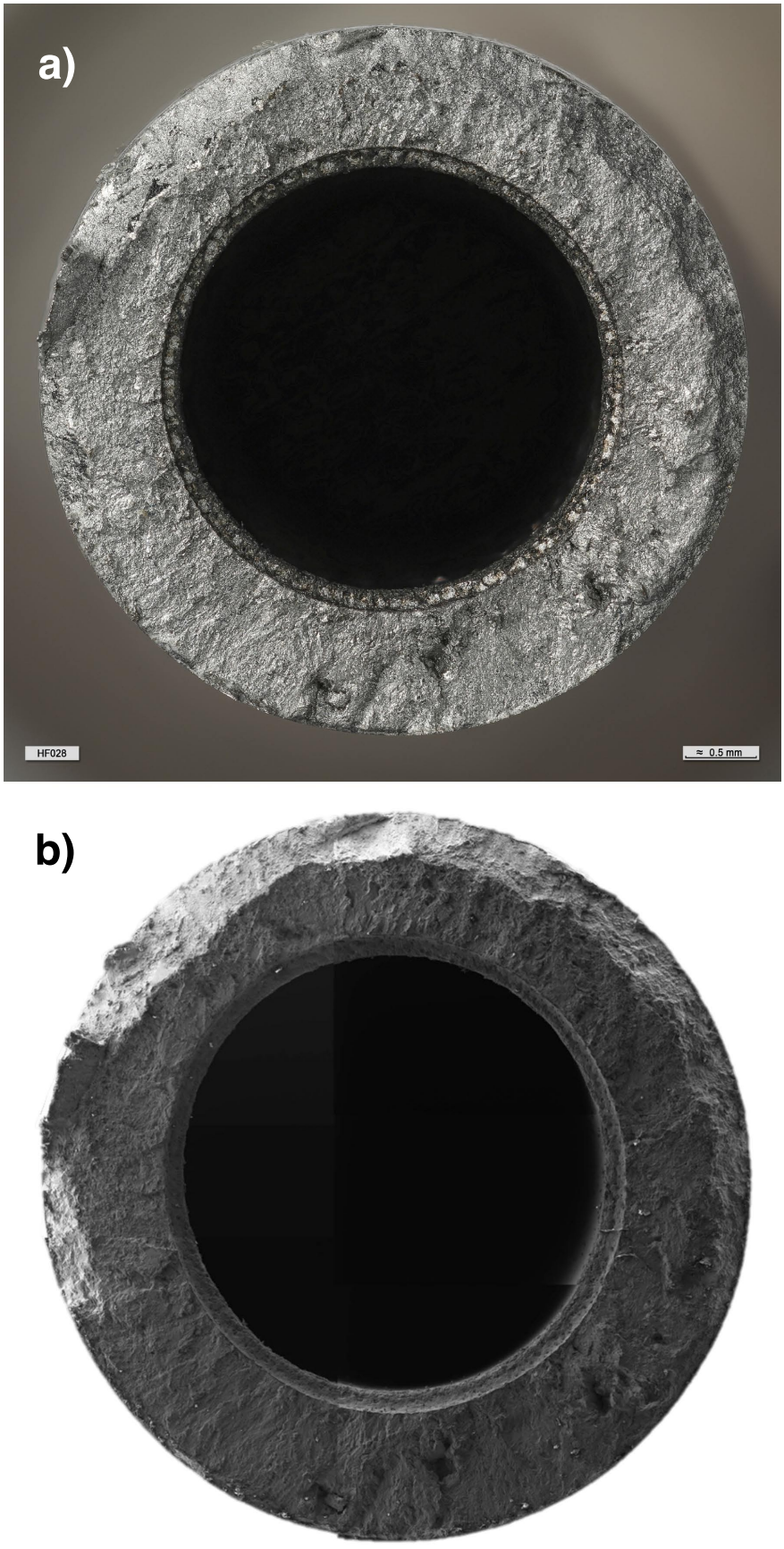

Figure 5.10: This figure shows a) an optical overview of a fracture from HF028 240ppmwN vacuum sample and b) an SEM overview of the same fracture face (SE, 5.00kV, WD 4.7mm)

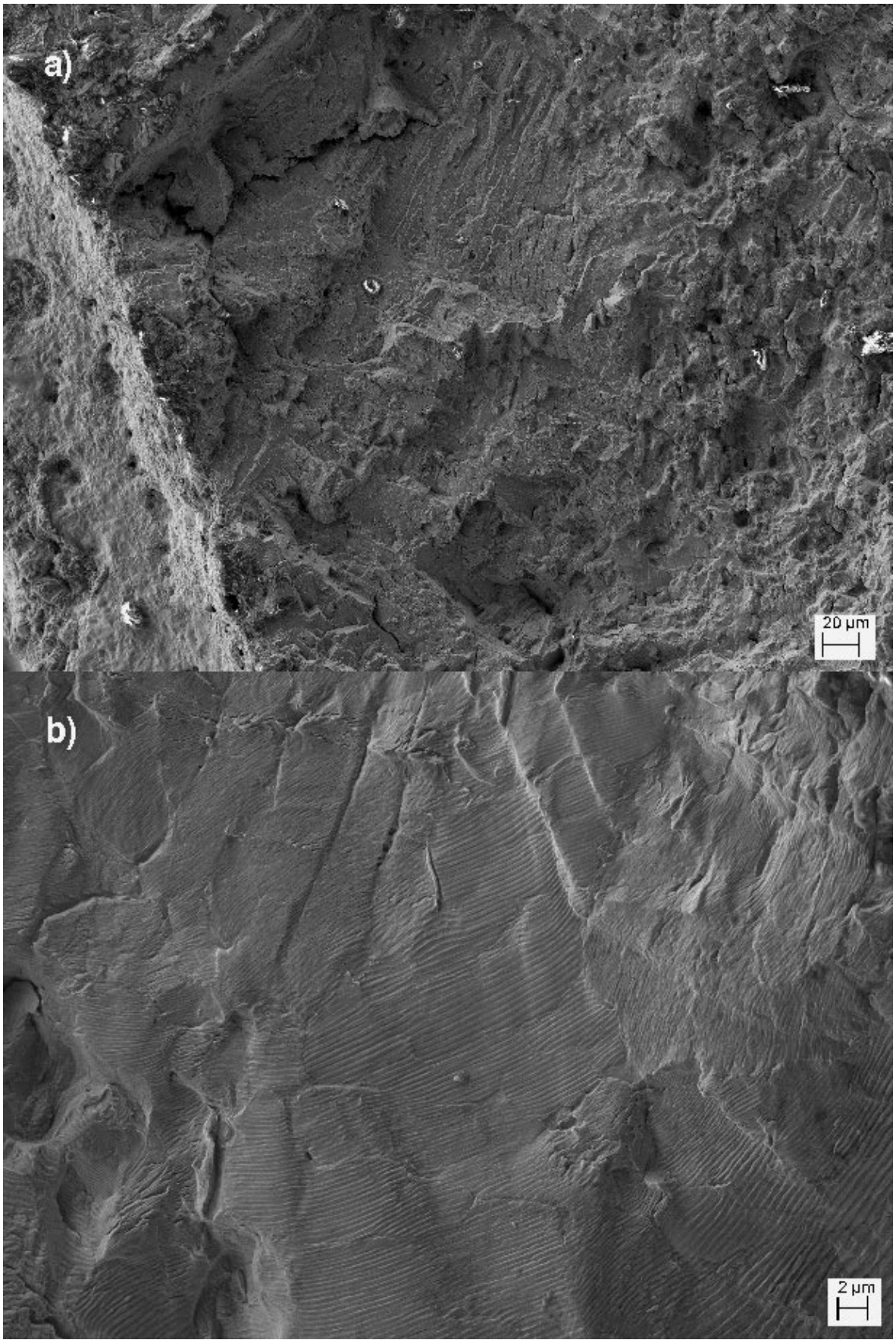

Figure 5.11: This figure shows an SEM fractograph showing a) a region of facetted growth originating from the notch (SE, 5.00kV, WD 4.8mm) and b) a region of striated growth (SE, 5.00kV, WD 4.7mm) from HF028 240ppmwN vacuum sample

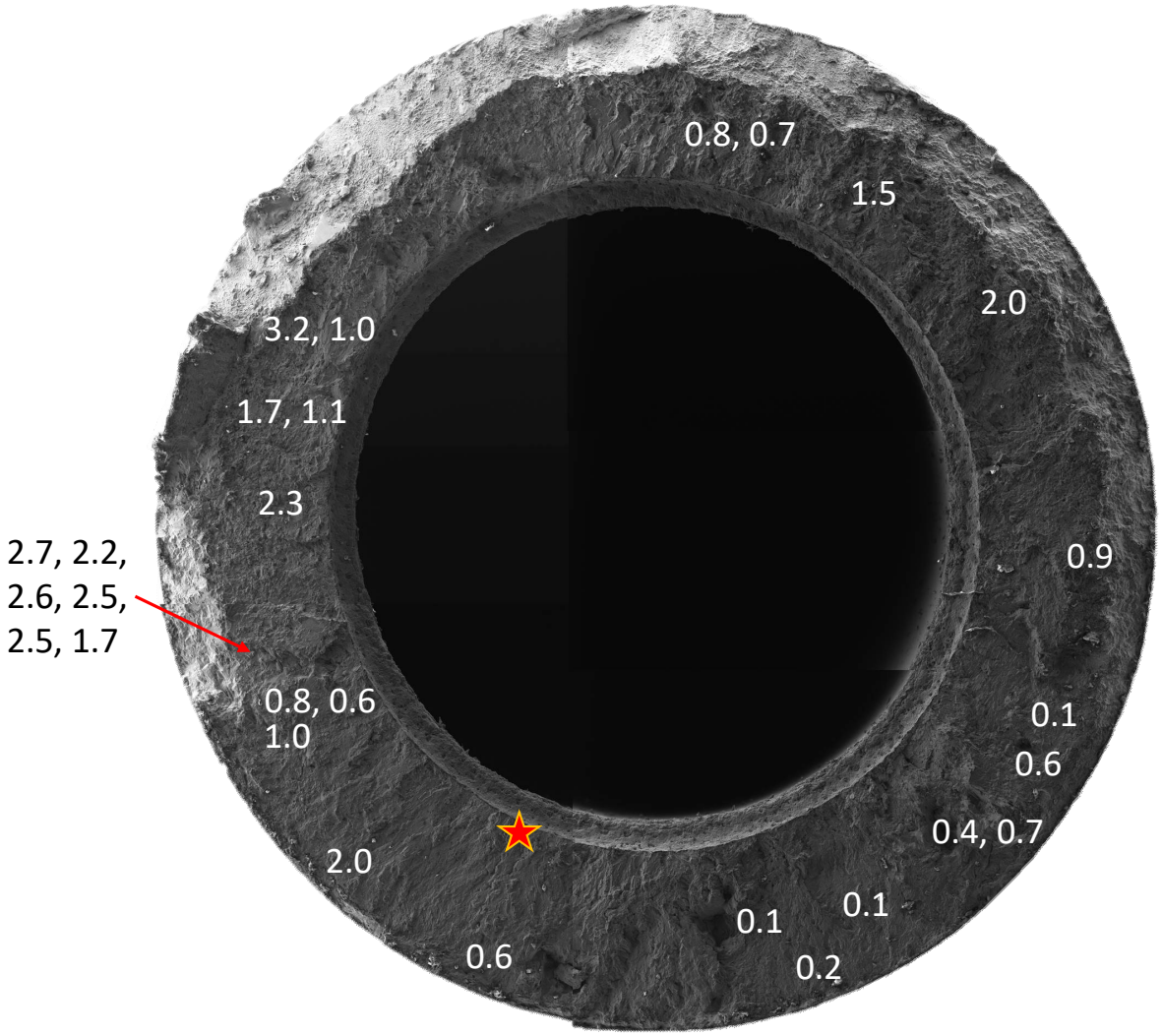

Figure 5.12: This figure shows the crack growth rates in µm per cycle at isolated locations as determined by SEM fractography for HF028 240ppmwN vacuum sample, the red star indicates the approximate area of intiation

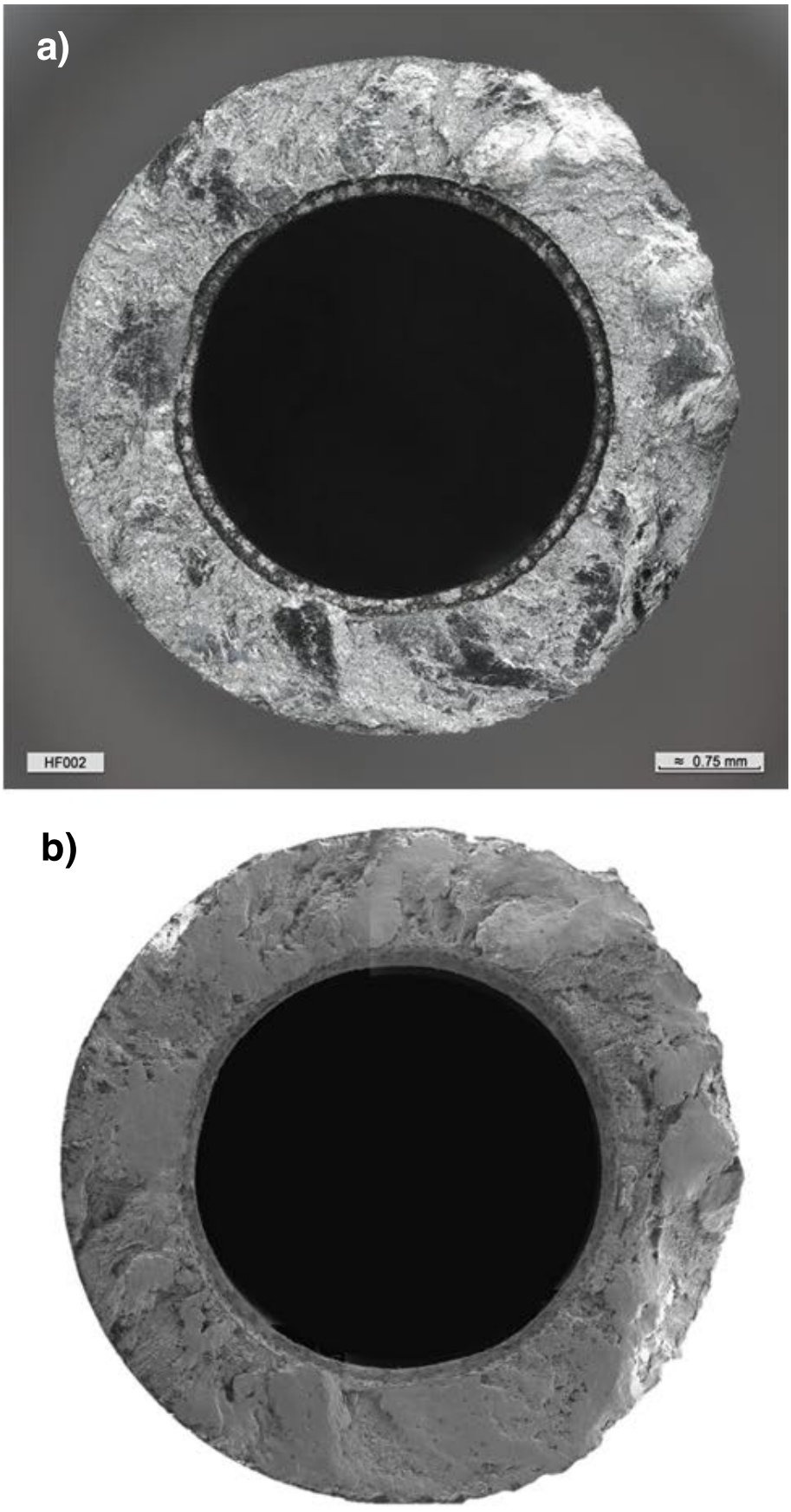

Figure 5.13: This figure shows a) an optical overview of a fracture from HF002 500ppmwN air sample and b) an SEM overview of the same fracture face (SE, 5.00kV, WD 4.7mm)

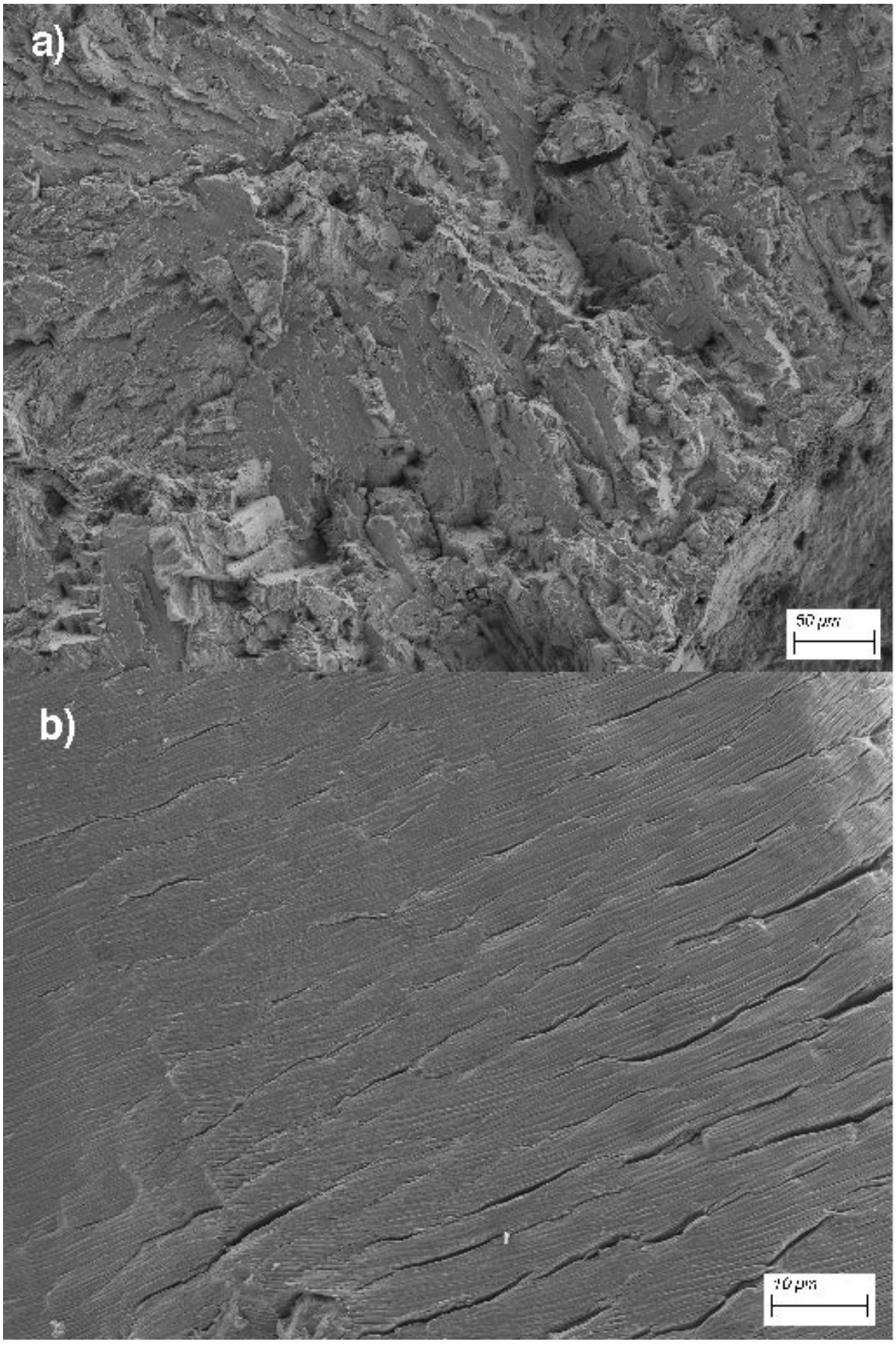

Figure 5.14: This figure shows an SEM fractograph showing a) a region of facetted growth originating from the notch (SE, 5.00kV, WD 4.7mm) and b) a region of striated growth (SE, 5.00kV, WD 4.7mm) from HF002 500ppmwN air sample

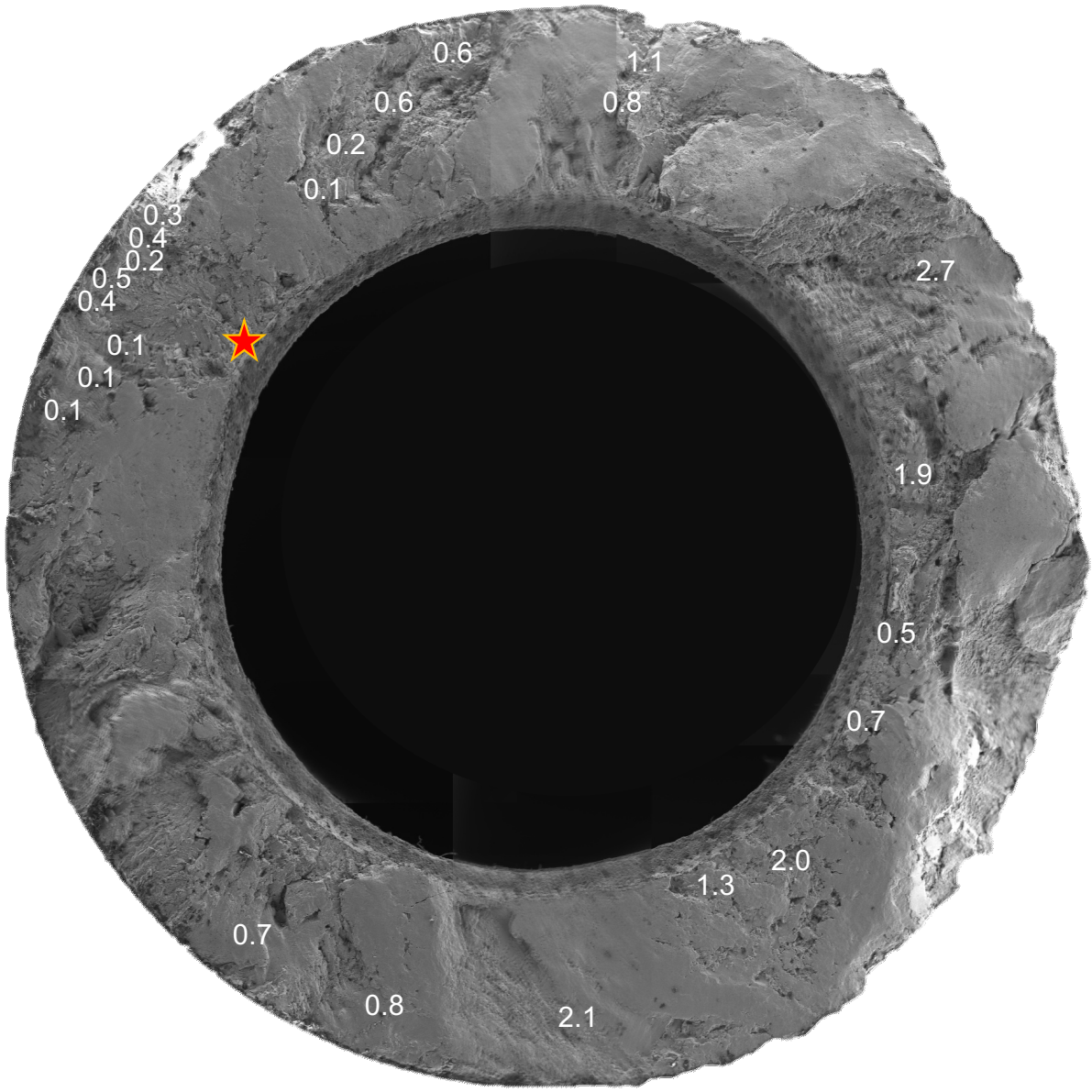

Figure 5.15: This figure shows the crack growth rates in µm per cycle at isolated locations as determined by SEM fractography for HF002 500ppmwN air sample, the red star indicates the approximate area of intiation

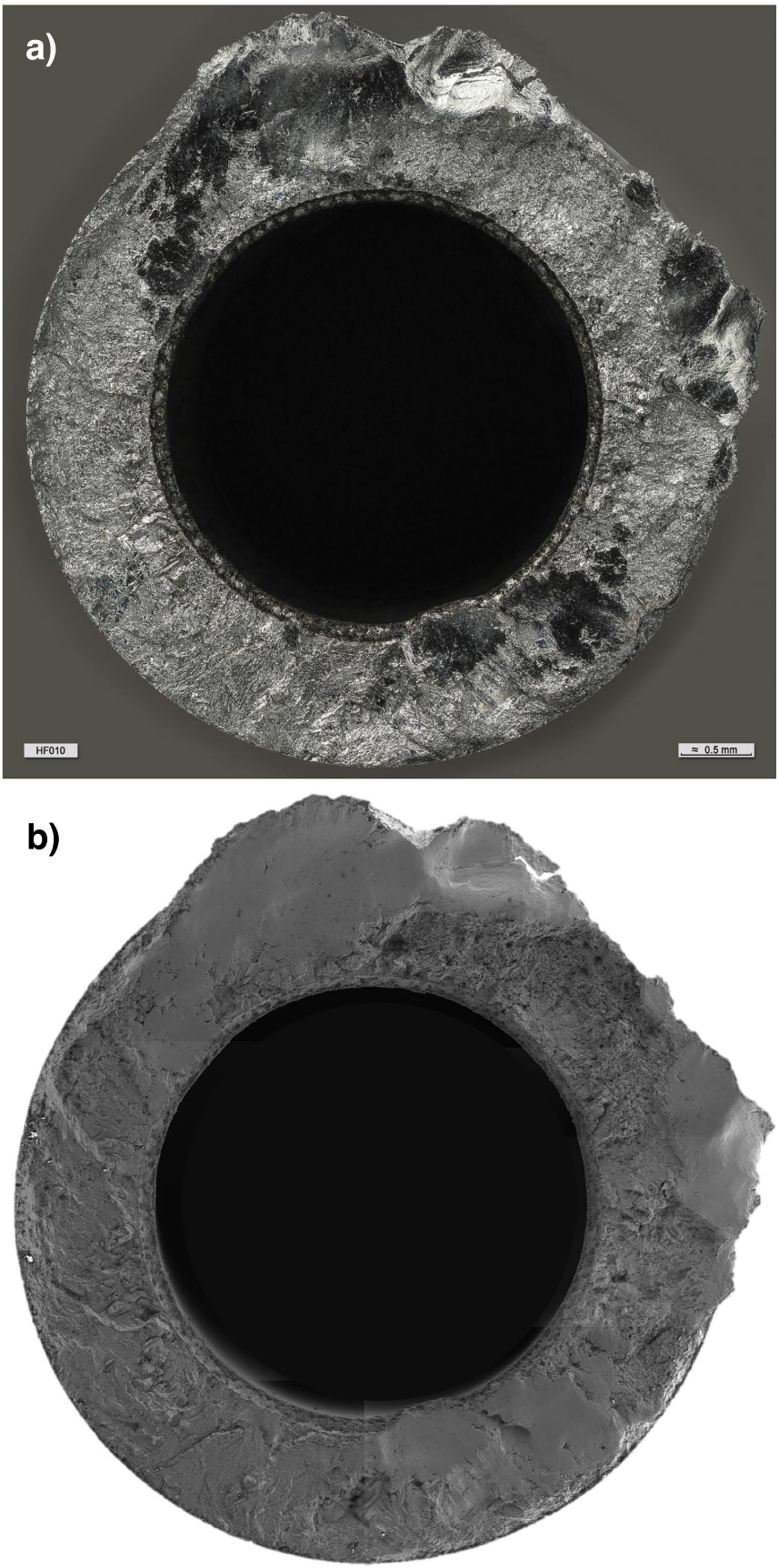

Figure 5.16: This figure shows a) an optical overview of a fracture from HF010 500ppmwN vacuum sample and b) an SEM overview of the same fracture face (SE, 5.00kV, WD 5.6mm) The flat regions of fracture face are from where the two sides of the fracture collided during run down on the test frame.

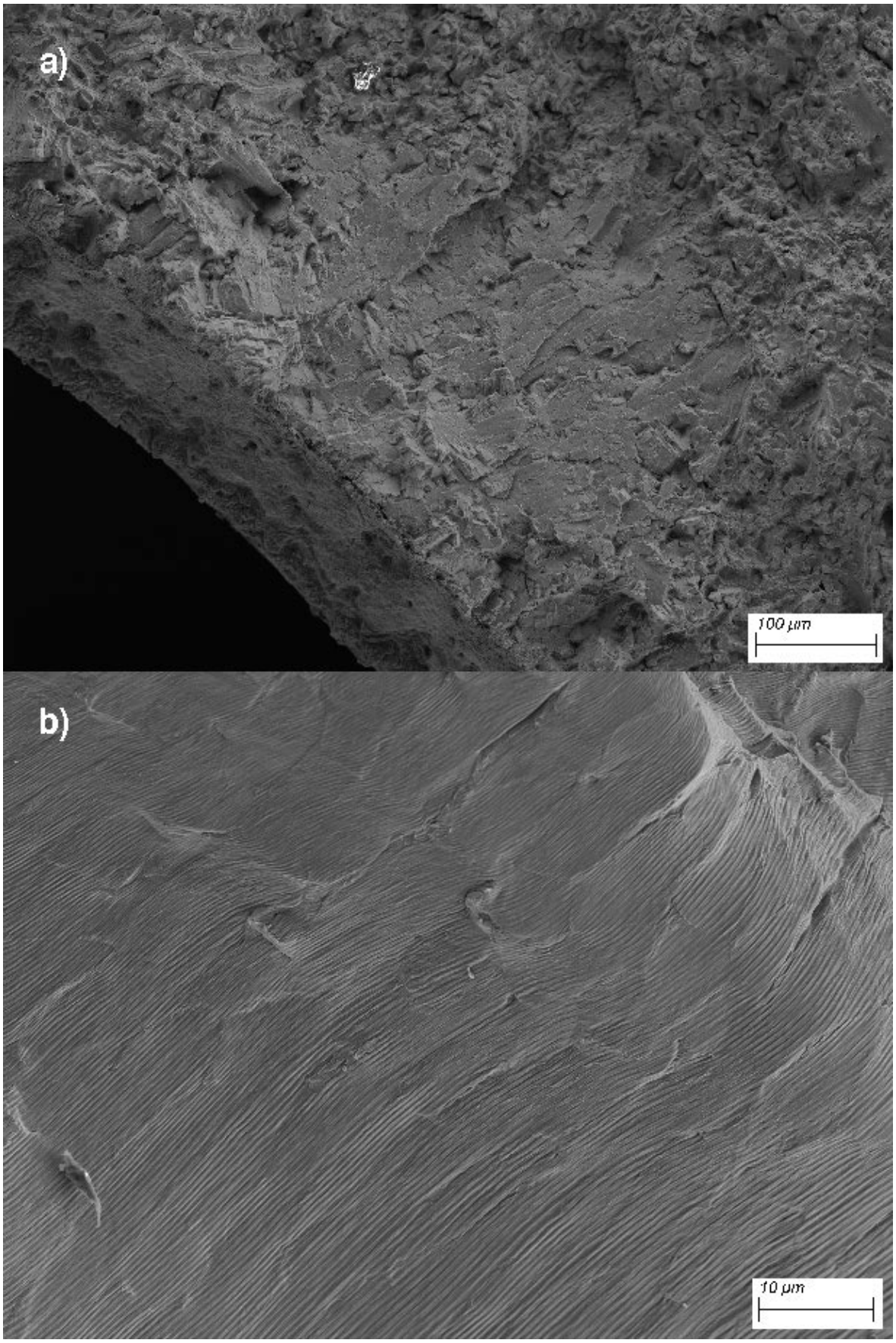

Figure 5.17: This figure shows an SEM fractograph showing a) a region of facetted growth originating from the notch (SE, 5.00kV, WD 5.6mm) and b) a region of striated growth (SE, 5.00kV, WD 5.8mm) from HF010 500ppmwN vacuum sample

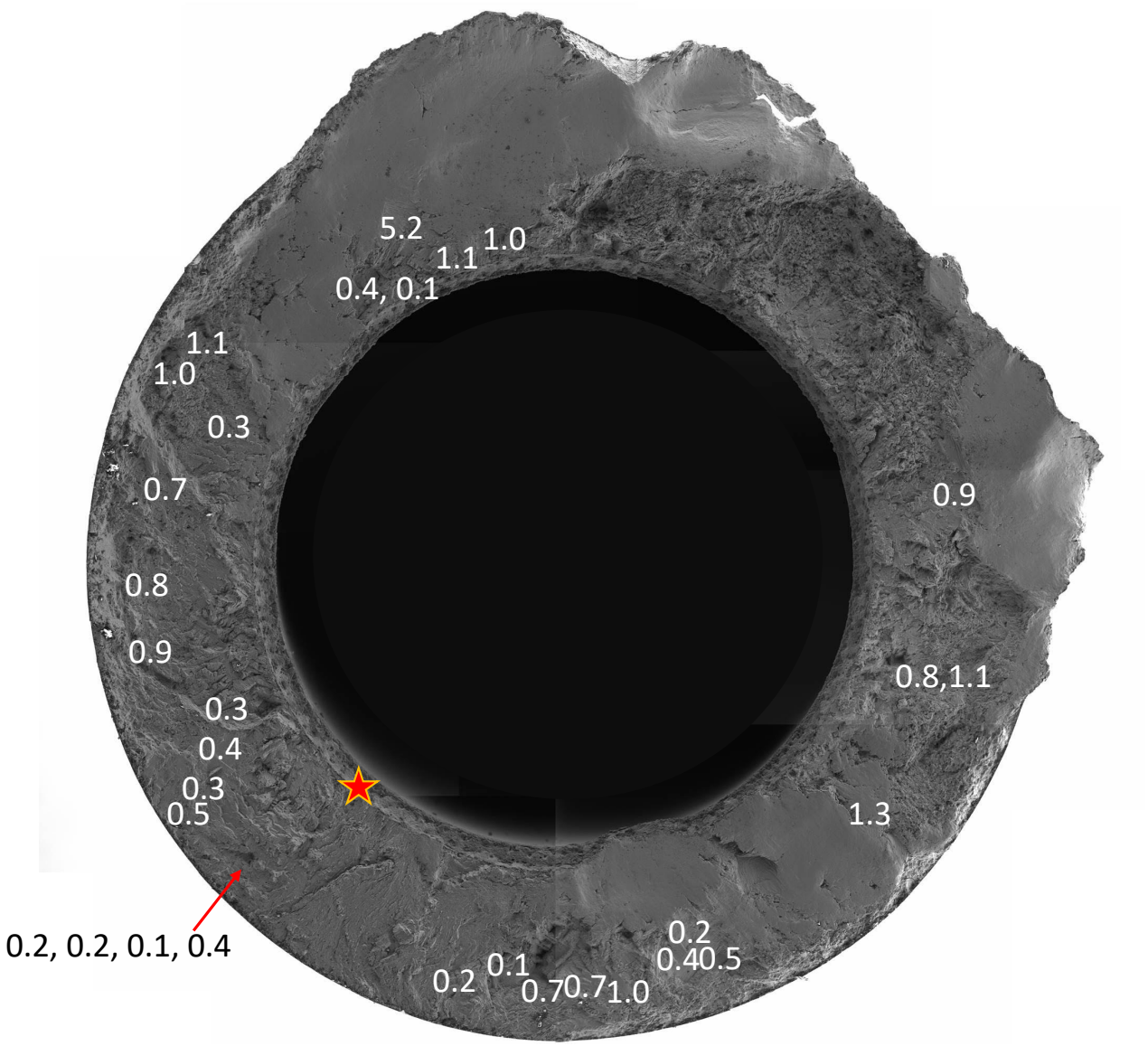

Figure 5.18: This figure shows the crack growth rates in µm per cycle at isolated locations as determined by SEM fractography for HF010 500ppmwN vacuum sample, the red star indicates the approximate area of initiation. The flat regions of fracture face are from where the two sides of the fracture collided during run down on the test frame.

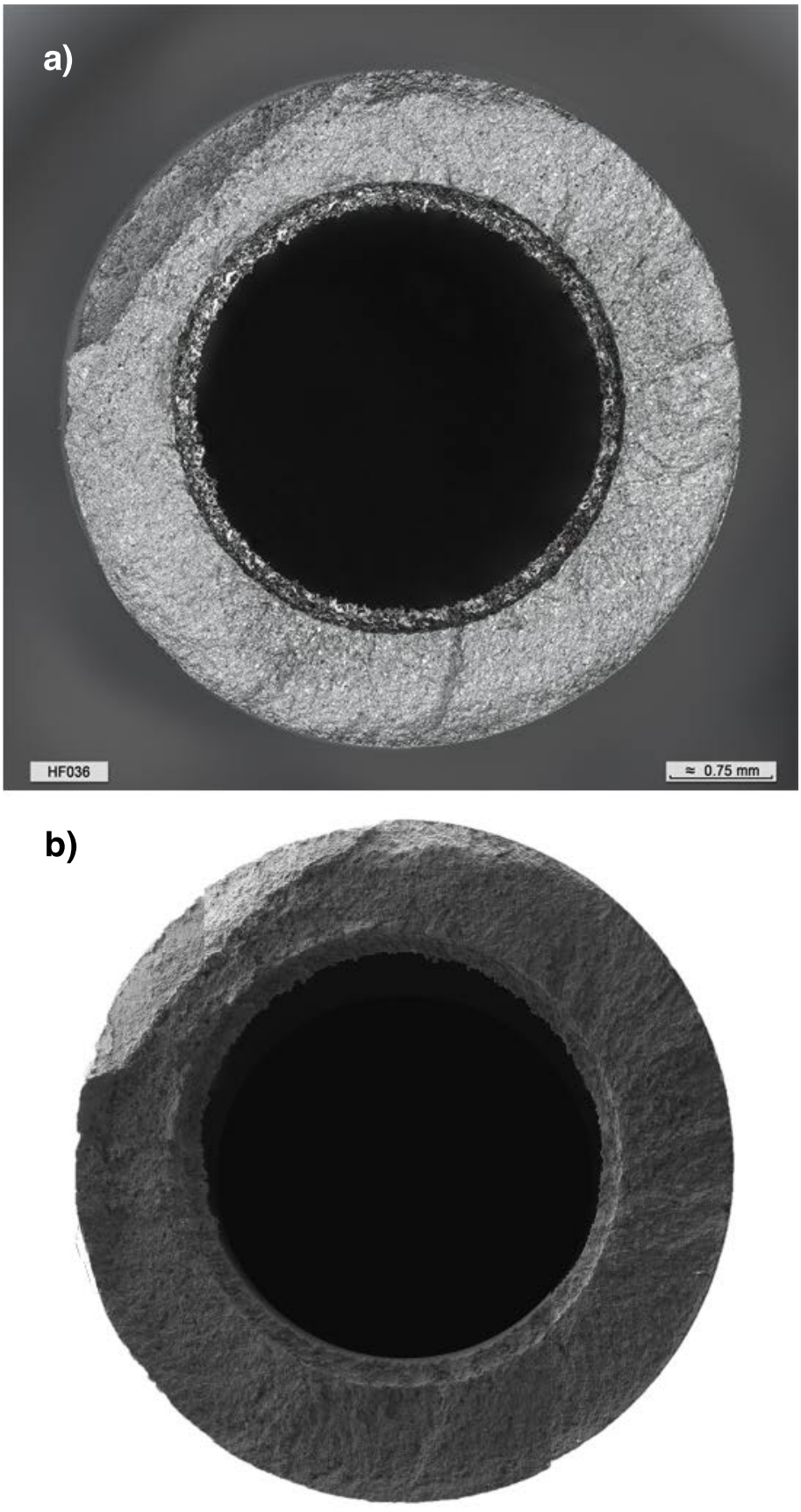

Figure 5.19: This figure shows a) an optical overview of a fracture from HF036 Cross-rolled plate air sample and b) an SEM overview of the same fracture face (SE, 5.00kV, WD 4.9mm)

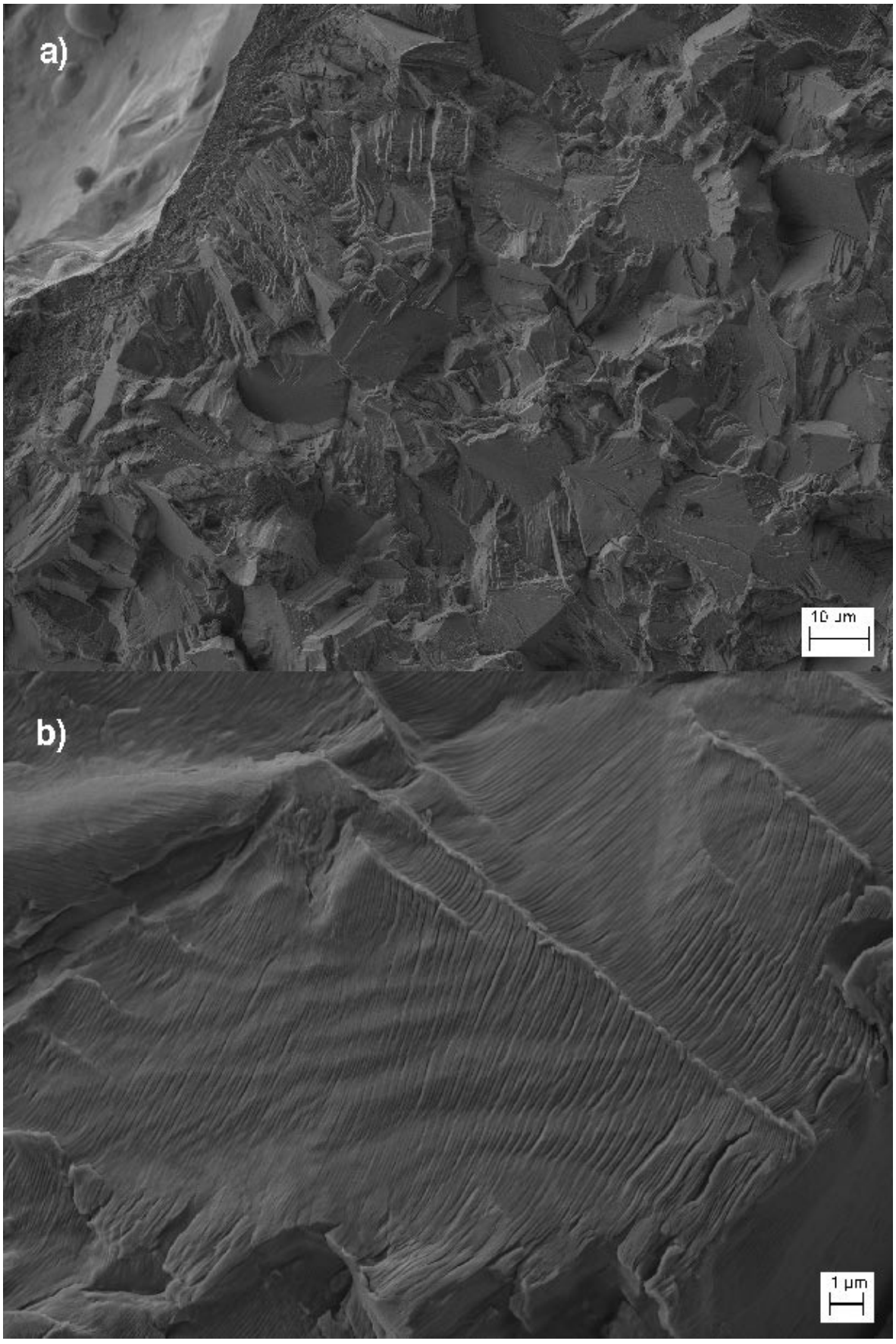

Figure 5.20: This figure shows an SEM fractograph showing a) a region of facetted growth originating from the notch (SE, 5.00kV, WD 4.8mm) and b) a region of striated growth (SE, 5.00kV, WD 4.7mm) from HF036 Cross-rolled plate air sample

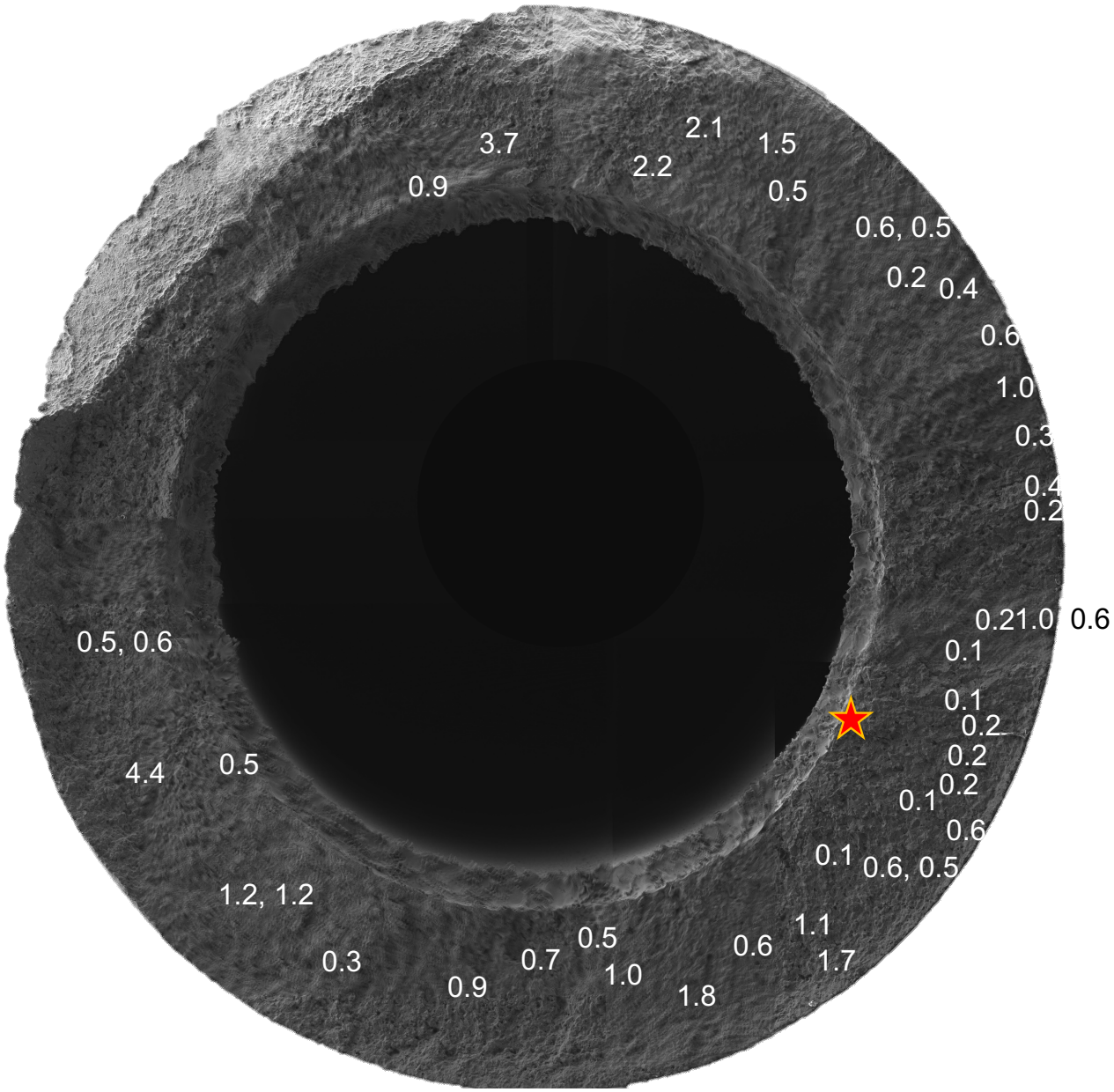

Figure 5.21: This figure shows the crack growth rates in µm per cycle at isolated locations as determined by SEM fractography for HF036 Cross-rolled plate air sample, the red star indicates the approximate area of intiation

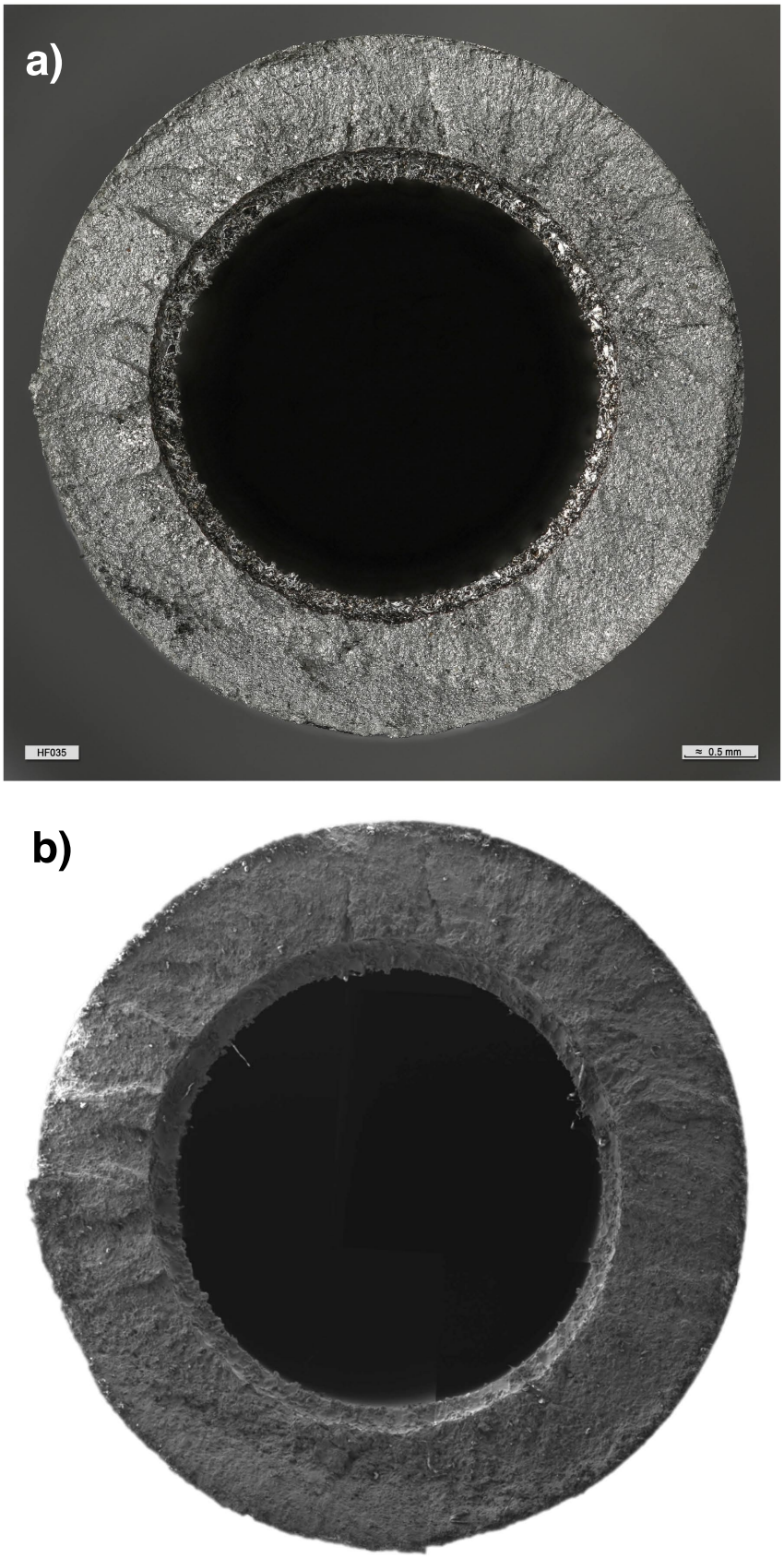

Figure 5.22: This figure shows an SEM fractograph showing a) a region of facetted growth originating from the notch (SE, 5.00kV, WD 4.8mm) and b) a region of striated growth (SE, 5.00kV, WD 5.1mm) from HF035 Cross-rolled plate vacuum sample

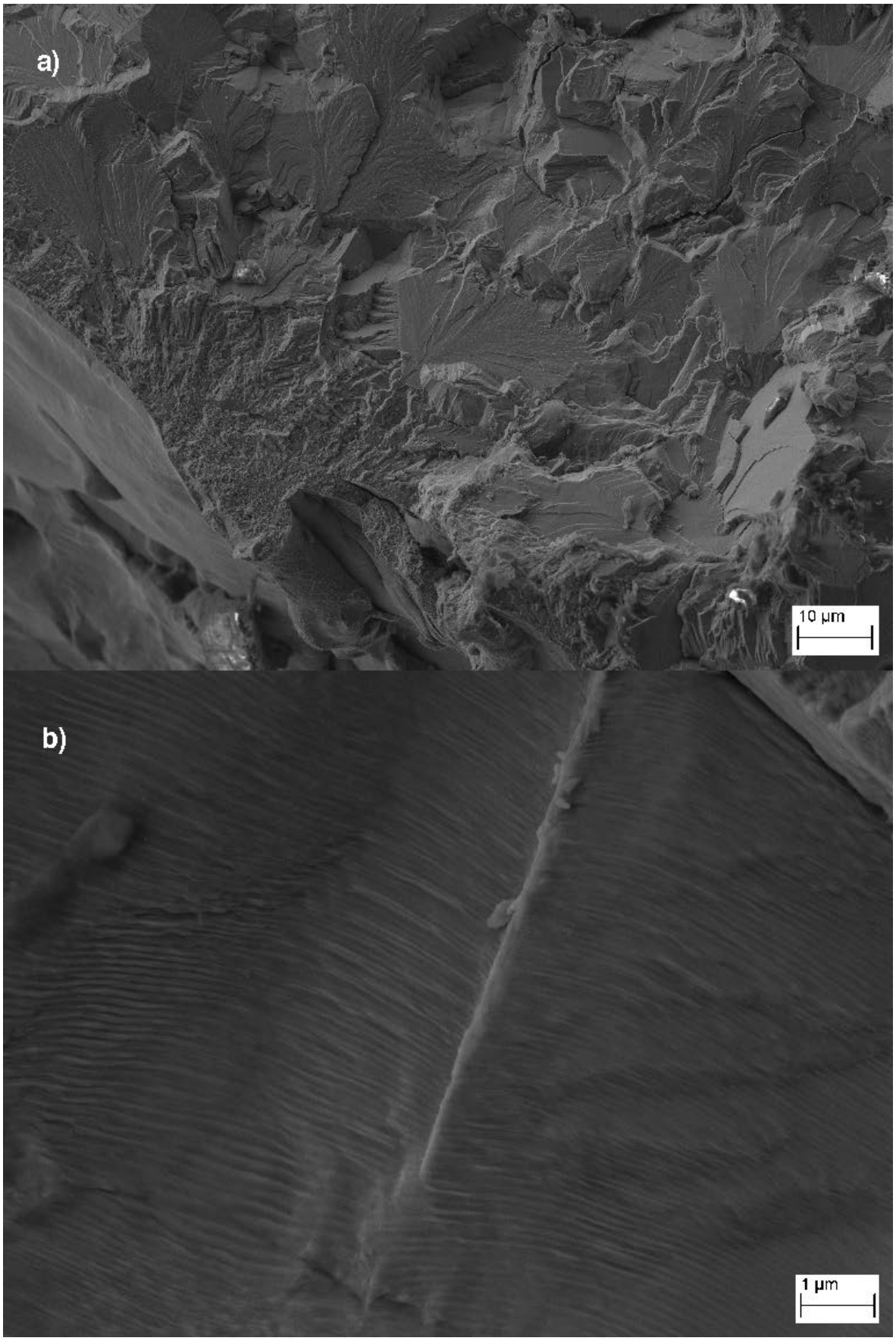

Figure 5.23: This figure shows an SEM fractograph showing a) a region of facetted growth originating from the notch (SE, 5.00kV, WD 4.9mm) and b) a region of striated growth (SE, 5.00kV, WD 4.9mm) from HF035 Cross-rolled plate vacuum sample

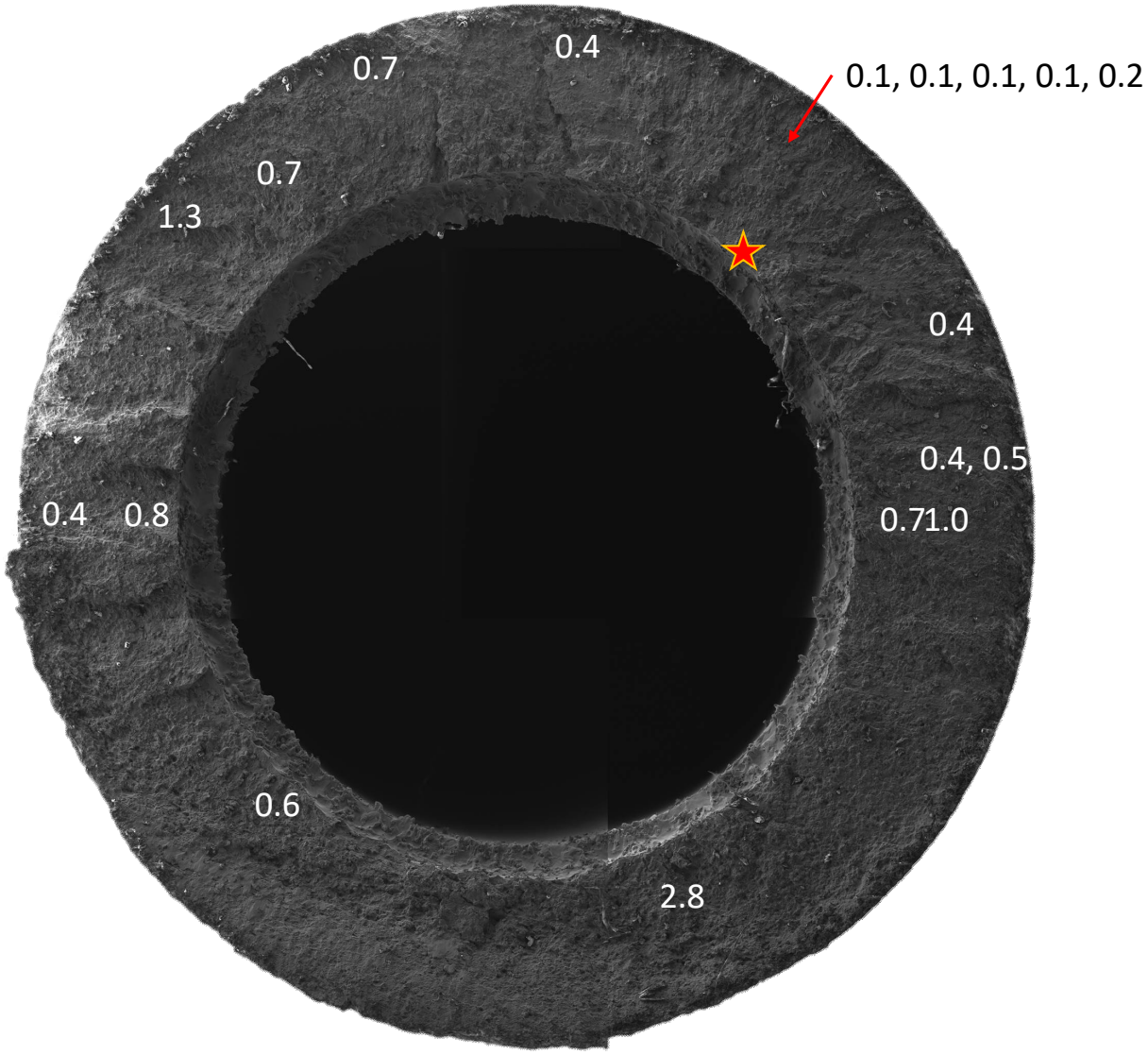

Figure 5.24: This figure shows the crack growth rates in µm per cycle at isolated locations as determined by SEM fractography for HF035 Cross-rolled plate vacuum sample, the red star indicates the approximate area of intiation

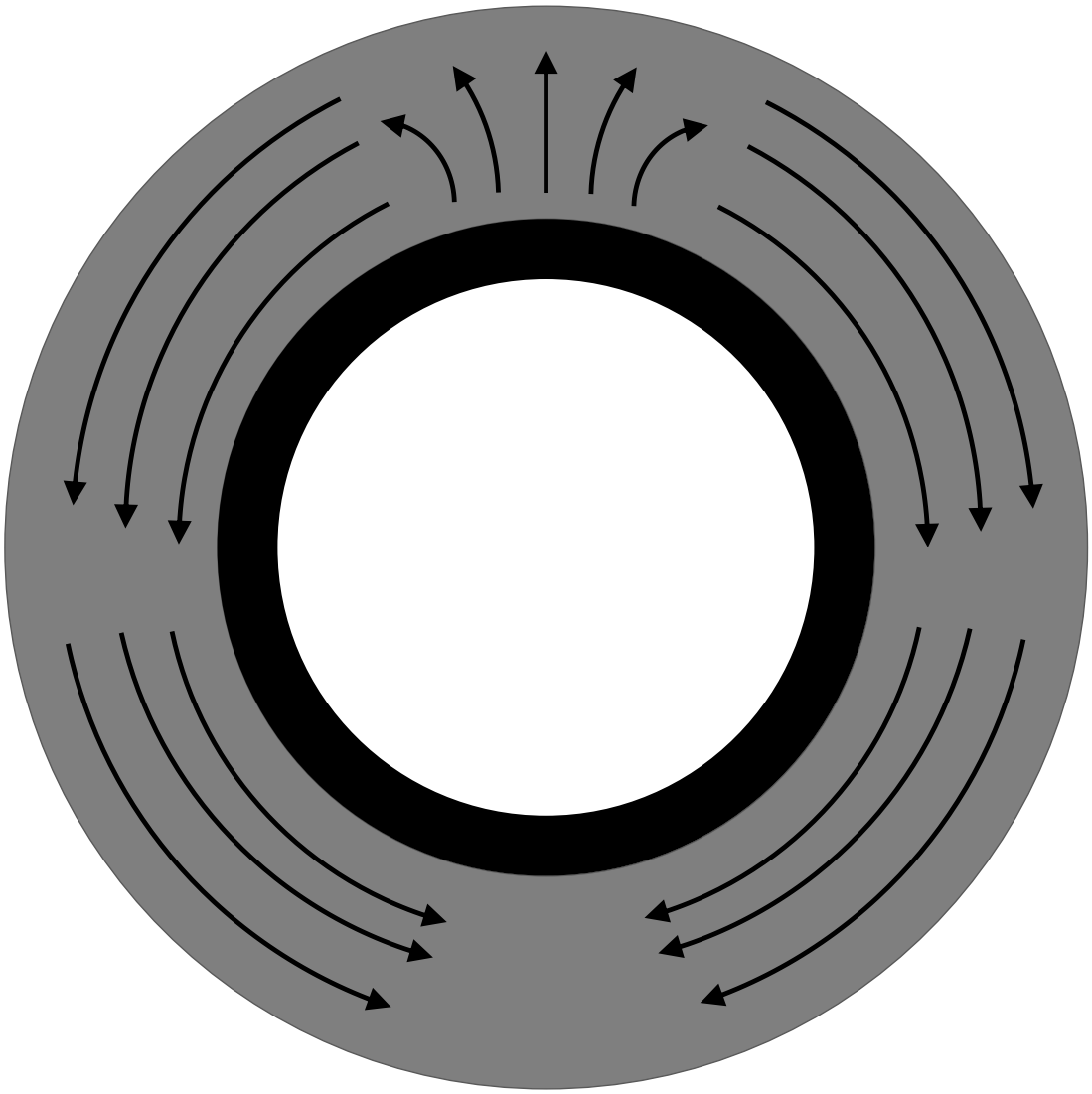

Figure 5.25: This figure shows a schematic indicating the general macroscopic crack propagation observed from the samples in this chapter

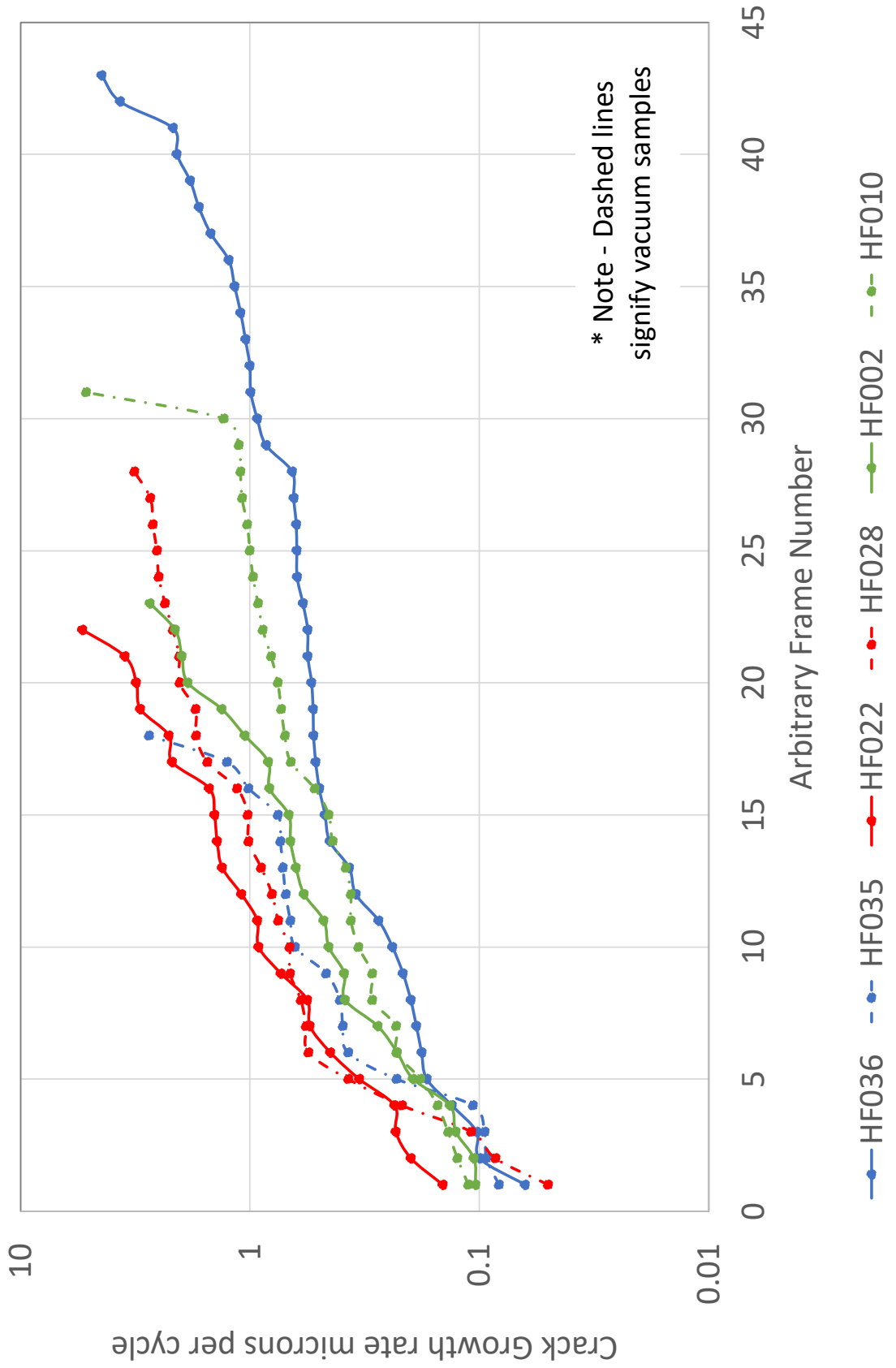

Figure 5.26: This figure shows a comparison of the range of crack propagation rates captured from the quantitative SEM fractography. Blue traces are Cross-rolled plate, Red traces are 240ppmwN and Green traces are 500ppmwN. This shows that the range of crack propagation rates was similar between all the samples measured

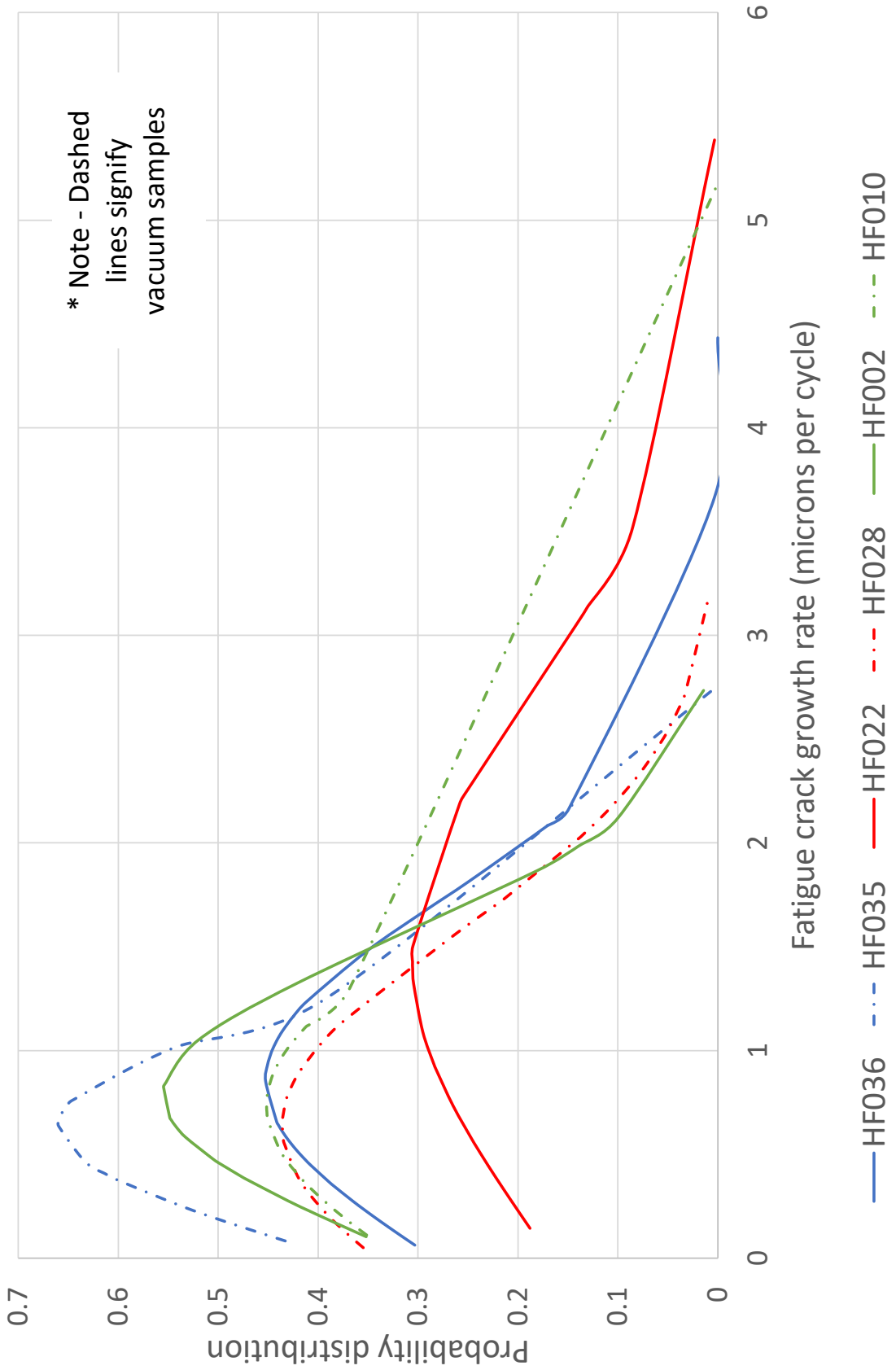

Figure 5.27: This figure shows a comparison of the probability distribution curves for each of the ex-situ samples using data from Figure 5.26. The information drawn from this plot is that all the samples have a similar spread of observed crack growth rates

Table 5.1: Test Sample Matrix

Composition	Air	Vacuum
Cross-Rolled Ti-6Al-4V	HF036 + HF042	HF035 + HF041
Cross-Rolled Ti-6Al-4V Reprocessed to 240ppmwN	HF016 + HF022	HF004 + HF028
Cross-Rolled Ti-6Al-4V Reprocessed to 560ppmwN	HF030 + HF002	HF014 + HF010

Table 5.2: Hiden cracking pattern guide excerpt [29]

Name	Peak 1		Peak 2		Peak 3	
	Mass weight	%	Mass weight	%	Mass weight	%
Air	28	100	32	16	14	7.2
Oxygen	32	100	16	11.4	34	0.4
Nitrogen	28	100	14	7.2	29	0.8
Methane	16	100	15	85.8	14	15.6

Table 5.3: Life test results

Sample	Air or Vac	Cycles to failure	Peak Stress (MPa)	HCF Strength (MPa)
HF041	Vac	19400	325	300
HF042	Air	326700	250	233
HF004	Vac	66400	350	327
HF016	Air	92400	250	227
HF014 est	Vac	89800	170	291
HF030	Air	288800	225	207

Table 5.4: Ex-situ CT scan intervals

Scan	Sample life at ex-situ CT scan					
	HF022 225MPa (*250)	HF028 325MPa	HF002 200MPa (*225)	HF010 300MPa	HF036 250MPa (*275, **325)	HF035 300MPa
Initial	0	0	0	0	0	0
1	1000	1000	1000	1000	1000	1000
2	2000	2000	2000	2000	2000	2000
3	3000	3000	3000	3000	3000	3000
4	4000	4000	4000	4000	4000	4000
5	5000	5000	5000	5000	5000	5000
6	6000	6000	6000	6000	6000	6000
7	7000	7000	7000	7000	7000	7000
8	12000	12000	12000	12000	8000	12000
9	17000	17000	17000	17000	13000	17000
10	22000	22000	22000	22000	18000	22000
11	32000	32000	32000	32000	19000	32000
12	52000	33000	52000	52000	29000	52000
13	72000	34000	72000	53000	39000	62000
14	112000	38400	112000	57700	59000	79400
15	*10000		*10000		99000	
16	*35000		*60000		*10000	
17	*60000		*80000		*35000	
18	*4100000		*107800		*60000	
19					**122500	

Table 5.5: Testing results for ex-situ monitored samples. *HF022 and HF036 were left to fail at the same stress despite going past the previously used step cycle limit. HCF strengths have been calculated on the basis of the samples being a run out.

Sample	Peak Stress (MPa)	Cycles at first CT indication	Cycles to Failure	HCF Strength (MPa)
HF036 XR Plate Air	325	N/a	122500	325*
HF035 XR Plate Vac	300	52000	79400	277
HF022 240ppmwN Air	250	N/a	4100000	250*
HF028 240ppmwN Vac	325	17000	38400	301
HF002 560ppmwN Air	225	60000	107800	227
HF010 560ppmwN Vac	300	22000	57700	276

Table 5.6: Overall HCF strength for each composition and environmental condition measured during this work. *HF022 and HF036 were left to fail at the same stress despite going past the step length, HCF strengths have been calculated on the basis of the samples being a run out. **These values have been calculated disregarding HF036.

Sample Type	HCF Strength (MPa)	Debit Air to Vacuum (MPa)	Debit Air to Vacuum (%)
XR Plate Air	279*		
XR Plate Vacuum	289	10 (**56)	3.5 (**19.4)
240ppmN Air	239*		
240ppmN Vacuum	314	75	23.9
560ppmN Air	217		
560ppmN Vacuum	284	67	23.6

Table 5.7: This table shows the data from the quantitative fractography

		Crack Growth Rate (Microns per Cycle)			
	Sample	Lowest	Highest	Range	Average
Vacuum	HF010 560ppmwN	0.112	5.178	5.07	0.7
	HF028 240ppmwN	0.050	3.190	3.14	0.6
	HF035 XR Plate	0.082	2.750	2.67	0.5
Air	HF002 560ppmwN	0.104	2.735	2.63	0.8
	HF022 240ppmwN	0.144	5.387	5.24	1.4
	HF036 XR Plate	0.063	4.433	4.37	0.9

Chapter 6

The effect of a surface gradient of nitrogen in Ti-6Al-4V on fatigue crack growth in a vacuum environment

Abstract

This stage of the work was the culmination of the data gathered so far, working to apply the novel hollow sample test method coupled with knowledge about the effect of nitrogen. Following on from chapter 5, oxygen and nitrogen gradients were formed in some of the hollow test pieces to simulate contamination seen in some reference samples. The gradients produced were compared to reference samples and were found to be close enough to be representative for the purposes of this study. The testing showed that the gradient significantly reduced the life to crack initiation and changed the location of initiation from a single point to a broad front around the notch. It was also found that the effect of the gradient on fractography and fatigue crack growth rates reduced to baseline as the gradient reduced back to normal chemistry.

6.1 Introduction

Titanium components manufactured via superplastic forming can be susceptible to the ingress of interstitial species into exposed surfaces during the forming process. Understanding the effect of any diffused gradient of interstitials on fatigue crack initiation, crack propagation

rate and fracture mode is key to understanding the variability seen in the service life of affected components. As explored in the previous chapter, the added complication is that these components are often then sealed with internal cavities pumped down to a coarse vacuum prior to sealing which is then followed by stress relieving heat treatments. This combination of effects means that any internally initiating fatigue crack is initiating and growing in a vacuum atmosphere through what could be visualised as a diffuse oxygen and nitrogen rich layer before reaching bulk material. Using air to introduce the gradient is representative of the balance of oxygen and nitrogen that occurs in the reference samples.

6.2 Experimental Procedure

The experimental work in this study has been designed to determine the deleterious effects of any diffused interstitial species on the internal surfaces of diffusion bonded superplastically formed (DB/SPF) components. Figure 6.1 shows the workflow each of the samples has gone through prior to being tested and figure 6.2 shows a schematic representation of the samples tested in this work. This work builds on the previous chapters by combining the information gathered on the effect of nitrogen on Ti-6Al-4V and the effect of vacuum on the fatigue crack properties of Ti-6Al-4V along with the proven test method for samples at vacuum.

As shown in Figure 6.1 the gradient was introduced into the samples (comprising of commercial grade Ti-6Al-4V rolled plate stock) by heating the notched hollow blanks in air in a furnace for varying lengths of time to introduce different levels of interstitials. The higher gradient samples were heat treated in air for 20 minutes at 915°C followed by a vacuum heat treatment for 240 minutes at 750°C. The lower gradient samples were heat treated in air for 5 minutes at 915°C followed by a vacuum heat treatment for 240 minutes at 750°C. The vacuum heat treatment was tailored to drive the interstitial content into the surface to create a gradient closer to that observed in the reference samples, see Figure 6.3 and Figure 6.4. The gradient was characterised by Loughborough Surface Analysis (LSA) using Dynamic Secondary Ion Mass Spectroscopy (DSIMS). Note, the plots are showing the combined interstitial content in counts per second as a function of depth in from the surface; the combined interstitial content has been

compiled using the following equation [56].

$$\text{Oxygen equivalent} = \text{Oxygen} + 2 \times \text{Nitrogen} + \frac{2}{3} \times \text{Carbon} \tag{6.1}$$

Examples of each of the sample variations (no gradient, low gradient and high gradient) were step tested to failure using an Amsler vibrophore to determine the high cycle fatigue (HCF) strength (similar to the work in the previous chapter) to allow for optimisation of loading and scheduling of the ex-situ computed tomography (CT). The results of these life tests were then utilised to set the peak stress for the loading of the samples being monitored for crack growth characteristics to try and achieve a similar number of load cycles and CT rounds before sample failure.

For the crack propagation characterisation, ex-situ CT was used, with a custom fabricated tensile rig (figure 6.6) for loading the samples into the CT machine. The author designed the rig utilising ideas from a rig used by Professor Peter Lee, but improved upon the design to ensure more consistent axial alignment and much faster change over of samples. For reference the CT machine used was a Nikon (XTech) XT H 225. The tensile rig allowed the samples to be loaded up to around 1.06kN (or around 10MPa) to allow the crack faces to be partially separated to enable better contrast and detection of any cracking present. This method was utilised to try and characterise approximate crack initiation life and macroscopic crack propagation rate. The CT scan data was processed using FEI's Avizo software.

Initially an optical overview was captured using a stepper motor controlled digital SLR camera which enabled for comparative feature recognition when examining the samples in the scanning electron microscope (SEM). A Zeiss Sigma 300 Field Emission Gun - Scanning Electron Microscope (FEG-SEM) was used for the electron microscope fractography. SEM fractographs were captured at a low magnification to give an overview comparative to the optical overview captured. Regions of interest were identified and where striations were present those were counted using a Rolls-Royce proprietary method to provide density measurements at a range of locations around the sample. The density measurements were compared to the CT images to give a coarse comparison.

6.3 Results

Table 6.1 contains the results of the life tests carried out as sighters for the ex-citu CT work. It shows that both of the populations of samples with a gradient of interstitial had similarly reduced HCF strengths in comparison to the plain samples with no gradient. The difference was a reduction of around 47MPa equating to around a drop of 17% from the plain no gradient samples. It was decided that ideally each of the three samples to be monitored by ex-situ CT would be tested at the same peak stress with that value picked based on achieving a workable lifetime on the gradient. The value chosen was 250MPa as the four gradient samples all failed around the 100k cycle mark at 250MPa.

Table 6.2 shows the approximate initiation life determined by ex-citu CT, percentage of total life to initiation, cycles achieved at failure and the calculated HCF strength of three samples monitored by ex-situ CT. The gradient samples show a reduced initiation life and similar total life/strength to the life tests.

Table 6.3 shows the results of collating all the life data from the samples tested. This table shows that with a larger number of samples, the life debit of the gradient samples is slightly reduced (to 24MPa equating to around a drop of around 9%) from the initial life tests.

Table 6.4 details the cumulative cycles between CT scans illustrating the variable intervals between scans. The intervals were changed based on reviews of the CT data after each scan, looking for evidence of cracking and/or crack growth.

Each of the three samples monitored by ex-situ CT was photographed and then examined in the SEM after failure. Figures 6.7, 6.11 and 6.15 show optical and SEM overviews for each sample. Examples of common fractographic features from each sample are shown in figures 6.8, 6.12 and 6.16 and include regions of both facets and striations. The macroscopic crack growth was observed to follow two patterns, one for samples with a gradient and one for samples with no gradient. Figure 6.19 shows the two patterns observed.

Examination of the CT scan data enabled an approximation of crack length development to be compiled as shown in figures 6.9, 6.13 and 6.17.

Quantitative SEM fractographic data with µm per cycle values located where the SEM

analysis was undertaken as shown in figures 6.10, 6.14 and 6.18. Figure 6.20 shows the result of the striation density measurements for the three ex-situ CT monitored samples. Table 6.5 shows the lowest, highest, range of rates and average fatigue crack growth rates for each of the ex-situ CT samples.

6.4 Discussion

6.4.1 Sample production

The combined interstitial content was used as both oxygen and nitrogen are absorbed into the surface of the reference samples and both have very similar effects on the alloy. The plots shown in Figures 6.3 & 6.4 illustrate that two distinct gradients were produced with similar properties to the reference samples. The main difference observed was that the initial interstitial content (i.e up to around 6 µm) was much higher than the reference plots with the profile dropping below the reference plots after that point. It was felt that the gradients generated in these samples were representative enough of the overall effect that would have been seen from the reference samples that the findings from this study are relevant and applicable for components exhibiting this phenomenon.

6.4.2 Numerical Results

The samples that had the interstitial gradient applied showed a clear trend of achieving a significantly reduced calculated HCF strength values of around 24MPa or 9% lower than the no gradient samples. This was expected from the conclusions of Chapter 4 which showed that even fairly modest levels of increased interstitials caused a significant drop off in fatigue capability. Although it was obviously known that the mechanical property reduction would only be present for as long as the crack was growing through material affected by the gradient. An inference from the results in Chapter 4 was that the initiation life on gradient samples would be the major factor in the reduction of life to failure. The reason behind this thinking was due to the large reduction in ductility observed when large amounts of interstitials are added, it was expected

that a crack would initiate from the notch early in the sample's life taking away the time taken to first crack which makes up a large portion of the sample life to failure. The work carried out in this chapter has been able to show a clear confirmation that it is indeed the initiation life that has been drastically reduced with the addition of the gradient, it was found that there was an approximate reduction in initiation life of around 50 000 cycles or 78%. Further confirmation that the initiation stage drove the difference, came through the comparative crack propagation speeds observed from the quantitative fractography which show that the range of crack propagation speeds are broadly similar for each sample, despite the different failure lives. Figure 6.20 shows the range of crack propagation data captured during the quantitative SEM fractography. Ordinarily this type of data would be correlated to crack depth; however, this sample geometry makes determining that in an accurate manner all but impossible. So, for the purposes of this figure, the data has been presented as isolated measurements showing the range of crack growth rates observed. All the data in Figure 6.20 has been captured in material outside of the applied gradient. This data generally agrees with the crack growth rates observed from the ex-situ CT work. Closer correlation hasn't been possible due to the coarse gaps in the ex-situ CT scans and the highly localised nature of the striation density measurements. As discussed in chapter 5, the underlying texture of the striated regions will also cause differences in the rates measured by the two methods with the CT method being averaged over a much large area of the sample due to the scan intervals.

6.4.3 CT and Fractographic Results

Although the coarse gaps in the crack growth rate gathered from the ex-situ CT monitoring leave something to be desired in comparison to Potential Drop (PD) monitoring, using it had potential other benefits such as being able to monitor crack shape development. Unfortunately this work wasn't able to be completed in time for inclusion in this thesis. However, examination of the raw data did show regions of the growing cracks not always having a clear route back to the notch in 2D section views. This is indicative of crack tunnelling, where the crack has followed preferential crystallographic orientation rather than a classical pure stress driven crack shape. Knowing how the crack shape had developed would allow visualisation that would illustrate a

correlation of fractographic features to the actual crack length rather than just the resultant distance from the initiation location. It is well known that in polycrystalline materials (especially hexagonal close packed materials) with multiple phases and complex varied crystallographic textures the grain level crack front will vary from the macroscopic crack front. The samples tested contained microscopically significantly sized primary alpha macrozones. Those primary alpha macrozones have responded in interesting ways, causing the crack to preferentially grow in directions outside of conventional modelled crack growth shapes, by providing regions of material that provide less of a hindrance to crack growth due to the close alignment of slip planes between the primary alpha grains. This is of particular interest when features such as striations are found on fracture faces at distances considered too close to the initiation location on the basis of assumption that the crack length at feature formation was equal to the distance to the initiation location. Even from limited observations made using ex-situ CT in this work, it was possible to add confidence to theories discussed within industrial circles (The author has led multiple discussion around fractographic practices on α+β titanium alloys with engineering fellows from his employers competition.) that crack path tortuosity caused by underlying crystallographic texture can provide opportunities for errors during post failure fractography with simple crack length measurements not always giving an accurate understanding of the actual crack length at time of feature formation.

The SEM fractography confirmed the differences in initiation between the samples with a gradient and those without. For reference when looking at the fractography, Figure 6.5 shows a shaded image of a fracture face from S013. The yellow shading indicates the testing fracture, the blue shading is the notch surface and the red shading represents the material that contains the gradient of interstitials. The gradient samples exhibited multiple initiation locations around the circumference characterised by brittle facets as shown in figure 6.12 for example, whereas the samples without the gradient typically exhibited a single initiation location as shown in figure 6.16. The gradient samples were also characterised by the change in fractography associated with the change from gradient to normal material, with the gradient containing material being characterised by brittle faceting with little to no ductility visible on the facet surfaces. What all the samples had in common however, was the presence of a significant amount

of striated growth. As discussed in Chapter 5, the work in this thesis has shown that Ti-6Al-4V does striate in a vacuum environment and the striations are clear and well formed.

6.5 Conclusions

1. The method used to introduce the gradient was found to have worked reasonably well with the results close enough to be representative of the reference samples for this work and provide relevant data. With further feedback iterations, a closer match to the reference samples would be achievable but would have been prohibitively expensive.

2. The gradient of interstitial content caused a drastic reduction in initiation life in the order of 80% leading to a shorter overall life to failure. It was observed however, that once the crack was growing in normal chemistry material the crack growth rates were within those observed in no gradient material. This finding is of great importance when taken into consideration alongside the fact that the majority of the fatigue life of titanium components is taken up with life to initiation. This finding shows that it is of great importance to keep any ingress of interstitials to a minimum to preserve the life to crack initiation.

3. Fractographically these samples have confirmed that the increase in interstitial content causes a change in fractography towards flat planar faceting, with the fracture appearance returning to as expected once the chemistry returns to nominal. The presence of clear striations formed in a vacuum environment has again been confirmed in this chapter. This is relevant to industrial failure analysis as it means that a lack of striated growth does not mean that the fracture was generated in a vacuum, rather other factors such as crystallographic orientation are having a dominant effect.

6.6 Figures and Tables

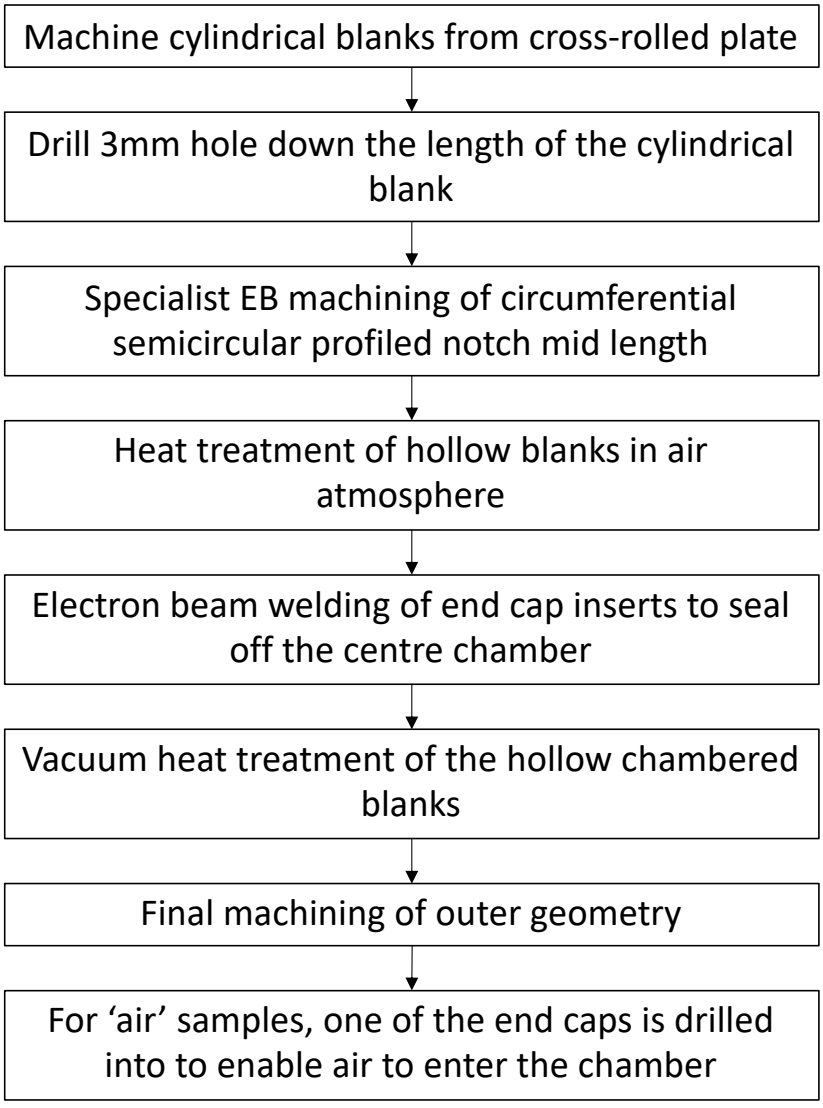

Figure 6.1: This schematic shows the steps taken to produce the samples for this study

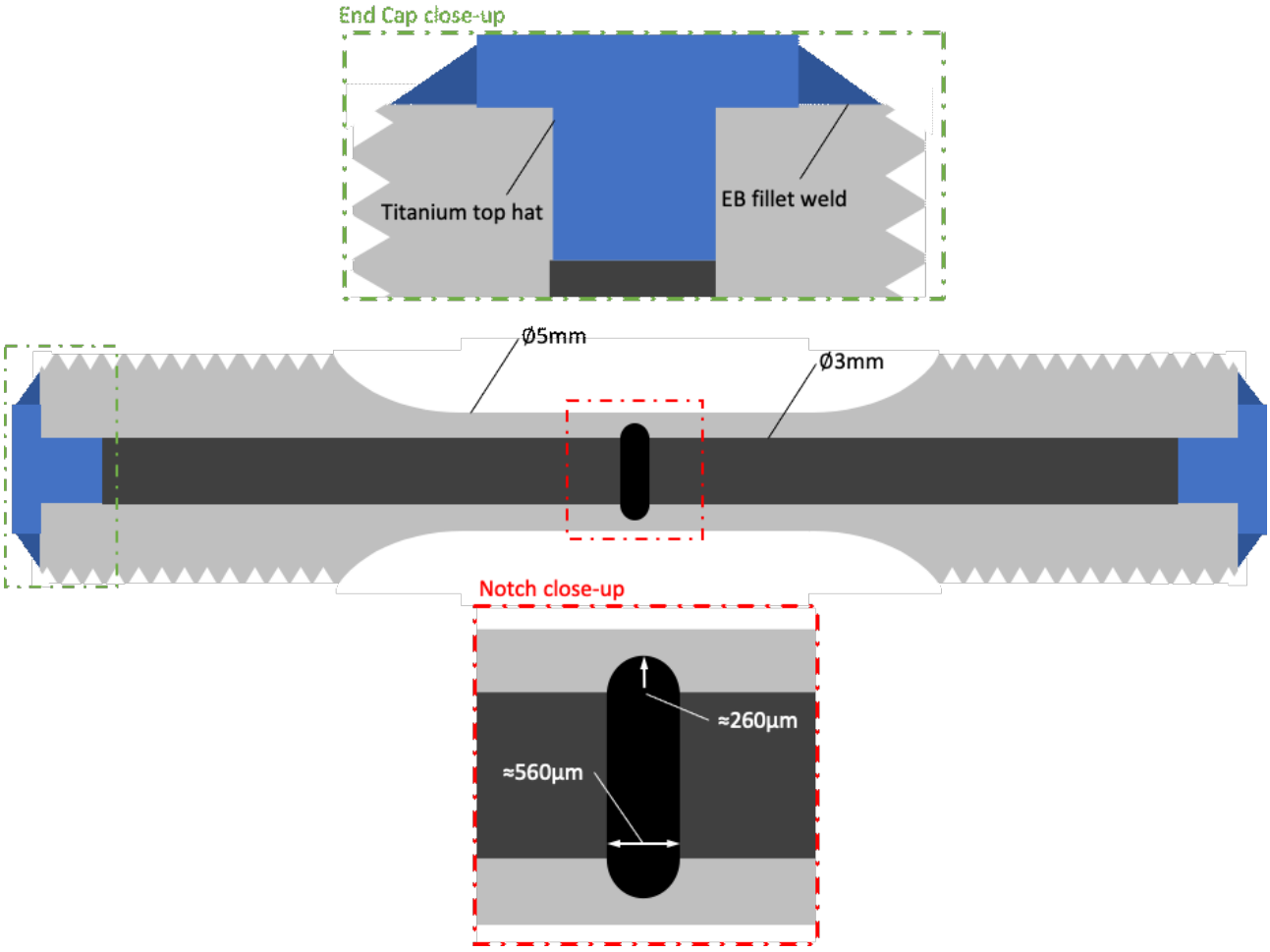

Figure 6.2: This schematic shows a cross-section representation of the samples tested in this work

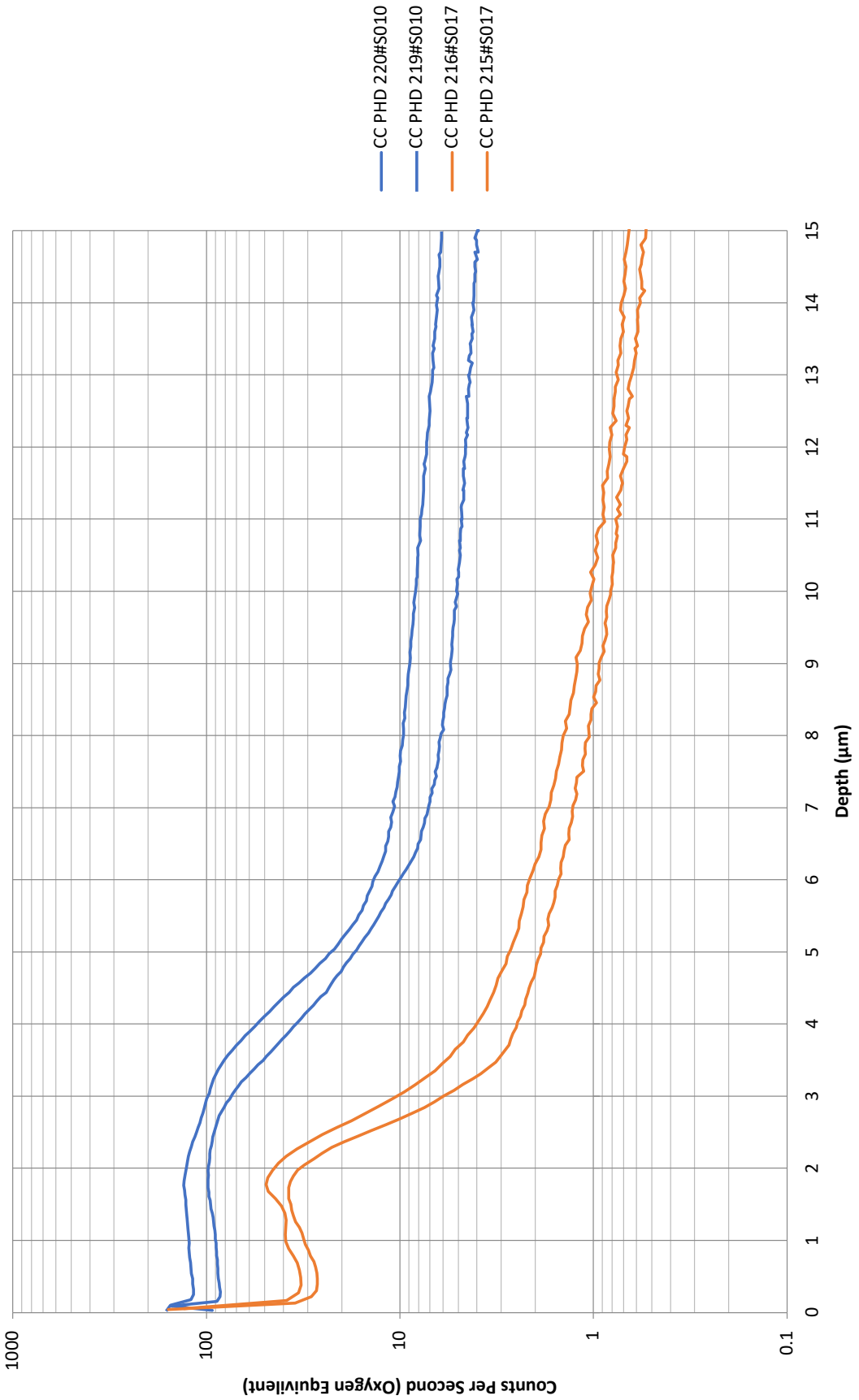

Figure 6.3: This chart shows the measured interstitial gradient via DSIMS of the lower and higher gradient samples. For reference, these gradients up to around 3 to 5µm, contain in the order of 3000-4000ppmw O + N

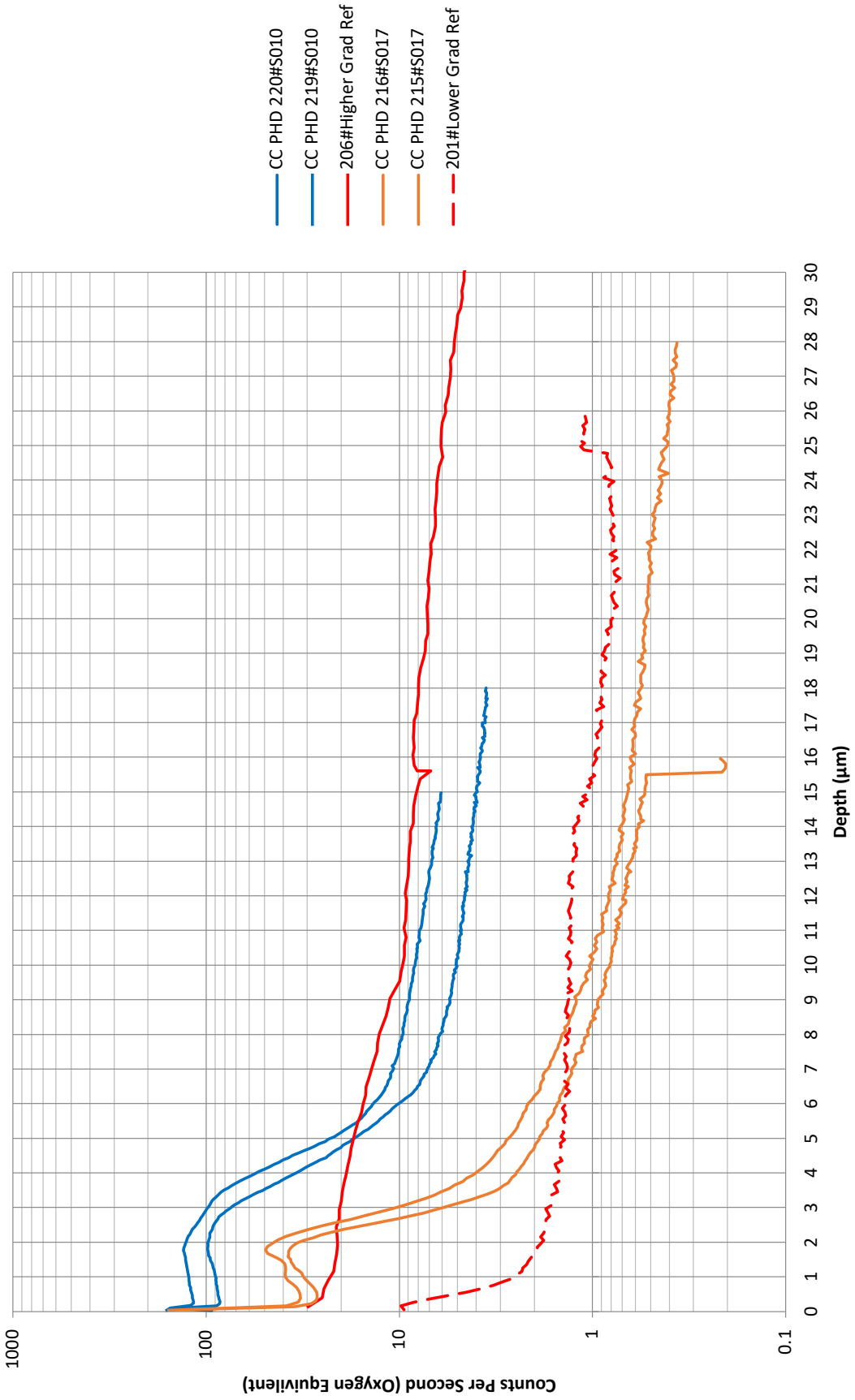

Figure 6.4: This chart shows the measured interstitial gradient via DSIMS of the lower and higher gradient samples compared to some component results

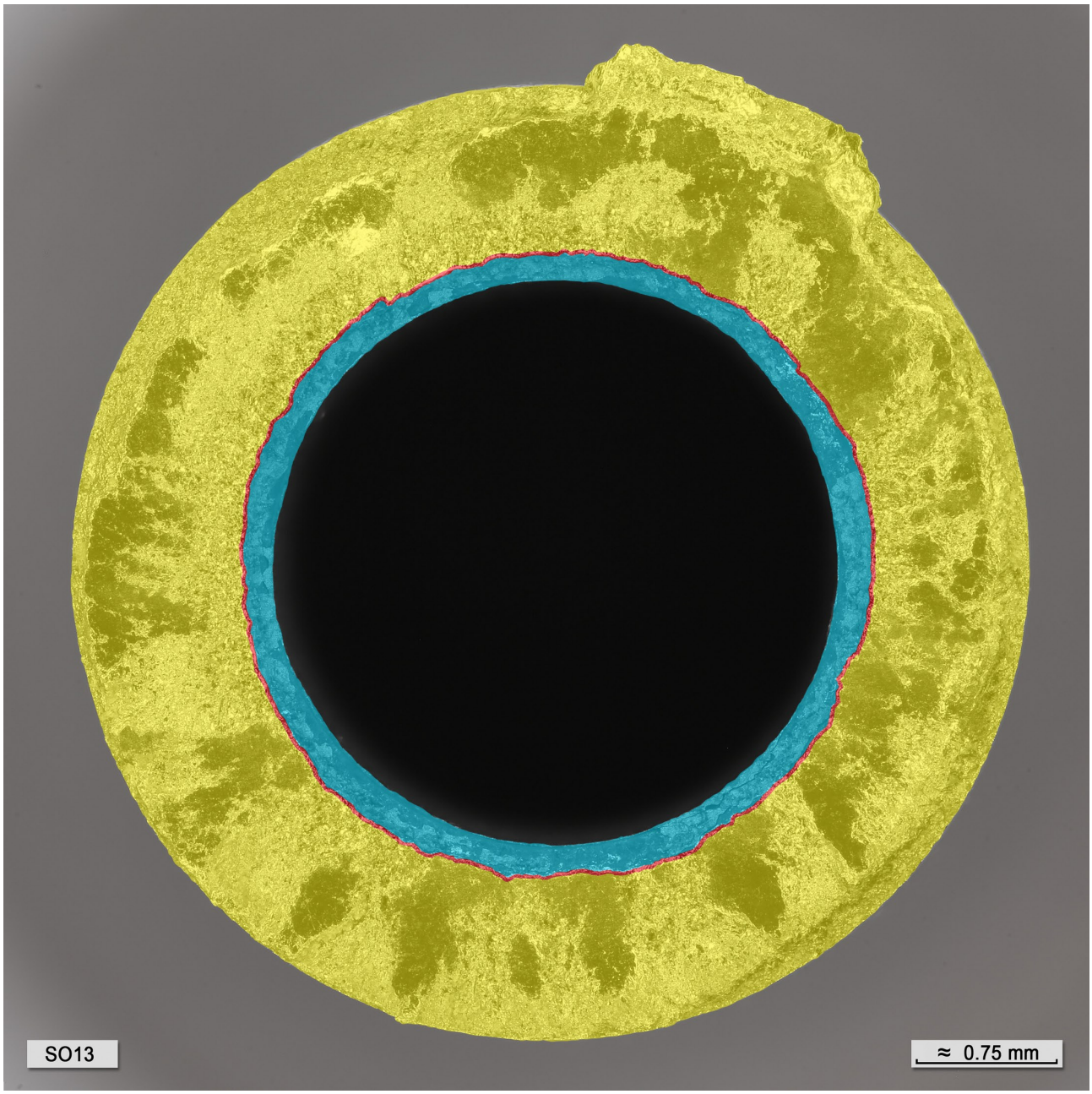

Figure 6.5: This figure shows the optical overview from HF035 with the notch surface highlighted in blue shading, the testing induced fracture shaded yellow and the red shading representing the material affected by the gradient of interstitials.

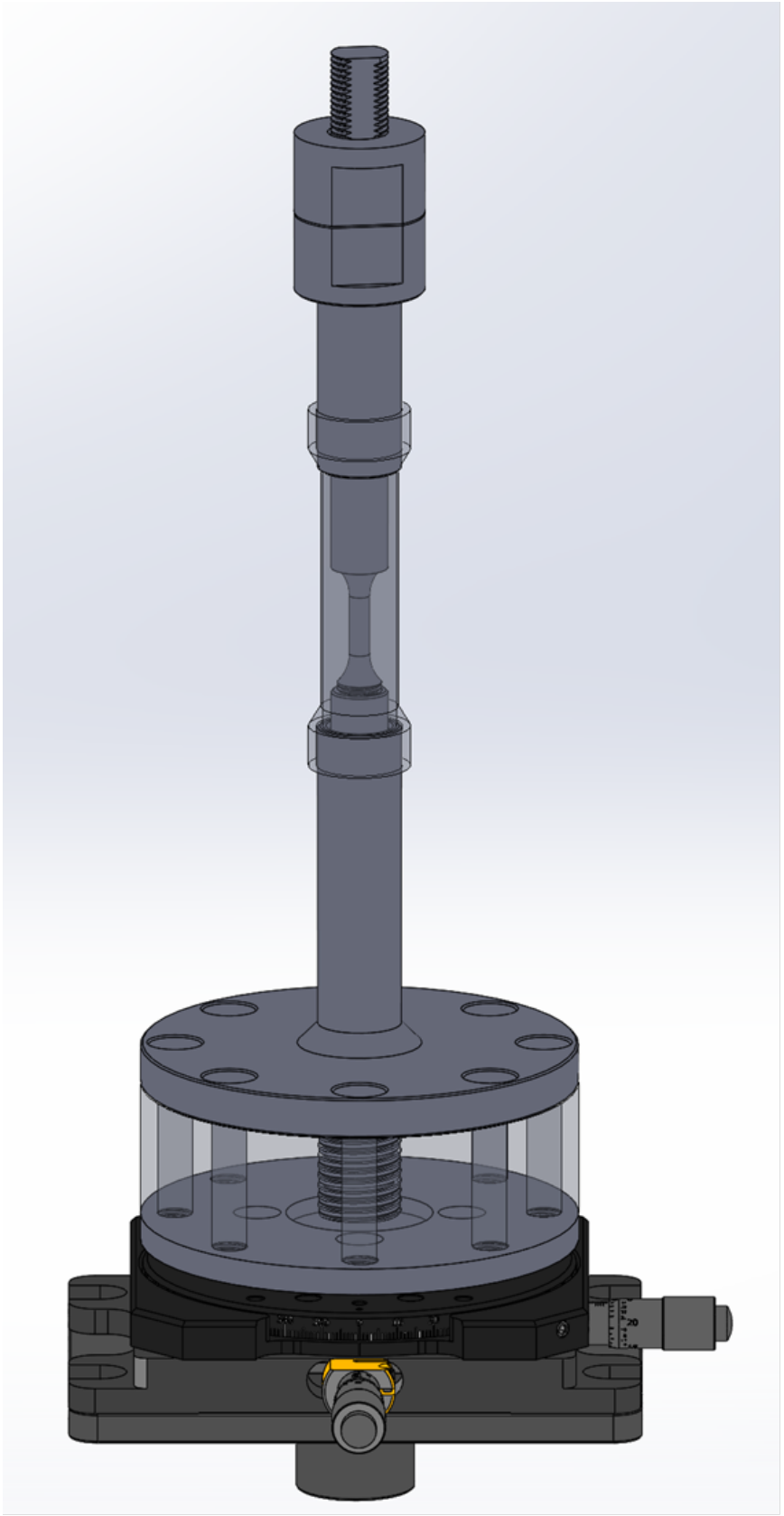

Figure 6.6: This figure shows a CAD representation of the custom tensile rig used during the ex-situ CT work. The base plate was movable by X and Y micrometers to allow for centring to the centreline of the detector. The sleeve around the sample (set to transparency here) had mating faces that allowed for rapid sample exchange keeping it straight in the vertical axis.

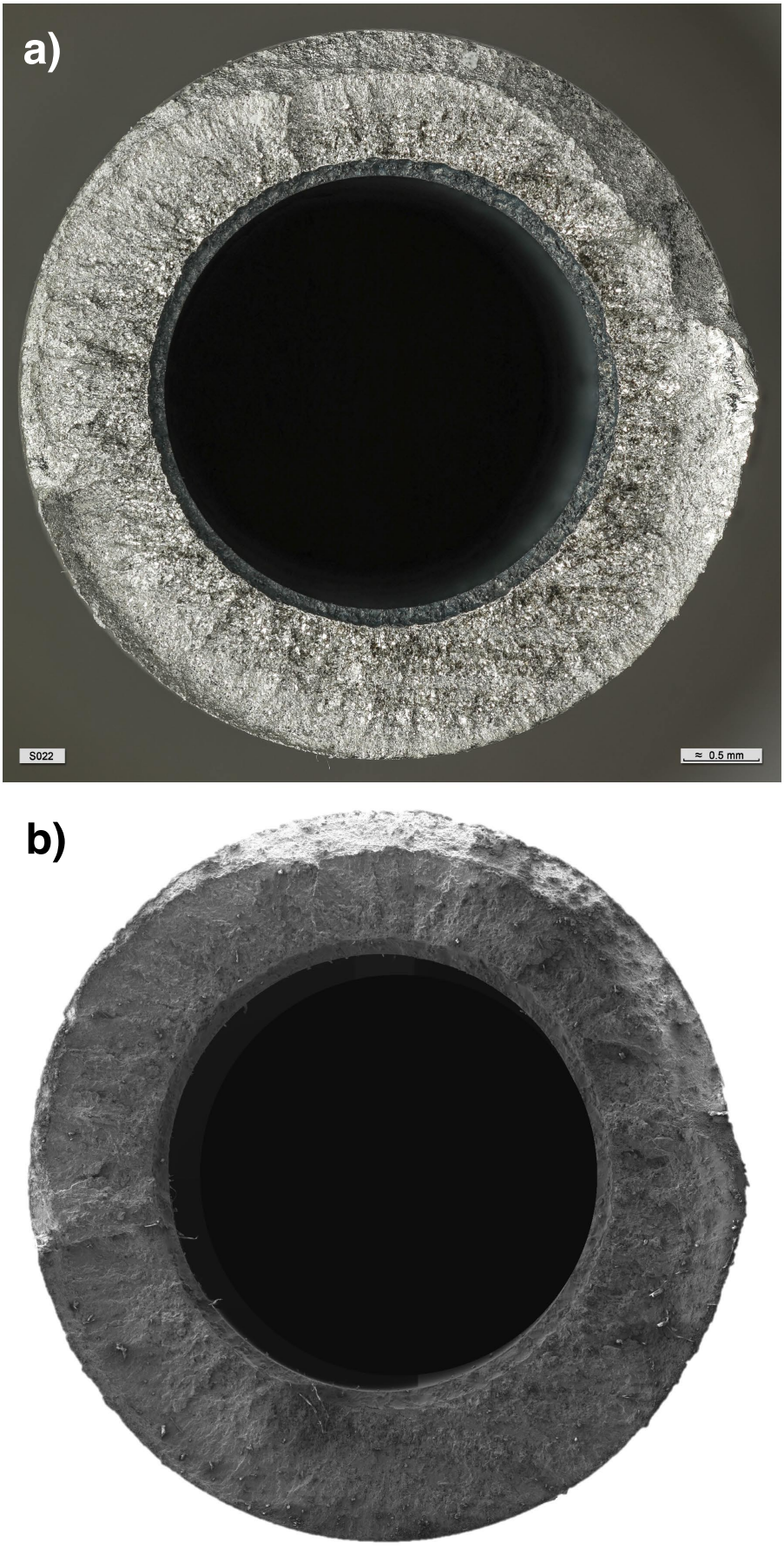

Figure 6.7: This figure shows a) an optical overview of a fracture from S022 Low gradient sample and b) an SEM overview of the same fracture face (SE, 5.00kV, WD 9.3mm)

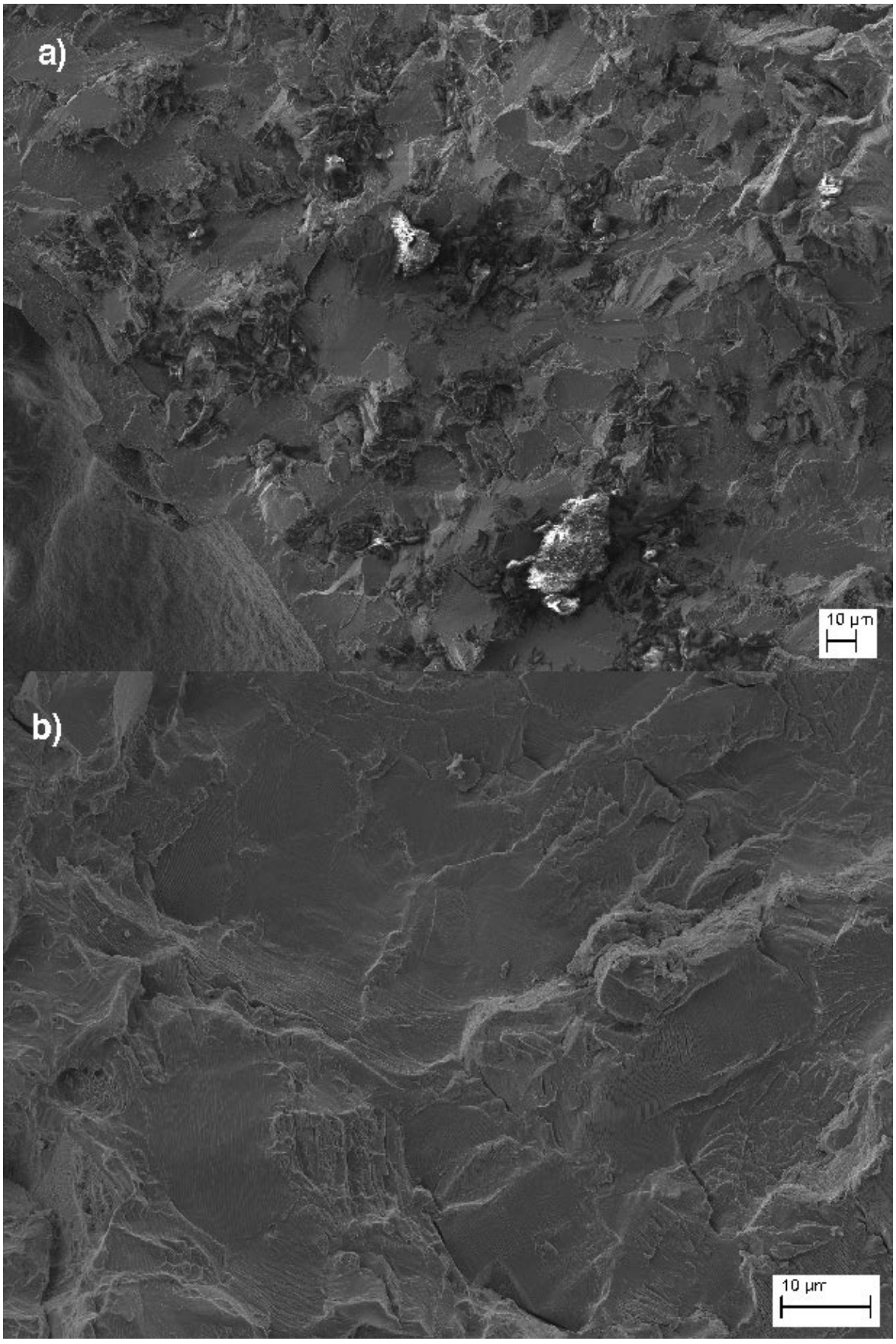

Figure 6.8: This figure shows an SEM fractograph showing a) a region of facetted growth originating from the notch (SE, 5.00kV, WD 9.4mm) and b) a region of striated growth (SE, 5.00kV, WD 9.4mm) from S022 Low gradient sample

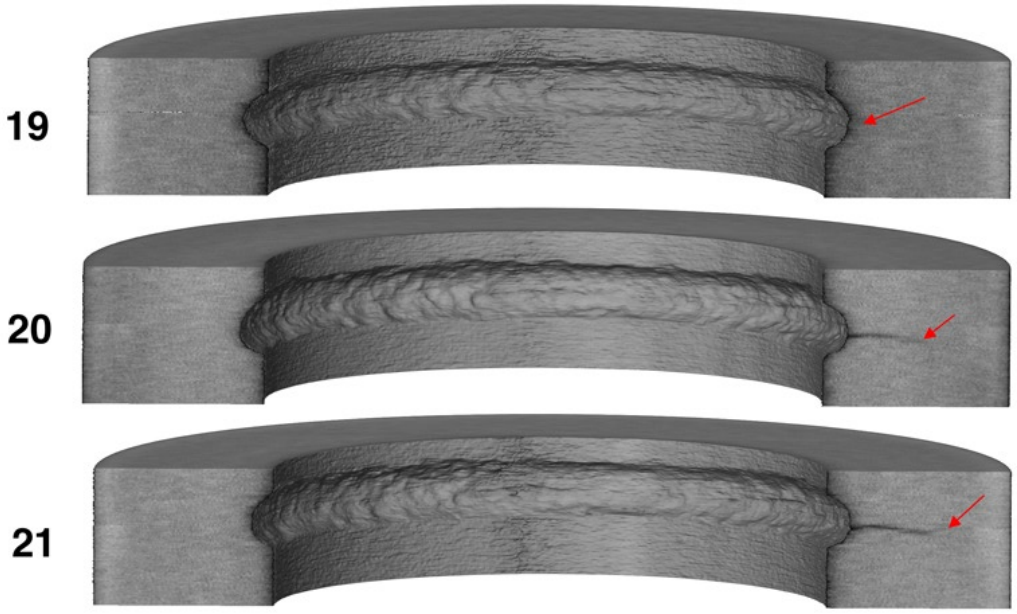

Figure 6.9: This figure shows a number of 3D CT reconstructions (unregistered) of S022 Low gradient sample illustrating the coarse crack growth through the sample. The number next to each image signifies the CT scan number and the red arrows are there to aid the reader to spot the extent of cracking

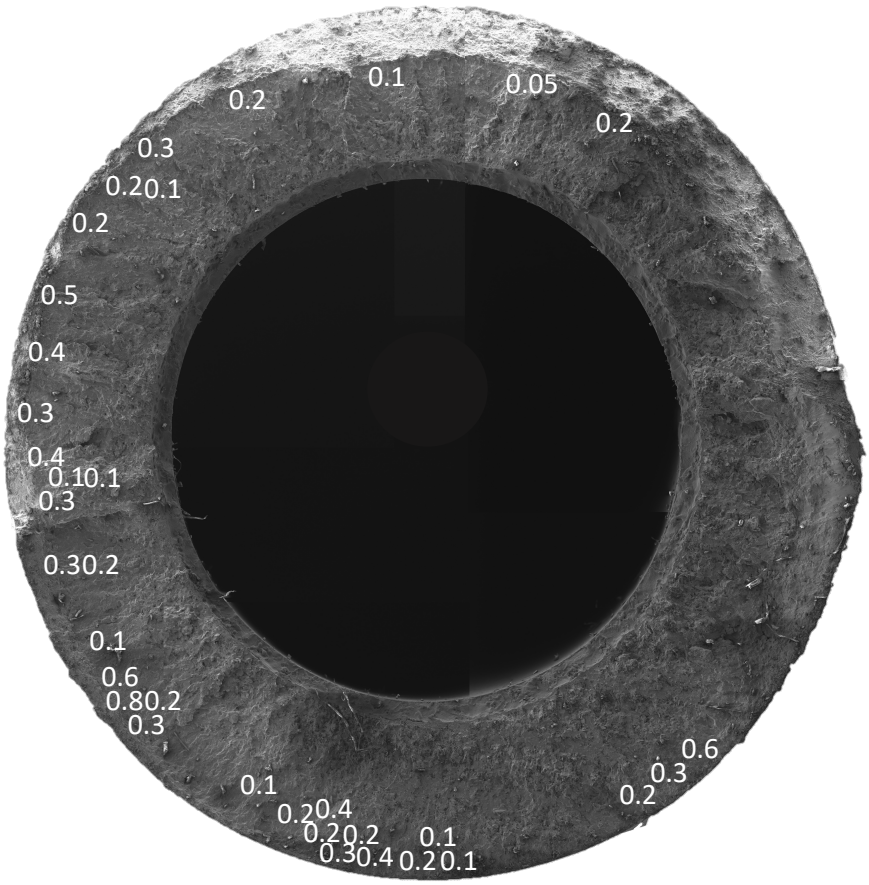

Figure 6.10: This figure shows the crack growth rates in µm per cycle at isolated locations as determined by SEM fractography for S022 Low gradient sample

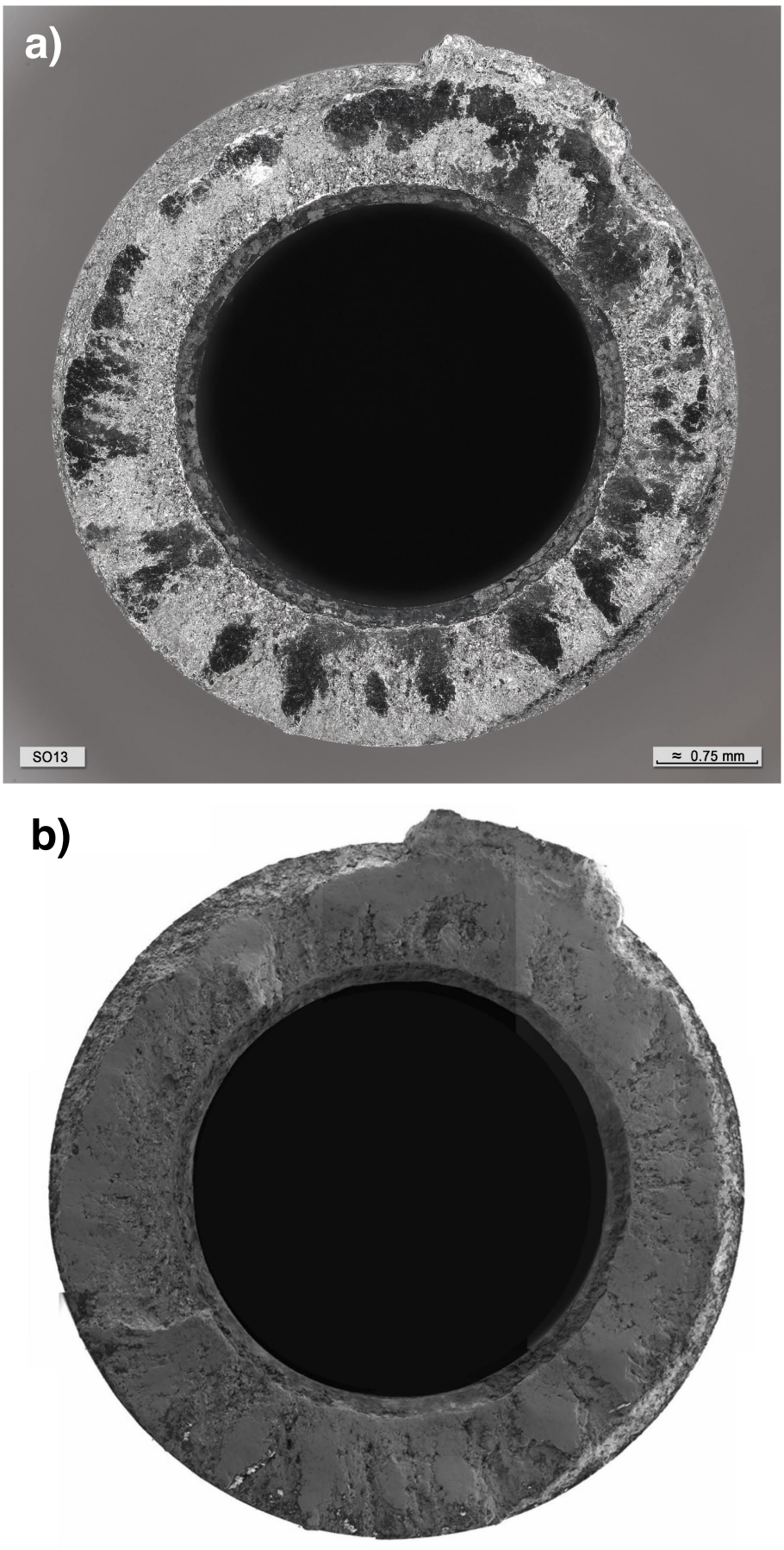

Figure 6.11: This figure shows a) an optical overview of a fracture from S013 High gradient sample and b) an SEM overview of the same fracture face (SE, 5.00kV, WD 5.3mm)

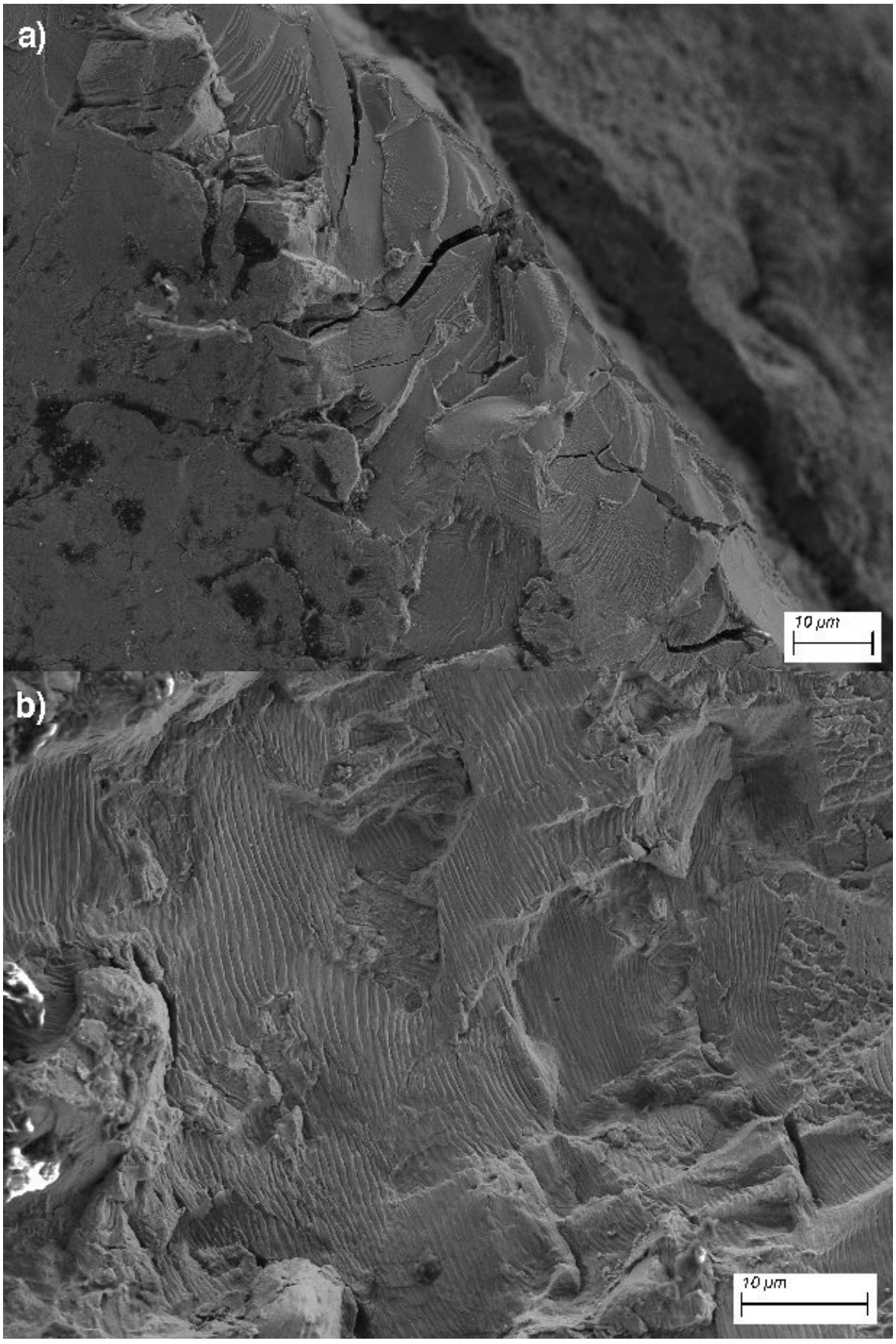

Figure 6.12: This figure shows an SEM fractograph showing a) a region of facetted growth originating from the notch (SE, 5.00kV, WD 5.0mm) and b) a region of striated growth (SE, 5.00kV, WD 5.1mm) from S013 High gradient sample

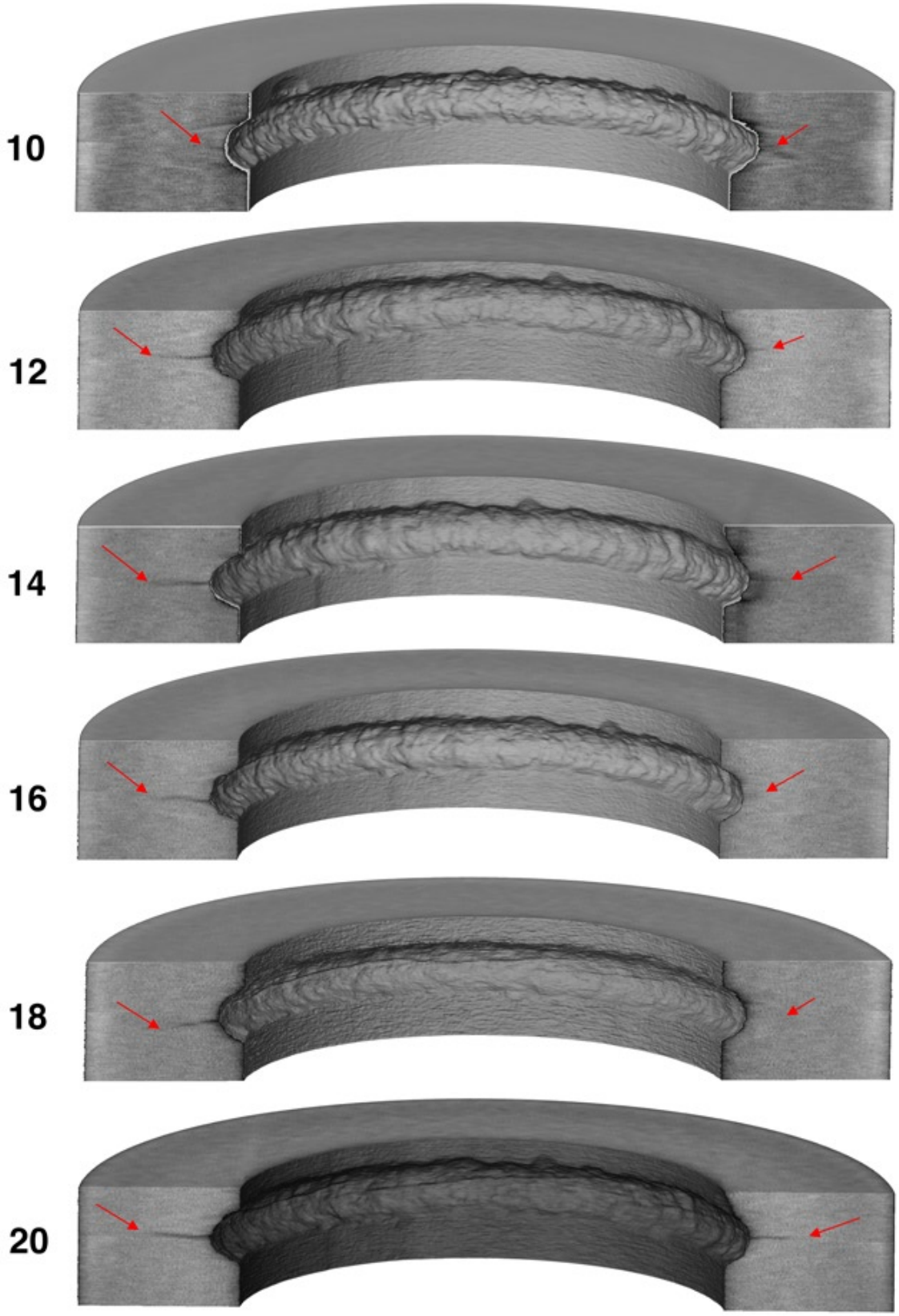

Figure 6.13: This figure shows a number of 3D CT reconstructions (unregistered) of S013 High gradient sample illustrating the coarse crack growth through the sample. The number next to each image signifies the CT scan number and the red arrows are there to aid the reader to spot the extent of cracking

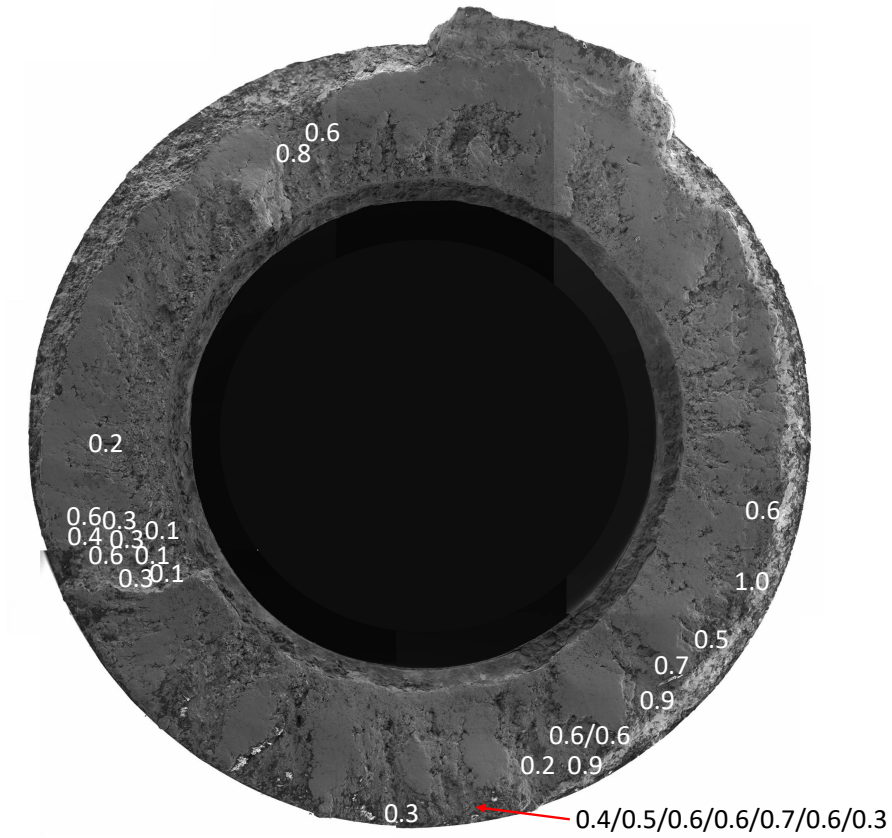

Figure 6.14: This figure shows the crack growth rates in µm per cycle at isolated locations as determined by SEM fractography for S013 High gradient sample

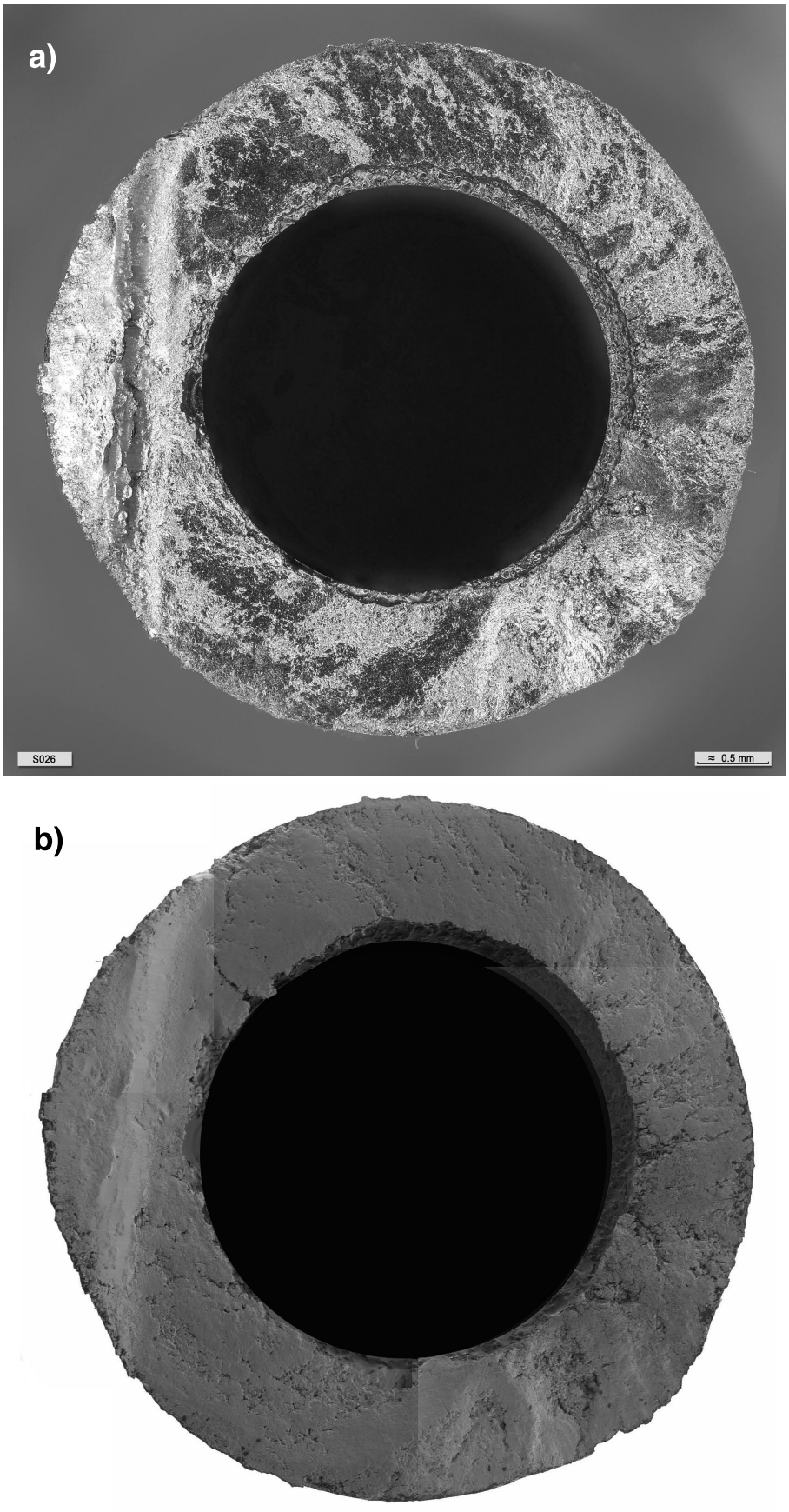

Figure 6.15: This figure shows a) an optical overview of a fracture from S026 No gradient sample and b) an SEM overview of the same fracture face (SE, 5.00kV, WD 4.7mm)

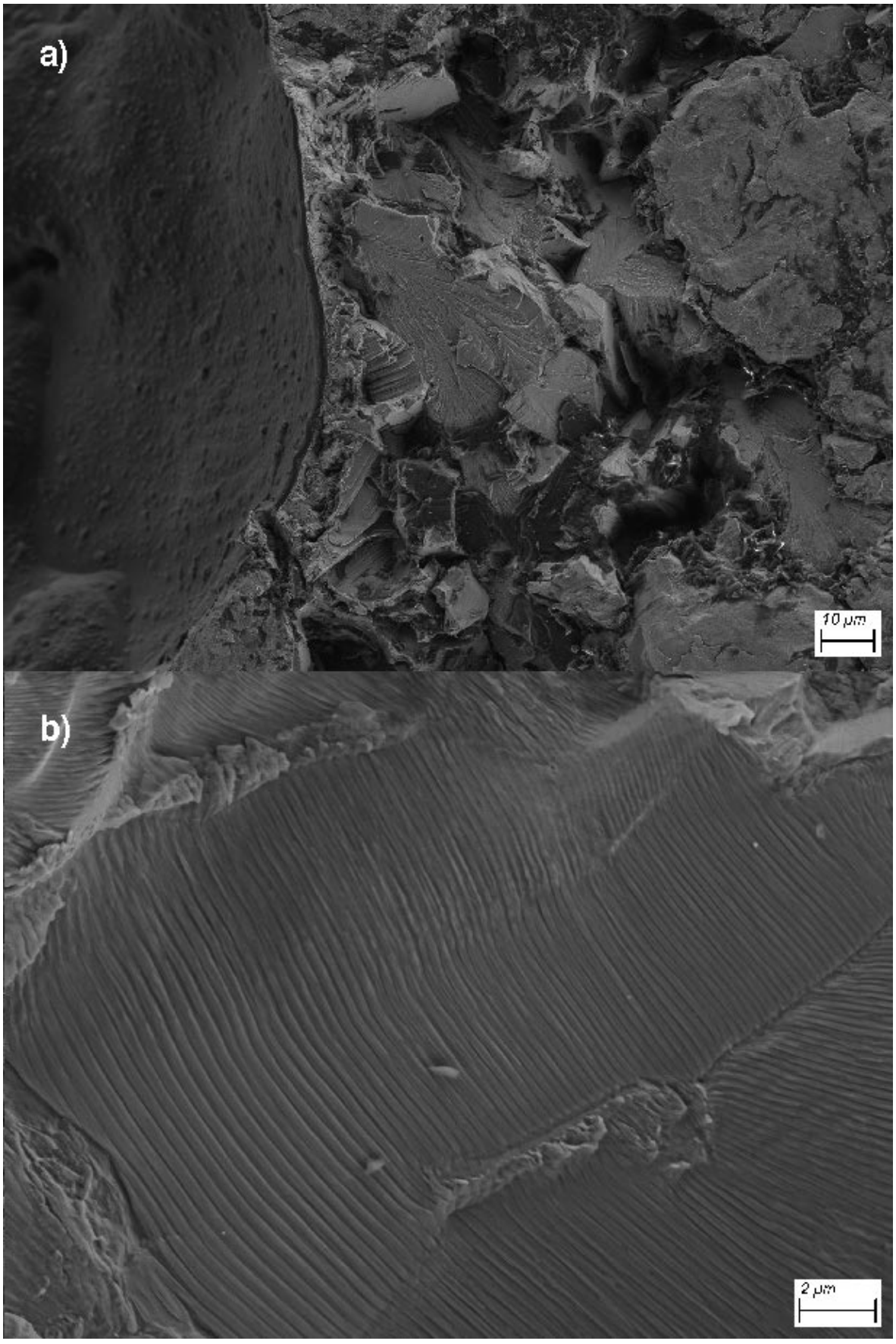

Figure 6.16: This figure shows an SEM fractograph showing a) a region of facetted growth originating from the notch (SE, 5.00kV, WD 4.7mm) and b) a region of striated growth (SE, 5.00kV, WD 4.7mm) from S026 No gradient sample

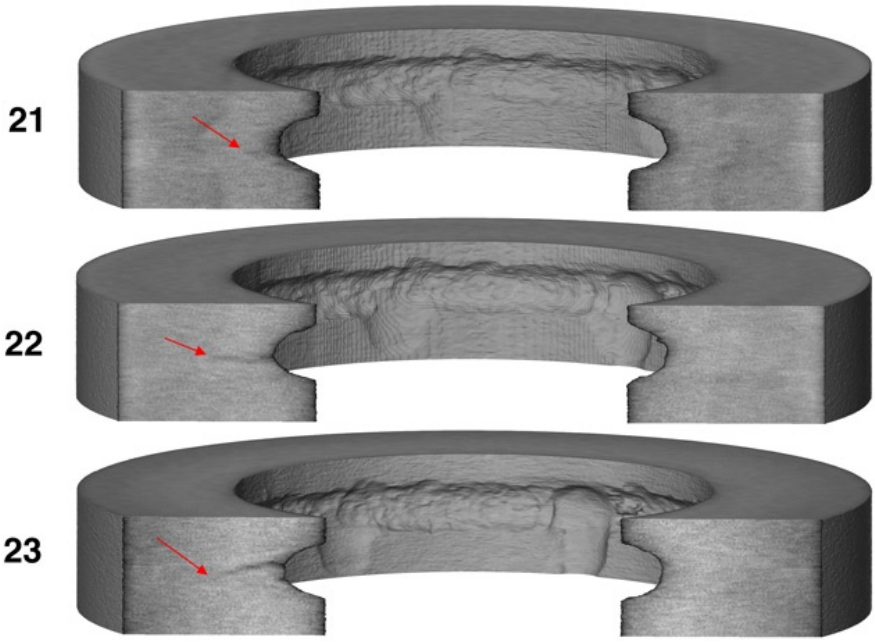

Figure 6.17: This figure shows a number of 3D CT reconstructions (unregistered) of S026 No gradient sample illustrating the coarse crack growth through the sample. The number next to each image signifies the CT scan number and the red arrows are there to aid the reader to spot the extent of cracking

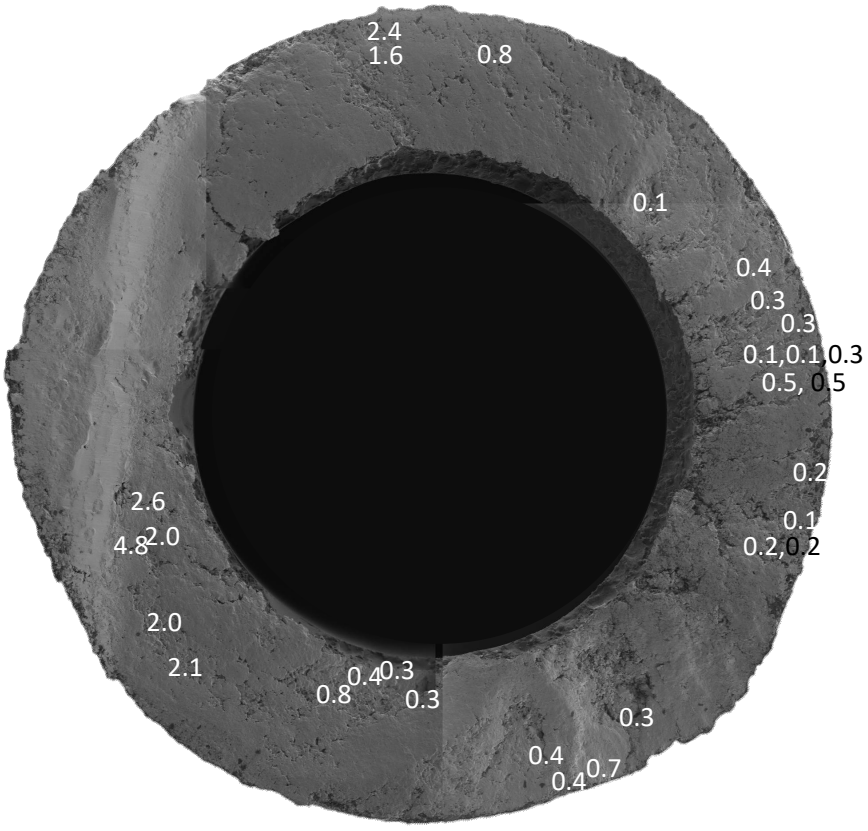

Figure 6.18: This figure shows the crack growth rates in µm per cycle at isolated locations as determined by SEM fractography for S026 No gradient sample

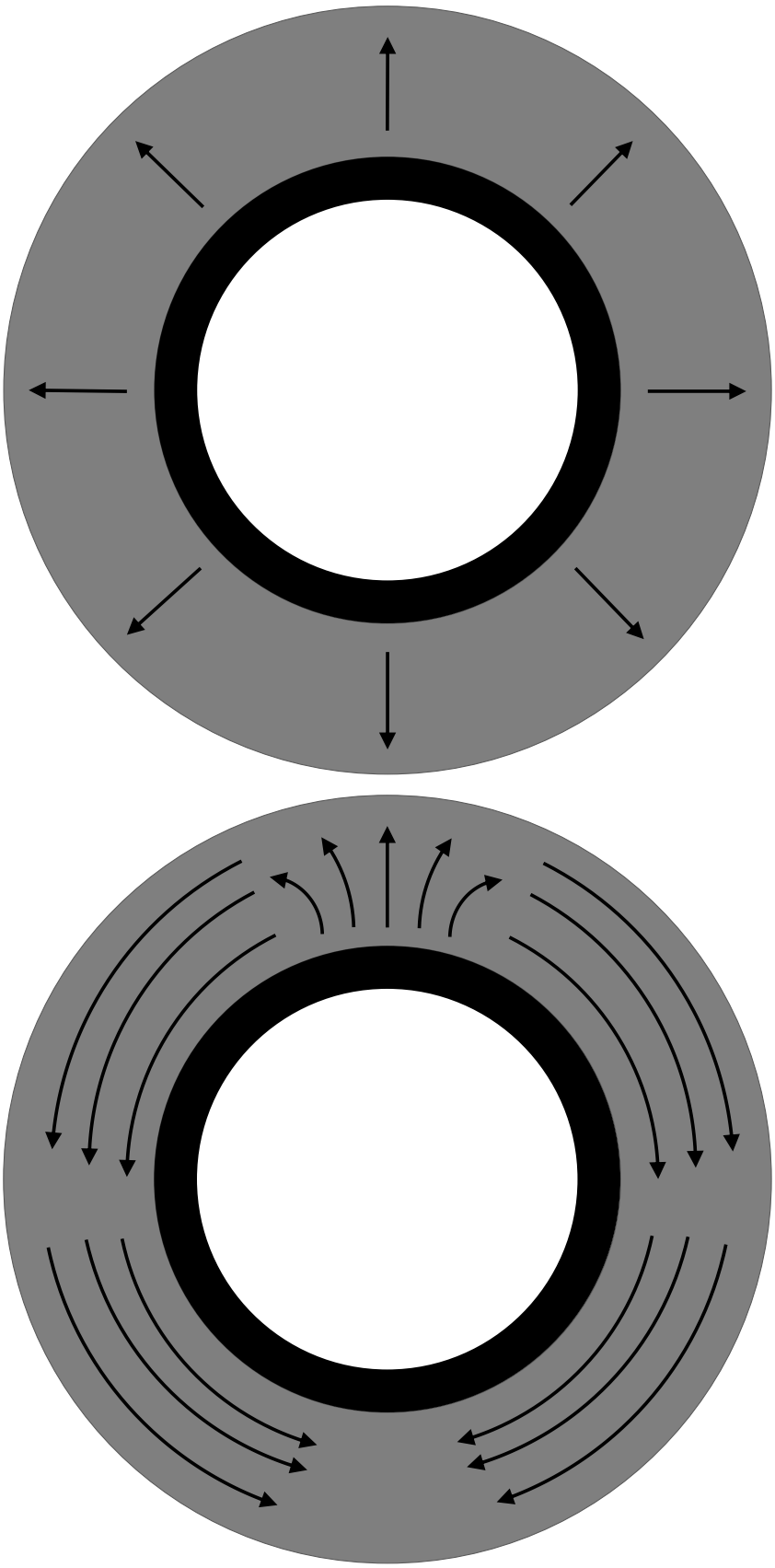

Figure 6.19: This figure shows two schematics indicating the general macroscopic crack propagation behaviours observed from the samples in this chapter. The top schematic shows what was observed on samples with a gradient and the lower schematic what was observed on the samples with no gradient (as was also observed in chapter 5)

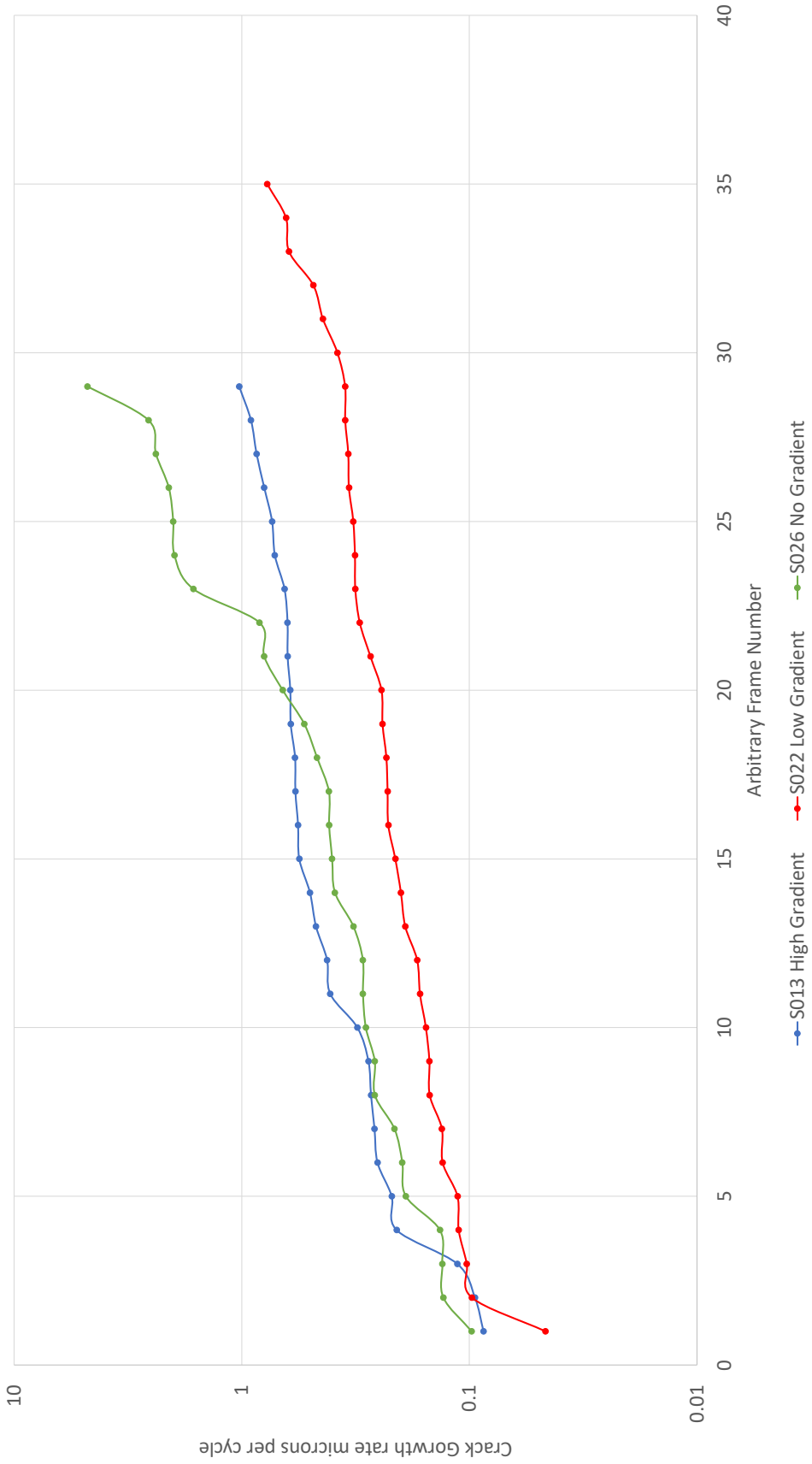

Figure 6.20: This figure shows a comparison of the range of crack propagation rates captured from the quantitative SEM fractography, all the data points have been captured from baseline material

Table 6.1: This table shows the results of the life tests carried out to determine test conditions for the ex-situ CT work

Sample	Cycles (000's) at Peak Stress (MPa)						Calculated HCF
	170	200	225	250	275	300	Strength (MPa)
No Gradient	R/o	R/o	R/o	507			238
				R/o	R/o	439	286
Low Gradient				127			228
				67			227
High Gradient				116			228
				110			228
* where R/o indicates a run out result							

Table 6.2: This table shows the initiation life in cycles, as a percentage of total life, total samples lives and the calculated HCF strengths from the ex-situ testing

Sample	Cycles at first CT indication	Percentage of total life	Cycles at 250MPa Peak Stress	Calculated HCF Strength (MPa)
No Gradient - S026	72000	41	175700	229
Low Gradient - S022	27000	16	171500	229
High Gradient - S013	6000	11	52300	226

Table 6.3: This table shows the average calculated HCF strength from the results of all the tested samples

Gradient Level	Average Calculated HCF Strength (MPa)
No Gradient	251
Low Gradient	228
High Gradient	227

Table 6.4: This table shows the scan intervals for the ex-situ CT scans - All cycles testing at a peak stress of 250MPa

Scan	Sample life at ex-situ CT scan		
	Low Gradient - S022	High Gradient - S013	No Gradient - S026
Initial	0	0	0
1	5000	5000	5000
2	6000	6000	6000
3	7000	7000	7000
4	8000	8000	8000
5	9000	9000	9000
6	10000	10000	10000
7	11000	11000	11000
8	12000	12000	12000
9	13000	13000	13000
10	14000	14000	14000
11	15000	15000	15000
12	16000	16000	16000
13	17000	17000	17000
14	22000	22000	22000
15	27000	23000	27000
16	32000	24000	32000
17	37000	25000	42000
18	47000	30000	52000
19	67000	40000	72000
20	97000	52300	92000
21	171500		97000
22			107000
23			175700

Table 6.5: This table shows the data from the quantitative fractography

	Crack Growth Rate (µm per cycle)			
Sample	Lowest	Highest	Range	Average
S026 No Gradient	0.098	4.767	4.67	0.9
S022 Low Gradient	0.046	0.772	0.73	0.3
S013 High Gradient	0.087	1.027	0.94	0.5

Chapter 7

Conclusions and Further Work

7.1 Overview of Chapter Conclusions

At the beginning of this work, the following subquestions were posed:

- What effect does nitrogen have on the mechanical properties of Ti-6Al-4V?
- What effect does a vacuum environment have on the fatigue properties of Ti-6Al-4V?
- What effect does a vacuum environment coupled with a diffused gradient of nitrogen have on the fatigue properties of Ti-6Al-4V?

From the experiments undertaken the following conclusions were reached:

7.1.1 Chapter 4 - What effect does nitrogen have on the mechanical properties of Ti-6Al-4V?

The effect of nitrogen additions on the fatigue behaviour of Ti-6Al-4V have been examined in a series of test bars that were processed to achieve nominally identical, near-equiaxed microstructures. The following conclusions can be drawn.

1. Nitrogen additions increased the beta transus temperature, whilst also increasing the required level of strain to break up the microstructure during hot processing. Increasing the nitrogen content up to around 560ppmwN shows a benefit to UTS with a small trade-off in ductility; however, beyond this point unacceptably low levels of ductility remained.

2. In R=0.1 testing at 820 MPa, low cycle fatigue endurance approximately halved from 22,000 to 13,000 cycles with doubling of nitrogen content from 240 to 560ppmwN. Similarly, a continuous decrease in HCF strength at the 10^6 cycle level was observed, from around 560 MPa in commercial product to around 360 MPa in heavily nitrogen-contaminated (3600ppmwN) material. No lower bound of additional nitrogen content was observed that did not have a detrimental effect - even levels of 240ppmwN and 560ppmwN showed a deficit compared to commercial product, and the effect of nitrogen on HCF strength per at.% was greater at smaller levels of addition, inversely following the effects on strength.

3. The HCF fracture surfaces in the samples with only small nitrogen additions were similar to those observed in conventional product, as previously reported by Bantounas et al [9], with striated fatigue crack growth in grains well oriented for <a>slip, but relatively flat fractography near the initiation site, which was just subsurface, although still with some evidence of plasticity. In contrast at high nitrogen contents, 1800ppmwN and above, the fracture surfaces showed a macroscopically rougher and more brittle appearance was observed, but with extensive evidence of ductility running along the length of each α_p plate and no observation of conventional striations that would aid in post-hoc fatigue crack growth lifetime assessment.

Therefore metallographic microstructure examination is not necessarily a reliable indicator of an absence of deleterious nitrogen contamination in surfaces; given the difficulty of measuring low levels of nitrogen in the electron microscope, this should be carefully recalled when assessing fracture initiation in potentially nitrogen affected components.

7.1.2 Chapter 5 - What effect does a vacuum environment have on the fatigue properties of Ti-6Al-4V?

1. The test method devised and undertaken in this chapter has proved to be successful at allowing a crack to be initiated and grown in a vacuum environment without relying on a vacuum test chamber. The quality of the vacuum in the samples was found to be very high when analysed. Although the cost and complexity in creating the samples could be seen as prohibitive, it has enabled the differences between laboratory test samples and in-service components to be

reduced which adds real value in reading across the test results.

2. A clear debit in the region of 20% has been found for sample lives when tested in air as opposed to vacuum. This makes a significant difference when component lifetimes are taken into consideration. Typical fatigue testing is undertaken in air and so could be found to give pessimistic life data when compared to a component being operated in a vacuum. Fatigue crack growth rates were found to be similar between air and vacuum samples with only a slight upward trend on the average growth rates in air vs vacuum. This finding is in disagreement with literature with the cause being put down to issues with inconsistent notch geometry, the coarse nature of the crack growth measurements and the limited number of samples tested.

3. From a fractography perspective, the presence of striations on the fracture faces from the samples tested with a vacuum environment was a finding that is in disagreement with published literature. The amount of striated growth was seen to be fairly consistent across all the samples examined with underlying crystallographic texture and composition differences found to be the primary factors in inhibiting striation formation. The quality of the striations formed in a vacuum was also found to be perfectly clear enough for analysis with no noticeable difference to air samples.

7.1.3 Chapter 6 - What effect does a vacuum environment coupled with a diffused gradient of nitrogen have on the fatigue properties of Ti-6Al-4V?

1. The method used to introduce the gradient was found to have worked reasonably well with the results close enough to be representative of the reference samples for this work and provide relevant data. With further feedback iterations, a closer match to the reference samples would be achievable but would have been prohibitively expensive.

2. The gradient of interstitial content caused a drastic reduction in initiation life in the order of 80% leading to a shorter overall life to failure. It was observed however, that once the crack was growing in normal chemistry material the crack growth rates were within those observed in no gradient material. This finding is of great importance when taken into consideration alongside

the fact that the majority of the fatigue life of titanium components is taken up with life to initiation. This finding shows that it is of great importance to keep any ingress of interstitials to a minimum to preserve the life to crack initiation.

3. Fractographically these samples have confirmed that the increase in interstitial content causes a change in fractography towards flat planar faceting, with the fracture appearance returning to as expected once the chemistry returns to nominal. The presence of clear striations formed in a vacuum environment has again been confirmed in this chapter. This is relevant to industrial failure analysis as it means that a lack of striated growth does not mean that the fracture was generated in a vacuum, rather other factors such as crystallographic orientation are having a dominant effect.

7.2 Summary of Conclusions and Review of the Problem

The primary question posed at the start of this work was - "What effect does an ingress of nitrogen have on the integrity of super-plastically formed titanium components". The summary of the conclusions reached from the experimental work undertaken to answer the subquestions drawn from that primary question allow for an answer to be reached.

Nitrogen has been shown to have deleterious effects on the mechanical capability of Ti-6Al-4V both in bulk quantities and in a broadly representative diffused gradient on a sample surface[1]. The final test methodology reached in Chapter 5 has allowed the author to conduct experiments on laboratory test samples that are able to better represent the material state of a contaminated super-plastically formed component than could have been achieved utilising a conventional test sample whilst being significantly more controlled and cheaper than equivalent testing on full scale components. Although not fully representative of a component that has had an ingress of nitrogen, the test samples are similar enough for the general conclusions to be applicable when read across to a component with some careful scaling of the magnitude of the effect required.

[1]Alongside this work, the author has conducted further work during the course of his day job that has provided further corroboration of the assertion that an increase in the interstitial content of internal surfaces of super-plastically formed components is deleterious for the mechanical capability of those components. In that work simple mechanical bend testing of sections removed from a contaminated component has shown microcracking present up to a depth correlating to the depth of interstitial ingress as measured using D-SIMS.

The main takeaway conclusions for the reader should be the following:

1. A gradient of nitrogen diffused into an internal surface in a super-plastically formed component will lead to a reduction in the mechanical capability of that surface. This is a particular concern when fatigue lifetimes are considered as there will be a reduction in life to crack initiation which makes up the majority of a titanium component's life to failure.

2. The nature of the gradient has a significant effect, a shallow deep diffusion profile will have less of a deleterious effect than a steep shallow diffusion profile as the higher concentrated content in the second case will lower the required localised strain to failure at the surface causing a crack to be initiated. However the depth of the diffusion profile will have a large bearing on the capability of the component to survive that initial starter crack.

3. Nitrogen content, the presence of a vacuum and the dominant underlying crystallographic texture of the material have significant effects on mode of fracture and the subsequent observable fractographic features. Care needs to be taken when examining fracture faces from super-plasctically formed titanium components or test samples to ensure the underlying crystallographic texture is understood and the presence of any diffused interstitial species is determined and characterised appropriately to enable more accurate conclusion to be drawn from any fractographic work.

7.3 Lessons learnt

As stated in the introduction, this work has been heavily affected by a number of interruptions (personal and day job driven) and trials arising from global events namely Covid 19. However, it is key for the development of an individual to explore any lessons learnt and possible 'better if's' so work contained within this thesis has been reflected upon and a number of things have been identified and are explained below:

1. It is recognised that the ambitious nature of the test work undertaken with its complex scheduling across multiple research establishments has caused numerous hold-ups during this work. In an ideal world this work would all have taken place under one roof so to speak. However, at the point of developing the experiments there was only one preexisting suitable tensile rig for

using in a laboratory CT setup and so the work was aligned to that setup. As it transpired the rig had to be recreated (at which point it was also reengineered to improve on some flaws with the original rig) due to clashes with programs needing to use it. This meant that in theory the work could have all been carried out at Imperial College with a custom rig created there, but as the partnership with Dr Azeem had already been started the work continued through his departmental facility at Leicester. This transpired to be a major cause of delays in the programme and the work wasn't completed in time for this submission leaving the CT analysis unfulfilled.

2. The scattered and varied nature of fatigue testing has played a significant part in the elongated nature of this program of work. Due to the high fabrication costs of the hollow sample design, the number of samples was very limited which led to a lack of confidence on the fatigue capability of each sample type being tested. This uncertainty led to inefficiencies during the ex-situ testing with too many scans being carried out at short intervals to begin with and then too larger intervals being used later in the test schedule due to the impending conclusion of this PhD. For any repeat work involving this type of sample, a clear improvement would be to undertake a larger number of life tests to gain much better confidence in the life time of samples to allow for better scheduling of the ex-situ CT work. Another approach would be to further tailor the samples to allow for testing in-situ at a beam line facility with sufficient flux to allow for live fatigue crack growth monitoring by CT.

7.4 Further work

Due to the testing overruns already discussed above, there are a number of analysis avenues that were left unexplored. The following work would be a starting point for any further work to glean as much information as possible from the material tested in the course of this work.

1. Further more detailed correlation between specific regions of observed non-uniform crack shape development, common fractographic features and the underlying crystallographic texture of those regions. These samples give the opportunity to provide clear detailed illustration of these tie-ups that have been suggested by other studies but without the ability to provide

knowledge of the crack shape development that would have been enabled by the use of CT crack growth monitoring in this work.

2. Correlation of the crack propagation rate as determined by ex-situ CT to the underlying crystallographic texture and fractographic features. There are two lines of enquiry that would be of particular interest from this work: Firstly it would be of interest to determine crack growth rates at equivalent crack depths in a range of different primary alpha orientations. Secondly, if the time resolution was sufficient, determining the crack growth rate through regions of facetted crack growth in comparison to regions of striated growth from equivalent crack depths would be of great value to the industrial fractography community.

3. Characterisation of the presence and density of dislocations in the region of the gradient samples where the gradient washes out into bulk chemistry. Included in this work would be some crack path strain analysis utilising high resolution EBSD of cross-sections of the fracture in the same location. The aim of this work would be to determine if there is a pause in crack growth as the crack passes out of the gradient material and into the bulk chemistry. If a pause was identified this would be of value when service management of contaminated components was being considered. An extension of this work would be to introduce an overload cycle after the crack has transitioned into bulk chemistry to see if that overload cycle could blunt the crack with the aim of increasing sample life to failure.

References

[1] Tomohiro Ando, Toshihiro Tsuchiyama, and Setsuo Takaki. Effect of nitrogen on tensile deformation behavior and development of deformation structure in titanium. *Nippon Kinzoku Gakkaishi/Journal of the Japan Institute of Metals*, 72(12):949–954, 2008.

[2] IJ Andrews, D. Rugg, and MJ Wallis. Method of making and joining an aerofoil and root, 2006.

[3] ASM International. Fatigue. In *Elements of Metallurgy and Engineering Alloys*, chapter 14, pages 243–265. ASM International, 2008.

[4] ASTM. E1409-13: Standard Test Method for Determination of Oxygen and Nitrogen in Titanium and Titanium Alloys by Inert Gas Fusion. *ASTM Standards*, pages 1–7, 2013.

[5] AXT. AXT - Computed Tomography 3D Imaging and Non-Destructive Testing (https://www.axt.com.au/computed-tomography/ - accessed September 2020).

[6] M.R. Bache, W.J. Evans, and M. McElhone. The effects of environment and internal oxygen on fatigue crack propagation in Ti-6Al-4V. *Materials Science and Engineering: A*, 234-236:918–922, 1997.

[7] P. A.J. Bagot, A. Radecka, A. P. Magyar, Y. Gong, D. C. Bell, G. D.W. Smith, M. P. Moody, D. Dye, and D. Rugg. The effect of oxidation on the subsurface microstructure of a Ti-6Al-4V alloy. *Scripta Materialia*, 148:24–28, 2018.

[8] I. Bantounas. *Microtexture and High Cycle Fatigue Cracking in Ti-6Al-4V*. PhD thesis, Imperial College London, 2008.

[9] I Bantounas, TC. Lindley, D Rugg, and D Dye. Effect of microtexture on fatigue cracking in Ti-6Al-4V. *Acta Materialia*, 55(16):5655–5665, 2007.

[10] CD Beachem and DA Meyn. Fracture by Microscopic Plastic Deformation Processes. *Electron Fractography*, ASTM STP43:59–88, 1968.

[11] M Benedetti and V Fontanari. The role of bi-modal and lamellar microstructures of Ti-6Al-4V on the behavior of fatigue cracks emanating from edge-notches. *Fatigue & Fracture of Engineering Materials and Structures*, 27(11):1073–1089, 2004.

[12] F. Bridier, P. Villechaise, and J. Mendez. Slip and fatigue crack formation processes in an alpha/beta titanium alloy in relation to crystallographic texture on different scales. *Acta Materialia*, 56(15):3951–3962, 2008.

[13] Benjamin P. Brown, Loren Picco, Mervyn J. Miles, and Charl F.J. Faul. Opportunities in high-speed atomic force microscopy. *Small*, 9(19):3201–3211, 2013.

[14] M. Brown, D. Wright, R. M'Saoubi, J. McGourlay, M. Wallis, A. Mantle, P. Crawforth, and H. Ghadbeigi. Destructive and non-destructive testing methods for characterization and detection of machining-induced white layer: A review paper. *CIRP Journal of Manufacturing Science and Technology*, 23:39–53, 2018.

[15] T. P. Chapman, R. J. Chater, E. A. Saunders, A. M. Walker, T. C. Lindley, and D. Dye. Environmentally assisted fatigue crack nucleation in Ti-6Al-2Sn-4Zr-6Mo. *Corrosion Science*, 96:87–101, 2015.

[16] T P Chapman, K M Kareh, M Knop, T Connolley, P D Lee, M A Azeem, D Rugg, T C Lindley, and D Dye. Acta Materialia Characterisation of short fatigue cracks in titanium alloy IMI 834 using X-ray microtomography. *Acta Materialia*, 99:49–62, 2015.

[17] N E Cherolis. Fatigue in the Aerospace Industry : Striations. *Failure analysis and prevention*, 8:255–258, 2008.

[18] C. Collins, F.F. Dear, D. Rugg, and D. Dye. Failure investigation as a route to improving integrity of titanium alloys in service. *MATEC Web of Conferences*, 321:04007, 2020.

[19] C. R. Collins, F. F. Dear, D. Rugg, and D. Dye. The Effect of Dissolved Nitrogen on the Fatigue Behavior of Ti-6Al-4V. *Metallurgical and Materials Transactions A: Physical Metallurgy and Materials Science*, 52(5):1596–1608, 2021.

[20] Chris Collins. Determining Factors in the Size of Macrozones in Fan Blade Plate. Technical report, Rolls-Royce PLC, Derby, 2019.

[21] W C Connors. Fatigue striation spacing analysis. *Materials Characterization*, 33(3):245–253, 1994.

[22] Hans Conrad. Effect of interstitial solutes on the strength and ductility of titanium. *Progress in Materials Science*, 26(2-4):123–403, jan 1981.

[23] L. De Chiffre, S. Carmignato, J. P. Kruth, R. Schmitt, and A. Weckenmann. Industrial applications of computed tomography. *CIRP Annals - Manufacturing Technology*, 63(2):655–677, 2014.

[24] P. H. DeVries, K. T. Ruth, and D. P. Dennies. Counting on fatigue: Striations and their measure. *Journal of Failure Analysis and Prevention*, 10(2):120–137, 2010.

[25] Claudius Dichtl, Zhenbo Zhang, Hazel Gardner, Paul Bagot, Anna Radecka, David Dye, Matthew Thomas, Rebecca Sandala, João Quinta da Fonseca, and Michael Preuss. Element segregation and $\alpha 2$ formation in primary α of a near-α Ti-alloy. *Materials Characterization*, 164(April):110327, 2020.

[26] W.L. Finlay and J.A. Snyder. No Title. *Trans. Amer. Inst. min. (metall.) Engrs*, 188:277, 1950.

[27] L D. Hefti. Innovations in the superplastic forming and diffusion bonded process. *Journal of Materials Engineering and Performance*, 17(2):178–182, 2008.

[28] E Hershko, N Mandelker, G Gheorghiu, H Sheinkopf, I Cohen, and O Levy. Assessment of fatigue striation counting accuracy using high resolution scanning electron microscope. *Engineering Failure Analysis*, 15:20–27, 2008.

[29] Hiden Analytical. Cracking Patterns (https://www.hidenanalytical.com/tech-data/cracking-patterns/ - Accessed June 2022), 2022.

[30] P. E. Irving and C. J. Beevers. The effect of air and vacuum environments on fatigue crack growth rates in Ti-6Al-4V. *Metallurgical Transactions*, 5(2):391–398, 1974.

[31] Z. N. Ismarrubie, H. Yussof, and M. Sugano. Fatigue damage mechanism of titanium in vacuum and in air. *Procedia Engineering*, 41(Iris):1559–1565, 2012.

[32] ISO. ISO GUIDE 31:2015 Reference materials Contents of certificates, labels and accompanying documentation. Technical report, ISO, 2015.

[33] ISO. ISO 17034:2016 General requirements for the competence of reference material producers. Technical report, ISO, 2016.

[34] ISO. ISO/IEC 17025:2017 General requirements for the competence of testing and calibration laboratories. Technical report, ISO, 2017.

[35] R.I. Jaffee. The physical metallurgy of titanium alloys. *Progress in Metal Physics*, 7:65–163, 1958.

[36] Vydehi Arun Joshi. *Titanium Alloys: An atlas of structures and fracture features.* CRC Press, 2006.

[37] H D Kessler, W Rostoker, and R J Van Thyne. Titanium Phase Diagrams. Technical report, Armour Research Foundation, Illinois Institute of Technology, 1953.

[38] C Laird and G C Smith. Crack propagation in high stress fatigue. *Philosophical Magazine*, 7(77):847–857, 1961.

[39] C Leyens and M Peters. *Titanium and titanium alloys fundamentals and applications.* Weinheim : Wiley-VCH, 2003.

[40] G. Lütjering. Influence of processing on microstructure and mechanical properties of (α+β) titanium alloys. *Materials Science and Engineering: A*, 243(1-2):32–45, mar 1998.

[41] G. Lutjering and J.C. Williams. Titanium : Engineering Materials and Processes. In *Edition SPRINGER*, volume second edi, pages 1–442. 2007.

[42] M. Mulyadi. *Hot Compression Behaviour of Two-Phase Ti-6Al-4V: Experiments and State-Variable Modelling*. 2007.

[43] Mackay TL. Stress Corrosion Cracking of Titanium Alloys At Ambient Temperature in Aqueous Solutions. *NASA Contractor Reports*, 1969.

[44] E. Maire and P. J. Withers. Quantitative X-ray tomography. *International Materials Reviews*, 59(1):1–43, 2014.

[45] R C McClung. Fatigue Behaviour of Titanium Alloys. *TMS 1999*, 1999.

[46] N. R. McDonald and G. R. Wallwork. The reaction of nitrogen with titanium between 800 and 1200C. *Oxidation of Metals*, 2(3):263–283, 1970.

[47] T. D. McKinley. Effect of Impurities on the Hardness of Titanium. *Journal of The Electrochemical Society*, 103(10):561, 1956.

[48] A.D. McQuillan and M.K. McQuillan. *Metallurgy of the Rarer Metals No. 4 - Titanium*. Butterworths Scientific Publications, London, 1st editio edition, 1956.

[49] P.P. Milella. Fatigue and Corrosion in Metals. Springer, Milan, 2012.

[50] R. Montanari, G. Costanza, M. E. Tata, and C. Testani. Lattice expansion of Ti-6Al-4V by nitrogen and oxygen absorption. *Materials Characterization*, 59(3):334–337, 2008.

[51] Takashi Nakamura, Hiroyuki Oguma, and Yuto Shinohara. The effect of vacuum-like environment inside sub-surface fatigue crack on the formation of ODA fracture surface in high strength steel. *Procedia Engineering*, 2(1):2121–2129, 2010.

[52] Sanjeev K. Nayak, Cain J. Hung, Vinit Sharma, S. Pamir Alpay, Avinash M. Dongare, William J. Brindley, and Rainer J. Hebert. Insight into point defects and impurities in titanium from first principles. *npj Computational Materials*, 4(1), 2018.

[53] T Nicholas. *High Cycle Fatigue: A Mechanics of Materials Perspective*. Elsevier, 2006.

[54] Yuhei Nukui, Hiroki Kubozono, Shoichi Kikuchi, Yoshikazu Nakai, Akira Ueno, Mie Ota Kawabata, and Kei Ameyama. Fractographic analysis of fatigue crack initiation and propagation in CP titanium with a bimodal harmonic structure. *Materials Science and Engineering A*, 716(November 2017):228–234, 2018.

[55] Fowler; J O. and B Richardson. Patent: Method of manufacturing an article by superplastic forming and diffusion bonding, 1995.

[56] RI Ogden, HR Jaffee. The effects of carbon, oxygen and nitrogen on the mechanical properties of titanium and titanium alloys. *Office of Assistant Secretary of Defense for Research and Development*, TML Report, 1955.

[57] RI Ogden, HR Jaffee and D.J. Maykuth. No Title. *Trans. Amer. Inst. min. (metall.) Engrs*, 188:1261, 1950.

[58] H. Oguma and T. Nakamura. Fatigue crack propagation properties of Ti-6Al-4V in vacuum environments. *International Journal of Fatigue*, 50:89–93, 2013.

[59] P. C. Paris, M. P. Gomez, and W. E. Anderson. A rational analytic theory of fatiuge, 1961.

[60] J Pauwels. BCR-059 The certification of oxygen in non-ferrous metals. Technical report, Joint Research Centre - Central Bureau for Nuclear Measurements, Geel, Belgium, 1979.

[61] A. L. Pilchak, A. Bhattacharjee, A. H. Rosenberger, and J. C. Williams. Low dK faceted crack growth in titanium alloys. *International Journal of Fatigue*, 31(5):989–994, 2009.

[62] A. L. Pilchak, C. J. Szczepanski, J. A. Shaffer, A. A. Salem, and S. L. Semiatin. Characterization of microstructure, texture, and microtexture in near-alpha titanium mill products. *Metallurgical and Materials Transactions A: Physical Metallurgy and Materials Science*, 44(11):4881–4890, 2013.

[63] J. Polak, T. Lepisto, and P. Kettunen. Surface topography and crack initiation in emerging persistent slip bands in copper single crystals. *Materials Science and Engineering*, 74(1):85–91, 1985.

[64] R. O. Ritchie, D. L. Davidson, B. L. Boyce, J. P. Campbell, and O. Roder. High-cycle fatigue of Ti-6Al-4V. *Fatigue and Fracture of Engineering Materials and Structures*, 22(7):621–631, 1999.

[65] D. L. Ritter and R. P. Wei. Fractographic observations of Ti-6Al-4V alloy fatigued in vacuum. 2(November):3229–3230, 1971.

[66] D. Rugg, T. B. Britton, J. Gong, A. J. Wilkinson, and P. A.J. Bagot. In-service materials support for safety critical applications - A case study of a high strength Ti-alloy using advanced experimental and modelling techniques. *Materials Science and Engineering A*, 599:166–173, 2014.

[67] M. T. Salehi, J. Pilling, N. Ridley, and D. L. Hamilton. Isostatic diffusion bonding of superplastic Ti6Al4V. *Materials Science and Engineering A*, 150(1):1–6, 1992.

[68] DG. Sanders and M Ramulu. Examination of Superplastic Forming Combined with Diffusion Bonding for Titanium: Perspective from Experience. *Journal of Materials Engineering and Performance*, 13(6):744–752, dec 2004.

[69] T. Seshacharyulu, S. C. Medeiros, W. G. Frazier, and Y. V R K Prasad. Microstructural mechanisms during hot working of commercial grade Ti-6Al-4V with lamellar starting structure. *Materials Science and Engineering A*, 325(1-2):112–125, 2002.

[70] M. Shimojo. Peculiar effects of inert gases on fatigue crack growth in an $(\alpha + \beta)$-titanium alloy. *Materials Science and Engineering A*, 354(1-2):24–30, 2003.

[71] M Simura. Plastic fractures of age-hardened aluminum alloys. *Journal of Japan Institute of Light Metals*, 18(11):561–569, 1968.

[72] V. Sinha and J. M. Larsen. Communication: Vacuum levels needed to simulate internal fatigue crack growth in titanium alloys and nickel-base superalloys: Thermodynamic considerations. *Metallurgical and Materials Transactions A: Physical Metallurgy and Materials Science*, 43(10):3433–3441, 2012.

[73] V. Sinha and J. M. Larsen. Communication: Vacuum levels needed to simulate internal fatigue crack growth in titanium alloys and nickel-base superalloys: Thermodynamic considerations. *Metallurgical and Materials Transactions A: Physical Metallurgy and Materials Science*, 43(10):3433–3441, 2012.

[74] R.E. Smallman and A.H.W. Ngan. *Modern Physical Metallurgy*. Butterworth-Heinemann - Elsevier, eigth edition, 2014.

[75] R. A. Smith and S. Hillmansen. A brief historical overview of the fatigue of railway axles. *Proceedings of the Institution of Mechanical Engineers, Part F: Journal of Rail and Rapid Transit*, 218(4):267–277, 2004.

[76] N. Stanford and P. S. Bate. Crystallographic variant selection in Ti-6Al-4V. *Acta Materialia*, 52(17):5215–5224, 2004.

[77] S. R. Stock. Recent advances in X-ray microtomography applied to materials. *International Materials Reviews*, 53(3):129–181, 2008.

[78] Alisa Stratulat, David E.J. Armstrong, and Steve G. Roberts. Micro-mechanical measurement of fracture behaviour of individual grain boundaries in Ni alloy 600 exposed to a pressurized water reactor environment. *Corrosion Science*, 104:9–16, 2016.

[79] M. Sugano, S. Kanno, and T. Satake. Fatigue behavior of titanium in vacuum. *Acta Metallurgica*, 37(7):1811–1820, 1989.

[80] S Suresh. *Fatigue of Materials*. Cambridge University Press, New York, second edition, 1998.

[81] Damir Tagirov, Elena Lashina, and Rustam Kaibyshev. Effect of liquid hot isostatic pressing on structure and mechanical properties of a sand-cast A356.02 alloy. *Metallurgical and Materials Transactions A: Physical Metallurgy and Materials Science*, 44(5):2369–2381, 2013.

[82] P. O. Tympel, T. C. Lindley, E. A. Saunders, M. Dixon, and D. Dye. Influence of complex LCF and dwell load regimes on fatigue of Ti-6Al-4V. *Acta Materialia*, 103:77–88, 2016.

[83] Peter O Tympel. Mechanics and micro-mechanisms of LCF and dwell fatigue in Ti-6Al-4V. (February), 2016.

[84] R J Van Thyne and H D Kessler. Influence of Oxygen, Nitrogen, and Carbon on The Phase Relationships of the Ti-Al System. *Trans. Amer. Inst. min. (metall.) Engrs*, 200:193, 1954.

[85] A. K. Vasudevan, K. Sadananda, and R. L. Holtz. Analysis of vacuum fatigue crack growth results and its implications. *International Journal of Fatigue*, 27(10-12):1519–1529, 2005.

[86] Mike Wallis and Dave Rugg. Patent: Method of manufacturing an article by diffusion bonding and superplastic forming, 2002.

[87] R. J H Wanhill, R. Galatolo, and C. E W Looije. Fractographic and microstructural analysis of fatigue crack growth in a Ti-6Al-4V fan disc forging. *International Journal of Fatigue*, 11(6):407–416, 1989.

[88] R P Wei and D. L. Ritter. The influence of temperature on fatigue-crack growth in a mill-annealed Ti-6Al-4V alloy. Technical report, Lehigh University, Bethlehem PA, 1971.

[89] J. C. Williams, R. R. Boyer, and M. J. Blackburn. The Influence of Microstructure on the Fracture Topography of Titanium Alloys. Technical report, 1968.

[90] P J Withers and M Preuss. Fatigue and Damage in Structural Materials Studied by X-Ray Tomography. *Annual Review of Materials Research*, 42:81–103, 2012.

[91] H. A. Wriedt and J. L. Murray. The N-Ti (Nitrogen-Titanium) system. *Bulletin of Alloy Phase Diagrams*, 8(4):378–388, 1987.

[92] Fumiyoshi Yoshinaka, Takashi Nakamura, and Kazuaki Takaku. Effects of vacuum environment on small fatigue crack propagation in Ti-6Al-4V. *International Journal of Fatigue*, 91:29–38, 2016.

[93] Zeiss. Zeiss - SEM Software (https://www.zeiss.com/microscopy/int/products/microscope-software.html - Accessed May 2020).

[94] Zeiss. Zeiss - SmartProof 5 (https://www.zeiss.com/microscopy/int/products/confocal-microscopes.html - Accessed May 2020).

[95] Zeiss. Zeiss - SmartZoom 5 (https://www.zeiss.com/microscopy/int/products/imaging-systems/smartzoom-5.html - Accessed May 2020).